Experiments in Quantum Optics: Scalable Entangled States and Quantum Computation with Cluster States

Seiji Armstrong

January, 2014

A thesis submitted for the degree of Doctor of Philosophy

This thesis is dedicated to my late father.
He would have loved this quantum stuff.

Acknowledgements

My PhD was an exceptional time for personal growth and I am extremely fortunate to have been surrounded by such wonderful people who are not only excellent scientists, but great companions, and great teachers. First, I would like to sincerely thank my supervisors Hans Bachor, Akira Furusawa, and Ping Koy Lam. Hans, for teaching me that interacting in the community is not only extremely fun and rewarding, but immensely useful in understanding the context of my research. And for being more than a supervisor, for being a friend and mentor who incredibly always made time for a chat. Thanks to your amazing enthusiasm my PhD included a day trip to the Barrier Reef with a nobel laureate, an opportunity to appear on National Television to explain multimode entanglement, and many many more wonderful times. Akira, for making me feel so welcome in the group, and for going well and truly beyond what is required as a supervisor to make sure that my time in Tokyo went as smoothly as possible. Organising Japanese lessons for my fiancé Stephanie is just one example of this and we are forever grateful for all that you have done. I especially enjoyed the daily lunches at the shokudo, with discussions on physics, politics, sport, and Japanese culture. Ping Koy, for adopting me when I returned from Tokyo and for always making time for discussions and chats. You bend over backwards to help every single student or staff member around you, and it has not gone unnoticed. It is truly inspiring. All three supervisors have filled their labs with amazingly talented people and have cultivated wonderful groups. I am extremely aware of how much this has shaped my own learning, and I am eternally grateful to have had the fortune to work with and learn from exceptional people.

Ryuji Ukai, thank you for teaching me everything I know about teleportation, cluster states, and so much more. You are an amazing experimentalist who knows more theory than most theorists. Thank you for writing programs in visual basic for other people to use, simply to make their lives easier. You truly are an inspiration. I am indebted to Jiri Janousek, who taught me everything I know about lab work, and who taught me that the most important thing is to have fun. Jean-Francois Morizur, I am in awe of your energy and quick mind, and learnt the importance of programming from you. Boris Hage, who seems to know every trick in the lab, I am privileged to have been able to work with you. Researching with you was a turning point for me, as you were the first to assign me a task that seemed impossible and proceeded to give me the confidence to complete it.

I am grateful to my colleagues both in Canberra and in Tokyo who made my PhD experience something special: John Bartholomew, Michael Stefszky, Helen Chrnaowski, Geoff Campbell, Ben Sparkes, Lachlan Nicholls, Pierre Vernaz-Gris, Mahdi Hosseini, Ben Buchler, Shota Yokoyama, Shuntaro Takeda, Hidehiro Yonezawa, Jun-ichi Yoshikawa, Wise-kun, Kaji-kun, and Hugo Benichi.

Thank you to my colleagues outside of Canberra and Tokyo, who I have learnt a great deal from, I have enjoyed every single collaboration immensely: Nick Menicucci, Rafael Alexander, Mile Gu, Christian Weedbrook, Qiongyi He, Margaret Reid, and Peter van Loock. It is testament to my excellent supervisors who gave me the opportunity to and encouraged me to maintain active collaborations with these international stars of quantum optics.

I am grateful to Peter Drysdale for providing invaluable mentorship and for creating wonderful opportunities for me. Peter, you are an inspiration and I aspire to learn from your selflessness and enthusiasm for life.

I have learnt that the secret to a well-functioning lab is extremely capable administrative staff, and I am especially grateful to Damien Burns, Yumiko san, and Amanda White.

My friends have been patient with me when I haven't had much time for them during the PhD, and have supported me all the way through it. Thank you for making me laugh when I needed a pick-me-up, especially Josh, Andy, Jimmy, Drew, Johnny, Utah, Ian, Peeps, Louis, and Amina.
To Steph's family, I owe so much. For providing me with a beautiful view of the lake at your coast house where I wrote some of this thesis, and for solving every problem that Steph and I ever have, I am truly indebted.
Above all, I would like to thank my family for the constant supply of love and support, and for encouraging me to pursue my passions in life, no matter if they are sport, travel, or science.
And finally, my beautiful fiancé Stephie, whom I love and adore. Thank you for making me laugh every single day. Your smile is a question that I want to spend my whole life answering.

Abstract

One of the primary goals of the quantum information science community is to build a fault-tolerant and large-scale quantum computer. This thesis presents experimental investigations in quantum optics that demonstrate progress towards this goal.

First, we explore scalable architectures that will facilitate a large number of quantised optical modes (qumodes) to be entangled together. The technique investigated to achieve this is multiplexing the qumodes in the same optical channel. By generating orthogonal spatial modes and engineering a sophisticated multi-photodiode homodyne detection scheme, we achieve the spatial multiplexing of up to eight qumodes, and introduce a scheme for emulating linear optics networks. This is done via virtual networks that are able to be programmed at the time of detection by projecting the beam into different spatial-mode bases.

We then demonstrate that multiplexing qumodes in the time domain is a much more successful method for creating large entangled states. We generate ultra-large entangled states that comprise of more than 20,000 individually accessible qumodes. The qumodes here are sequentially propagating wave-packet modes from the continuous output of optical parametric oscillators. The entanglement structure is fully characterised, and the entanglement is qualitatively visualised as correlations in quadrature amplitudes. The generated quantum state is named the dual-rail EPR-graph state. The entanglement structure leads us to conclude that these states are one possible extension of the Einstein-Podolsky-Rosen (EPR) states to an ultra-large basis. The dual-rail EPR-graph state is derived to be equivalent to a cluster state (up to local phase shifts), which are a class of entangled states shown to be a resource for universal quantum computing.

In the final partition of this thesis, we explore the paradigm of measurement-based quantum computing, which employs cluster states as a resource. A cluster state is treated as a blank quantum circuit board, and the logic to be imprinted is dictated by the choice of measurements on the cluster. Information and gates are then teleported through the cluster. We demonstrate two experiments that together provide a universal set of gates for universal multimode Gaussian quantum computation. The first experiment demonstrates universal one-mode Gaussian operations on a four-mode cluster state. Here, universality is achieved with a combination of rotation and squeezing transformations. The second experiment introduces a tuneable entanglement gate, a robust example of a multimode gate. The gate is defined generally, and a proof of principle experiment follows. The experiment involves two independent inputs and a resource three-mode cluster. The inputs are coupled into and propagated through the cluster, with entanglement being teleported onto them at the output. The entanglement gate is fully tuneable by the choice of measurements performed on the cluster, and we verify the full range of entanglement strength on the output state for seven different regimes.

While there are still many more issues that must be solved before the construction of a useful and large-scale quantum computer is possible, this thesis has demonstrated important advances in two areas: the scalability of entangled systems, and universal Gaussian operations.

Contents

List of Figures

List of Tables

Chapter 1

Introduction

Quantum optics as a field of research is concerned with the quantum description of light waves. The discovery of photon bunching in 1956 by Hanbury Brown and Twiss [1] invigorated the now rich field of fundamental research. The modern theoretical framework of quantum optics was developed by Roy J. Glauber in the early 1960s, with treatments on quantum coherence and explanations of the Hanbury Brown-Twiss experiments [2]. Experimental quantum optics was born in the same period with the invention of the first ruby laser by Theodoe H. Maiman [3], making coherent light accessible in the laboratory. Squeezed light was demonstrated in the 1980s [4, 5] as a result of investigations into non-linear optics spurred on by the development of powerful laser systems at various wavelengths in the 1960s and 1970s. Alain Aspect provided evidence of the genuine existence of entanglement [6, 7] by experimentally demonstrating the violation of Bell's inequalities in 1982[1] [9, 10, 11]. The relative ease of producing squeezed light via parametric amplification [12, 13] has led to entangled light now being routinely created deterministically in laboratories by mixing and manipulating squeezed light.

Quantum entanglement, heralded as one of the fundamental signatures of quantum mechanics, has remarkably turned out to be useful for quantum computation. Quantum computers will process information units that are no longer abstract mathematical entities, as formulated by the pioneer of information theory Claude Shannon [14], but rather truly physical objects that are described by quantum mechanics. David Deutsch, who was first to offer a formulation of quantum information in 1985 [15], remarked that not only is information physical, it is quantum physical. A breakthrough in quantum computing came as recently as the turn of this century [16] with the theoretical development of measurement-based models, using entangled states with associated graphs as universal resources for quantum computation. The resource states are cluster states, and rely on quantum teleportation [17, 18, 19] for the propagation and arbitrary manipulation of quantum states. With the invention of cluster state computing, quantum algorithms no longer rely on precisely controlled sequences of reversible gates, but rather the algorithms are dictated by the choice of measurements on a previously prepared cluster state. In other words, the difficulty has been shifted to the preparation of the cluster state, and once this resource is available the quantum computation becomes much more feasible to implement than in the originally proposed circuit model [20]. Quantum information science has propelled quantum optics into the spotlight, and is by its own right a fascinating interdisciplinary field of research attracting physicists, information scientists, and mathematicians. A rare and wonderful feature of optical quantum information science is that it simultaneously allows for the investigations of fundamental concepts as well as applications-based investigations that are paving the way for new forms of communication and computation.

[1] Freedman and Clauser were first to violate Bell's inequalities in the 1970s [8]. Aspect importantly introduced timing constraints precluding signalling between parties.

1.1 Outline of the thesis

There are three parts to this thesis, as shown in figure 1.1. Part I introduces quantum optics broadly and describes the relevant theory and experimental techniques that are necessary for understanding the experimental chapters. Part II describes several experiments that all share the same common goal; to demonstrate an architecture capable of entangling together a large number of quantum modes of light. Part III investigates quantum computing using continuous-variable cluster states, and showcases two demonstrations of measurement-based quantum computing protocols.

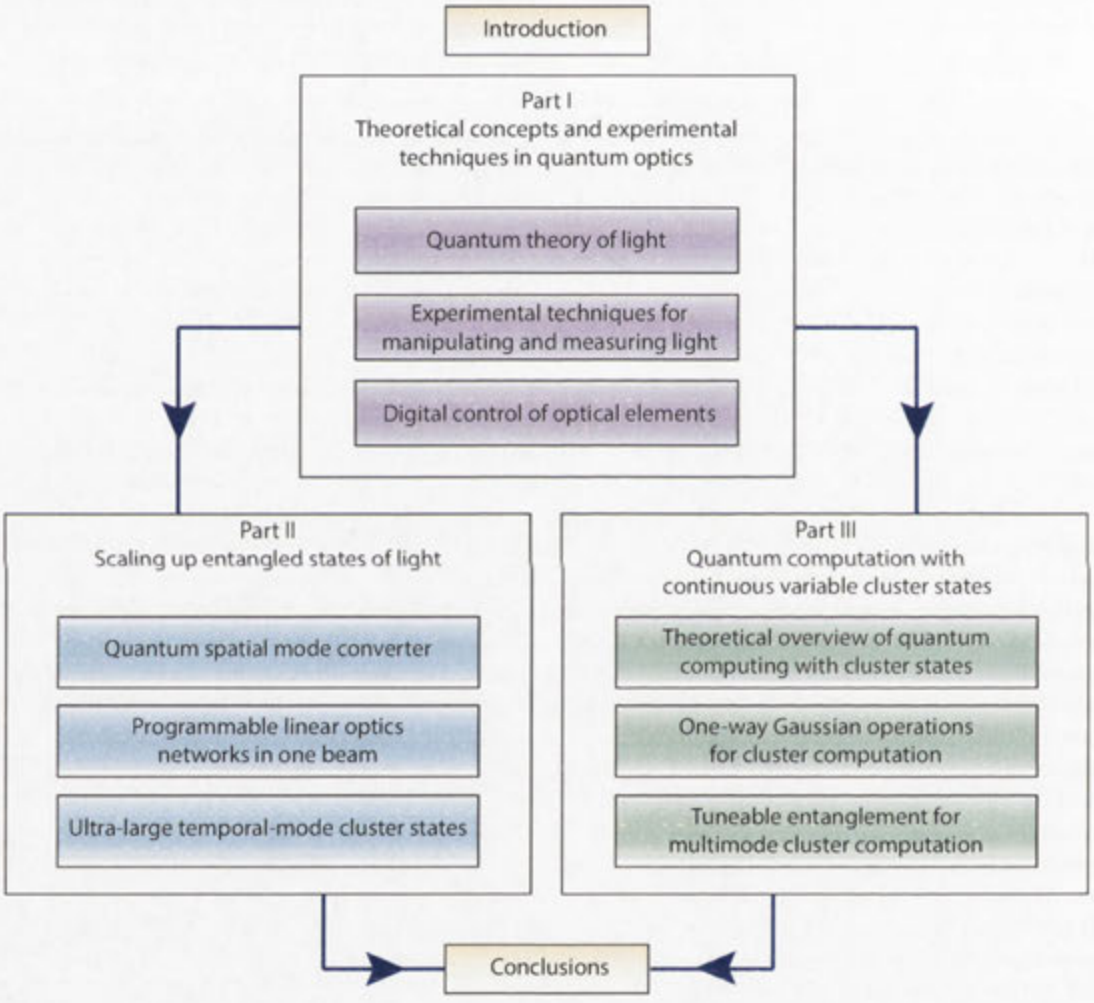

Figure 1.1: Structure of this thesis.

Part I: Theoretical concepts and experimental techniques in quantum optics

Chapter 2: Quantum theory of light. This review chapter details the necessary theoretical framework and concepts required to understand the subsequent experiments presented in this thesis. After a brief look at some fundamental aspects of quantum mechanics, we explore some of the more common quantum states of light that will be generated and manipulated in our experiments.

We end the chapter with a treatment of cluster states, a particularly useful class of entangled states that play a central role in part III of this thesis as well as in chapter 7.

Chapter 3: Experimental techniques for manipulating and measuring light. Chapter 3 provides a brief treatment of the main techniques used frequently in the experiments throughout my PhD. Techniques related to the generation, control, manipulation, and detection of quantum light are treated.

Chapter 4: Digital Control of optical elements. Chapter 4 explores three different digital control suites developed in order to provide active feedback control to various optical elements and devices. This chapter is included as quantum optics experiments are progressing in complexity and more and more laboratories are implementing digital control in favour of analogue electronics for certain tasks. All control suites were custom-written in the programming language of National Instruments LabVIEW. The first two suites are treated very briefly, primarily to indicate inefficient programming techniques that we must avoid, before spending considerable time detailing the third control suite.

Part II: Scaling up entangled states of light

Chapter 5: Quantum spatial mode converter. In chapter 5 we investigate the spatial manipulation of a signal beam in order to match it to a realistic fixed detection system. We present the experimental demonstration of a unitary spatial mode converter, which allows the arbitrary spatial manipulation of squeezed light. The losses induced on the squeezed light are shown to be due only to the passive optical loss and not from the mode converter itself. As a proof of principle demonstration we spatially convert a squeezed TEM_{00} mode into the higher order TEM_{10}, TEM_{20}, and TEM_{30} modes, and show that the converted modes still retain their quantum nature. Spatial mode conversion can be generalised to mode mixing in one beam, leading to considerations of spatially multiplexing different spatial modes of light.

Chapter 6: Programmable linear optics networks in one beam. In chapter 6 we build on the techniques developed in chapter 5 and construct a device capable of emulating linear optics networks. We include a full theoretical treatment of the virtual networks accessible via our scheme. Our method relies on spatially multiplexing up to eight orthogonal modes of light on one beam, and dictating a spatial basis at the time of detection. By employing multi-photodiode detectors capable of detecting the beam in eight different regions, we measure up to eight-mode entanglement and explore both the advantages and the limitations of the scheme. Although successful, we find that there are many technological challenges that limit the potential extension of this scheme.

Chapter 7: Ultra-large temporal-mode cluster states. In chapter 7 we present the experimental preparation of an ultra-large cluster state. The previous record for the largest entangled state was 14 [21], and in this experiment we entangle more than 20,000 wave-packets of light together, beating the record by 3 orders of magnitude. Our technique follows a theoretical proposal [22] and employs multiplexing in the time domain. We provide a detailed treatment of the generated state, which we name the dual-rail EPR-graph state, and explore the associated graph's entanglement structure. The quantum correlations that manifest between wave-packet temporal modes is visualised by parametric plots and various quadrature amplitudes. Details are given on a robust digital control scheme that facilitated a "sample and hold" scheme, which made it possible to alternate between an active feedback control regime and a phase modulation free measurement regime.

Part III: Quantum computation with continuous variable cluster states

Chapter 8: Theoretical overview of quantum computing with cluster states. In chapter 8 we provide a theoretical treatment of continuous-variable cluster state computing. The experiments that follow in subsequent chapters will provide a universal set of gates for multimode Gaussian transformations, and as such the emphasis in this chapter is on Gaussian unitary operations. A summary of the most common Gaussian operations is provided before detailing quantum teleportation in the framework developed in the chapter. It is shown that two sequential teleportations is sufficient to perform an arbitrary one-mode Gaussian operation, and this is derived first for a cluster state, and then extended to the EPR basis in order to be compatible with the dual-rail EPR-graph state generated in chapter 7. While the first half of the chapter is review, the treatment of sequential teleportation is original research, albeit a modest extension of theory developed at the Furusawa laboratories, at the University of Tokyo.

Chapter 9: One-way Gaussian operations for cluster computation. An experimental demonstration of one-way Gaussian operations is presented in chapter 9. By utilising a four-mode linear cluster state as a blank quantum circuit board, we showed that different Gaussian operations may be performed on an input state that is being teleported through the cluster, simply by our choice of measurement basis. The measurements performed are homodyne measurements, and the classical feed-forward channel necessary for implementing quantum teleportation is described. The cluster state was chosen to be a four-mode linear cluster as this is the smallest resource state that offers the requisite degrees of freedom to implement universal one-mode Gaussian operations (which follows from the result derived in chapter 7). An input state is coupled to the four-mode cluster and the Fourier transform operation is performed on the state as it is teleported through the cluster. The output state is characterised and the fidelity of the operation is measured to be $F = 0.68$.

Chapter 10: Tuneable entanglement for multimode cluster computation. In chapter 10 a new addition to the cluster state computing toolbox is introduced. A tuneable entanglement gate is presented, and a rigorous theoretical derivation is provided. The gate provides a method for coupling an arbitrary number of independent inputs into a cluster state, with the ability to tune the entanglement of the output state after the state has been teleported through the cluster. This is a robust example of a multimode gate, necessary for universal multimode Gaussian operations. After the gate has been introduced, a proof of principle experiment is presented. Two arbitrary inputs are coupled into a linear three-mode cluster state and propagated through with the entanglement being teleported onto them. The tuneable entanglement gate is operated in seven different regimes, corresponding to seven different strengths of entanglement that is teleported onto the two inputs, appearing on the output state. The output states of the seven regimes are fully characterised by measuring each covariance matrix and calculating the symplectic eigenvalues of the partially transposed covariance matrices. Full tuneability of the entanglement strength is demonstrated, and it is shown that even the ability to turn off the entanglement is possible.

Chapter 11: Conclusions: In the concluding chapter the research presented in this thesis is summarised. A brief outlook is also presented with an emphasis on universal quantum computing, and what further steps are necessary to achieve this ambitious goal.

1.2 Academic publications and presentations

The majority of the research that appears in this thesis has been published, submitted to, or accepted for publication in international peer-reviewed journals. The following is a list of academic publications, along with details of the conferences where I presented the research either as oral or poster presentations:

1. J.-F. Morizur, L. Nicholls, P. Jian, S. Armstrong, N. Treps, B. Hage, M. Hsu, W. Bowen, J. Janousek, and H.-A. Bachor, "Programmable unitary spatial mode manipulation.," *Journal of the Optical Society of America. A, Optics, image science, and vision* **27**, 2524 (2010).
   Presented at: Quantum Information School and Workshop II, Paraty, Brazil (2009), and The 19th Congress of the Australian Institute of Physics, Melbourne, Australia (2010).

2. J.-F. Morizur, S. Armstrong, N. Treps, J. Janousek, and H.-A. Bachor, "Spatial reshaping of a squeezed state of light," *The European Physical Journal D* **61**, 237 (2011).
   Presented at: The Tenth International Conference on Quantum Communication, Measurement and Computation, Brisbane, Australia (2010), and The 5th Asia Pacific Conference on Quantum Information Science, Shanxi Province, China (2010).

3. S. Armstrong, J.-F. Morizur, J. Janousek, B. Hage, N. Treps, P. K. Lam, and H.-A. Bachor, "Programmable Multimode Quantum Networks," *Nature communications* **3**, 1 (2012) 0403121.
   Presented at: The European Conference on Lasers and Electro-Optics, Munich, Germany (2011), and The 18th Central European Workshop on Quantum Optics, Madrid, Spain (2011).

4. R. Ukai, N. Iwata, Y. Shimokawa, S. C. Armstrong, A. Politi, J.-I. Yoshikawa, P. van Loock, and A. Furusawa, "Demonstration of Unconditional One-Way Quantum Computations for Continuous Variables," *Physical Review Letters* **106**, 240504 (2011).
   Presented at: The Australian Centre of Excellence for Quantum Computation and Communication Technology Kick Off Meeting, Sydney, Australia (2011).

5. R. N. Alexander, S. C. Armstrong, R. Ukai, and N. C. Menicucci, "Noise analysis of single-qumode Gaussian operations using continuous-variable cluster states," *arXiv preprint* (2013) arXiv:1311.3538v1.
   Presented at: The 20th Congress of the Australian Institute of Physics, Sydney, Australia (2012).

6. S. Yokoyama, R. Ukai, S. C. Armstrong, C. Sornphiphatphong, T. Kaji, S. Suzuki, J.-I. Yoshikawa, H. Yonezawa, N. C. Menicucci, and A. Furusawa, "Ultra-large-scale continuous-variable cluster states multiplexed in the time domain," *Nature Photonics* **7**, 3 (2013).
   Presented at: The Australian Centre of Excellence for Quantum Computation and Communication Technology Workshop, Maroochydore, Australia (2013), and Quantum Information School and Workshop IV, Paraty, Brazil (2013).

7. S. Yokoyama, R, Ukai, S. Armstrong, J-I. Yoshikawa, P. van Loock, A. Furusawa, "Fully tuneable entangling gate for continuous-variable cluster computation," *In preparation* (2013).
   Presented at: The 19th Central European Workshop on Quantum Optics, Sinaia, Romania (2012).

8. S. Armstrong, M. Wang, R. Y. Teh, Q. H. Gong, Q. He, J. Janousek, H.-A. Bachor, M. Reid, P. K. Lam. "Genuine tripartite entanglement and multipartite Einstein-Podolsky-Rosen steering with optimised networks," *To appear in Nature Physics* (2014).
   Presented at: Quantum Information School and Workshop IV, Paraty, Brazil (2013).

9. B. Hage, J. Janousek, S. Armstrong, T. Symul, J. Bernu, H. M. Chrzanowski, P. K. Lam, and H. a. Bachor, "Demonstrating various quantum effects with two entangled laser beams," *The European Physical Journal D* **63**, 457 (2011).

10. K. Wagner, J. Janousek, S. Armstrong, J.-F. Morizur, P. K. Lam, and H.-A. Bachor, "Asymmetric EPR entanglement in continuous variable systems," *arXiv preprint* (2012) arXiv:1203.1980.

As a result of some of the research presented in this thesis (especially the first four publications listed above) I have been awarded the Prime Minister's Australia-Asia Award.

Part I

Theoretical concepts and experimental techniques in quantum optics

Overview

The first three chapters of this part of the thesis provide an introduction to the essentials of performing experiments in quantum optics. The first chapter is a review of the theory of quantum light, the second chapter explores experimental techniques and concepts, and the third chapter presents details of digital control systems used to provide active feedback control of some of the experimental apparatus. The treatment on digital control can be seen as an extension of the experimental techniques chapter, and is included in this thesis for the following reason. Digital control is becoming increasingly ubiquitous in modern day quantum optics labs, and yet it is still difficult to access literature on efficient methods of designing and implementing digital control suites. Further, at least two of the experiments presented in this thesis (the generation of the dual-rail EPR-graph state, chapter 7, and the demonstration of the tuneable entanglement gate, chapter 10) would simply not have been feasible without these digital control suites.

The theory presented in the first chapter is almost entirely in the continuous variables regime of quantum optics. Further, there is an emphasis on Gaussian states of light, which play a central role in this thesis due to being experimentally accessible. Remarkably, many of the essential and fundamental features of quantum mechanics (such as entanglement) and quantum information science (such as teleportation) are accessible by manipulating and measuring Gaussian states of light. One reason for this is that Gaussian light can be remarkably well characterised. In fact, a Gaussian state can be completely characterised by its first two statistical moments, which can be measured with over 99 % efficiency using routinely available techniques, such as homodyne detection.

Chapter 2

Quantum theory of light

Here we provide the relevant quantum optics theory required to understand the experiments performed in this thesis[1]. We begin with a brief treatment of quantum mechanics and establish the formalism that will be used throughout the thesis. A review of the quantum harmonic oscillator then leads into a detailed look at useful states of quantum light that are generated, manipulated, and measured in the experiments that will be treated in the later chapters. Cluster states, a type of entangled state useful for quantum computation, are introduced in the second half of this chapter, as well as the stabiliser and nullifier formalism. Further theoretical background relevant to each of the experiments performed is provided at the beginnings of subsequent experimental chapters.

2.1 States and operators

A pure quantum state $|\psi\rangle$ is described by a vector that lives in Hilbert space. Any quantum state can be expanded in an arbitrary basis such as $\{|m_n\rangle\}_{n\in I}$,

$$|\psi\rangle = \sum_{n\in I} c_n |m_n\rangle, \quad \text{where} \quad c_n = \langle m_n|\psi\rangle\,, \tag{2.1}$$

or for example in the position basis

$$|\psi\rangle = \int dx |x\rangle c(x), \quad \text{where} \quad c(x) = \langle x|\psi\rangle\,. \tag{2.2}$$

An operator is defined as

$$\hat{A} \equiv \sum_a a|a\rangle\langle a| \tag{2.3}$$

with eigenvalues a for each of the eigenvectors $|a\rangle$. An operator $\hat{A}$ is Hermitian if $\hat{A}^\dagger = \hat{A}$ ensuring that the measurement results a are real.

2.1.1 Density matrix operator

When we have a system which can be found in several quantum states $|\psi_n\rangle$ with probabilities p_n, we define the density matrix operator $\hat{\rho}$ to describe this statistical ensemble of physical states:

$$\hat{\rho} = \sum_n p_n |\psi_n\rangle\langle\psi_n| \tag{2.4}$$

Any quantum state is fully characterised by its density matrix. When dealing with states that exist in low-dimensional Hilbert spaces such as single or few photon states, density matrices are

[1] For further reading the reader is referred to the following references [23, 24, 25]

typically used to investigate the state. In this thesis we deal with continuous-variables, and the quantum states most often used[2] live in infinite-dimensional Hilbert spaces. As this corresponds to a density matrix which would contain infinite dimensions, we typically employ other representations such as phase space representations of quadrature operators, and deal with the covariance matrix of the state (see section 2.5).

2.1.2 Heisenberg picture and Schrödinger picture

There are two main formulations of quantum mechanics that differ only by a basis change with respect to time dependency. In the Heisenberg picture the initial state does not evolve (time independent), whereas the operators do evolve (time dependent). Conversely, in the Schrödinger picture the operators do not evolve (time independent), whereas the initial state does evolve (time dependent). Given a time independent Hamiltonian $\hat{H}$, the unitary evolution operator $\hat{U}(t)$ is used in both the Heisenberg and Schrödinger representations. The time invariance of $\hat{H}$ implies that it is a conserved quantity and represents energy [23].

The evolution operator is given as

$$\hat{U}(t) = e^{-\frac{i}{\hbar}\hat{H}t}, \tag{2.5}$$

with the requirements $i\hbar\frac{d\hat{U}}{dt} = \hat{H}\hat{U}$ and $\hat{U}(t_0) = \mathbb{1}$.

The evolutions of both operators and states in either representation is summarised below:

	Schrödinger	Heisenberg
State	$\|\psi(0)\rangle \to \|\psi(t)\rangle = \hat{U}(t)\|\psi(0)\rangle$	$\|\psi(0)\rangle \to \|\psi(0)\rangle$
Operator	$\hat{A} \to \hat{A}$	$\hat{A} \to \hat{A}(t) = \hat{U}(t)^\dagger \hat{A}\hat{U}(t)$

2.2 The Heisenberg uncertainty principle

The first few decades of the 20th century witnessed a remarkable shift in the accepted scientific notions of the day. Quantum mechanics was formualted in the 1920s largely in Göttingen, and Copenhagen, led by physicists such as Werner Heisenberg, Niels Bohr, Paul Dirac, Erwin Schrödinger, Albert Einstein, and Max Born. In 1927 Werner Heisenberg presented the famous Heisenberg uncertainty principle which states that complete knowledge about a system is impossible to obtain [26]. More precisely, there is a fundamental limit as to how well one can simultaneously measure two non-commuting variables.

The uncertainty principle dictates that for two non-commuting observables $\hat{A}$ and $\hat{B}$ the products of their variances are bound as

$$\langle(\Delta\hat{A})^2\rangle\langle(\Delta\hat{B})^2\rangle \geq \frac{1}{4}|\langle[\hat{A},\hat{B}]\rangle|^2 \tag{2.6}$$

where the variance of a given observable $\hat{A}$ for a quantum state is given by

$$\langle(\Delta\hat{A})^2\rangle \equiv \langle(\hat{A} - \langle\hat{A}\rangle)^2\rangle = \langle\hat{A}^2\rangle - \langle\hat{A}\rangle^2, \tag{2.7}$$

with the brackets denoting expectation values: $\langle\hat{A}\rangle = \langle\psi|\hat{A}|\psi\rangle$ and $\langle\hat{A}^2\rangle = \langle\psi|\hat{A}^2|\psi\rangle$.

The commutator is defined for two Hermitian operators $\hat{A}$ and $\hat{B}$ as

$$[\hat{A},\hat{B}] \equiv \hat{A}\hat{B} - \hat{B}\hat{A} = \hat{C} \tag{2.8}$$

[2] for example: coherent states, squeezed states, entangled states, and cluster states.

where $\hat{C}$ is an anti-Hermitian operator with $\hat{C}^\dagger = -\hat{C}$. For two non-commuting variables such as the position and momentum of a particle, $|C| > 0$.

The Heisenberg uncertainty principle sets an absolute bound on the maximum precision to which we can simultaneously know two non-commuting observables. The currently accepted interpretation of this is that the observables themselves do not exist with any better precision than dictated by the uncertainty principle. A direct consequence of this is the superposition principle, which allows several different outcomes to exist simultaneously, until a measurement projects the state and returns one measurement outcome. This in turn forms the basis of entanglement. In this thesis we investigate the ability to infer information, steer measurement outcomes, and perform measurement-based quantum computations, all as a consequence of different types of entanglement.

2.3 Hamiltonian of a quantum harmonic oscillator

The Hamiltonian of a single quantum mode in a harmonic oscillator is given by

$$\hat{H} = \hbar\omega(\hat{n} + \frac{1}{2}), \tag{2.9}$$

for a frequency ω, and occupation number operator $\hat{n}$. This may also be written as

$$\hat{H} = \frac{\hat{P}^2}{2m} + \frac{1}{2}m\omega^2\hat{X}^2. \tag{2.10}$$

with position and momentum operators $\hat{X}$ and $\hat{P}$, respectively. In quantising the electromagnetic field a pair of normalised non-commuting operators $\hat{x}$ and $\hat{p}$ are commonly introduced, referred to as quadrature operators

$$\hat{x} \equiv \sqrt{\frac{m\omega}{2\hbar}}\hat{X}, \qquad \hat{p} \equiv \frac{1}{\sqrt{2\hbar m\omega}}\hat{P}. \tag{2.11}$$

This allows us to re-write the quantum harmonic oscillator in terms of an electromagnetic oscillator

$$\hat{H} = \frac{\hbar\omega}{2}(\hat{x}^2 + \hat{p}^2) \tag{2.12}$$

where a single quantum mode is an oscillator with position $\hat{x}$ and momentum $\hat{p}$.

2.4 Useful states of quantum light

Here we introduce the quantum states of light that are generated, manipulated, and have measurements performed on them in this thesis.

2.4.1 Photon number states

The Hermitian photon number operator $\hat{n}$ has eigenstates $|n\rangle$, such that

$$\hat{n}|n\rangle = n|n\rangle \tag{2.13}$$

where $n = 0, 1, 2, \ldots, \infty$ is the number of photons present in the state $|n\rangle$. In general n gives the occupation or excitation number of the harmonic oscillator. Photon number states are physical states that could in principle be prepared perfectly in the lab. The number operator is defined in

terms of raising and lowering operators, as

$$\hat{n} \equiv \hat{a}^\dagger \hat{a} \tag{2.14}$$

The non-Hermitian operators $\hat{a}^\dagger$ and $\hat{a}$ have the following Bose commutation relation

$$[\hat{a}, \hat{a}^\dagger] = 1. \tag{2.15}$$

In the context of quantum optics the lowering operator $\hat{a}$ removes one photon from the state and is referred to as the annihilation operator. Conversely the raising operator $\hat{a}^\dagger$ adds one photon to the state and is termed the creation operator,

$$\hat{a}|n\rangle = \sqrt{n}|n-1\rangle, \qquad \hat{a}^\dagger|n\rangle = \sqrt{n+1}|n+1\rangle. \tag{2.16}$$

Vacuum state

The eigenvector $|0\rangle$ with eigenvalue $\hat{n}|0\rangle = 0$ defines the ground state of the harmonic oscillator and is termed the vaccum state, also satisfying $\hat{a}|0\rangle = 0$. The ground-state (zero-point) energy of the oscillator is $\frac{1}{2}\hbar\omega$ and importantly is non-zero. This zero-point energy arises from vacuum fluctuations, sometimes referred to as quantum noise. The vacuum state is a minimum uncertainty state.

Photon number states from vacuum

Starting from the ground state we may obtain any of the number states $\hat{n}$ by successively applying the creation operator $\hat{a}^\dagger$,

$$|n\rangle = \frac{(\hat{a}^\dagger)^n}{\sqrt{n!}}|0\rangle \tag{2.17}$$

The number operator has a discrete, countable spectrum and is indicative of a particle representation in the quantum oscillator. The number states form an orthonormal basis $\langle n|m\rangle = \delta_{nm}$ as well as being complete, $\sum_n |n\rangle\langle n| = \mathbb{1}$.

2.4.2 Quadrature states

A single mode of the electric field operator for a single polarisation is given by [24]

$$\hat{E}_k(\mathbf{r}, t) = E_0[\hat{a}_k e^{i(\mathbf{k}\cdot\mathbf{r}-\omega_k t)} + \hat{a}_k^\dagger e^{-i(\mathbf{k}\cdot\mathbf{r}-\omega_k t)}], \tag{2.18}$$

for position $\mathbf{r}$ and wave vector $|\mathbf{k}| = \frac{\omega_k}{c}$. This may also be represented

$$\hat{E}_k(\mathbf{r}, t) = E_0[\hat{x}_k \cos(\omega_k t - \mathbf{k}\cdot\mathbf{r}) + \hat{p}_k \sin(\omega_k t - \mathbf{k}\cdot\mathbf{r})]. \tag{2.19}$$

Here we have two operators $\hat{x}$ and $\hat{p}$ that represent the in-phase and out-of-phase components of the electric field amplitude, respectively. These are the position and momentum operators of the quantum harmonic oscillator (equation (2.12)) and have nothing to do with the position and momentum of the photons. They are termed quadrature operators and represent the real and imaginary components of the annihilation and creation operators

$$\hat{a} = \frac{1}{\sqrt{2\hbar}}(\hat{x} + i\hat{p}), \qquad \hat{a}^\dagger = \frac{1}{\sqrt{2\hbar}}(\hat{x} - i\hat{p}), \tag{2.20}$$

$$\hat{x} = \sqrt{\frac{\hbar}{2}}(\hat{a} + \hat{a}^\dagger), \qquad \hat{p} = -i\sqrt{\frac{\hbar}{2}}(\hat{a} - \hat{a}^\dagger). \tag{2.21}$$

The rotated quadrature operators are also defined here, given as:

$$\hat{x}_\theta = \hat{x}\cos(\theta) + \hat{p}\sin(\theta), \qquad \text{and} \qquad \hat{p}_\theta = \hat{p}\cos(\theta) - \hat{x}_\theta\sin(\theta). \tag{2.22}$$

While the annihilation and creation operators are not measurable, since they are non-Hermitian, the phase quadrature operators $\hat{x}$ and $\hat{p}$ are Hermitian operators and have associated eigenvector bases $\{|x\rangle\}_{x\in\mathbb{R}}$ and $\{|p\rangle\}_{p\in\mathbb{R}}$. The eigenstates form an uncountably infinite basis, consistent with an unbounded and continuous spectrum of amplitude and phase values of the harmonic oscillator. For this reason $\hat{x}$ and $\hat{p}$ are also sometimes referred to as the amplitude and phase quadrature operators. This is indicative of a wave interpretation of the harmonic oscillator, complementary to the particle interpretation we encountered earlier with the photon number states.

The eigenvector relationship is given by

$$\hat{x}|x = a\rangle = a|x = a\rangle, \qquad \hat{p}|p = b\rangle = b|p = b\rangle \tag{2.23}$$

and they have the following commutation relation

$$[\hat{x}, \hat{p}] = i\hbar \tag{2.24}$$

and in this thesis we set $\hbar = \frac{1}{2}$.
It follows that the phase quadrature operators have the following uncertainty relation

$$\langle(\Delta\hat{x})^2\rangle\langle(\Delta\hat{p})^2\rangle \geq \frac{1}{4}|\langle[\hat{x}, \hat{p}]\rangle|^2 = \frac{1}{16}. \tag{2.25}$$

The bases are orthogonal: $\langle x|x'\rangle = \delta(x - x')$ and $\langle p|p'\rangle = \delta(p - p')$, and complete,

$$\int_{-\infty}^{+\infty} dx|x\rangle\langle x| = \int_{-\infty}^{+\infty} dp|p\rangle\langle p| = \mathbb{1}. \tag{2.26}$$

Note that although the bases are orthogonal they are not orthonormal as for example the photon number basis is. This is due to the quadrature states being un-normalisable and hence un-physical. A perfect eigenstate of a quadrature operator would require infinite energy, as its value would be fixed precisely for all values in the conjugate phase space. For this reason they fundamentally cannot be generated experimentally, and approximate states are generated instead.

The x and p quadrature eigenstates are related to each other by the Fourier transformation

$$|x\rangle = \frac{1}{\pi}\int_{-\infty}^{+\infty} e^{-2ixp}|p\rangle dp, \qquad |p\rangle = \frac{1}{\pi}\int_{-\infty}^{+\infty} e^{+2ixp}|x\rangle dx. \tag{2.27}$$

2.4.3 Coherent states

Coherent states $|\alpha\rangle$ are the output states of an ideal laser source, and are the quantum states closest to a classical description of wave-like states of the electromagnetic oscillator. They were first introduced by Roy Glauber[3] [27].

Coherent states are eigenstates of the annihilation operator:

$$\hat{a}|\alpha\rangle = \alpha|\alpha\rangle, \tag{2.28}$$

where the eigenvalues α are complex, due to the annihilation operator $\hat{a}$ being non-Hermitian. The mean photon number of a coherent state $|\alpha\rangle$ is given by

$$\langle\alpha|\hat{n}|\alpha\rangle = \langle\alpha|\hat{a}^\dagger\hat{a}|\alpha\rangle = |\alpha|^2, \tag{2.29}$$

[3]For which he won the 2005 Nobel Prize in Physics.

so that the mean energy of $|\alpha\rangle$ is given by

$$\langle \hat{E} \rangle = \langle \alpha | \hat{a}^\dagger \hat{a} + \frac{1}{2} | \alpha \rangle = |\alpha|^2 + \frac{1}{2}. \tag{2.30}$$

We now introduce the displacement operator $\hat{D}$ in order to understand the relationship between a coherent state and the vacuum state. The displacement operator is defined as:

$$\hat{D}(\alpha) = e^{\left(\alpha \hat{a}^\dagger - \alpha^* \hat{a}\right)} = e^{\left(2ip_\alpha \hat{x} - 2ix_\alpha \hat{p}\right)}, \tag{2.31}$$

where $\alpha = x_\alpha + ip_\alpha$. The displacement operator is unitary, as $i\left(\alpha \hat{a}^\dagger - \alpha^* \hat{a}\right)$ is Hermitian. Acting on $\hat{a}$ with $\hat{D}$ displaces the amplitude by the complex number α:

$$\hat{D}^\dagger(\alpha) \hat{a} \hat{D}(\alpha) = \hat{a} + \alpha, \tag{2.32}$$

and we see that phase space displacements are given on the quadrature operators as:

$$\hat{D}^\dagger(\alpha) \hat{x} \hat{D}(\alpha) = \hat{x} + x_\alpha, \quad \text{and} \quad \hat{D}^\dagger(\alpha) \hat{p} \hat{D}(\alpha) = \hat{p} + p_\alpha. \tag{2.33}$$

Finally we see that the coherent state may be viewed as a displaced vacuum state:

$$|\alpha\rangle = \hat{D}(\alpha)|0\rangle. \tag{2.34}$$

From this we can see that the coherent state is also a minimum uncertainty state. The variance of the vacuum state is equal to the variance of the coherent state, and is given by:

$$\langle (\Delta \hat{x}^{(0)})^2 \rangle = \langle (\Delta \hat{x}^{(\alpha)})^2 \rangle = \frac{\hbar}{2} = \frac{1}{4}. \tag{2.35}$$

2.4.4 Squeezed states

Squeezed light may be viewed as the optical incarnation of the manipulation of the Heisenberg Uncertainty Principle. It is possible to create quantum states of light that have quantum fluctuations in one quadrature below the standard quantum limit[4], at the expense of an increase in fluctuations in the conjugate quadrature. Such a state is a squeezed state of light.

The squeezing operator $\hat{S}(r)$ is unitary, is parametrised by the real number r, and is defined as

$$\hat{S}(r) = e^{\left(\frac{r}{2}\left(\hat{a}^2 - \hat{a}^{\dagger 2}\right)\right)}. \tag{2.36}$$

The squeezing operator acting on $\hat{a}$ gives

$$\hat{S}^\dagger(r) \hat{a} \hat{S}(r) = \hat{a} \cosh(r) - \hat{a}^\dagger \sinh(r), \tag{2.37}$$

and the squeezing operator acting on the quadrature operators gives

$$\hat{S}^\dagger(r) \hat{x} \hat{S}(r) = e^{-r} \hat{x}, \quad \text{and} \quad \hat{S}^\dagger(r) \hat{p} \hat{S}(r) = e^{+r} \hat{p}. \tag{2.38}$$

We interpret the squeezing operator $\hat{S}(r)$ as an evolution operator (equation (2.5)) describing the result of the following interaction Hamiltonian that is quadratic in the creation and annihilation operators[23]:

$$\hat{H}_{int} = \chi^{(2)} \left(b^* \hat{a}^2 - b \hat{a}^{\dagger 2}\right). \tag{2.39}$$

[4]Defined as the variance of the vacuum state

The product of the amplitude b, the coupling constant $\chi^{(2)}$ and the interaction time is encapsulated in the squeezing parameter r. In the vast majority of quantum optics experiments, and certainly in every experiment detailed in this thesis, squeezed light is produced by the process of degenerate parametric amplification, following the interaction described in equation (2.39). In our experiments we use crystals that have high non-linear coefficients such as lithium niobate (LiNbO3) and potassium titanyl phosphate (KTP) inside a cavity in order to enhance the interaction.
The cavity containing the non-linear crystal is referred to as a optical parametric amplifier (OPA) or optical parametric oscillator (OPO) depending on whether or not a seed beam is injected, and both devices are pumped by a strong beam with amplitude $|b|$. In a degenerate parametric amplification procress, pump photons of frequency 2ω are converted into pairs of photons of frequency ω. If the pairs of photons are not at the same frequency the process is non-degenerate and the pair of photons will be entangled in frequency. As we will see in subsequent experimental chapters entangled light is generated by mixing squeezed light together, which can be understood intuitively by understanding that squeezed light is the mixture of degenerate entangled light.
An OPO produces squeezed vacuum states:

$$|s = r\rangle = \hat{S}(r)|0\rangle, \tag{2.40}$$

and an OPA produces displaced squeezed vacuum states:

$$|\alpha, s = r\rangle = \hat{D}(\alpha)\hat{S}(r)|0\rangle. \tag{2.41}$$

The variances of the squeezed states are given as:

$$\langle(\Delta\hat{x})^2\rangle = e^{-2r}\langle(\Delta\hat{x}^{(0)})^2\rangle, \quad \text{and} \quad \langle(\Delta\hat{p})^2\rangle = e^{+2r}\langle(\Delta\hat{p}^{(0)})^2\rangle. \tag{2.42}$$

2.5 Gaussian states

All of the quantum states of light manipulated in the experiments described in this thesis have exactly Gaussian shaped Wigner functions. By definition these are Gaussian states, and are for example the vacuum states, coherent states, squeezed states, EPR states, GHZ-like states, and cluster states.

2.5.1 Wigner formalism

There are many ways to represent continuous-variable quantum states in phase space. One particularly elegant quasi-probability distribution is the Wigner function, originally formulated in order to implement quantum corrections to classical laws [28]. The Wigner function is uniquely defined from the density matrix operator ρ to provide a classical-like phase space distribution in quantum mechanics:

$$W(x,p) = \frac{1}{2\pi}\int_{-\infty}^{+\infty} e^{ixy}\langle p + \frac{y}{2}|\hat{\rho}|p - \frac{y}{2}\rangle dy. \tag{2.43}$$

The Wigner function is real for Hermitian operators ρ, $W^*(x,p) = W(x,p)$, and can be extended to a two-mode Wigner function $W_{1,2}(x_1,p_1,x_2,p_2)$ which describes the subsystems $(\hat{x_1},\hat{p_1})$ and $(\hat{x_2},\hat{p_2})$. The overlap formula is given by:

$$\mathrm{tr}\{\hat{A}_1\hat{A}_2\} = 2\pi\int_{-\infty}^{+\infty}\int_{-\infty}^{+\infty} W_1(x,p)W_2(x,p)dxdp, \tag{2.44}$$

for arbitrary operators $\hat{A}_1$ and $\hat{A}_2$, and corresponding Wigner functions $W_1(x,p)$ and $W_2(x,p)$, respectively, from which we may calculate expectation values and transition probabilities between

the pure states $|\psi_1\rangle$ and $|\psi_2\rangle$.

The Wigner function for a vacuum state is given by the Gaussian distribution:

$$W_{|0\rangle}(x,p) = \frac{1}{\pi} e^{\left(-x^2-p^2\right)}, \tag{2.45}$$

and the Wigner functions for the position and momentum eigenstates are given as:

$$W_{|x=a\rangle} = \delta(x-a), \quad \text{and} \quad W_{|p=b\rangle} = \delta(p-b), \tag{2.46}$$

respectively.

2.5.2 Covariance matrix

Any Gaussian state can be fully described by their first and second statistical moments of the quadrature operators $\hat{x}$ and $\hat{p}$. The first order moments are the quadrature amplitudes and are arbitrarily adjusted by local unitary operations such as displacements in phase space, see equation (2.31). The second order moments are given by the Gaussian covariance matrix Γ defined by:

$$\Gamma = \frac{1}{2} \begin{pmatrix} \langle(\Delta\hat{x})^2\rangle & \langle(\Delta\hat{x}\Delta\hat{p})\rangle \\ \langle(\Delta\hat{x}\Delta\hat{p})\rangle & \langle(\Delta\hat{p})^2\rangle \end{pmatrix}. \tag{2.47}$$

The Wigner function of any Gaussian state can be written using the Gaussian covariance matrix Γ [29]:

$$W(R) = \frac{1}{\pi\sqrt{\mathrm{Det}\Gamma}} e^{-\frac{1}{2}R\Gamma^{-1}R^T}, \tag{2.48}$$

for a real phase-space vector $R = (x_1, p_1, \cdots x_N, p_N)$.

We return to Gaussian states and Gaussian operations in Part III of this thesis when we explore measurement-based quantum computations.

2.6 Cluster states

Cluster states are a type of entangled state that have the remarkable property of being robust to local measurements. Stated another way, a subsystem within the cluster may remain entangled even when other subsystems are measured. This is in stark contrast to other multipartite entangled states such as the GHZ or W states, where a measurement on any subsystem will collapse the entire state. This will become conceptually clear when we describe cluster states as being associated with graphs.

There are two very nice consequences of this entanglement structure, which form the basis of Parts II and III of this thesis, respectively.

- **Scalability:** The amount of squeezing required does not grow with the size of the cluster state, and only depends on how many local entanglement links there are in each subsystem. This is quite remarkable, as other states such as the GHZ state require larger levels of squeezing as the entangled state grows. Experiments investigating the scalability of entangled states comprise the 4 chapters in part II of this thesis.

- **Quantum Computing:** Local measurements on the cluster do not destroy the entanglement in other subsystems, instead they project the rest of the cluster into a different state. The projection is dependent on the measurement basis, and this forms the basis of measurement-based quantum computing, which is a universal quantum computing architecture. A review of this method of quantum computing, as well as 2 experiments demonstrating implementations of cluster state computing are presented in part III of this thesis.

2.6.1 Generating cluster states

In 2001 Raussendorf and Briegel presented a formulation of cluster states in the context of measurement-based quantum computing [16]. We provide a full treatment of this in chapters 8, 9, and 10. For now we detail how these cluster states are generated.

Qubits

First we define qubits, which are necessary in the formulation of discrete-variables cluster states. Qubits live in a two-dimensional Hilbert space, and are the fundamental unit of information typically used in quantum information processing. A general pure qubit state can be represented as

$$|\psi_{\theta,\phi}\rangle = \cos(\frac{\theta}{2})|0\rangle + \sin(\frac{\theta}{2})e^{i\Phi}|1\rangle. \tag{2.49}$$

Stated another way, a qubit can either be in state $|0\rangle$, or $|1\rangle$, or in an arbitrary superposition of these two states $|\psi\rangle = \alpha|0\rangle + \beta|1\rangle$, with $|\alpha|^2 + |\beta|^2 = 1$.

Discrete-variables

In the original formulation, the generation of cluster states were presented in a discrete-variables setting (in a finite-dimensional Hilbert space), as follows.

- Initialise a number of qubits in the state $|+\rangle = \frac{1}{\sqrt{2}}(|0\rangle + |1\rangle)$.
- Apply controlled phase gates (two-qubit entangling gate) between any two qubits that you wish to form into a cluster state.

The resulting cluster state will have an associated graph comprised of a set of vertices (qubits) and a set of edges. Two qubits are neighbours if there exists an edge that connects them.

Continuous variables

Cluster states were reformulated for continuous variables in 2006, pioneered by Michael Nielsen [30], Jing Zhang [31], and Nicolas Menicucci [32]. Essentially, the formulation comprises of replacing the discrete-variable elements with continuous-variable analogues, as follows.

- Initialise a number of quantum modes (qumodes) in momentum-squeezed states $|p = 0\rangle$.
- Apply $C_Z = e^{2i\hat{x}_1\hat{x}_2}$ gates between $|p = 0\rangle$ qumodes in order to entangle them.

The C_Z gate is a type of quantum non-demolition (QND) interaction, and is quite difficult to implement experimentally due to the need of online squeezing [33].

An alternative method for cluster state generation is given by a concatenation of offline squeezers and linear optics, as formulated by Peter van Loock using Bloch-Messiah reduction [34]. These are referred to as Gaussian cluster states, as opposed to the original canonical formulation, and are the states treated extensively in Part III of this thesis.

2.6.2 Stabilisers

An operator $\hat{M}$ is a stabiliser operator of state $|\psi\rangle$ if $|\psi\rangle$ is an eigenstate of $\hat{M}$ with unit eigenvalue: $\hat{M}|\psi\rangle = |\psi\rangle$. For example, the stabiliser operator of the vacuum state is given by the exponentiated mode operator $\hat{a}$,

$$e^{\hat{a}}|0\rangle = e^{\hat{x}+i\hat{p}}|0\rangle = |0\rangle. \tag{2.50}$$

Note that even though $\hat{a}$ is non-Hermitian and $e^{\hat{a}}$ is non-unitary, $e^{\hat{a}}$ is nonetheless a stabiliser of $|\hat{0}\rangle$, returning a unit eigenvalue.

Weyl-Heisenberg displacement operators

We now introduce two important operators and observe their actions on the quadrature states.

The position displacement Weyl-Heisenberg (WH) operator $\hat{X}(s)$ and the momentum displacement WH operator $\hat{Z}(s)$ are given by

$$\hat{X}(s) \equiv e^{-2is\hat{p}}, \qquad \text{and} \qquad \hat{Z}(s) \equiv e^{2is\hat{x}}, \qquad \text{respectively.} \tag{2.51}$$

They each impart a displacement when acting on their own space and have the following actions:

$$\hat{X}(s)|x = a\rangle = |x = a + s\rangle, \qquad \hat{X}(s)|p = b\rangle = \mathrm{e}^{-2isp}|p = b\rangle \tag{2.52}$$

$$\hat{Z}(s)|p = b\rangle = |p = b + s\rangle, \qquad \hat{Z}(s)|x = a\rangle = \mathrm{e}^{2isx}|x = a\rangle \tag{2.53}$$

Stabilisers for cluster states

A quantum state $|\psi\rangle$ may be specified by the generators of its stabiliser group, which turns out to be a useful formalism when describing cluster states. An arbitrary continuous-variable cluster state has the following stabilisers,

$$\hat{X}_a(s_a) \prod_{b \in N_a} \hat{Z}_b(s_b). \tag{2.54}$$

where the modes a represent the vertices of graph associated with the cluster state, and $b \in N_a$ represent the nearest neighbours of mode a, *i.e* modes a and b are directly linked by an edge in the graph representing a C_Z gate.

Expanding the displacement Weyl-Heisenberg operators (equation (2.51)) we arrive at

$$e^{-2is_a\hat{p}_a} \prod_{b \in N_a} e^{-2is_a\hat{x}_b} = e^{-2is_a(\hat{p}_a - \sum_{b \in N_a} \hat{x}_b)}, \tag{2.55}$$

such that when applied to a cluster state $|C\rangle$, the stabiliser condition gives

$$e^{-2is_a(\hat{p}_a - \sum_{b \in N_a} \hat{x}_b)}|C\rangle = |C\rangle. \tag{2.56}$$

2.6.3 Nullifiers

The nullifier formalism first appeared in Mile Gu's thesis [35], and offers a useful variation of the stabiliser formalism, by recognising that the group of stabilisers is conveniently described by its Lie algebra, the space of operators $\hat{H}$ such that $\hat{H}|C\rangle = 0$. Every stabiliser is the exponential of a nullifier. This results in the set of nullifiers for ideal cluster states to be defined as

$$\hat{H}_a = \hat{p}_a - \sum_{b \in N_a} \hat{x}_b \tag{2.57}$$

where an ideal cluster state assumes infinite squeezing, and is therefore unphysical. Therefore, we define cluster states as multimode Gaussian states for which the following quadrature combinations become perfect in the limit of infinite squeezing,

$$\hat{p}_a - \sum_{b \in N_a} \hat{x}_b \to 0. \tag{2.58}$$

Approximate cluster states

As mentioned previously, ideal cluster states require infinite squeezing and are thus physically impossible to generate experimentally. Graphical calculus developed by Nicolas Menicucci [36] provides an elegant formalism for describing approximate cluster states, which we will visit in chapter 7. Any Gaussian pure state $|\psi_{\mathbf{Z}}\rangle$ satisfies a set of exact nullifier relations based on its associated complex symmetric matrix $\mathbf{Z}$,

$$(\hat{\mathbf{p}} - \mathbf{Z}\hat{\mathbf{x}})\,|\psi_{\mathbf{Z}}\rangle = \mathbf{0}, \tag{2.59}$$

where $\hat{\mathbf{p}} = (\hat{p}_1, ..., \hat{p}_n)^T$ and $\hat{\mathbf{x}} = (\hat{x}_1, ..., \hat{x}_n)^T$ are column vectors of the p and x quadrature operators, respectively [36, 37], and $\mathbf{Z} = i\mathbf{U} + \mathbf{V}$ where $\mathbf{U} = \mathbf{U}^{\mathrm{T}}$ and $\mathbf{V} = \mathbf{V}^{\mathrm{T}}$ are real and $\mathbf{U} > 0$.

Nullifiers of common states

The nullifier for a vacuum state $|0\rangle$ is simply the annihilation operator $\hat{a}$,

$$\hat{a}|0\rangle = 0. \tag{2.60}$$

Let's verify that we arrive at this from the graphical calculus of equation (2.59). The complex matrix $\mathbf{Z}$ associated with n vacuum states is given by $\mathbf{Z} = i\mathbf{I}$ [36] so that we get

$$\begin{pmatrix} \hat{p}_1 \\ \hat{p}_2 \\ \vdots \\ \hat{p}_n \end{pmatrix} = \begin{pmatrix} i & 0 & \cdots & 0 \\ 0 & i & \cdots & 0 \\ \vdots & \vdots & \ddots & \vdots \\ 0 & 0 & \cdots & i \end{pmatrix} \begin{pmatrix} \hat{x}_1 \\ \hat{x}_2 \\ \vdots \\ \hat{x}_n \end{pmatrix} \begin{pmatrix} |0\rangle_1 \\ |0\rangle_2 \\ \vdots \\ |0\rangle_n \end{pmatrix} = \mathbf{0} \tag{2.61}$$

which leaves us with a vector of nullifiers that is a vector of annihilation operators $\hat{a}$.

The momentum squeezed state is nullified simply by the momentum operator,

$$\hat{p}|p = 0\rangle = 0, \tag{2.62}$$

and linear combinations of nullifiers are also nullifiers,

$$(a + b)\hat{p}|p = 0\rangle = a\hat{p}|p = 0\rangle = b\hat{p}|p = 0\rangle = 0. \tag{2.63}$$

We define the EPR state $|\psi_{\mathrm{EPR}}\rangle$ as the quantum state nullified by the set $\{\hat{x}_1 - \hat{x}_2,\ \hat{p}_1 + \hat{p}_2,\ \hat{x}_2 - \hat{x}_1,\ \hat{p}_2 + \hat{p}_1\}$ so that we have:

$$\hat{x}_1 - \hat{x}_2|\psi_{\mathrm{EPR}}\rangle = \hat{p}_1 + \hat{p}_2|\psi_{\mathrm{EPR}}\rangle = 0. \tag{2.64}$$

2.7 Statistics of quantum light

Photon number distributions

Coherent states and vacuum states have a Poissonian photon number distribution, meaning that the probability of counting n photons is given by a Poissonian. It follows then that on average $|\alpha|^2$ photons will be present in a coherent state $|\alpha\rangle$, and the standard deviation of the photon number is $\Delta n = |\alpha|$. It is a consequence of the Poissonian distribution that means the photon distribution of a coherent state is entirely random.

Quadrature amplitudes

The quadrature probability distributions of coherent states and vacuum states are Gaussian. This is apparent by viewing the position and momentum wavefunctions:

$$\psi_\alpha(x) = \pi^{-\frac{1}{4}} e^{\left(-\frac{(x-x_0)^2}{2} + ip_0 x - \frac{ip_0 x_0}{2}\right)}, \tag{2.65}$$

$$\psi_\alpha(p) = \pi^{-\frac{1}{4}} e^{\left(-\frac{(p-p_0)^2}{2} + ix_0 p - \frac{ip_0 x_0}{2}\right)}, \tag{2.66}$$

respectively.

2.8 Summary

We have provided a brief treatment of the theoretical concepts required to understand quantum optics. Useful quantum states of light have been introduced, as well as several methods that will be used throughout the thesis to analyse them. Chapter 8 extends the review presented in this chapter with a focus on the manipulation of quantum information. This will be in the context of Gaussian operations on continuous-variables cluster states. In the next chapter we will explore some common experimental techniques for quantum optics research in the laboratory.

Chapter 3

Experimental techniques for manipulating and measuring light

Figure 3.1: A typical high performance quantum optics lab. We see two optical benches surrounded by an organised chaos of electronics. This particular laboratory belongs to the Furusawa Group at the University of Tokyo, Japan.

The experiments detailed in this thesis involve the precise control, manipulation, and detection of laser light, followed by a statistical analysis of the measured parameters. A typical experiment will be conducted on a bench that is around two square meters in area, containing several hundred optical elements such as mirrors, beam-splitters, lenses, and crystals. Electronics - both off the shelf and custom made - are employed extensively in order to control the optical elements. For example the precise position of a mirror is voltage controlled, and the refractive index of a crystal is modulated electronically in order to modulate the amplitude or phase of the light that is passing through it. An experiment might take between three months to one year depending on the difficulty. In this chapter we outline some of the more important ideas and techniques that are recurring in the thesis. Each experimental chapter will contain a treatment of the experimental apparatus and techniques relevant to the particular demonstration.

3.1 Laser light

3.1.1 Department of Quantum Science, The Australian National University: 1064 nm

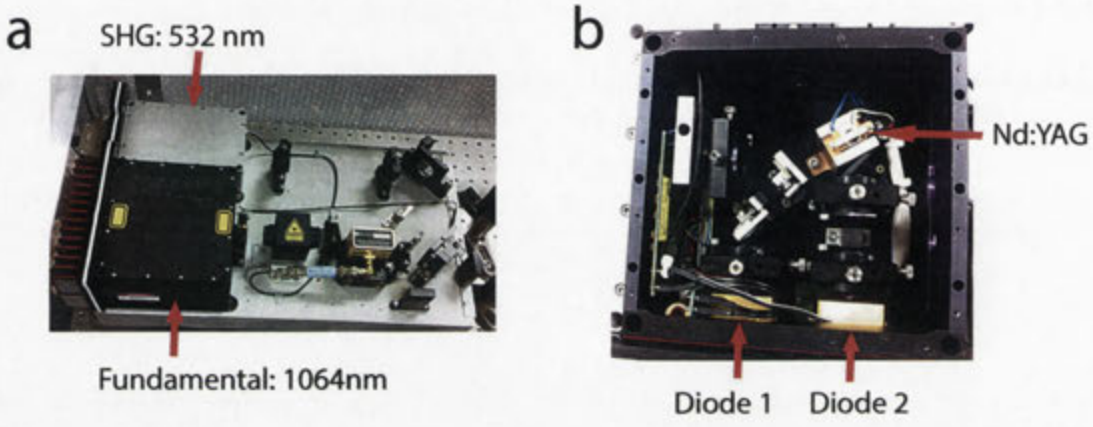

Figure 3.2: Diablo laser from Innolight. a) Both the fundamental and the second harmonic (SHG) wavelengths are generated in the Diablo laser system. b) Two diodes pump an Nd:YAG crystal to produce 1064nm light.

The experiments conducted at the Autralian National University were with the Quantum Imaging Group under the supervision of Professor Hans Bachor, as well with the Quantum Optics group under the supervision of Professor Ping Koy Lam, both within the Department of Quantum Science. These experiments were based on an Innolight Diablo Nd:YAG producing laser light at both the fundamental 1064 nm and the second harmonic at 532 nm. This ultrastable continuous-wave dual wavelength laser is all-solid-state and diode-pumped. The Diablo features a monolithic nonplanar ring geometry (NPRO) cavity which is the source of the high stability in frequency, and the full-width at half maximum linewidth of the laser is less than 1 kHz. The resonant relaxation oscillation of the laser has a peak at around 1 MHz and couples noise into its power spectrum. The peak frequency of 1 MHz can be regarded as the atomic cycling frequency from the ground state of the Nd:YAG energy level system to the laser level. A noise eater is employed within the Diablo system that supresses this laser noise by 25 dB electronically.
The output power at 1064 nm is around 180 mW, while there is 1 W of power at 532 nm. The second harmonic field at 532 nm is generated within the Diablo system in an internal second harmonic generation cavity employing a lithium niobate crystal. This doubler utilises phase modulation at 12 MHz generated via an electro-optic-modulator (EOM) in order to keep the cavity on resonance and maintain stability using active feedback in a Pound-Drever-Hall (PDH) configuration.

3.1.2 Department of Applied Physics, The University of Tokyo: 860 nm

The experiments conducted at the University of Tokyo were with the Cluster State Group under the supervision of Professor Akira Furusawa at the Deparment of Applied Physics. The three experiments performed in Tokyo utilised a continuous-wave titanium sapphire laser producing light at the fundamental wavelength of 860 nm from the Scottish company M Squared Lasers. A 10 W laser-diode pumped and frequency-doubled Nd:YVO_4 laser from Coherent, the Verdi-V10, is used to pump the SolsTiS-SRX which produces around 2 W of 860 nm laser light in the fundamental TEM_{00} Gaussian mode. Unlike the Diablo laser used at the Australian National University, the

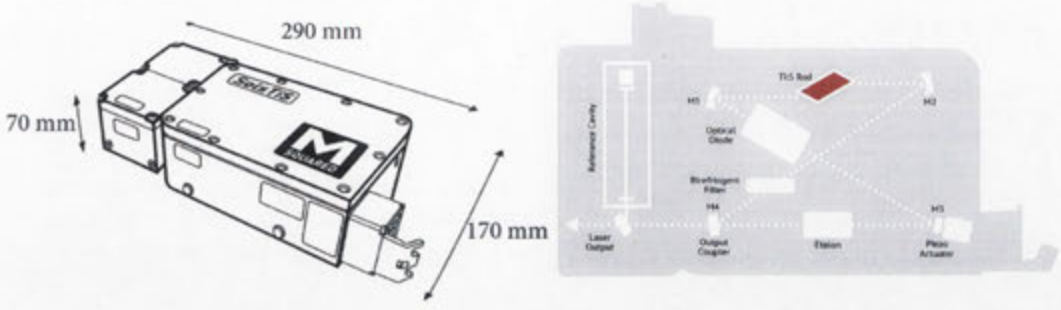

Figure 3.3: SolsTiS laser from M Squared. Source: SolsTiS data sheet (June 2013).

SolsTiS requires an external cavity for producing the second-harmonic field, and this is done by employing a $KNbO_3$ crystal in a bow-tie cavity.

3.1.3 Hermite Gaussian modes

This is a particularly useful spatial basis of light for most quantum optics experiments, as the Hermite-Gaussian modes span a basis of spatial modes that are resonant in optical cavities. Note that this is true for any mode basis part of the Ince-Gauss family, for example the well-known Laguerre-Gauss basis. The difference between the Hermite-Gaussian and Laguerre-Gaussian families is rectangular symmetry and rotational symmetry, respectively, along the propagation axis. The fundamental mode of the Hermite-Gaussian basis describes the fundamental output beam of a laser, denoted as TEM_{00}. Any mode TEM_{mn} in this basis is described by the following:

$$TEM_{mn}(x,y,z) = \frac{C_m n}{\omega(z)} H_m\left(\frac{\sqrt{2}x}{\omega(z)}\right) H_n\left(\frac{\sqrt{2}y}{\omega(z)}\right) exp[-\frac{x^2+y^2}{\omega(z)^2} + ik_0\frac{x^2+y^2}{2R(z)} - i(n+m+1)\Phi_G(z)] \tag{3.1}$$

where

$$C_{mn} = \left(\pi 2^{n+m+1} n!m!\right)^{-\frac{1}{2}}, \tag{3.2}$$

$$\omega(z) = \omega_0\sqrt{1+\left(\frac{z}{z_R}\right)^2}, \tag{3.3}$$

$$R(z) = z + \frac{z^2}{z_R}, \tag{3.4}$$

$$z_R = \frac{\pi\omega_0^2}{\lambda}, \tag{3.5}$$

$$\Phi_G(z) = \arctan\left(\frac{z}{z_R}\right). \tag{3.6}$$

The beam is propagating along the z axis. The wavelength of light is represented by λ, and in our experiments λ ranges between 430 nm and 1064 nm. ω_0 is the beam waist radius (typically on the order of μm to mm), z is the distance propagated along the z axis from the waist, and z_R is the Rayleigh range. $\Phi_G(z)$ is the Guoy phase shift with respect to the fundamental mode and H_m is the mth degree Hermite Polynomial, which are usually given by the following recurrence relation

$$H_0(x) = 1, \qquad H_1(x) = 2x, \qquad H_{n+1} = 2xH_n(x) - 2nH_{n-1}x. \tag{3.7}$$

$\omega(z)$ represents the beam radius when $n = m = 0$, that is, for TEM_{00}. For TEM_{mn} with non-zero m, n, $\omega(z)$ does not represent the radius as the spatial extension of the mode increases as m, n go to higher orders. There will be m and n zeros on the x and y axes respectively. This corresponds to $m+1$ and $n+1$ lobes along the respective axes. Figure 3.4 displays the transverse profiles of several TEM modes for three arbitrary m and n values. The vertical axis represents the normalised electrical field envelope, and the colouring is included simply as a guide to the eye.

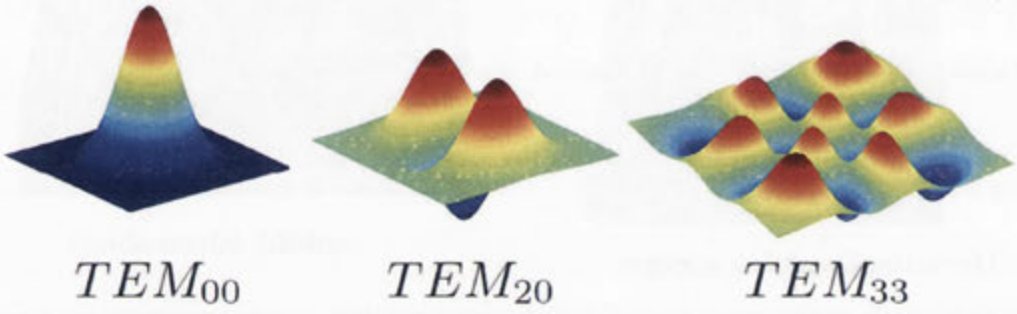

Figure 3.4: Transverse profiles of three TEM modes. The vertical axis represents the normalised electrical field envelope. Source [38].

3.2 Beam-splitters

The humble beam-splitter is a simple yet crucial optical element used extensively for mixing together beams of light. Linear optics networks are built around a concatenation of beam-splitters. The beam-splitter is essentially a piece of glass with coatings. There are four ports to a beam-splitter: two inputs and two outputs, as seen in Fig 3.5.

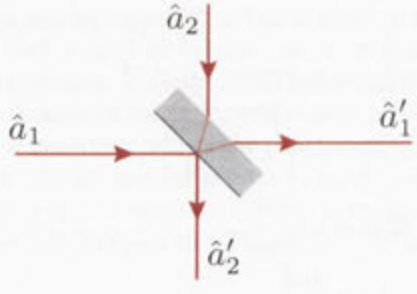

Figure 3.5: A beam-splitter with input modes $\hat{a}_1$, $\hat{a}_2$, and output modes $\hat{a}'_1$, $\hat{a}'_2$.

In classical optics, the complex amplitudes α_1 and α_2 are mixed through the following linear transformation:

$$\begin{pmatrix} \alpha'_1 \\ \alpha'_2 \end{pmatrix} = B \begin{pmatrix} \alpha_1 \\ \alpha_2 \end{pmatrix} = \begin{pmatrix} B_{11} & B_{12} \\ B_{21} & B_{22} \end{pmatrix} \begin{pmatrix} \alpha_1 \\ \alpha_2 \end{pmatrix}. \tag{3.8}$$

In quantum optics, the linear transformation has the same relationship [23]. By replacing the complex amplitudes by the annihilation operators $\hat{a}_1$ and $\hat{a}_2$ we obtain:

$$\begin{pmatrix} \hat{a}_1' \\ \hat{a}_2' \end{pmatrix} = B \begin{pmatrix} \hat{a}_1 \\ \hat{a}_2 \end{pmatrix} = \begin{pmatrix} B_{11} & B_{12} \\ B_{21} & B_{22} \end{pmatrix} \begin{pmatrix} \hat{a}_1 \\ \hat{a}_2 \end{pmatrix}. \tag{3.9}$$

The beam-splitter matrix B is unitary, and obeys the following:

$$|B_{11}|^2 + |B_{12}|^2 = |B_{21}|^2 + |B_{22}|^2 = 1, \qquad B_{11}B_{21}^* + B_{12}B_{22}^* = 0. \tag{3.10}$$

The action of the beam-splitter is given in the Heisenberg picture by the unitary operator $\hat{B}$ and the following input-output relationship:

$$\begin{pmatrix} \hat{a}_1' \\ \hat{a}_2' \end{pmatrix} = \hat{B} \begin{pmatrix} \hat{a}_1 \\ \hat{a}_2 \end{pmatrix} \hat{B}^\dagger = B \begin{pmatrix} \hat{a}_1 \\ \hat{a}_2 \end{pmatrix}. \tag{3.11}$$

One of the beam-splitter matrix elements B_{ij} will represent a π phase shift due to the conservation of energy in wave mechanics. In this thesis we use the following notation to denote the orientation of the beam-splitter[1]:

$$B^{(1)}(\sqrt{r}) = \begin{pmatrix} -\sqrt{r} & \sqrt{t} \\ \sqrt{t} & \sqrt{r} \end{pmatrix}, \qquad B^{(2)}(\sqrt{r}) = \begin{pmatrix} \sqrt{t} & -\sqrt{r} \\ \sqrt{r} & \sqrt{t} \end{pmatrix}, \tag{3.12}$$

$$B^{(3)}(\sqrt{r}) = \begin{pmatrix} \sqrt{t} & \sqrt{r} \\ -\sqrt{r} & \sqrt{t} \end{pmatrix}, \qquad B^{(4)}(\sqrt{r}) = \begin{pmatrix} \sqrt{r} & \sqrt{t} \\ \sqrt{t} & -\sqrt{r} \end{pmatrix}, \tag{3.13}$$

where r denotes the reflectivity and $t = 1 - r$ denotes the transmission of the beam-splitter. An important feature of the beam-splitter is that it is always a four-port device. Even if only one beam is incident, the unused input port will couple in a vacuum state (section 2.4.1). This rather profound quantum artefact is routinely used by experimentalists to model passive optical losses, as we see for example in section 5.2.3.

3.3 Optical cavity parameters

Optical cavities are used extensively in quantum optics experiments. In the experiments presented in this thesis, they are predominantly used for spectral and spatial mode cleaning, as well as for power enhancement to improve the effective non-linearity during optical parametric amplification. Many wonderful treatments exist for both the classical and quantum behaviours of cavities and the reader is referred to references [40, 41, 25]. Here we simply define the key parameters used to characterise cavities.

Finesse

The finesse is a measure of how efficiently the cavity resonates. An intuitive physical description is that this is equivalent to the number of round trips the photons will do of the cavity before exiting. The Finesse of a cavity with relatively high reflecting mirrors is defined as [42]:

$$\mathcal{F} = \frac{\pi\sqrt{r}}{1-r}, \tag{3.14}$$

where r is defined as the product square root of the three reflectivity coefficients which are sources of cavity decay:

[1] There is unnecessary ambiguity that arises from the usual beam-splitter notation. For linear optics networks containing numerous beam-splitters it helps to be precise about the location of the π phase shift for modelling purposes. The notation used here follows that of reference [39].

$$r = \sqrt{R^l \times R^{in} \times R^{out}}, \tag{3.15}$$

with the input and output couplers denoted by in and out, and optical loss denoted by l.

Free spectral range

The Free spectral range (FSR) of the cavity represents a measure of the spacing between resonances and is given as:

$$\text{FSR[Hz]} = \frac{c}{L}, \tag{3.16}$$

where L is the optical path length of one round trip of the cavity and c is the speed of light. Note that the optical path length is equal to the physical path length of the cavity with relevant paths multiplied by the refractive indices of the materials which are present in the cavity. This is important for example when considering cavities that contain crystals inside, such as the optical parametric amplifiers and optical parametric oscillators detailed in the experimental chapters.

Linewidth

In this thesis we define the linewidth of the cavity to be the full width at half maximum (FWHM) of the resonance peak. The FWHM is a measure of the bandwidth of each resonance of the cavity, and is defined as the ratio between the FSR and the finesse, $\mathcal{F}$:

$$\delta l[\text{Hz}] = \frac{\text{FSR}}{\mathcal{F}} \tag{3.17}$$

The bandwidth of the cavity is important when considering how to define our quantised optical modes (qumodes) in experiment. For example, sideband encodings in the low MHZ are typically used in quantum optics experiments and this does not require bandwidths exceeding 10 to 20 MHz. However, for multimode wave-packet encodings of qumodes, used for example in chapter 7, and references [43, 44], larger bandwidths are necessary in order to extract an optimal amount of squeezing. This is due to the qumode being defined over several MHz, rather than the tens of kHz in sideband encodings, and the bandwidth of the non-linear gain is limited by the bandwidth of the cavity.

3.4 Homodyne measurement

Homodyne detection is used to measure the quantum fluctuations of a signal beam in a given phase quadrature. The amplitude of any arbitrary phase quadrature of the signal beam is accesssed by interferring with and varying the optical phase of a reference beam, termed the local oscillator. The local oscillator beam has a much higher intensity, allowing us to treat it as a classical state of light. Figure 3.6 contains a schematic for balanced homodyne detection. A mode cleaning cavity is shown in the same figure, as they are typically employed for spectral and spatial filtering of the laser beam in order to facilitate high efficiency mode matching with the signal beam.

After the signal $\hat{a}$ and the local oscillator $\hat{b}$ are mixed on a balanced beam-splitter (reflectivity $r = 50\%$), the output modes are given by:

$$\hat{c} = \frac{1}{\sqrt{2}}(\hat{a} + \hat{b}), \qquad \hat{d} = \frac{1}{\sqrt{2}}(\hat{a} - \hat{b}). \tag{3.18}$$

The photocurrents from the subsequent measurements are proportional to the photon numbers of the detected beams, given by:

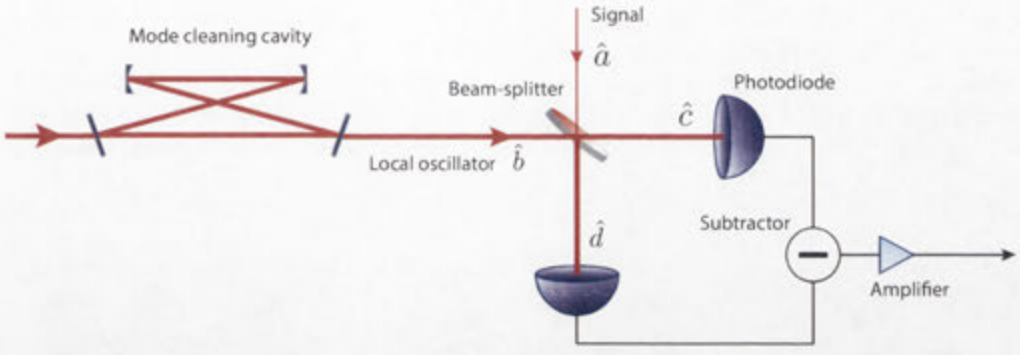

Figure 3.6: Optical homodyne detection. A mode cleaning cavity is typically used for the spectral and spatial filtering of the local oscillator in order to achieve optimal mode overlap with the signal beam. The beam-splitter is balanced.

$$\hat{n}_c = \hat{c}^\dagger \hat{c}, \qquad \hat{n}_d = \hat{d}^\dagger \hat{d}. \tag{3.19}$$

The photocurrent from the two detectors are then subtracted from each other in order to produce the homodyne measurement. We are therefore interested in the subtracted photocurrent, $\hat{s}$:

$$\hat{s} = g(\hat{n}_c - \hat{n}_d) = g(\hat{a}^\dagger \hat{b} + \hat{b}^\dagger \hat{a}), \tag{3.20}$$

for some real value g that has absorbed any proportionality terms such as the photodiode conversion gain. We now recognise that the local oscillator may be treated as a classical field since it is much greater in power than the signal beam, allowing us to substitute the annihilation operator of the local oscillator $\hat{b}$ for its complex amplitude α_{LO}. We therefore arrive at:

$$\hat{s} = g\left(\alpha_{LO}\hat{a}^\dagger + \alpha_{LO}^*\hat{a}\right). \tag{3.21}$$

Now from equations (2.21),(2.22) and expressing the local oscillator in terms of its phase θ, as in $\alpha_{LO} = |\alpha_{LO}|e^{i\theta}$, we arrive at:

$$\hat{s} = g'\hat{x}_\theta = g'\left(\hat{x}\cos(\theta) + \hat{p}\sin(\theta)\right), \tag{3.22}$$

where again the real valued g' has absorbed more proportionality terms, such as $|\alpha_{LO}|$.

Experimentally, the following steps are used in order to implement homodyne detection:
1) Spatially and spectrally mode match the bright local oscillator to the signal beam;
2) Block the signal beam and measure only the local oscillator;
3) Control the phase of the local oscillator with respect to the signal beam;
4) Measure the desired phase quadratures.

Step (2) ensures that there is a reference noise level, termed the shot noise, with which to normalise the measured signal beam during data analysis.

3.5 Data acquisition

Most of the experiments conducted in this thesis employed a digital data acquisition system of some kind. Typically, we would use a Digitizer from National Instruments to acquire the AC signals from the photo-detectors. Custom scripts, named VIs in the software package LabVIEW, were written in order to be able to efficiently acquire the required signals. These data acquisition

(DAQ) cards typically have a trade-off between bandwidth and vertical resolution. A typical card might have a 100MHz bandwidth and 14-bit resolution.
We can learn a lot from qualitative glances at the raw and unfiltered acquired data. Figure 3.7 contains three examples of measurements under different acquisition conditions. In all cases the measurements are taken with the same photodiode. The local oscillator is scanned slowly, at around 30 Hz.

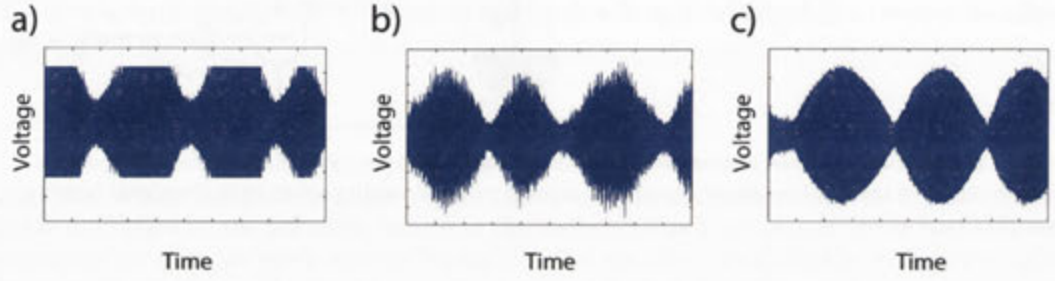

Figure 3.7: Raw data acquired from a typical experiment. a) Vertical range too low resulting in clipping. b) Unwanted noise is visible. c) Qualitatively speaking this data set looks perfect.

In the first case, Fig. 3.7(a), we see that the vertical range is too low. In this example the range is set to 100mV, and we see that the signal exceeds this range, resulting in clipping. The experimenter must be mindful of effects such as these, as automated data analysis algorithms will not necessarily report this and the measurement could contain invalid statistics as a result. A trade-off must be carefully determined, as a vertical range that is too high will result in a low resolution, essentially under-sampling the data and again leading to a misrepresentation of the quantum statistics.
In Fig. 3.7(b), we see that the range and resolution seem to be in acceptable regimes. However, the signal looks rather noisy, suggesting non-optimal calibration of the experimental parameters. Experimentalists will be familiar with this problem, and investigating what is going wrong constitutes a large part of the entire experiment. In our case, we built monitors into the digital control scheme so that we could tweak various optics while observing changes in the measured homodyne signal in real time.
Figure 3.7(c) shows the measurement of the same signal displayed in Fig. 3.7(b) after the following improvements. Several mirror mounts were tightened and dampened in order to increase the mechanical resonance frequencies; various locks were optimised and set to operate in more stable regimes. The latter resulted in the largest improvement, unsurprisingly. We see that qualitatively speaking there is nothing wrong with this measurement. The best probe we have in these experiments is to measure the squeezing value of the desired phase variance, as any technical noise will manifest as phase noise and quickly degrade the sensitive squeezing values.

Chapter 4

Digital control of optical elements

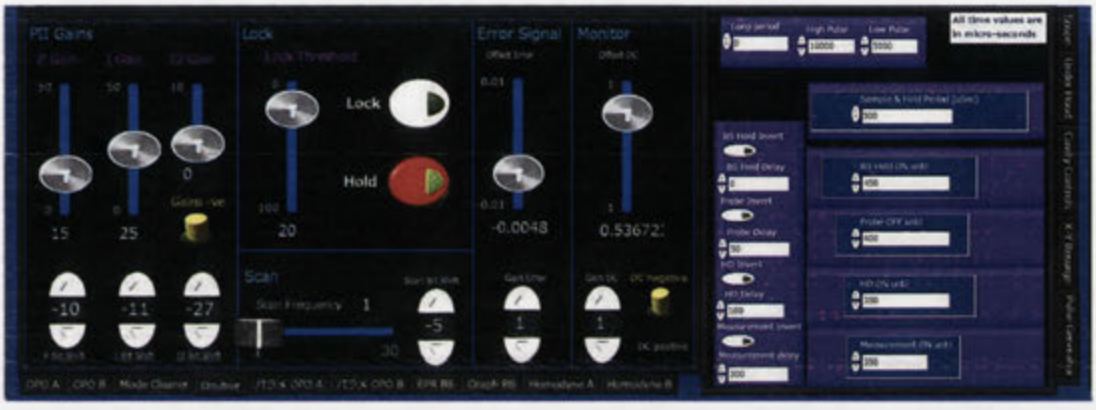

Figure 4.1: Digital Controls used to manipulate optical elements and electronics.

As quantum optics experiments become increasingly complicated, current methods of controlling optical elements are becoming inadequate. The complexity stems from having more optics on the lab table, which means that with regard to control, there are more optical cavities to be held on resonance, and larger numbers of phase locks required between different optical beam paths. Control systems based solely on analogue electronics quickly become cumbersome with their inherent inflexibility and lack of automation. Digital control offers the scope for automation and reconfigurability. Certain tasks can be performed more efficiently with a digital control scheme, and in this chapter we present examples of these tasks.
I will outline three exemplary digital control suites designed and implemented over the course of my PhD. Broadly speaking the first system is the simplest, the second system is the most complicated, and the final system is the most efficient. The first two systems are treated briefly, in order to emphasise inefficient practises to avoid. Considerable time is spent in detailing the final system, which appears on GitHub and is fully commented and ready for use[1].
The language that I used for the digital control was LabVIEW, from National Instruments, but many of the techniques detailed in this chapter are applicable to any programming language.

4.0.1 Feedback control of optical path length

The main objective of the digital control programs is to dictate the optical path length of various laser beams on the table. This is typically done by the voltage control of a piezo-electric transducer (PZT) attached to the backs of mirrors. The PZT will expand or contract on a nano-metre scale,

[1] Please email me at seiji.armstrong@gmail.com for the link.

and the optical path length of the light is transformed accordingly. Two situations where this is most useful are when a cavity needs to be held on resonance, and when the relative phase between two beams mixing on a beam-splitter needs to be held constant.
When we wish to run the experiment and measure observables of the quantum state, all the relevant phases and cavities must be actively controlled, or phase locked. Typically, the final offsets of the mirror positions are actively tuned while observing some figure of merit. A reliable and robust digital control system will allow the final measurements to be as accurate as possible, and facilitate the measurement process by incorporating automated features such as automated relocking when a phase lock fails.

Pound-Drever-Hall locking

The error signals used for locking the relative phases of our optical beam paths are generated externally following the Pound-Drever-Hall (PDH) technique. There exist many excellent treatments on this well established technique, and I recommend the following references to the reader if they are not well versed in PDH theory and phase control in general: chapter 4 of Dan Shaddock's PhD thesis [45], chapter 2 of Warwick Bowen's PhD thesis [25], and Eric Black's technical note written while working on LIGO at Caltech [46].

Tips for programming with LabVIEW

In LabVIEW, each module that contains programming logic is termed a VI. Each control suite is a collection of VIs that contribute to the overall system. I hope the reader will benefit from the multitude of time-intensive mistakes that I have made over the years while learning how to program efficiently in LabVIEW. Below are some general recommendations that will help to make your programs accessible to others when they want to make modifications and/or perform debugging.

- Ensure the control logic in each VI can be displayed on one screen.
- Modularise your VI with subVIs that each perform one task.
- Always flow information (wires) from left to right.
- Always use 'bundle by name' in order to comment your VIs.
- Avoid any logic that confuses the user.

Three exemplary control suites

We now detail two control systems briefly, providing short descriptions of functionality before outlining what is wrong with these two systems. This is done in order to emphasise techniques to avoid, and to promote good programming habits.

4.1 Control system 1: Programmable Networks (2010)

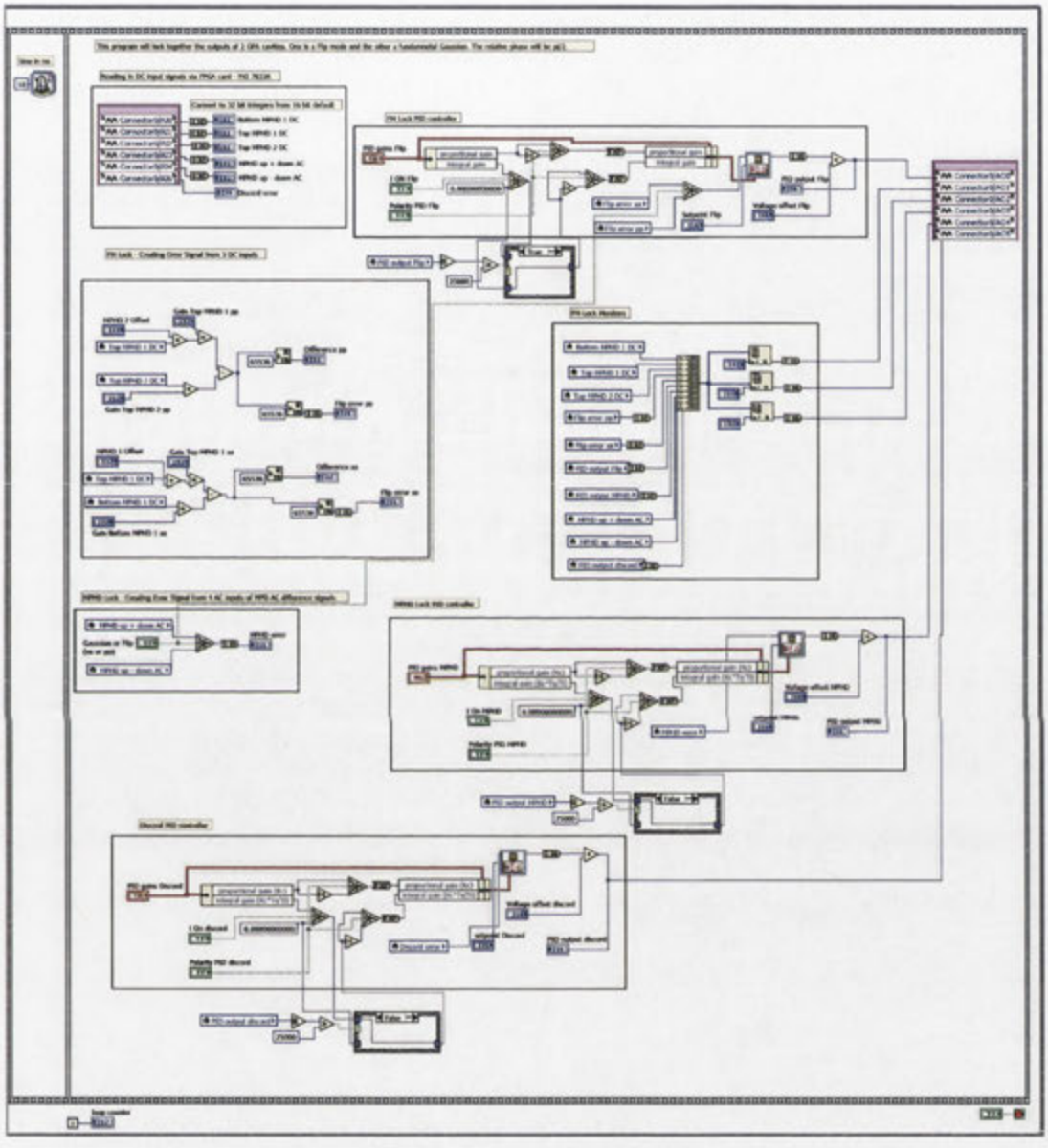

Figure 4.2: GHZ.vi in its entirety.

Overview

The VI shown above in Fig. 4.2 comprises the entire control suite. The experiment is detailed in chapter 6 as well as in reference [47]. Three phase locks are controlled via this control suite with error signals generated on board. Influenced and based on designs by Boris Hage. Any inefficient programming designs are my own.

4.1.1 A quick look at GHZ.vi

Hardware and software

The software package used was National Instruments LabVIEW 2009, operating on Windows XP, on a desktop PC. A National Instruments FPGA card (NI PXI-7833R) was used via a 5-slot PXI chassis (NI PXI-1033). Breakout boxes for BNC and SMA inputs and outputs were custom made.

Functionality

There are three phase locks that are controlled in GHZ.vi. The logic is built around a PID controller that comes as a LabVIEW subVI. It can be seen near the top right of Fig. 4.3.

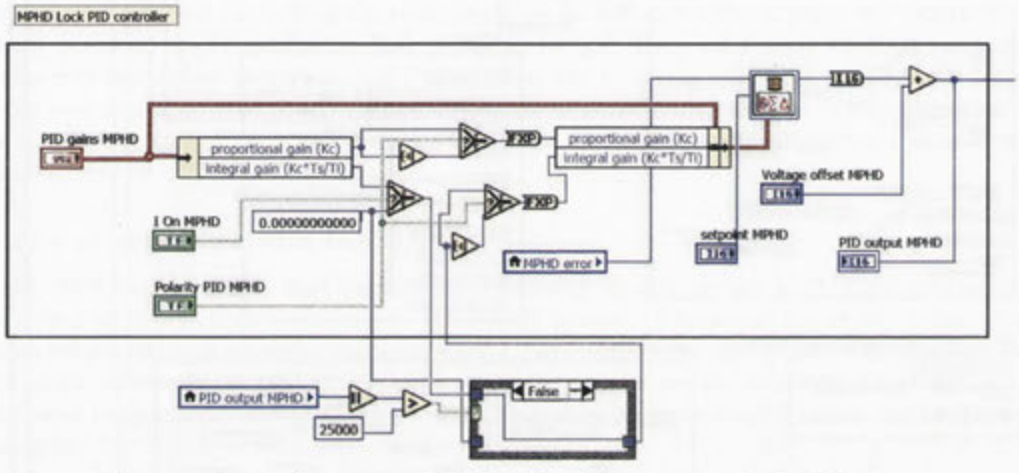

Figure 4.3: A subsection of GHZ.vi that implements the PID logic.

Various error signals are generated on the FPGA board itself via the logic shown in Fig. 4.4. This logic replaces analogue electronics and the obvious advantage is the reconfigurability, which makes modifying the logic of the circuit a simple task.

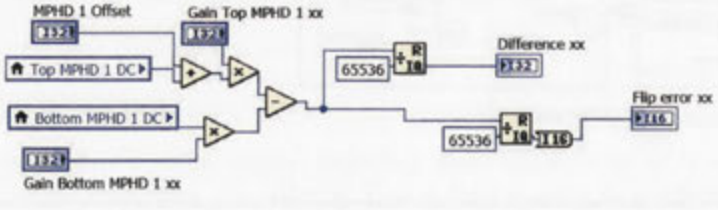

Figure 4.4: Error signal generation. Several DC signals are combined in order to create error signals for phase locking.

Another function of the control suite is to give access to a host of signals that can be monitored externally. The front panel shown in Fig. 4.5 displays three dials that dictate which three signals will be outputted for monitoring on external oscilloscopes.

4.1.2 What's wrong with the GHZ control suite

- **The VI doesn't fit on one screen:** The obvious impediment is that the VI is difficult to navigate. This makes it unnecessarily complicated to follow the flow of information and logic, making debugging difficult, as well as making modifications hard to implement.

- **Lack of modularisation:** There are no user-created subVIs in this control suite. As a consequence, we observe the problems listed above. In order to ameliorate these related issues, it is a good idea to create subVIs that each perform one task. The control suite has 4 subVIs, including the LabVIEW PID VIs. Metrics tell us that there are 270 nodes, for a modularity index of 1.48. This is extremely low. A benchmark figure to aspire to is 3.0, as recommended in reference [48] where the modularity index is defined in the following way:

$$\text{Modularity Index} = 100 \times \frac{\text{number of subVIs}}{\text{number of nodes}} \tag{4.1}$$

- **Name of VI is uninformative:** The user has no idea what function GHZ.vi performs based on its name. Further, how the VI fits within the structure of the suite is unclear.

- **Inefficient logic:** The LabVIEW PID controllers contain much more logic than the user needs. For example, the Derivative portion of the logic (the D in PID) is unused. This uses up precious resources on the FPGA at the expense of other logic.

- **Only a small portion of entire experiment is controlled:** There are several phase locks in the experiment that are controlled via analogue electronics, independent of this control suite. The relationship between the analogue and digital systems is unclear, and when either fails the other will not know, and this could result in unexpected behaviour.

- **No displays or monitors:** Shown in Fig. 4.5 are the controls that are used to monitor and lock the various phases that the suite has access to. While there are dials for toggling which signals are outputted, the user must rely on external equipment for viewing the signals.

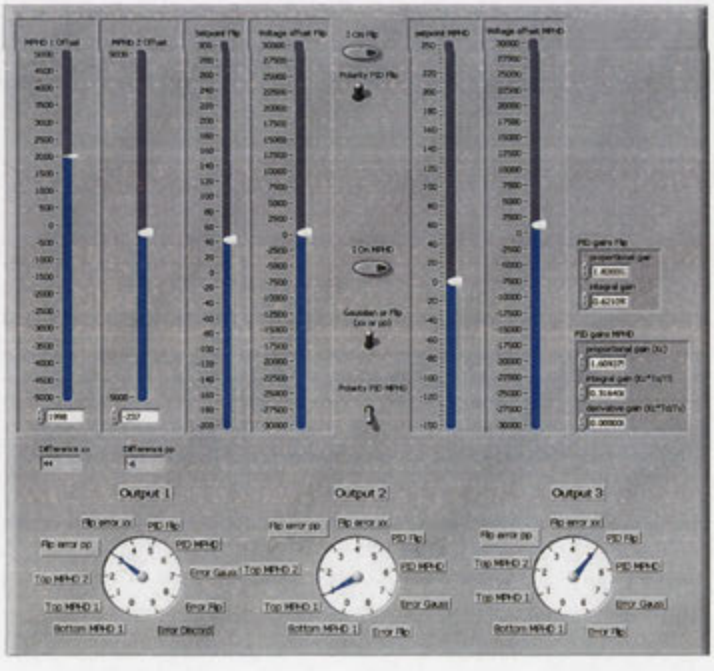

Figure 4.5: Front panel of GHZ.vi. We see controls for the phase locks, and controls for various output signals. Note the lack of displays or monitors.

4.2 Control system 2: Tuneable Entanglement (2011)

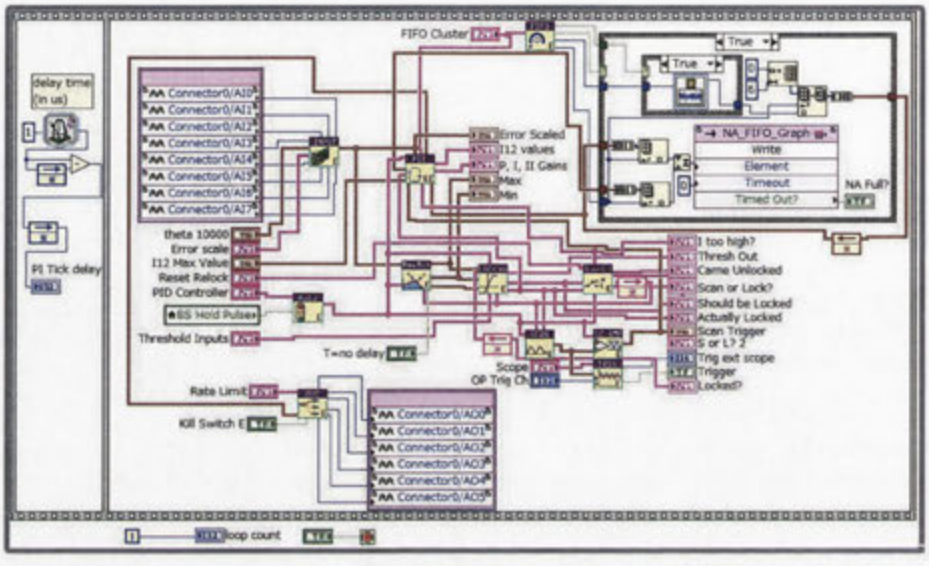

Figure 4.6: **Master_E.vi.** There are 5 FPGA-level VIs like this that each process 8 analogue inputs.

Overview

This control suite is by far the most complicated of the three that we treat in this chapter. There are a total of 40 analogue inputs, processed on 5 FPGA cards and over 100 VIs that control 33 phase locks. The experiment is described in chapter 10, with further details of the control suite in section 10.3.4. It should be noted that the entire suite may be viewed as a (considerable) extension of the control suite developed by Dr Ben Sparkes, detailed in [49].

4.2.1 A quick look at Tuneable Entanglement

Hardware and software

National Instruments LabVIEW 2010 was used, operating on Windows 7, 64-bit, on a desktop PC. 5 FPGA cards were used (4 × NI PXI-7853R and 1 × NI PXI-7854R) installed on a 5-slot PXI chassis (NI PXI-1033). Breakout boxes for BNC inputs and outputs were custom made. Digital TTL signals were created using logic and analogue outputs with controllable voltage levels.

Functionality

A top level VI running on the PC facilitates access to the 33 phase locks across the 5 FPGA cards. Each of the 5 FPGAs runs a variation of the VI shown in Fig. 4.6. Further, each of the phase locks is aware of its place in the system and is part of an elaborate automated re-locking scheme, based on logic created by Ben Sparkes [49]. There are over 100 useful subVIs that I developed that facilitate the modularisation of the suite. To give an example, one such subVI takes 2 error signals that are $\frac{\pi}{2}$ out of phase and combines them in such a way as to produce an error signal used to lock two beams together at precisely any phase rotation between 0 and 90 degrees.

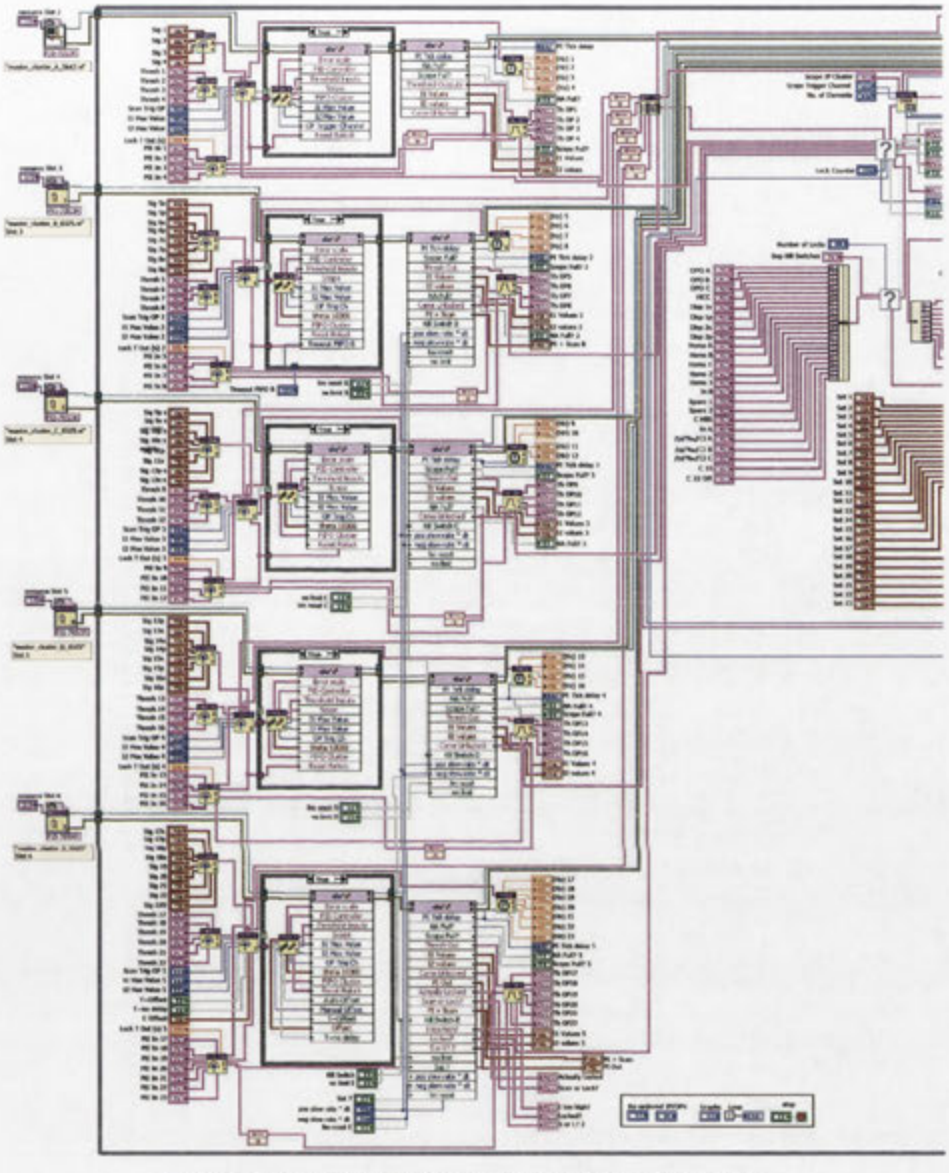

Figure 4.7: Left half of remote_tuneable_cluster.vi.

4.2.2 What's wrong with the Tuneable Entanglement suite

- **The top level VI doesn't fit on one screen:** It's not even close. The two halves are shown in Figs 4.7 and 4.8, respectively, after considerable shrinking. Scrolling in both the vertical and horizontal axes is required to find a particular piece of logic, and the complexity makes this a very unfriendly VI.
- **Inefficient modularisation:** We can see 11 subVIs in the FPGA level VI shown in Fig. 4.6. I've over compensated for the previous lack of modularisation and the trouble now is that it is unclear what the relationship between the subVIs is. Since the information is flowing every which way, it is very hard to track the logic, and this is a nightmare to debug. The top level VI has 2472 nodes and 56 subVIs for a low modularity index of 2.27.

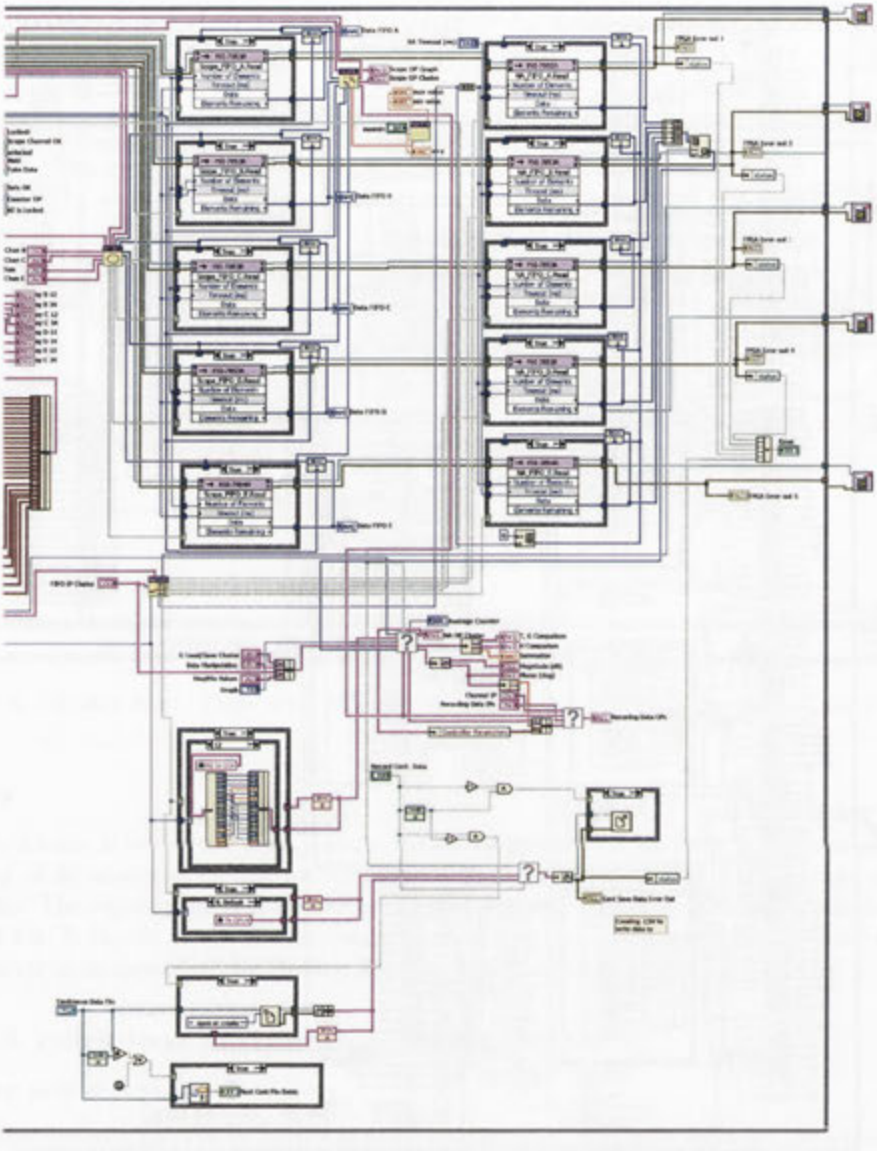

Figure 4.8: Right half of remote_tuneable_cluster.vi.

4.2.3 What's good about the Tuneable Entanglement suite

- **It behaves extremely well:** The experiment would have been extremely difficult to control with analogue electronics alone and the measurements would have suffered phase noise without the digital automation and control. Each of the 5 FPGA cards were running at over 90% capacity, and with over 3500 nodes and over 100 subVIs this control suite pushes the limit in terms of automated optical phase control in table-top laboratory experiments.
- **Structure is logical:** The suite offers glimpses of good programming techniques. The idea of a top level VI calling FPGA level VIs is not only efficient, it is standard practise for well designed LabVIEW programs. And although the complexity of the top-level VI is unforgivable, the information in general flows from left to right. We are now in a position to appreciate the efficient programming shown in control system 3.

4.3 Control system 3: Temporal Clusters (2012)

Overview

This control system receives a considerably more in-depth treatment than the other two as it provides a useful architecture that is logical and clear, facilitating modifications. The goal of this experiment was to create the world's largest cluster state. The experiment was a great success; we managed to entangle more than 20,000 quantum modes together to make an ultra-large cluster state. Our technique that gives us the advantage over present-day systems is to multiplex quantum modes in the time domain. The experiment is detailed in chapter 7 as well as in reference [37].
The digital control system for this ultra-large cluster state experiment controls 10 phase locks: 4 of which are cavity-based, and 6 of which are interference-based. Further, there is a TTL pulse generator that outputs 4 precisely timed TTL pulses, in sync with the phase locks. The user interface gives access to these 10 locks and 4 TTL pulses on one screen complete with an oscilloscope. The TTLs are used to switch various electronic equipment in the experiment.

Hardware and software structure

The software package used was National Instruments LabVIEW 2010 (service pack add-on), operating on Windows 7, 64-bit, on a desktop PC. 2 FPGA cards were used (NI PXI-7853R) installed on a National Instruments 5-slot PXI chassis (NI PXI-1033). Custom-made breakout boxes for BNC inputs and outputs were employed.

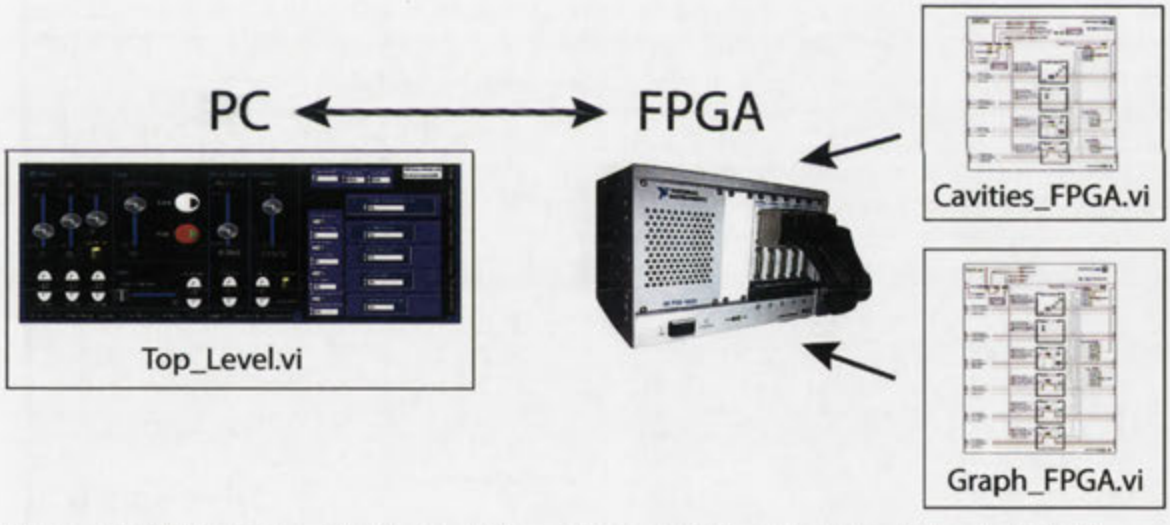

Figure 4.9: VI hierarchy. The Top_Level VI provides a graphical user interface that controls the 2 FPGA level VIs.

4.3.1 FPGA level VIs

There are two FPGA level VIs. One controls 4 cavities, and is named 'Cavities_FPGA.vi'. The other is named 'Graph_FPGA.vi' and controls the phase locks necessary to create an entangled graph state. These FPGA level VIs perform most of the logic that is required to control the different phase locks, and a top level VI (detailed later) provides the user interface that allows access to the various FPGA level controls in a user friendly way.

Cavities_FPGA.vi

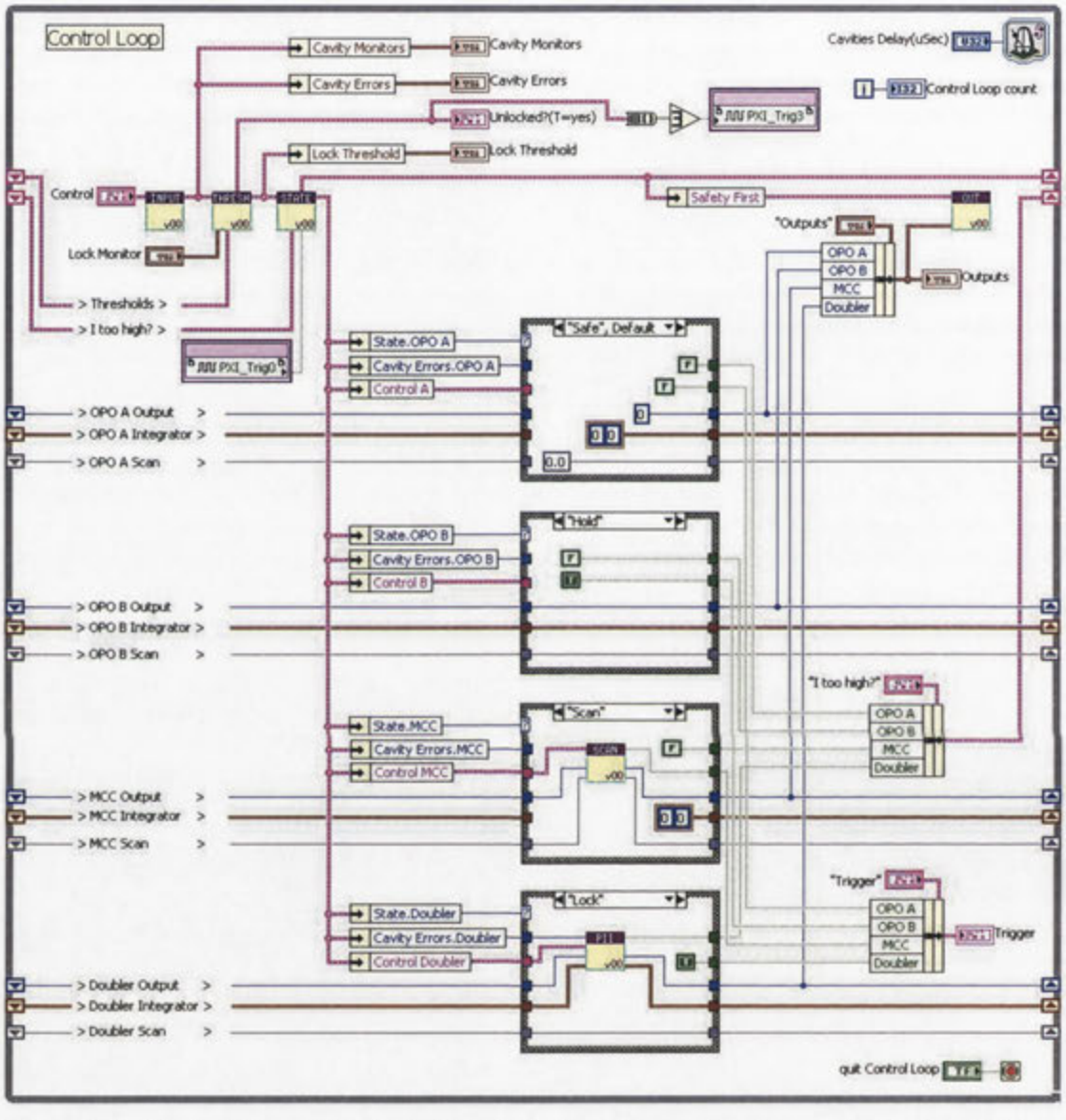

Figure 4.10: Control loop of Cavities_FPGA.vi. 4 cavities are digitally controlled in this FPGA level VI.

The FPGA level VI has 4 parallel while loops - Control loop, Oscilloscope loop, Pulse generator loop, and a timing synchronisation loop. The most important of these is the Control Loop, shown in Fig. 4.10. I will treat the other 3 loops in section 4.3.4. The functionality of the Control loop should be apparent upon inspection. There are 4 subVIs arranged in a line near the top of the loop. As is good LabVIEW coding practice, information here only ever flows left to right (or up and down) and never right to left.
The Input subVI reads in data from the photodetectors on the lab table via an FPGA card. This input (after being scaled) is fed to the Thresholds subVI which performs various tests in order to tell if the cavity is on resonance or not - determined by being above or below a certain voltage

threshold. The State subVI will decide on the desired state of each cavity from threshold tests and user inputs. The Output subVI then applies the necessary voltage to each cavity's PZT mirror, via the FPGA outputs and external amplifiers. In between the State subVI and Output subVI we see that there are 4 case structures, 1 for each cavity.
Each case structure determines the state of each of the cavities, as dictated by the State VI. This control loop can therefore be seen as a State Machine architecture, with 4 parallel systems (cavities) being controlled. In this state machine, each system can be acted on by one of 4 states:

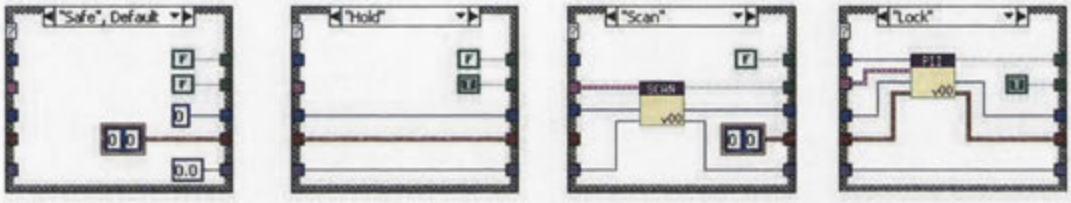

Figure 4.11: **The 4 possible states of each cavity.** Each cavity exists in one state at a time.

1) Safe: Output 0 voltages and falsify all booleans. Basically, do nothing.
2) Hold: Pause the output voltage and hold this constant until further notice.
3) Scan: Apply a variable saw-tooth wave voltage in order to scan the cavity's optical length.
4) Lock: Apply a PII controller on the error signal and lock the cavity on resonance.

Modularity

This FPGA-level VI has 13 subVIs and 436 nodes, for a modularity index of 2.98. This meets the recommended modularity of 3.0 that we mentioned with regard to equation 4.1. Note that not all 13 subVIs are visible in Fig. 4.10 as some subVIs are nested within other subVIs or case structures. The structure of this VI makes modifications accessible, and logical. For example if we wish to add functionality, we only need to add another state in the case structure, and modify the State VI accordingly.

4.3.2 FPGA level sub-VIs

There are 6 subVIs visible in the Control loop of 'Cavities_FPGA.vi'. They are each programmed to serve one purpose, which is represented by the name of the subVI. It is good practise to write code in this way, because it is kind to the user. What I mean by this is that if the user would like to modify something in the control loop, the user need only to modify the subVI that is responsible for the desired action. For example if the user would like to specify another behaviour of the control system, the user could simply add another case to the case structure so that it contains 5 states, and modify the subVI responsible for determining the state of the cavity, 'Cavities_State.vi'. Another related reason as to why this type of modularising is in general a good idea, is that it helps to facilitate the debugging process.
The 6 subVIs will now be detailed, before we move on to discuss the differences in the other FPGA level VI.

Input_Scale.vi

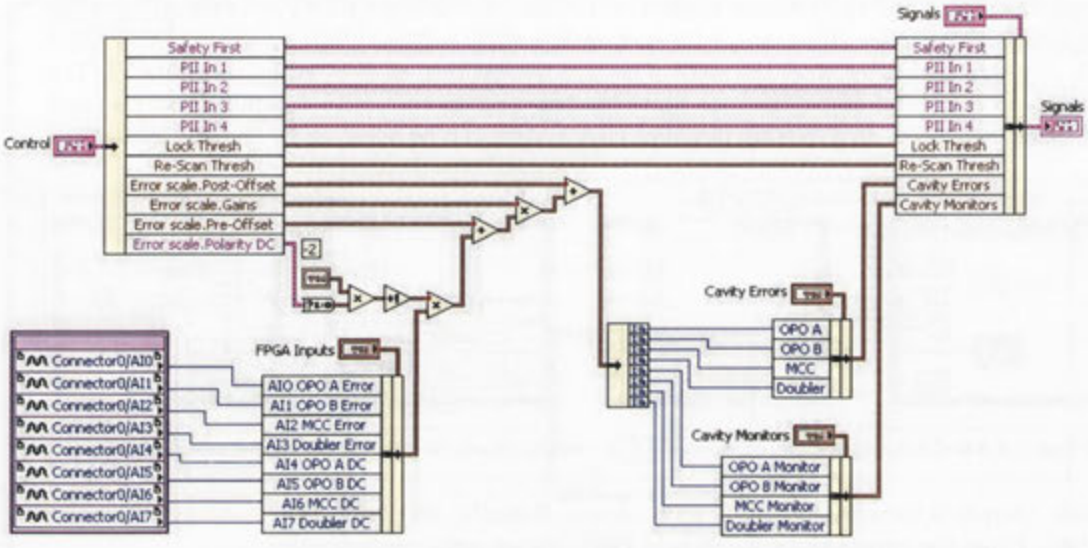

Figure 4.12: Input_Scale.vi. Scales and bundles 8 inputs from the FPGA card. There is a DC monitor and a PDH error signal for each of the 4 cavities.

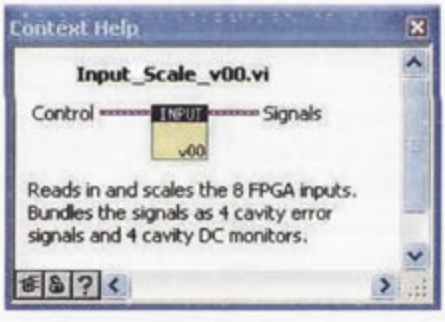

FPGA inputs are bundled by name in order to label the wires before being scaled by user-defined parameters. We see that in this experiment we have 2 optical parametric oscillators (OPOs), a mode cleaning cavity (MCC) and a doubler. After the error signals and DC monitors are scaled they are packaged into the Signals cluster.

Note that wherever possible I use the 'bundle by name' and 'unbundle by name' functions. This is a form of commenting, and allows us to keep track of the various wires before and after logic operations are applied to them. The controls that are fed into these 'bundle by name' functions are type definitions, which allow us to easily modify all instances of this control as well as to call on the same controls in other VIs. If for example one wanted to modify the entire control system to control the cavities in their experiment, they would only need to modify the type definitions found in this subVI. The other instances in the Control loop will then be automatically updated.

Threshold.vi

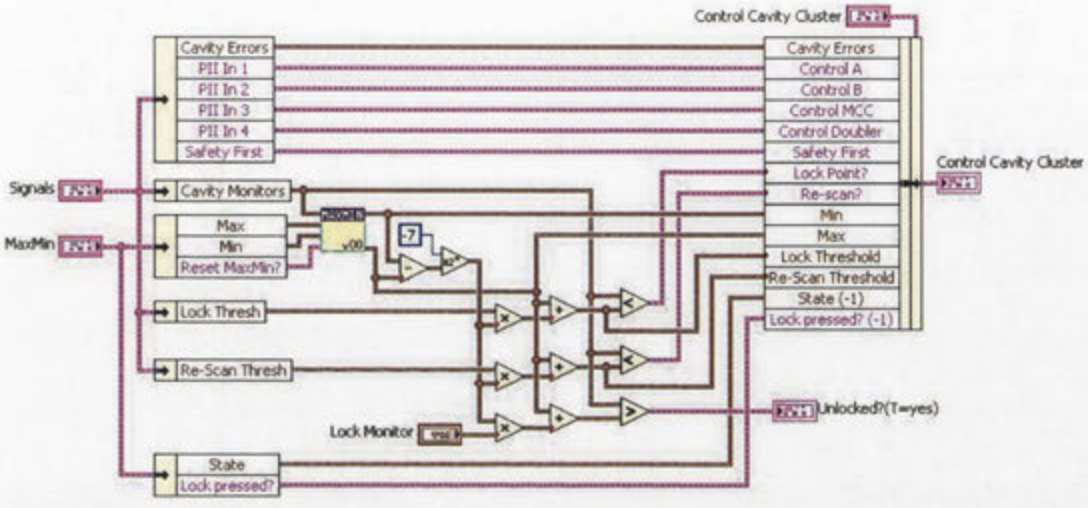

Figure 4.13: Threshold.vi. Monitors the DC signal from a scanned cavity in order to see if it is on resonance.

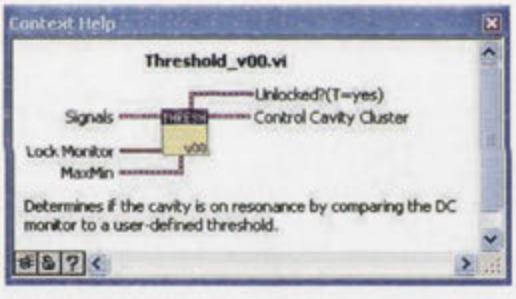

The idea behind 'Threshold.vi' is that when we scan the optical path length of a cavity, we can tell where the cavity is on resonance by monitoring the light level of either the reflected or transmitted field. When observing the reflected field for example the reflected optical power will be much less on resonance. This information is represented in the 'Cavity Monitors' cluster. The 'MaxMin' subVI simply computes the absolute maximum and minimum values of these monitors in order to be able to compare a user-defined threshold value that must be crossed in order to characterise the cavity to be on resonance. This threshold value will be a percentage of the resonance peak, and will be visible on the digital oscilloscope as we see in Fig. 4.21 in section 4.3.3.

Cavities_State.vi

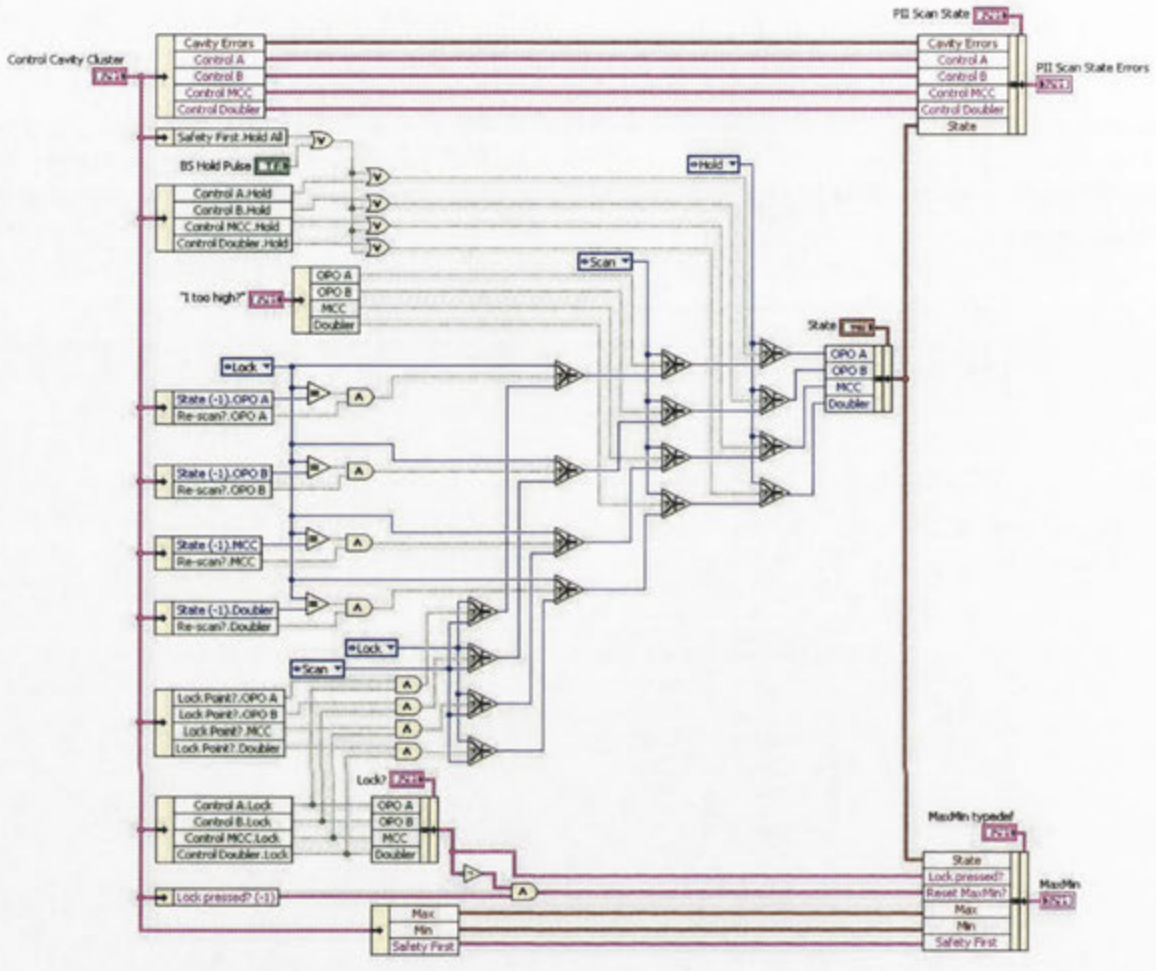

Figure 4.14: Cavities_State.vi. Determines the state of each cavity.

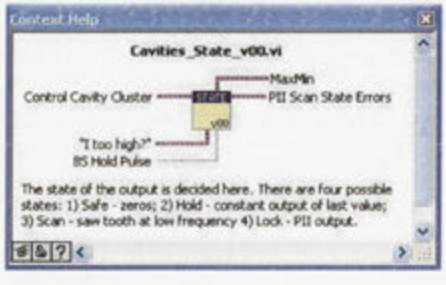

We see that 3 of the 4 possible states of each cavity discussed earlier are determined in this subVI. The other state, which is 'Safe', has been omitted for clarity. A simple boolean that over-rides the logic in this subVI can be included with minimal effort.
The default state of each cavity is 'Scan'. The 'Hold' state over-rides any logic that has previously been addressed, so that when the 'Hold' button is pressed the system is put into the 'Hold' state with no exception. The 'Scan' and 'Lock' states are coupled, as in general a scan must be

performed before the cavity can be locked on resonance. For this reason simply pressing on the 'Lock' control (which we will illustrate in section 4.3.3 dealing with the top level VI) does not automatically project the cavity into the locked state. Rather, the system will remain in the 'Scan' state until several logic conditions are satisfied, the most exemplary of which is the threshold condition detailed in the 'Thresholds' subVI. There is also logic that takes the previous state of the cavity into account, by comparing the two states (previous state and current desired state) in order to see if we are trying to re-lock a cavity that has become unlocked.

Scan.vi

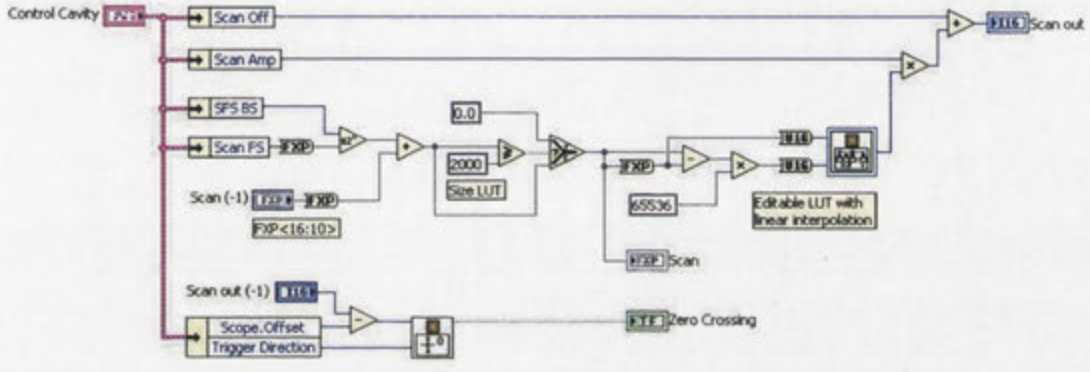

Figure 4.15: Scan.vi. Creates a saw tooth wave from a look-up table.

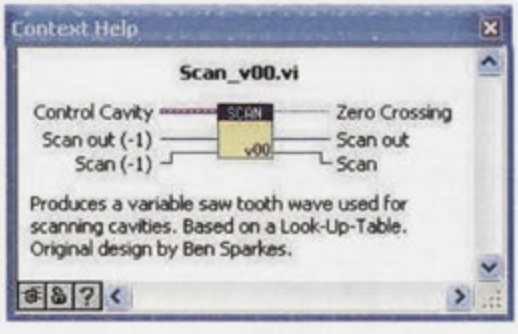

The Scan subVI is based around the LabVIEW express VI 'Look-Up Table 1D'. User-defined controls such as scan frequency and scan amplitude are fed into the look-up table via logic that interprets them. The logic and the use of the look-up table is based on a design by Ben Sparkes [49].

PII_Controller.vi

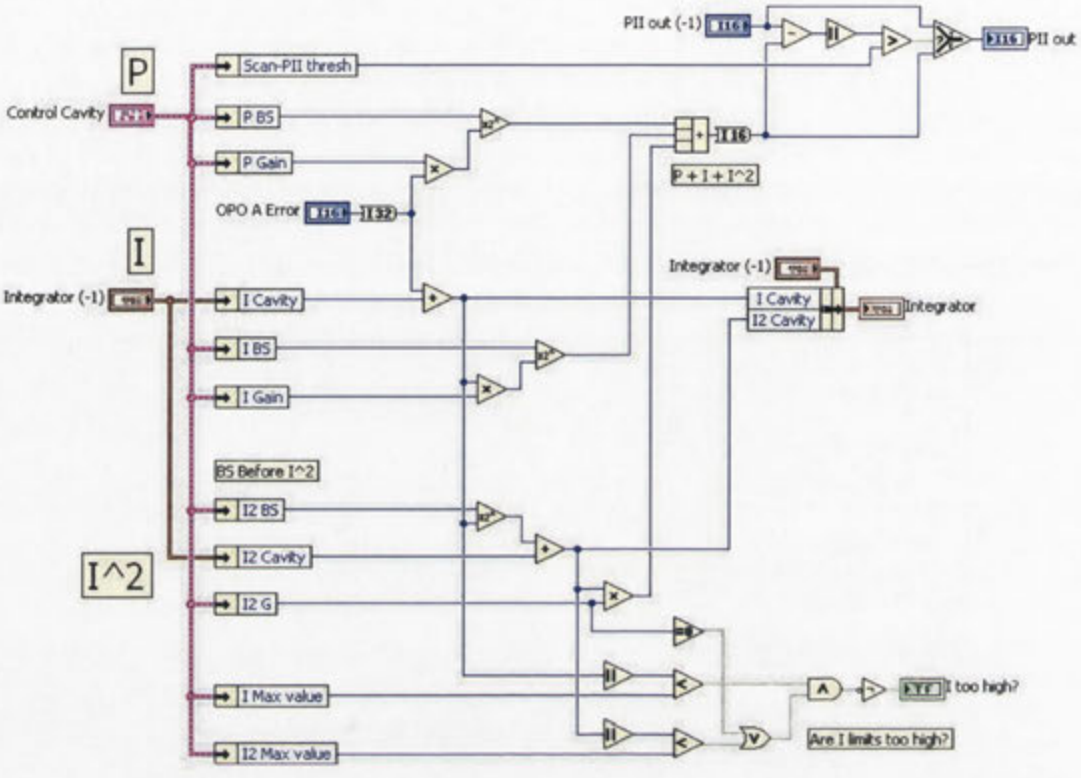

Figure 4.16: PII_Controller.vi. Applies a PII controller to an error signal in order to lock the cavity on resonance. Heavily inspired by a design by Ben Sparkes.

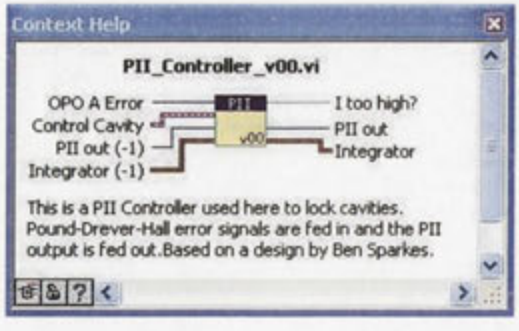

The 'PII_Controller' subVI is the central piece of logic in the entire control system. The sole action of the PII_Controller subVI is to take an error signal that represents the proximity to resonance of that cavity, and apply different gains to it in order to produce an output that will direct the cavity mirror's PZT towards resonance. PID controllers are extensively used for active control, and are ubiquitous in engineering systems. In place of the derivative gain found in PID controllers, here we use an I^2 gain. The I^2 gain is extremely sensitive and for typical cavities it is unused. It has been shown to be useful for low frequency noise [49].
This PII controller was inspired by a PII controller designed by Ben Sparkes in [49]. One important difference here is the comparison logic found in the top right corner of the subVI. The previous

output of the PII controller is compared to the current output of the PII controller. If the difference between these two values is larger than a user-defined threshold 'Scan-PII thresh', then the output will be the same as the previous value. This will continue (at an iteration rate of around 500 kHz) until the PII controller output is near enough to the original value. A subtlety here is that what I referred to as "the previous output of the PII controller" is more often than not the last output of the Scan subVI, just before the locking logic kicked in. This ensures that once the cavity is scanned onto resonance and the logic kicks over the state machine into the PII state, the change in voltage sent to the PZT will be controllably minimal so that the cavity is not kicked out of resonance by an unnecessarily large change in voltage. This was found to be very effective during testing phases and is the trimmed down version of many possible logic operations that mimic this effect.

Output.vi

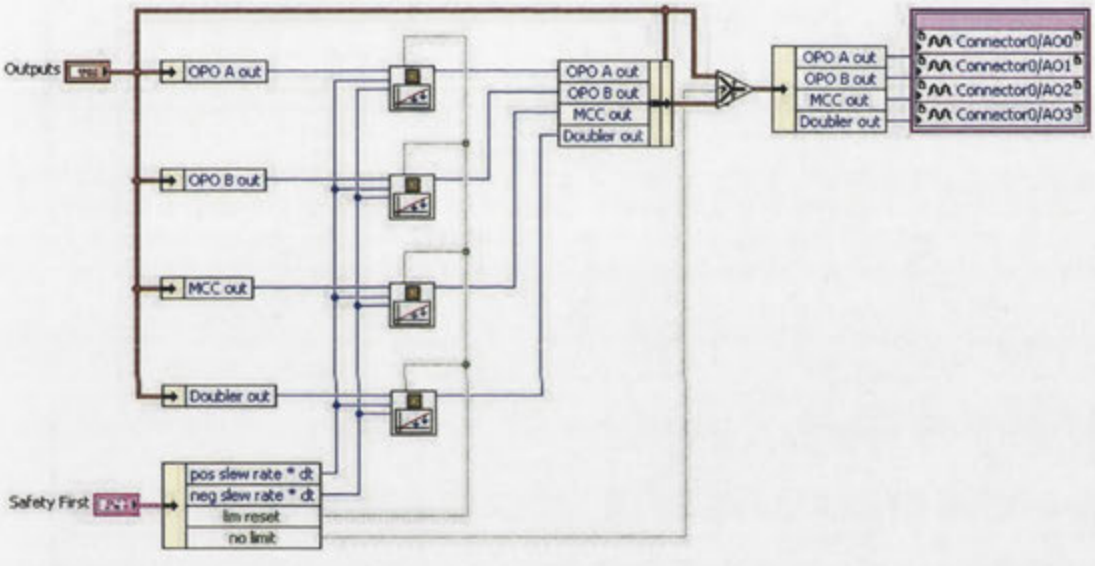

Figure 4.17: Output.vi. Limits the rate of change in the output voltage before feeding the signals to the FPGA output nodes.

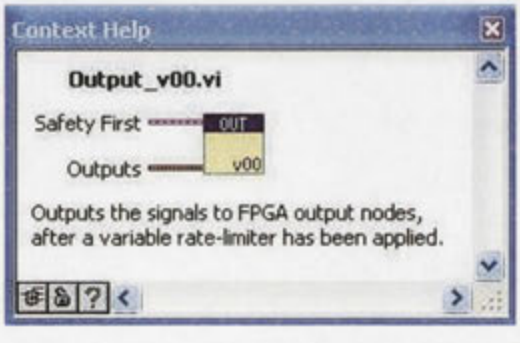

An important consideration when feeding signals to FPGA output nodes is the following. At what rate and by how much do the signals vary? In our experiments the outputs of the FPGA are fed directly into high voltage amplifiers before reaching the PZTs that are attached to mirrors. If the change in voltage is too large and the frequency of change is too high, it becomes a challenge

for the combined mirror-PZT system to hold onto each other. LabVIEW has a great 'Rate limiter' subVI that is employed here to compute the desired logic. Note that limiting the output too severely will adversely affect the locking bandwidth and therefore a balance between safety and performance must be achieved.

Graph_FPGA.vi

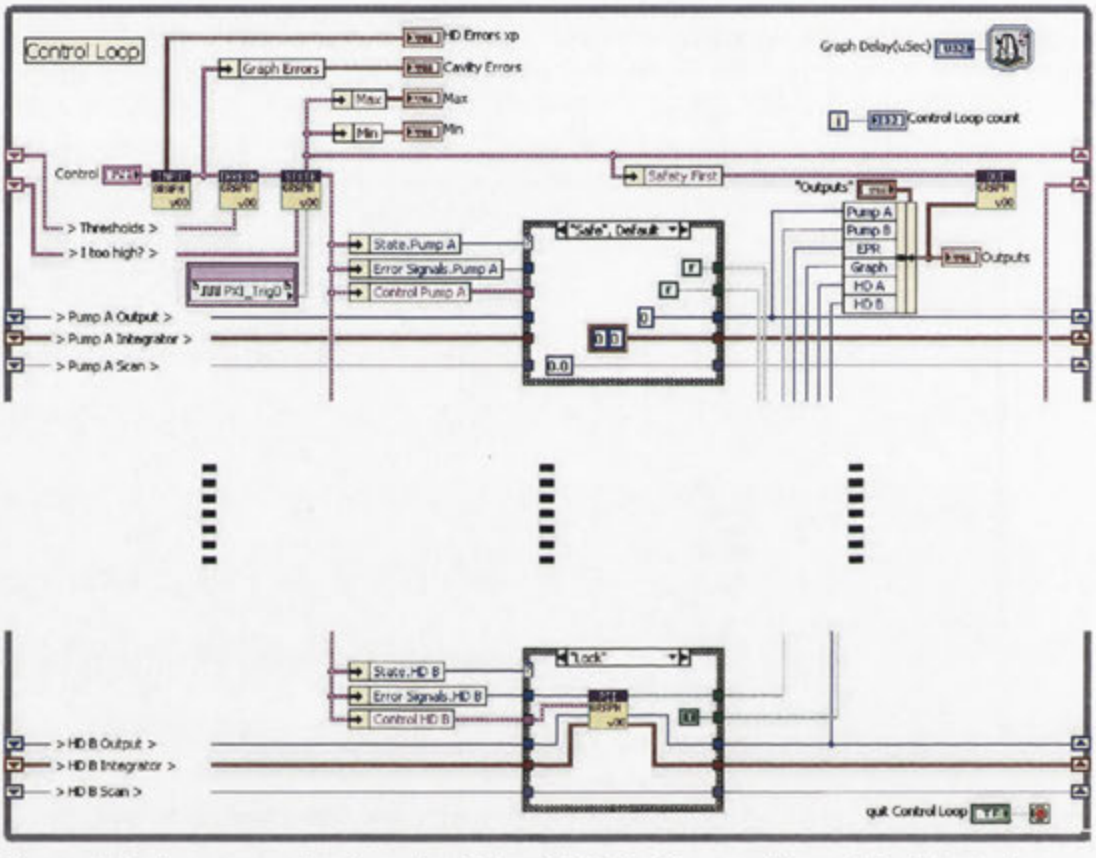

Figure 4.18: A compressed schematic of Graph_FPGA.vi's control loop. The design is the same as that of Cavities_FPGA.vi with an extension here to 6 phase locks.

'Graph_FPGA.vi', the other FPGA level VI, controls six phase locks that are based on the interference of two beams at a beam-splitter. The logic in this VI allows us to lock the relative phases of the two homodyne measurements at any phase angle (not just 0 or $\frac{\pi}{2}$).

The six phase locks that are controlled here are:
1) Parametric gain of OPO A (relative phase between pump beam A and squeezed beam A)
2) Parametric gain of OPO B (relative phase between pump beam B and squeezed beam B)
3) EPR beam-splitter (relative phase between squeezed beam A and squeezed beam B)
4) Graph beam-splitter (relative phase between EPR beam A and delayed EPR beam B)
5) Homodyne A (relative phase between Graph beam A and local oscillator A)
6) Homodyne B (relative phase between Graph beam B and local oscillator B)

As you can see from the control loop shown in Fig. 4.18, the architecture here is the same as in Cavities_FPGA.vi. There are 6 parallel case structures (only 2 shown for brevity), 1 for each

phase lock described above. The 6 subVIs found in Graph_FPGA.vi perform the same tasks and contain essentially the same logic as the 6 subVIs in Cavities_FPGA.vi. Notable differences are found only in the Input subVI and the Threshold subVI.

Input_Graph.vi

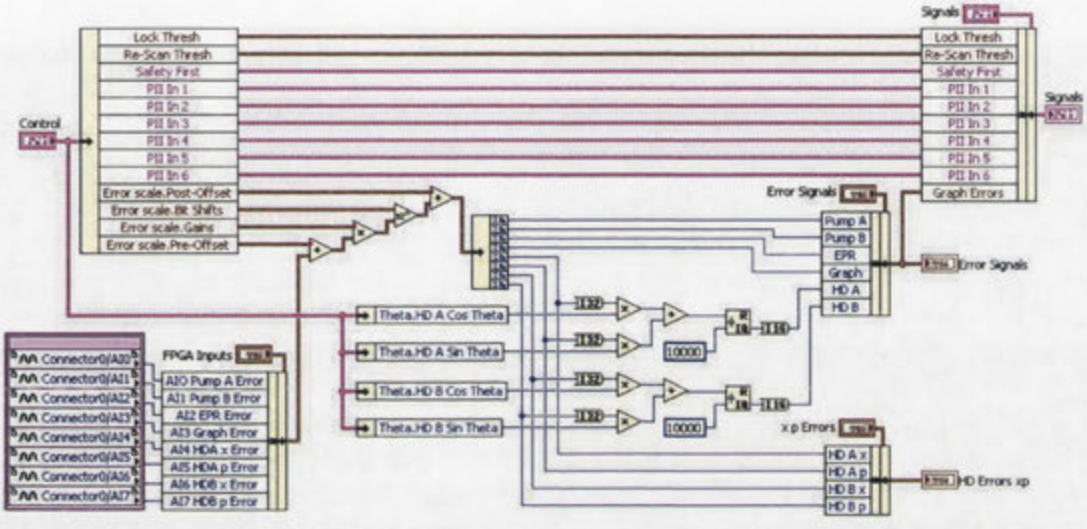

Figure 4.19: Input_Graph.vi Scales and bundles 8 inputs from the FPGA card. There are 4 error signals that each correspond to a single phase lock, and then 4 error signals that correspond to 2 homodyne detection.

One can see that the architecture and logic here is very similar to Input_Scale.vi, with one notable exception. The homodyne locks require two error signals each, that are combined in order to be able to lock the local oscillator to any arbitrary relative phase to the signal beam. This means that we can lock to and measure any phase quadrature of the signal beam, $\hat{x}_\theta = \hat{x}\cos(\theta) + \hat{p}\sin(\theta)$. The keen observer will notice that there are no DC monitors being read in. This is because the error signal contains all of the information we need. The absolute value of an error can be taken in order to produce an all positive signal that we may use as a monitor for our threshold logic. This is precisely what happens in the Graph version of Threshold.vi, and the relevant logic is shown below in Fig. 4.20.

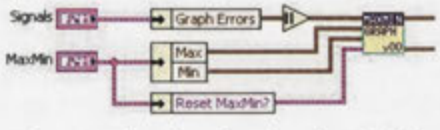

Figure 4.20: Absolute value of error signal taken for threshold monitor. This logic appears in Graph_Threshold.vi.

4.3.3 Top level VI

The top level VI runs on the PC and accesses the VIs compiled on the FPGA in order to update parameters and to read data that is being communicated. A user interface was developed that allows us to visualise the relevant signals as well as adjust the required parameters.

Front Panel

Figure 4.21: Front panel of Top_level.vi. All of the 10 phase locks as well as the TTL pulses are controlled here with an oscilloscope available for viewing the state of each phase lock.

There are 3 different structures on the front panel that provides the graphical user interface. The display on top serves as an oscilloscope with 4 channels. We see on this screen shot that the state of the cavity is in Scan. On the oscilloscope we can see the DC monitor of the scanned cavity, the error signal, and a threshold line. There is also an output channel that has been omitted here for clarity, which appears as a saw tooth wave during the scan state.
The control panel in the bottom left allows access to most of the relevant parameters required to control the various states of each phase lock. A Tab design is used here and when a different phase lock is selected the oscilloscope will change to the relevant phase lock. On the bottom right distinguished by the purple background we see another tab structure, this time showing timing controls for the TTL pulse generator. All of the other controls are placed within this bottom right tab control, including rate limiters and oscilloscope controls.

Block diagram of Top level VI

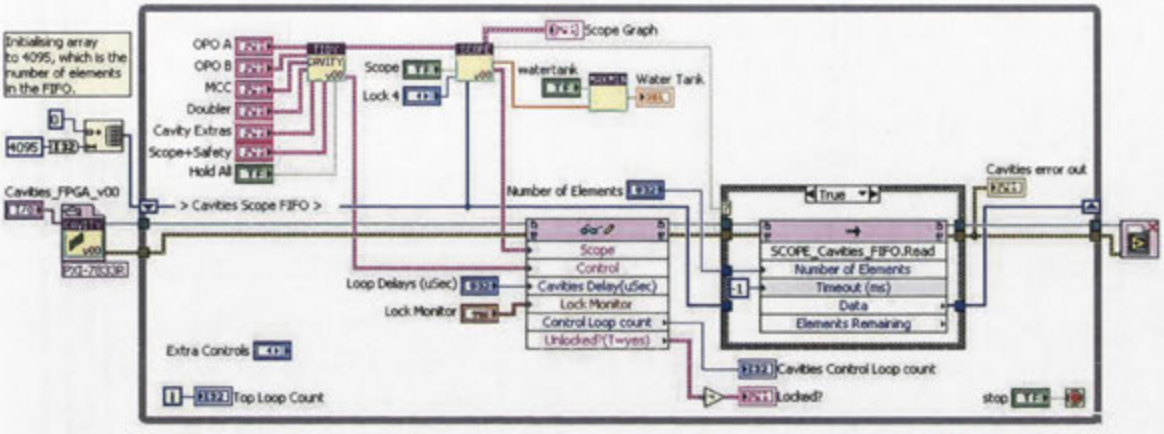

Figure 4.22: Block diagram of simplified Top level.vi. User friendly controls are packaged and sent to the FPGA to update parameters. A FIFO is used to read signals from the FPGA that are visualised on an oscilloscope.

Shown above in Fig. 4.22 is a simplified version of the block diagram pertaining to the Top level VI. We see that on the very left an FPGA reference is opened. Here, the compiled bitfile for Cavities_FPGA.vi is opened, and the reference is fed first into a read/write control function. This is where the controls on the FPGA are accessed and updated from the graphical user interface we saw on the front panel. The controls used in the top level are user friendly but quite clunky and inefficient with regard to the FPGA level controls. For this reason they are first tidied and repackaged for efficiency in the Tidy_Cavity SubVI, before being fed into the FPGA read/write control function. The FPGA reference is then fed into a FIFO which reads data that has been sent from the FPGA via a Direct Memory Access (DMA) channel. We will visit this in section 4.3.4. This data is used to produce the front panel oscilloscope in the Scope SubVI. Finally, the FPGA reference is closed before reporting an error cluster that is used for debugging.
The logic pertaining to the Graph_FPGA.vi reference is exactly the same as the process described above, and has been omitted from the block diagram for clarity.

4.3.4 TTL pulses and oscilloscope

Oscilloscope

We have seen that the top level VI running on the PC communicates with the FPGA-level logic by opening and then writing to the FPGA reference. Another way that the FPGA card and the PC communicate is via the FIFO method, used in this experiment in order to visualise the signals on the front panel oscilloscope. There are 3 DMA FIFO channels on our FPGA cards (other cards have different quantities), and they allow for very fast data streams between a target and host.

The Cavities Scope Loop sits in the Cavities_FPGA.vi in its own parallel while loop so that it can run at an independent speed from the Control Loop. Note that as this loop is reading local variables from the Control Loop the oscilloscope will ultimately be only as fast as the Control Loop speed.
The FIFO here uses the default 4095 elements and the data type used is an unsigned 64-bit integer (U64). This U64 is created by concatenating 4 16-bit integers, allowing 4 channels to be sent via the FIFO at the same time. The method of the FIFO in the Scope Loop is set to 'write', while the method of the FIFO in the Top Level VI is set to 'read'.

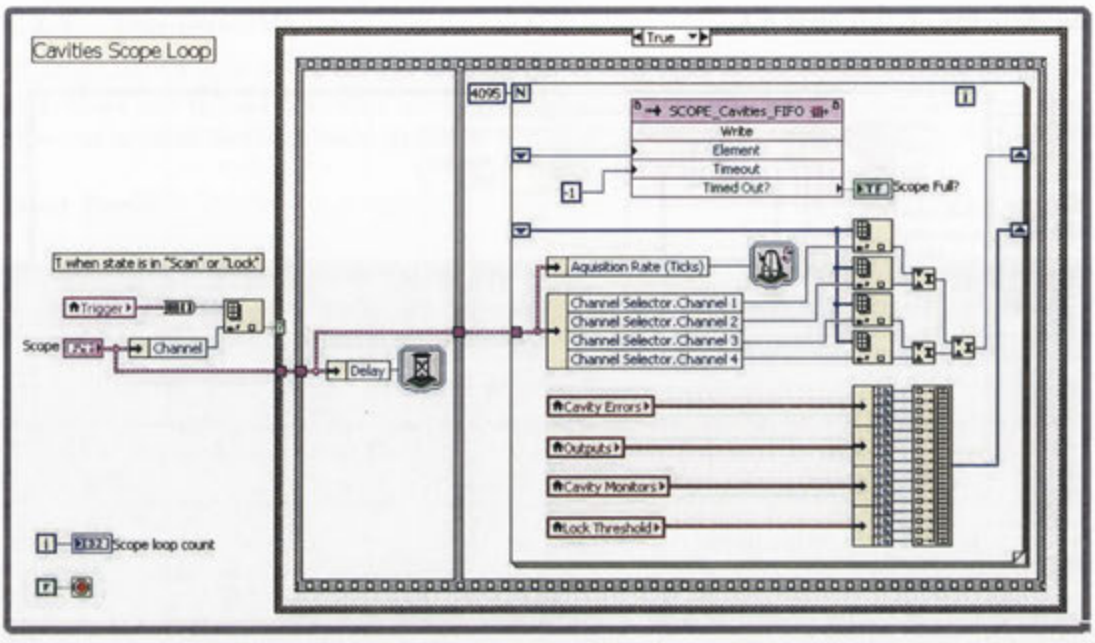

Figure 4.23: Cavities Scope loop in Cavities_FPGA.vi. Error signals, DC monitors, lock thresholds, and output signals are sent to the Top Level VI via a FIFO DMA channel allowing very fast data streams. Based on a FIFO design by Ben Sparkes.

TTL Pulses

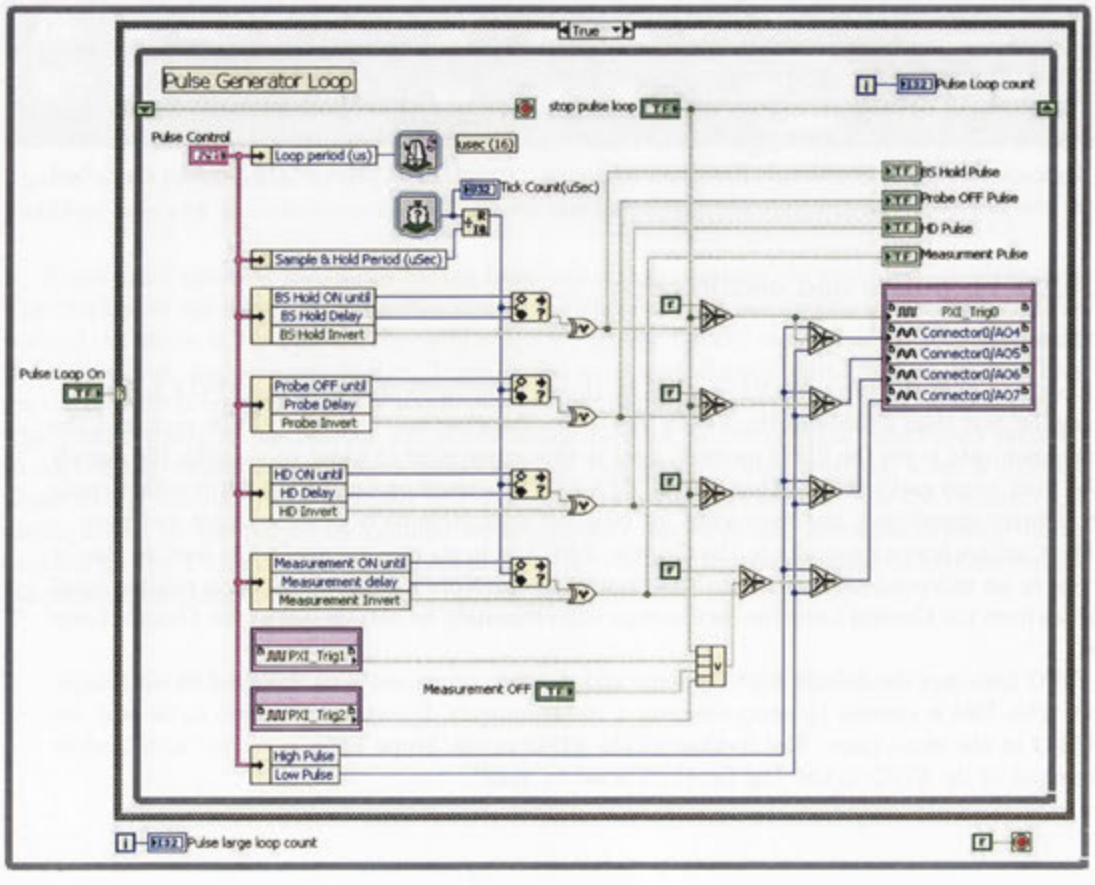

Figure 4.24: Pulse generator loop in Cavities_FPGA.vi.

In order to synchronise the TTL pulses between the two FPGA cards we use PXI trigger lines that are inherent to the PXI chassis that holds the 2 FPGA cards.
We use a PXI-1033 chassis which has a PXI backplane local bus that is a daisy-chained bus that connects each slot to adjacent slots. All the slots in the chassis share 8 PXI trigger lines via this backplane that allows high-speed TTL signals to be passed between FPGA cards. The PXI trigger lines are synced by a 10MHz clock. Note that it is possible to send pulses up to 100MHz via a star trigger from slot 2, but for our system this speed was not necessary.
There are 4 TTL pulses that are created in this loop. They each operate within a period dictated by the Sample & Hold Period, which might be on the order of 500 μs to a few milliseconds. The logic here allows for the pulse to start after a certain delay time as well as finish at a specified time for full flexibility of the pulse duration and temporal location. TTL pulses were necessary in this experiment for switching electronics as well as to sync the 2 FPGA VIs. During the measurement phase of the experiment the states of all locks were set to Hold, and the TTLs were used to switch off any noisy electronics. See section 7.4 for details on the experimental implementation.
Digital FPGA outputs are typically used for TTL outputs. Here we create TTLs by logic and employ analogue outputs in order to be able to specify maximum and minimum voltage levels. These are indicated in figure 4.24 as 'High Pulse', and 'Low Pulse', respectively. These values are controlled from the graphical user interface on the top level.

4.3.5 Final notes

The state machine system outlined in this section as control system 3 has been successfully adopted and implemented in several experimental groups at the Australian National University as well as the University of Tokyo. An advantage of the program's simple and modularised structure is that modifications and debugging become simplified and intuitive.
The project files necessary to compile and use the digital control suite outlined in this section can be found at GitHub, an online repository.
The link is here: https://github.com/Seiji-Armstrong/PDH-state-mach

Part II

Scaling up entangled states of light

Overview

Entanglement between large numbers of quantum entities is the quintessential resource for future technologies such as the quantum internet. The three chapters that form this part of the thesis investigate techniques of scaling up the number of quantised optical modes (qumodes) that form an entangled state. Entanglement was first proposed in the context of fundamental science, by the famous Einstein-Podolsky-Rosen thought experiment of 1935 [6] that would either prove quantum mechanics wrong or else deny local realism. Nearly 50 years later, in the early 1980s, two remarkable things happened. The first was a rigorous violation of Bell's inequalities[2] [7, 10] that would give evidence to the genuine existence of entanglement. The second was the birth of quantum information theory as a field, based on the idea that entanglement could be used as a resource for arbitrary manipulations of quantum information. Richard Feynman and David Deutsch were responsible for this remarkable insight [50, 15].

There are two techniques that are investigated in the following three chapters. Both techniques are concerned with multiplexing qumodes on the same physical channel. This is done in order to reuse optical and electronic components, as conventional schemes that require an increase in experimental apparatus in order to achieve an increase in the number of entangled qumodes are demonstrably not scalable. We look at multiplexing spatial modes in chapter 6, the idea itself developed from spatial mode conversion experiments presented in chapter 5. By designing a robust and flexible detection scheme, we are able to choose the basis of measurement at the time of detection, leading to a range of spatial mode bases available for measurement. We achieve up to eight-qumode entanglement, which was at the time the largest entangled state to be multiplexed on one beam. More interesting than the size of the entangled state is the idea of emulating linear optics networks within the beam, and this is given a considerable theoretical treatment in the chapter. The final technique demonstrated in this part of the thesis is based on multiplexing qumodes in the time domain, presented in chapter 7. The experimental demonstration was based on concepts that Nicolas Menicucci has been developing [51, 52, 22] over the past few years. By treating continuous beams of light as a sequence of independent wave-packets, each one a qumode, we were able to create ultra-large entangled states. A full theoretical treatment of the entanglement structure is formulated, following the graphical calculus presented in [36].

[2] John Bell formulated the famous inequalities in the 1960s, and these were first violated experimentally by Freedman and Clauser in the 1970s [8].

Chapter 5

Quantum spatial mode converter

It is often assumed that the spatial properties of the light to be measured are well understood before measurement. There are many instances where this is untrue, such as in medical imaging, or astronomy to name a few. In order to extract the maximum amount of information from a measurement, one must completely match the optical field of interest with the detection apparatus.
In this chapter we detail a quantum imaging project that deals with the spatial manipulation of a signal beam in order to match it to a fixed detection system. The demonstration uses homodyne detection, an efficient method of measuring quadrature variances in continuous-variable quantum optics. A spatial mode converter was designed and constructed by the Quantum Imaging Group, led by Jean-Francois Morizur. The mode converter was able to reshape an arbitrary spatial mode to match the homodyne detector's local oscillator. This was tested for classical light inputs and performed remarkably well. My contribution was to inject the mode converter with non-classical light, in this case squeezed light. The performance of the device as a quantum mode converter is characterised by noise analysis. The design and construction of extremely sensitive and well-aligned optical paths, as well as the optimisation of our optical parametric amplifier led to three demonstrations of the spatial conversions of squeezed light, each time while retaining their quantum nature.

The results from this chapter have been summarised in the following publications:

- J.-F. Morizur, L. Nicholls, P. Jian, S. Armstrong, N. Treps, B. Hage, M. Hsu, W. Bowen, J. Janousek, and H.-A. Bachor, Programmable unitary spatial mode manipulation., *Journal of the Optical Society of America. A, Optics, image science, and vision* **27**, 2524 (2010).
- J.-F. Morizur, P. Jian, S. Armstrong, N. Treps, W. Bowen, J. Janousek, and H.-A. Bachor, Spatial reshaping of a squeezed state of light, *The European Physical Journal D* **61**, 237 (2011).

5.1 Classical mode converter

In the late 1970s, a Russian mathematician Zenon Ivanovich Borevich published a series of theorems related to complex unitary matrices [53]. Pu Jian and Jean-Francois Morizur from our Quantum Imaging Group at the Australian National University reformulated Borevich's results in terms of reshaping the transverse amplitude profile of a laser beam.
Given a finite number of phase deformations and optical Fourier transforms applied to the light, it is possible to perform any desired unitary transform of the spatial mode profile, asymptotically reaching perfect conversion efficiency. As a specific example, Morizur and Jian showed that an arbitrary beam-splitter operation can be performed between co-propagating spatial modes with perfect conversion efficiency given 17 successions of phase profile deformations and Fourier

transforms. Further, simulations revealed that it is possible to achieve relatively high conversion efficiencies between certain spatial modes. It was shown experimentally [54] that 3 successions are enough to convert a TEM_{00} fundamental mode from the Hermite-Gauss basis into either a TEM_{10}, TEM_{20}, or a TEM_{30} mode with over 80% efficiency. For a complete theoretical treatment the reader is encouraged to read Morizur's PhD thesis [38].
The classical mode converter constructed by Morizur and Nicholls performs 3 phase profile deformations with 2 optical Fourier transforms in between, as shown in Fig. 5.1.

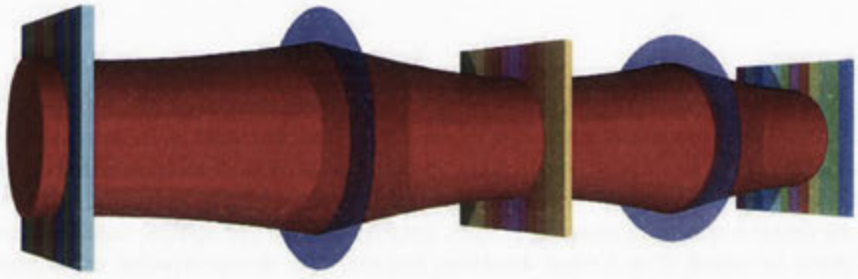

Figure 5.1: Phase and amplitude transformations of light. The spatial profile of the beam undergoes 3 phase transforms via the phase plates and 2 amplitude transforms via Fourier optics. Source: [38].

A simple glass plate with a varying thickness profile would suffice to deform the beam's phase profile. Indeed, this is essentially what is used in the experiment detailed in the *Programmable linear optics network* chapter of this thesis in order to create a very simple orthogonal basis. However, there are two limitations that this imposes. First, we are limited to one phase profile per glass plate. Second, and much more serious, is that the desired phase profile must be known prior to designing the glass plate. For complex mode transforms, analytical solutions for successive phase profiles are extremely difficult to calculate. For these two reasons we employed a deformable mirror from Boston Micromachines that can be adaptively optimised in order to find an optimal phase profile.

5.1.1 Phase deformation by adaptive optics

The deformable mirror was purchased from Thorlabs (DM140-35-UM01) and manufactured by Boston Micromachines. The surface of the continuous gold membrane is 4.4 mm wide and is malleable and deformable, which allows for arbitrary phase profiles to be imprinted onto the incident light. The membrane has 140 electrostatic actuators behind it laid out in a 12×12 grid with the 4 corners removed. Each actuator is individually controlled via a voltage with 14-bit resolution. The range of each actuator is 3.5 μm, or several wavelengths, such that the smallest increment is 0.21 nm. A useful mental image to consider is a tent sheet with 140 tent poles underneath it, with the freedom to move each tent pole individually with extreme precision.

As these deformable mirrors cost on the order of US$17,000, it was not plausible to purchase more than one for the experiment. A trade-off between the performance of the experiment and financial constraints led to the elegant solution of using the surface of the deformable mirror 3 times, at the expense of the horizontal axis. In other words, the horizontal axis essentially acts as a mirror, and we only perform spatial transforms in the vertical axis. Operating within the Hermite-Gaussian basis, we are constrained to TEM_{m0} modes. This is achieved by focusing the

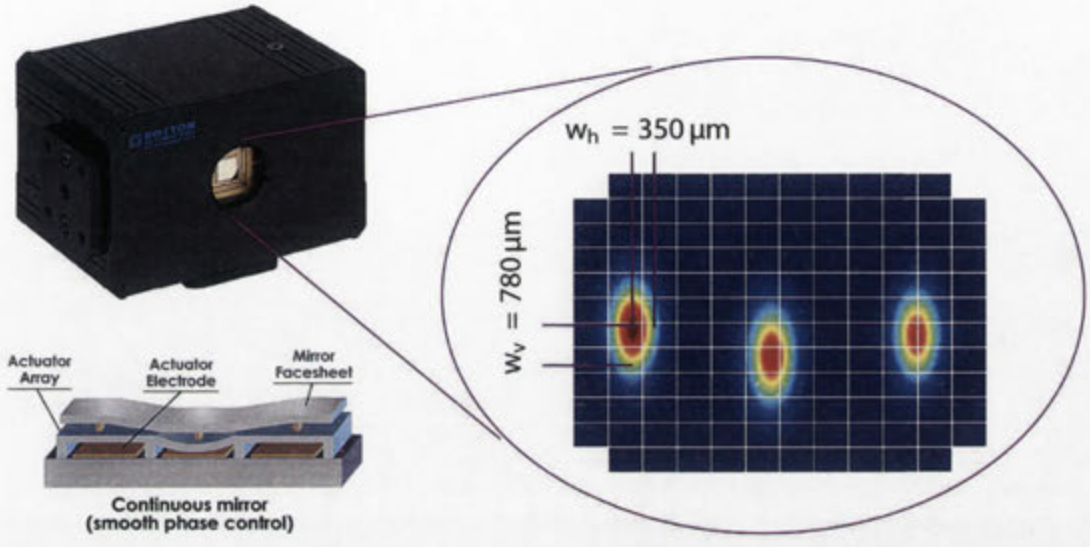

Figure 5.2: Deformable mirror from Boston Micromachines. The width of the deformable mirror is 4.4 *mm*, and there are 140 individually accessible pixels in a 12 × 12 grid (minus the corners). Each pixel width is 370 *µm*. Source: [54] and [55].

beam elliptically as shown in Fig. 5.2. The horizontal waist, w_h, is 350 *µm* ensuring that there is no cross talk between the 3 designated regions of the surface. The vertical waist, w_v, is 780 *µm* so that around 99% of the beam power is incident on 10 pixels.

The original mode converter

The actual device is rather compact and looks like a purposefully misaligned triangle cavity, as can be seen in Fig. 5.3. The light encounters 3 round trips before exiting as a different spatial mode.

The light is coupled in and out of the mode converter via polarisation optics. One large spherical mirror of focal length 300 *mm* and diameter 2" is used by each of the 6 optical paths, in conjunction with a cylindrical lens of focal length 50 *mm* in order to perform the necessary Fourier transforms between the phase deformations. Per round trip, we get 3 Fourier transforms (equivalent to 1) in the vertical axis, and 2 Fourier transforms in the horizontal axis, which have no effect. This ensures that we get a sequence of phase and amplitude transforms in the vertical axis for each of the 3 round trips.

Finding optimal phase profiles

The precise analytical derivation of optimal phase profiles quickly becomes infeasible due to the high number of coupled degrees of freedom. Any deformation of the first phase profile will necessarily modify the optimal deformations in the subsequent reflections in both amplitude and phase space. For this reason, the phase profiles are optimised by employing a genetic algorithm developed largely by Morizur. Each of the 140 actuators is moved individually until its position maximises the desired conversion before moving on to the next actuator. This is done iteratively until the relative change in efficiency is very small, indicative of a local minima that approaches the global minima. In our experimental runs this tends to be on the order of 10^5 iterations, which take around 3 hours.

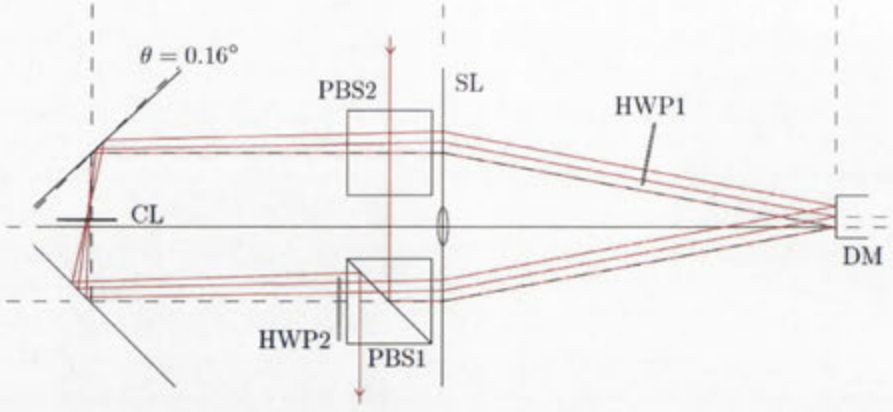

Figure 5.3: The original classical mode converter. Designed and constructed by Morizur, Jian, and Nicholls, this mode converter uses 3 spatially separated segments on the deformable mirror to emulate 3 deformable mirrors. The lenses in between are for Fourier optics, and the polarising optics are for input/output coupling. PBS: polarising beam-splitter, HWP: half-wave plate, SL: spherical lens, CL: cylindrical lens, DM: deformable mirror. Source: [54].

5.2 Shaping squeezed light via unitary transforms

5.2.1 The optical parametric amplifier (Australian National University, 2009)

The Quantum Imaging Team had an old optical parametric amplifier (OPA) that was built by Jiri Janousek several years prior, which had the potential to be optimised for use here. Over the course of several months we optimised the performance of the OPA in order to produce reliable high quality squeezed light. Much of this process was concerned with the systematic elimination of phase noise, not only inherent to the OPA but to the entire optical path leading up to detection.

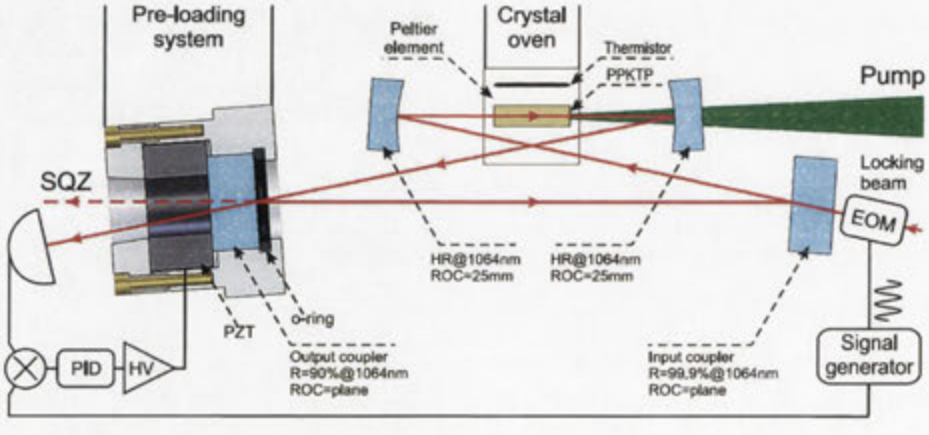

Figure 5.4: Optical parametric amplifier (OPA) used for quantum mode converter. A non-linear crystal is placed within a bow-tie cavity in order to enhance the non-classical cavity mode. The crystal, PPKTP, is placed inside a crystal oven with its temperature regulated via a peltier element. The electronics are there for controlling the optical cavity length, and to hold the cavity on resonance via feedback. Source: [56].

The OPA is displayed in Fig. 5.4. This squeezer is a type I OPA, which means that both photons in the down-converted pair are in the same polarisation. The non-linear crystal is a periodically poled KTP that is quasi-phase matched, and the OPA is operated below threshold, in a de-amplification regime such that amplitude-squeezed light is produced. There are two input beams to this OPA: a seed beam at 1064 nm and a pump beam at 532 nm. The seed beam used here makes this device an OPA rather than an optical parametric oscillator (OPO). An electro-optic modulator (EOM) is used to modulate the seed beam by passing the light through the voltage-driven crystal within the EOM. The phase modulation imparted on the seed beam via the EOM is at 14 MHz, and this is used for creating an error signal that dictates the position of one of the cavity mirrors such that the cavity is held on resonance. The feedback process used is Pound-Drever-Hall (PDH) locking.

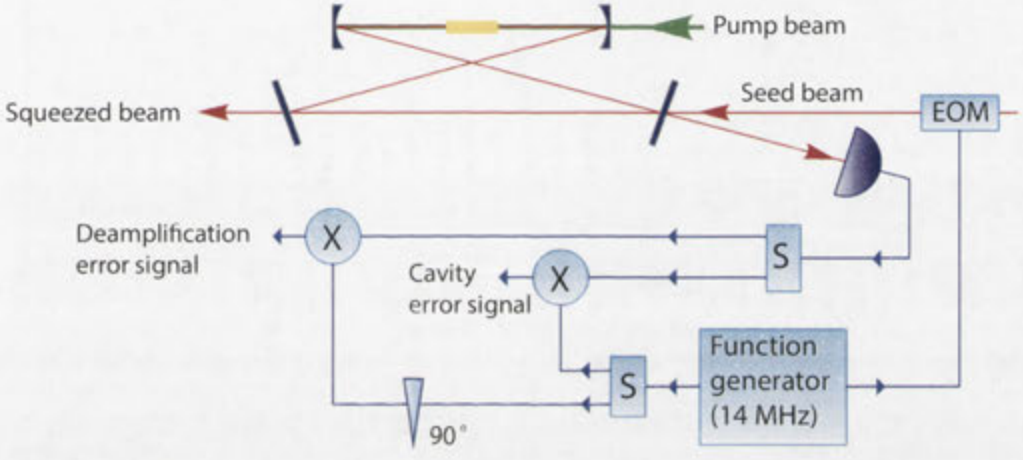

Figure 5.5: Feedback and control of the OPA. Phase modulation at 14 MHz is used in a Pound-Drever-Hall configuration in order to control both the cavity resonance and the pump beam phase to achieve de-amplification. X: Mixer, S: Splitter, EOM: Electro-optic-modulator.

The reflection of the seed beam is detected, split, and mixed with two different signals (Fig. 5.5. Both signals come from the function generator that is driving the EOM (14 MHz) with a relative phase of 90 degrees between them. The 0 degree mixed signal gives the cavity error signal, while the 90 degree mixed signal gives the de-amplification error signal in order to lock the green pump (532 nm) to the infrared (1064 nm) signal.

Parametric gain of OPA

The parametric gain of the OPA is measured by varying the pump power. As we can see from table 5.1, the temperature of the PPKTP crystal needs to be optimised each time, but stays within a range of 1%.

Power (mW)	**0**	**50**	**100**	**150**	**200**	**250**	**300**	**350**
Temp	32.03	32.03	32.00	31.97	31.96	31.94	31.92	31.88
G_+	1	2.45	4.04	6.37	10.85	19.72	44.91	169.8
G_-	1	0.55	0.47	0.39	0.35	0.32	0.29	0.27

Table 5.1: Parametric gain of OPA.

The measured parametric gain values are found to agree extremely well with the theory, as shown in Fig. 5.6. Here, the threshold power is 411 mW. The same figure shows measured

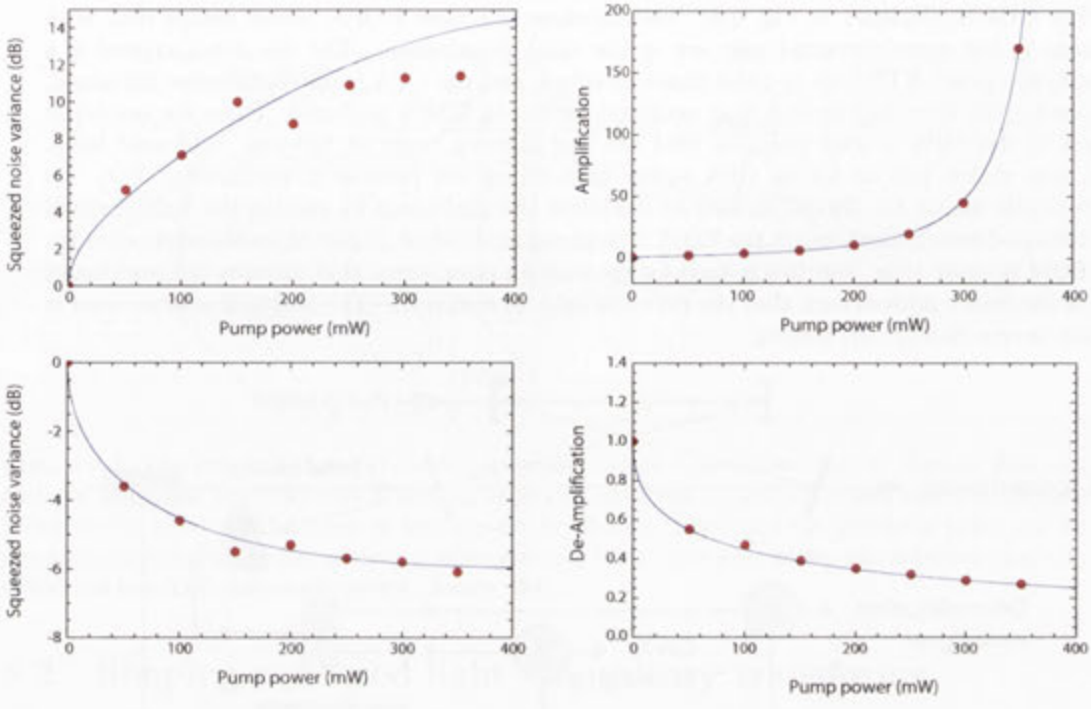

Figure 5.6: Squeezing and anti-aqueezing values of OPA. Squeezing values, anti-squeezing values, and parametric gain values as a function of pump power. In all traces the red circles are experimental data points, and the blue solid line is theory. Uncertainties for amplification/de-amplification are too small to be plotted. Uncertainties in squeezed noise variances are between ±0.2 dB and ±0.7 dB for high pump powers (error bars not plotted for clarity).

squeezing values taken immediately after the OPA for a sideband mode at 2.7 MHz and resolution bandwidth 30 kHz.

5.2.2 Injecting the mode converter with squeezed light

The squeezed output of the OPA must be mode-matched to the input coupler of the mode converter in order to ensure the maximum conversion efficiencies. This requires a selection of lenses and mirrors, which contribute to an unavoidable amount of propagation losses as each optical element introduces a small amount of optical loss. In order to characterise the performance of the mode converter with respect to the quantum noise properties of the light, we compare the amount of squeezing in the input light to the amount of squeezing in the output light, and take passive optical loss into account. For this reason we measure the squeezing value of the input light directly before the mode converter as well as directly afterwards.

We find the input squeezed light directly before the mode converter to be consistently at -5 ± 0.1 dB in the squeezed quadrature, and 6.4 ± 0.2 dB in the anti-squeezed quadrature. The output mode of the quantum mode converter is then measured at a second homodyne detector and the squeezing values are tabulated below for the various mode conversions.

We see from the measurements in table 5.2 that the quantum mode converter successfully reshapes the input TEM_{00} mode into 3 higher order modes in the Hermite-Gaussian basis, and remarkably preserves squeezing below the quantum noise limit. In all of the demonstrations the measured squeezing level of the output mode is comfortably below -1 dB, recovering up to -1.6 ± 0.1 dB noise suppression for the TEM_{10} mode. Note that this is the first demonstration of this

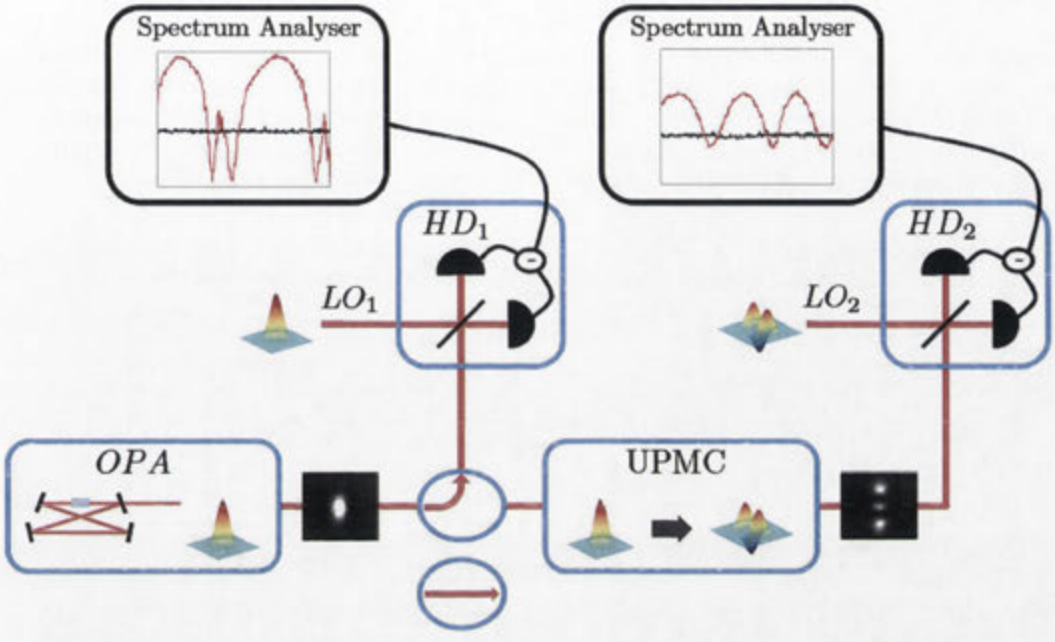

Figure 5.7: Shaping squeezed light. The amount of squeezing present in the signal beam is measured before and after the mode transformation, at HD 1, and HD 2, respectively. Source: [57].

Mode:	Input	TEM_{00}	TEM_{10}	TEM_{20}	TEM_{30}
Squeezed noise variance (dB)	-5.0	-1.7	-1.6	-1.3	-1.4
Anti-squeezed noise variance (dB)	6.4	4.4	4.4	3.3	4.0

Table 5.2: Measured noise variances after quantum mode conversions. All uncertainties are ±0.1 dB except for the anti-squeezed quadrature for the input, which is ±0.2 dB.

kind and paves the way for mode conversions of quantum light.

5.2.3 Optical loss

In order to characterise the performance of the quantum mode converter, we must systematically investigate where the losses in squeezing are occurring. We are concerned with two types of loss: phase noise that is added by the mode converter, and passive optical loss that is introduced by lossy optical components. A detailed study of the optical beam path revealed that there is 51% loss, consistent with measurements of the difference in power between the input to the mode converter and the output of the mode converter.

We find that there are three main categories of loss:

1) Losses due to reflections from the deformable mirror;
2) Losses due to beam propagation through polarisation optics;
3) Losses due to beam propagation through non-polarising optics.

Reflections from the deformable mirror

The gold surface of the deformable mirror is protected by a broadband anti-reflection (AR) coated protective window that is on an angle of 6°. Reflections from the deformable mirror can therefore be separated into reflections from two subsystems: the protective window and the gold membrane surface. Figure 5.8 depicts the specified reflection coefficients obtained from the manufacturer (Boston Micromachines) via the vendor of the device (Thorlabs) for the two subsystems.

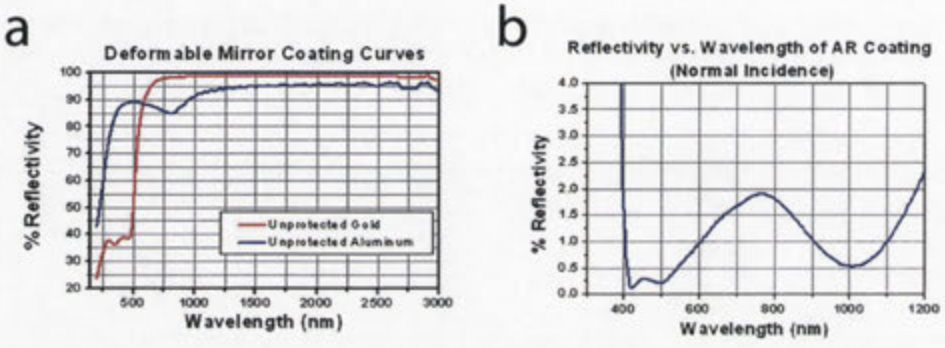

Figure 5.8: Reflecitivities of various surfaces of the deformable mirror. (a) The reflectivity of the gold membrane as a function of wavelength as provided by the manufacturer. Our experiment uses light at 1064 *nm*. (b) The reflectivity of the protective window. Source: [55].

We see that for our wavelength of 1064 *nm* the loss from the gold surface of the deformable mirror is on the order of 0.5%. We also see that the AR coating of the protective window has around 0.7% loss under normal incidence. Note that Fresnel's equations tell us that the reflection coefficient has minimal change for up to 6 degrees. As there are four surfaces of the protective window that the beam experiences upon one reflection from the deformable mirror (front surface and back surface on the incident beam followed by back surface and front surface of the reflected beam), we should get on the order of 2.8% loss[1]. Our total of 3.3% loss is consistent with what the manufacturer Boston Micromachines specifies.
This needed further investigation and so we set up the schematic of Fig. 5.9 in order to precisely measure the amount of optical loss from the deformable mirror.

Incident light is first split on a balanced beam-splitter so that the two beams exiting the beam-splitter have precisely the same power. This is verified by using flip mirrors in the top beam path so that the beam does not see the deformable mirror, and the two beam powers are carefully calibrated using two identical detectors. Then, the flip mirrors are flipped down allowing the top beam to be reflected from the deformable mirror, and the difference of the two detectors gives us a precise measure of the optical loss due to the deformable mirror. This technique is much more reliable than using a power meter for example, as any fluctuations in the laser power will be cancelled out due to the classical intensity correlations created by the balanced beam-splitter.
Changing the polarisation of the incident light had no effect on the amount of loss measured, contrary to initial expectations. Repeated careful measurements revealed a 6.5% loss upon reflection of the deformable mirror and protective window system, for an incident angle of 2.8° with respect to the axis perpendicular to the face of the deformable mirror. Increasing this angle saw a nearly linear increase in loss, for example up to 10% for an angle of 8.1°. Closer inspection of the window revealed faint reflections both at a slight angle above and a slight angle below the optical plane. In order to see this effect, we hit the deformable mirror with light normal to the face, and clearly observed the two unwanted reflections, as depicted in Fig. 5.10. This provided visible confirmation

[1] Morizur reports in his thesis that "each reflection from the deformable mirror is responsible for a 4.2% loss... consistent with the reflectivity of the gold membrane of the DM and the coatings used on the protective window".

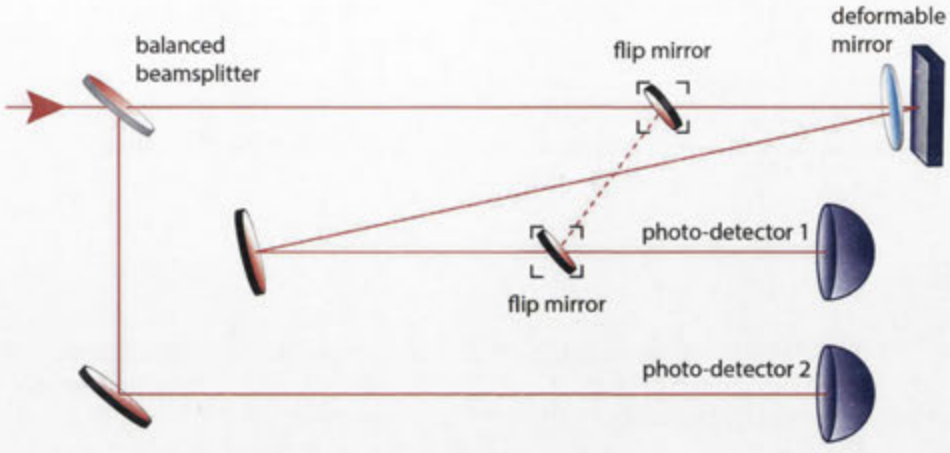

Figure 5.9: Measuring losses from deformable mirror. The optical power loss induced by the deformable mirror is measured by comparing alternate beam paths.

of the less than desirable quality of the AR coating on the protective window.

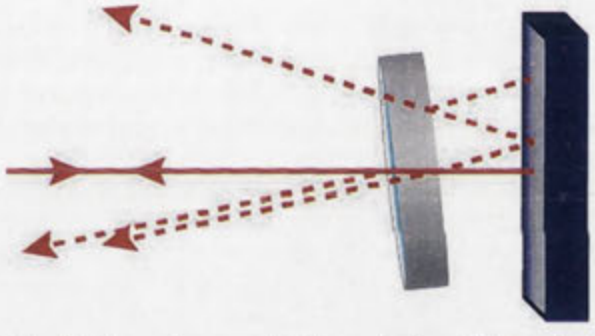

Figure 5.10: Unwanted reflections from protective window. We see that there are several reflections per surface of the protective window. The width of the window is exaggerated in order to show the reflected beam paths.

A group at the Jet Propulsion Laboratory, NASA, were using the same device for nulling interferometry. They custom ordered their deformable mirror from Boston Micromachines without the protective window, and could observe 99% reflectivity from the mirror. This served as conclusive evidence that the optical loss in each reflection from our deformable mirror is due to the poor anti-reflection coating of the protective window. Correspondence with Boston Micromachines convinced me that removing the window at this stage was not an option as it was hermetically sealed.

Optics that contribute to loss

All of the optical elements that comprise the mode converter are summarised in table 5.3.

The original mode converter had 2 polarising beam-splitters (PBS) along with strategically placed half-wave plates that were responsible for coupling in and out the signal beam. One PBS was used as both the input coupler and the output coupler. The second PBS was necessary for alignment purposes - ensuring symmetry in the optical path lengths - due to the change in refractive index seen by transmission through the first PBS. As these PBS are specified to have a touch less than 5% loss when used for transmission, the total loss from 6 transmissions would be on the order of $1 - (1 - 0.05)^6 = 26.5\%$.

Item	Manufacturer	Serial number
$2''$ $f = 300$ mm lens	Thorlabs	LA1256-C
f=50 mm cylindrical lens	Thorlabs	LJ1659L2-C
$1''$ Polarising Beam Splitter	Newport	10BC16PC.3
Deformable Mirror	Boston Micromachines	17W025#089-400D16
1064 nm Half Wave Plate	Newport	10RP12-34

Table 5.3: Optical elements in mode converter.

Calculating the optical losses of all optical elements besides the deformable mirror and the polarising beam-splitters by using the specifications of their coatings reveals around 18% loss [38]. This gives us $1 - (1 - 0.05)^6(1 - 0.065)^3(1 - 0.18) = 51\%$ loss, consistent with the 51% difference in power measured between the input and output of the mode converter.

Spatial conversion efficiencies

The final source of loss necessary to identify in order to characterise the performance of the mode converter is due to the spatial mode mismatch between the signal beam and a reference beam. Here, the reference beam is generated by a misaligned mode converter on the local oscillator beam-path. A reasonable question would be the following. If we can create spatially near perfect higher order Hermite-Gaussian modes by misaligning mode cleaning cavities, why not pass the squeezed beam through a misaligned mode converter in the first place? The answer of course is that this is an inherently lossy process, and wasteful of the precious squeezing resource.
The degree of mode matching between the spatially reshaped signal beam exiting the mode converter and the reference beam are tabulated in table 5.4. Note that the power transferred from one spatial mode to another is defined here as the square of the visibility.

	TEM_{00}	TEM_{10}	TEM_{20}	TEM_{30}
Measured visibility (v)	98.5%	95.4%	92.2%	90.0%
Power conversion (v^2)	97%	91%	85%	81%

Table 5.4: Mode conversion efficiencies. Uncertainties in power conversions are $\pm 0.1\%$

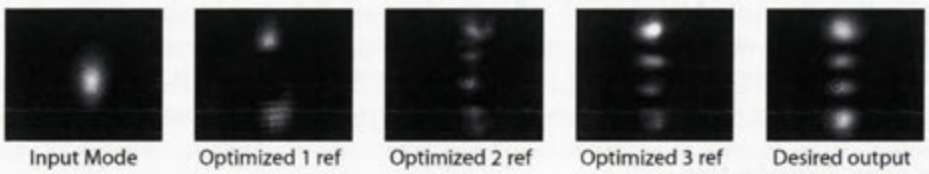

Figure 5.11: Progression of conversion from a TEM_{00} mode to a TEM_{30} mode. The CCD images after each reflection from the deformable mirror are shown. The final mode conversion resembles the desired output, but is not a perfect conversion. Source: [54].

We see in Fig. 5.11 that the spatial transformation to a TEM_{30} mode is visibly not perfect. The measured visibility for this transformation is $v = 90$ %. It is also interesting to visualise the progression of the mode transformation after each iteration of the mode converter. Clearly after only 1 reflection from the deformable mirror the mode has no resemblance to the desired output.

Degradation of squeezing

The important assumption that we must verify or falsify here is that the measured optical loss is consistent with the measured degradation in squeezing value. This will tell us if the deformable mirror is behaving as we assume - by not introducing any phase noise. For this, we model the mode converter as a black loss box that mixes the signal beam with vacuum on a 51% beam-splitter.

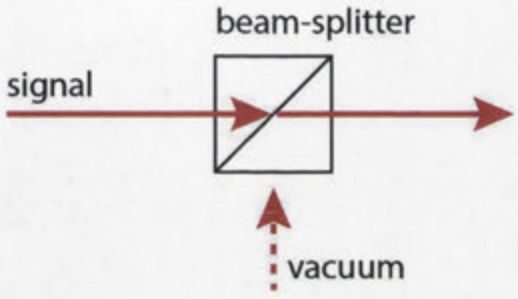

Figure 5.12: Modelling optical loss as beam-splitter interaction with vacuum. The transmission coefficient, η, of the beam-splitter represents the propagation efficiency.

Both the squeezed quadrature and the anti-squeezed quadrature will have their variances brought closer to the vacuum by an amount proportional to the reflectivity of the beam-splitter used to model the loss. The new variance after the loss is given by

$$\Delta^2 \hat{x}_{out} = \eta \Delta^2 \hat{x}_{sig} + 1 - \eta \tag{5.1}$$

$$\Delta^2 \hat{p}_{out} = \eta \Delta^2 \hat{p}_{sig} + 1 - \eta \tag{5.2}$$

where η represents the transmission of the loss-inducing process, such that $1-\eta$ is the reflectivity of the beam-splitter in the loss model. With respect to optical power loss, η is simply the power difference between the input and output measurements. With respect to spatial mode mismatch, $\eta = v^2$. By applying this model of loss twice - once for the measured optical loss, and once for the spatial mode mismatch - we arrive at the following predicted variances, tabulated in table 5.5 with the measured variances.

	TEM_{00}	TEM_{10}	TEM_{20}	TEM_{30}
Predicted squeezing (dB)	-1.7	-1.6	-1.5	-1.4
Measured squeezing (dB)	-1.7	-1.6	-1.3	-1.4
Predicted anti-squeezing (dB)	4.2	4.0	3.8	3.7
Measured anti-squeezing (dB)	4.4	4.4	3.3	4.0

Table 5.5: Comparison of predicted and measured squeezing values. All values have uncertainties of ±0.1 dB.

We conclude that the quantum mode converter degrades the quantum states only in the sense of passive optical power loss. Importantly, there is no additional phase noise that degrades the squeezing. This result lends itself to the possibility of an improvement in the amount of optical loss induced passively.

5.2.4 Optimising the setup

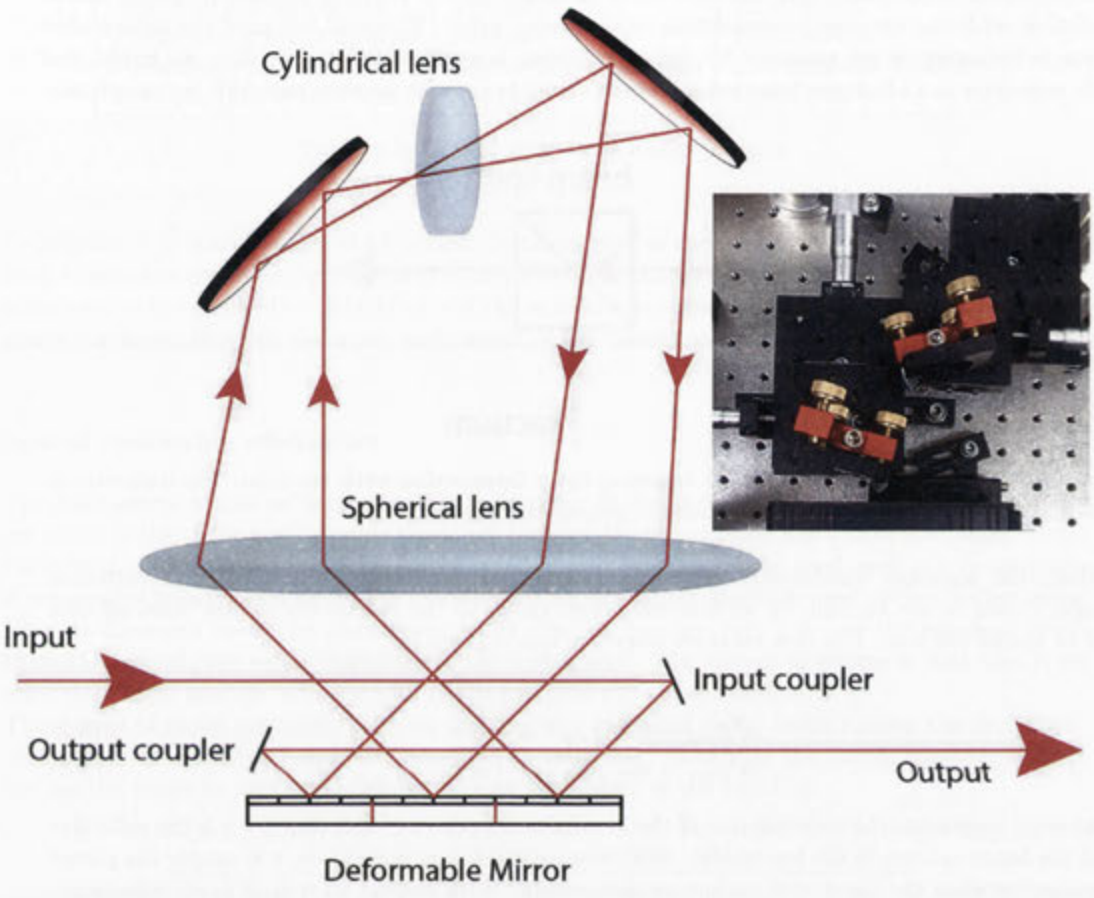

Figure 5.13: The optimised quantum mode converter. This mode converter has polarisation free input and output couplers. The inset shows the actual half mirrors used in the lab as input and output couplers.

Reducing optical loss

In order to optimise the optical setup, we must remove or replace the main culprits that are responsible for passive optical loss. We have learnt from the analysis detailed previously that removing any polarisation optics will be beneficial. In order to do this we modified the input and output coupling to make it polarisation-free. The 2 PBS and 2 half-wave plates were removed, and instead 2 half-mirrors were carefully placed to act as input and output couplers respectively. As these mirrors should only reflect one beam and not interfere with the other beam paths, half mirrors were used, reducing the physical space required.

The optimised mode converter

Figure 5.13 shows the polarisation optics-free setup. The mode matching into the mode converter was modified as well in order to account for the modified beam paths. The method employed here for alignment was to first align the mode converter as a cavity by allowing only one reflection from the deformable mirror. This simplifies the alignment of the mirrors and lenses within the

mode converter by reducing the degrees of freedom. Once this is optimal, we systematically rotate one of the steering mirrors within the mode converter and re-align until we have the 3 desired reflections on the designated regions of the deformable mirror. The baseline visibility of 98.5% was again attained after careful alignment. The optimised quantum mode converter is pictured in its entirety in Fig. 5.14.

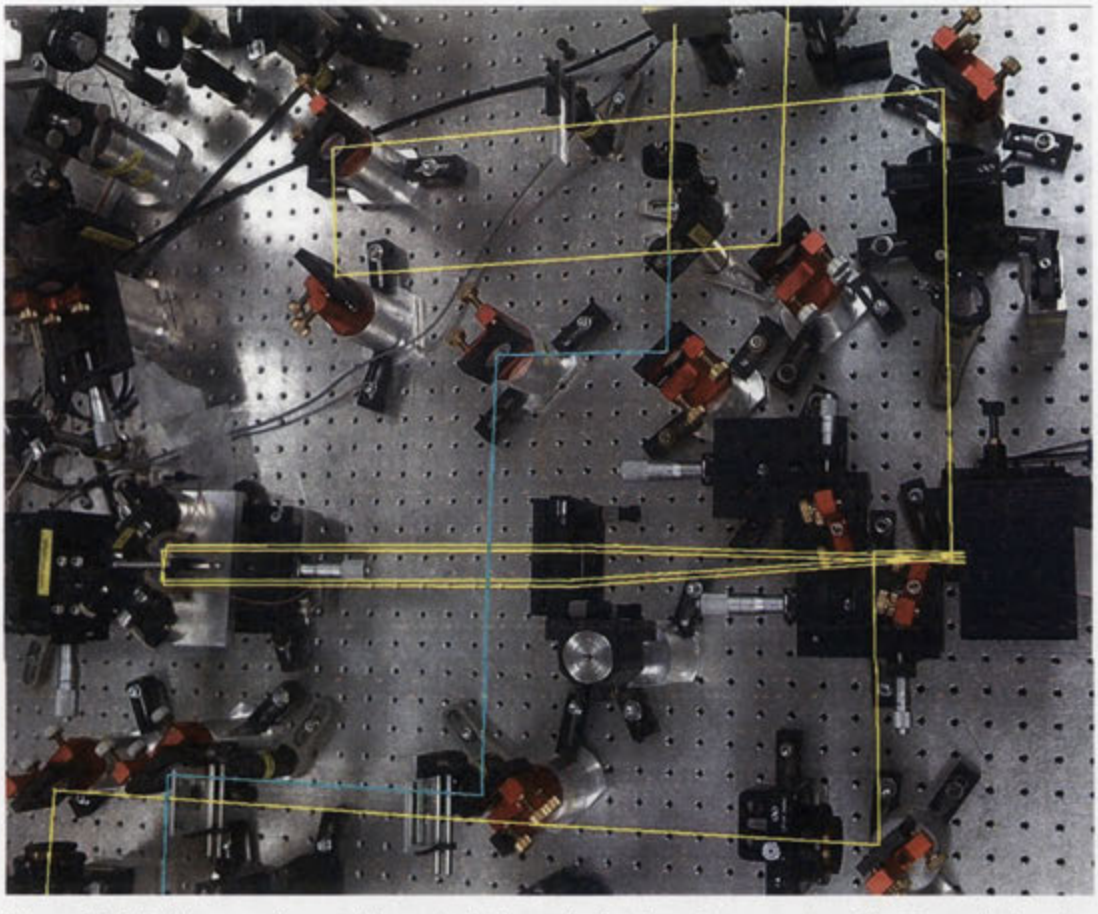

Figure 5.14: The experimental layout of the optimised mode converter. The 3 round trips that perform the spatial mode conversion within the quantum mode converter are shown by the yellow paths near the centre of the image. Note the absence of polarisation optics, and the addition of input and output couplers. The local oscillator's path is shown in cyan. The optics below the quantum mode converter are for mode matching, and the optics above are for homodyne detection.

5.3 Conclusion of project and outlook

5.3.1 Optimised mode conversion efficiencies

The difference in power between the input and the output of the mode converter is now reduced to 30.0% due to the replacement of the input and output coupler, and the removal of the half-wave plates. This is consistent with the predicted value of loss taking into account the optical loss per pass through each element.
Timing constraints forbade me from performing updated squeezing measurements after the mode conversions, as our team was in a transitioning stage with group members coming and going, and the experimental setup had to be modified overnight for some entanglement measurements. This is all part of working in a team with parallel interests and projects. The mode conversions are not affected by the change in input and output couplers however, as demonstrated by the same maximum limit of 98.5% visibility obtained when using the mode converter as the identity operation (a mirror). Therefore we can sensibly predict what the new squeezing measurements might have been, and they are summarised in table 5.6.

	TEM_{00}	TEM_{10}	TEM_{20}	TEM_{30}
Predicted squeezing (dB)	-2.7	-2.5	-2.3	-2.1
Predicted anti-squeezing (dB)	5.2	5.0	4.8	4.6

Table 5.6: Predicted squeezing values for optimised setup. All values have uncertainties of ±0.1 dB.

5.3.2 Further research into co-propagating spatial modes

This project has paved the way for further explorations into one-beam quantum networks. The simplified mode converter based on 3 successive phase and amplitude transforms constructed in our labs can be regarded as a beam-splitter between any two modes co-propagating in the beam. The case when we convert one spatial mode completely into another can then be regarded as a beam-splitter with $r = 100$ % reflectivity. If we were to have N modes co-propagating in the beam, given a finite number of successions of phase profiles and Fourier transforms, an ideal mode converter could function as a complete linear optics network, with the freedom of choosing as many beam-splitters as desired as well as the capacity to implement arbitrary phase shifts at any stage of the network.
An obvious extension of this work is to encode two squeezed spatial modes onto the same beam, in an orthogonal basis, and to perform beam-splitter operations. This would give us a flexible device for producing entanglement within one beam. This is exactly the direction that we took next, and that research is the focus of the next chapter. We extend the concepts investigated here, and develop a simplified and powerful process to emulate linear optics networks in one beam.

Single-photon metrology

In 2012, a similar result as the work presented in this chapter appeared from the group of Marco Bellini in Florence, Italy, in the context of adaptively shaping single photons. I wrote a Research Highlight for Nature Photonics and it appears in reference [58].

CAILabs

The idea of being able to mulitplex spatial modes in one optical beam and to apply unitary transforms on the modes has worked remarkably well. The technology developed by the Quantum Imaging Group (largely by Morizur) has been patented and Jean-Francois Morizur is currently in the process of developing the technology for commercial interests as the CEO of CAILabs.

The team

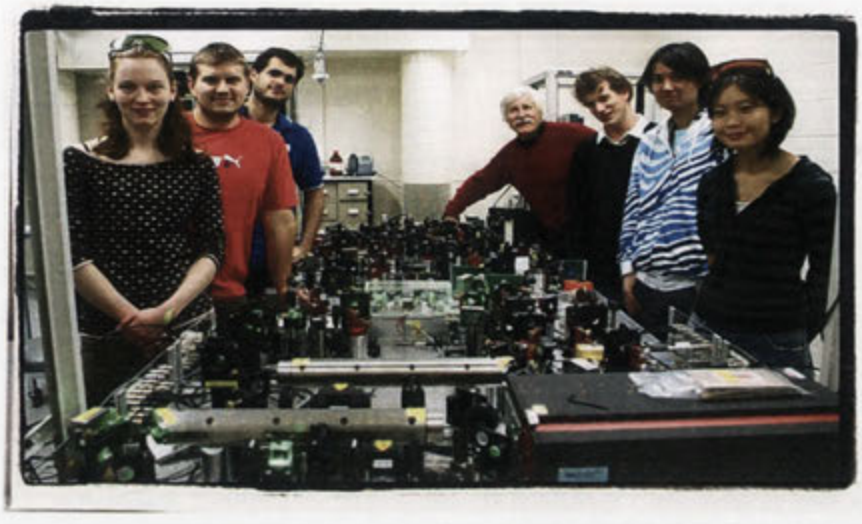

Figure 5.15: The Quantum Imaging Group, led by Professor Hans Bachor. Left to right: Kate Wagner, Jiri Janousek, Jean-Francois Morizur, Hans Bachor, Lachlan Nicholls, Seiji Armstrong, Pu Jian. Taken at the Australian National University, 2009.

Chapter 6

Programmable linear optics networks in one beam

The conventional method for generating entanglement in table-top quantum optics is to create a linear optics network of beam-splitters that mix together different quantum states of light. In continuous-variables quantum optics, one would mix together squeezed modes of light while carefully controlling the phases between various beam paths. The contribution of each of the input modes is controlled by the various reflectivities of the beam-splitters. This method has thus far proven to be successful in demonstrating the creation of a modest number of entangled modes, such as 4, 6, or more recently 8 [59, 60, 61]. However, each network is inherently inflexible in that the beam-splitter ratios are necessarily fixed. In order to change the ratios of the input modes that are mixed, the beam-splitters must be physically replaced and realigned. This is a time-consuming and arduous task. Further, if we want to increase the number of modes in the network, we need to increase the number of optical components, as well as the electronics required to actively control the relative optical phases, quickly leading to a very complex and unscalable system[1]

The spatial mode conversion experiments from the previous chapter inspired a treatment of the possibilities of spatial-mode engineering in one beam. Jean-Francois Morizur showed in his mathematically rigorous theory [54] that given a beam containing orthogonal squeezed modes and enough iterations of phase deformations and lenses, one could engineer a quantum mode converter of sorts that would mix the co-propagating beams. This mixing would precisely mimic an optical beam-splitter; the measurable modes contained in the beam after the mode converter would be equivalent to the output modes of a beam-splitter. This scheme would replace the arduous task of exchanging and re-aligning physical optical components with modifying the software that drives the phase masks. While this was a beautiful idea, there were some drawbacks to the proposed scheme. As we found out, while possible, it is extremely difficult to significantly minimise the optical loss in the quantum mode converter, and so shaping the beam containing the squeezed modes is not optimal. Also, one fixed deformation on the phase masks would correspond to one fixed beam-splitter network, ultimately limiting the measurement scheme in the same way that conventional linear optics networks do.

One exciting idea is to shape the local oscillator instead of the signal beam. Is this mathematically equivalent? If so, one could preserve every drop of squeezing in the signal beam, as loss on the local oscillator is only a technical issue that can be overcome by increasing the optical power as it is a classical beam. We arrive at the idea of engineering the measurement basis at the time of detection, using both an un-shaped local oscillator and an un-shaped signal beam. By designing a versatile measurement scheme, the measurement basis is chosen by selecting precise weighted combinations of the detected spatial components of the beam. We propose to do this by using detectors comprising of multiple photo-diodes, with individually addressable electronic gains.

[1] While this is an impediment for present-day table-top technologies, there is impressive research being conducted that might alleviate these issues by going to wave-guide (and other miniaturisation) technologies. [62, 63].

In our experimental demonstration, we employ multi-pixel homodyne detectors (built by Boris Hage, with initial designs from Morizur). Each detector has 8 pixels each, so that we record the light beam in 8 different spatial sections. Of course if we choose to set all of the 8 electronic gains to unity, this detector is equivalent to a standard "bucket" detector comprised of one photo-diode. Setting non-uniform gains on the detector pixels corresponds to some kind of mixing of the spatial modes within the beam. By defining a mapping of electronic gains to arbitrary linear optics networks, we gain access to a plethora of different entangled bases by simply modifying the software that drives the gains.
In this way we were able to to access our desired linear optics networks in a versatile and controlled way. Our approach is to co-propagate all possible spatial modes of light within one beam. This multiplexing in the spatial dimension leads to a much more efficient method for mixing the modes. By introducing a powerful mode shaping process, it is now possible to engineer complex networks of beam-splitters with any desired reflectivities by software only.

The theory and experiment discussed in this chapter are summarised in the following publication:

- Seiji Armstrong, Jean-Francois Morizur, Jiri Janousek, Boris Hage, Nicolas Treps, Ping Koy Lam, Hans Bachor. *Programmable multimode quantum networks.* Nature Communications, **3**, 1026 (2012).

It should be noted that co-propagating 2 spatial modes in one beam has been previously demonstrated by Jiri Janousek and the ANU group a couple of years ago [64], as well as Ulrik Andersen's group in DTU [65]. There are also some excellent demonstrations coming out of Olivier Pfister's group at the University of Virginia, where they employ multiplexing in the frequency domain [66, 67]. Nicolas Treps and Claude Fabre at the University of Pierre and Marie Curie have also recently demonstrated entanglement between frequency modes in frequency combs [68].

6.1 A simple one-beam network

The concept of being able to program different linear optics networks via software, as opposed to modifying hardware, is a powerful one. We use matrix mechanics to systematically build up the networks from unitary (reversible) operations. We begin our treatment with a walk-through of a simple network. This reveals the underlying mechanisms of our technique, and help develop the intuition required to appreciate the more complex networks treated later in the chapter.

Entanglement between two halves of a beam

The simplest possible network that we create contains 2 inputs that are transformed to 2 outputs. By engineering two spatial modes that are orthogonal, they are able to propagate on the same beam. Crucially, they are able to be measured independently. If we choose to measure half of one mode and half of the other mode, we have emulated a simple beam-splitter operation.

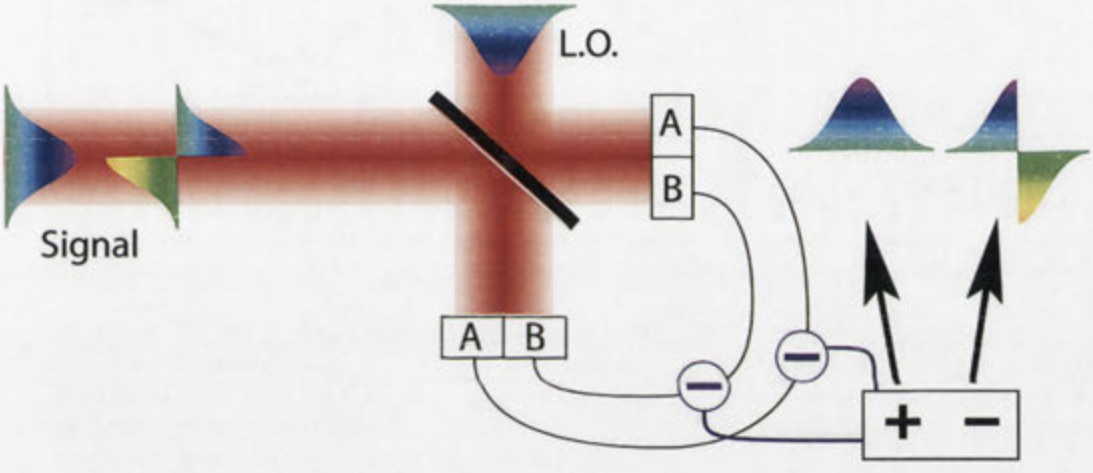

Figure 6.1: EPR entanglement in one beam. 2 squeezed modes that are spatially orthogonal propagate on the same signal beam. Depending on if the 2-pixel homodyne signal is summed or subtracted we can measure either squeezed mode independently.

In this demonstration the two spatial modes are a fundamental Gaussian, TEM_{00}, and a phase-flipped version of a Gaussian TEM_{00}. The phase-flipped mode, referred to from here-on-in as a flip mode, simply has one half of its spatial profile phase shifted by π or 180° such that it is precisely orthogonal to the TEM_{00} mode. Experimentally this is achieved by delaying one half of the Gaussian TEM_{00} by exactly half a wavelength. The phase-flipped mode was introduced by Delaubert in reference [69].

Now comes the detection and subsequent measurement. You will notice from the schematic in Fig. 6.1 that we have a homodyne setup with a fundamental Gaussian local oscillator. The detectors however are not standard single photodiode detectors. They contain 2 photodiodes each so that the beam is measured in two halves. After performing two standard homodyne subtractions between the two signal beams (one for each half, as in Fig. 6.1), we are left with homodyne current from detector A as well as homodyne current from detector B. In this demonstration we either sum A and B or take the difference of A and B. The sum of A and B results in the measurement of the fundamental Gaussian TEM_{00} mode, while the flip mode is not measured. Conversely, the difference of A and B results in the complete measurement of the flip mode while the Gaussian mode is entirely not measured. This can be understood by observing that the right half of the flip mode is precisely the inverse of the left half. Therefore if the two halves are added together (current in A + current in B) the measurement result will be zero: $\begin{pmatrix} 1 & 1 \end{pmatrix} \begin{pmatrix} 1 \\ -1 \end{pmatrix} = 0$.

Now that we have understood how to measure the input mode independently, we arrive at the exciting part, the virtual networks. We know from our linear optics experience that if we combine two squeezed modes (in quadrature) on a balanced beam-splitter the outputs will be entangled. A balanced beam-splitter simply combines the two modes and distributes them equally in the output ports, with a π phase shift on one mode. In our one-beam scheme we may now emulate this 2-mode network by combining the two recovered input modes. Preserving the phase relationship of beam-splitters, one output port will be the sum of the two input modes while the other output port will be the difference of the input modes due to the π phase shift.

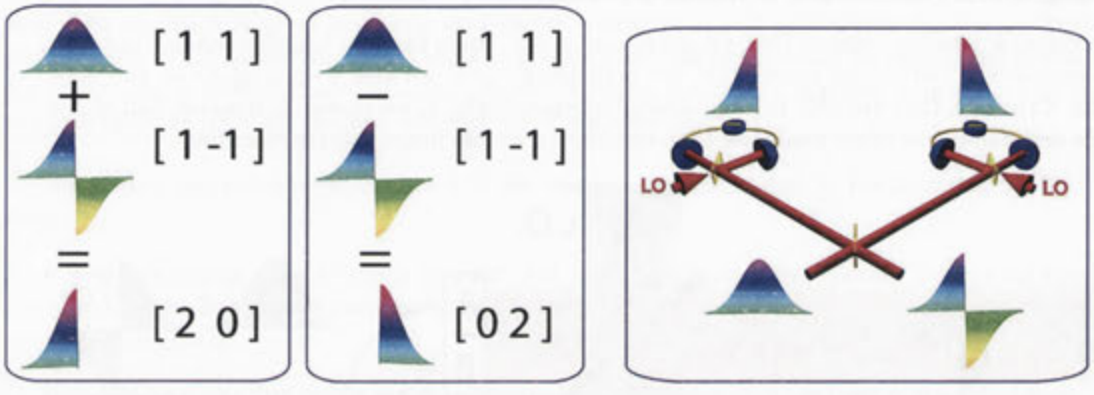

Figure 6.2: EPR entanglement between two halves of one beam. Linear combinations of recovered input modes lead to entanglement between the left half and the right half of the same beam.

Performing these combinations, we realise that one output port is precisely the left half of the beam, while the other output port is the right half of the beam, as illustrated in Fig. 6.2. We see that in this way we can determine which modes we wish to measure by combining the 2-pixel homodyne detection current in different ways. More generally, we scale the homodyne current by electronic gains that range between -1 to 1. The different modes measured as a consequence of different electronic gains applied in this simple demonstration are summarised below.

	Input Modes		Output Modes	
Mode Profiles				
Electronic Gains	[1 1]	[1 -1]	[2 0]	[0 2]
Spatial Mode	Gaussian	Flip	Left Half	Right Half

A useful way to think about the electronic gains of the multi-pixel detectors is to imagine that we are spatially modifying the local oscillator beam. Only the components of the signal beam that are matched to the shaped local oscillator are measured. The modes that span the input basis are orthogonal, and so are the modes that span the output basis. However, it is worth stating explicitly that in general, modes in the input basis will not be orthogonal to modes in the output basis. This is fairly intuitive, as the output modes in general contain non-zero contributions of the input modes - this is how they are generated, after all. As a final note, here I have ignored normalisation constants as we are interested in conveying the idea of these networks. A full mathematical treatment follows in this chapter, and we ensure that all bases are orthonormal.

6.2 Programmable networks

6.2.1 8 spatial modes in one beam

As seen in the powerful example of two-mode entanglement, we radically extend the idea of one-beam entanglement by introducing the notion of emulating linear optics networks. This is done by programming virtual networks that mix together different spatial regions of the light beam. These software-based networks calculate the precise weighted combinations of the spatial regions required to emulate the physical networks. This is possible because the linear optical components in a typical network simply perform reversible operations, and can be represented by unitary matrices.

In our complete setup, we are able to create networks that manipulate up to 8 modes. Our scheme may be represented as in Fig. 6.3 below:

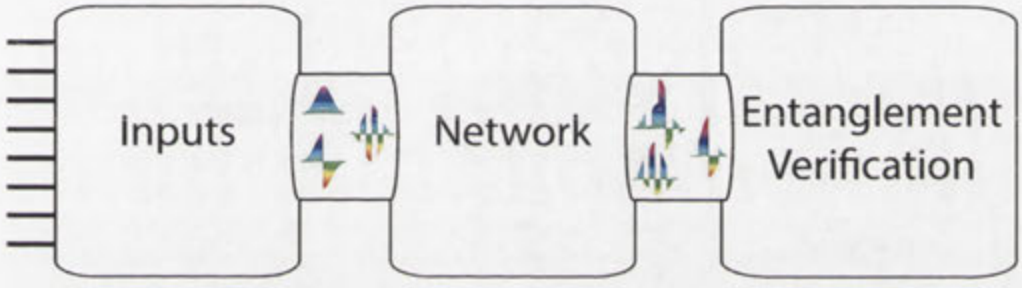

Figure 6.3: Multimode entanglement via emulated linear optics networks. The programmable networks are split into 3 steps. First, the input modes are recovered. A subset of input modes are then mixed together on virtual linear optics networks, creating output modes. Entanglement between the output modes is then verified using inseparability measures.

The first step is to select how many modes will form the input basis from the 8 spatial modes that we can measure. The N input modes that we select are fed into a programmable virtual network that emulates a given linear optics network. The linear optics networks that we have access to are arbitrary concatenations of beam-splitters and π phase shifts. This produces N output modes that we then measure and characterise with a given criteria for verifying entanglement.

6.2.2 Experimental overview

We use a dual-wavelength continuous-wave Nd:YAG laser at 1064 nm and 532 nm. The optical parametric amplifiers (OPA) each contain a periodically poled KTP crystal in a bow-tie cavity. The squeezed beams are almost identical in purity, with squeezing levels of approximately -6 dB and anti-squeezing of 8.5 dB. The beam containing the 8 spatially orthogonal modes is made highly elliptical in order to be measured by the multi-photodiode homodyne detector (MPHD), which has a linear array of 8 photodiodes. The photodiode array is a Hamamatsu InGaAs PIN array (G7150) which actually has 16 photodiodes however we choose to use only 8 of these in the present experiment. The filling factor for the array is 90%, meaning that 10% of the light does not hit an active surface. The quantum efficiencies for the photodiodes are 80% at 1064 nm.
Full experimental details including a treatment on the squeezing resources, active control of the co-propagating beam, and the detection scheme including the process of data analysis are presented in section 6.4 of this chapter.

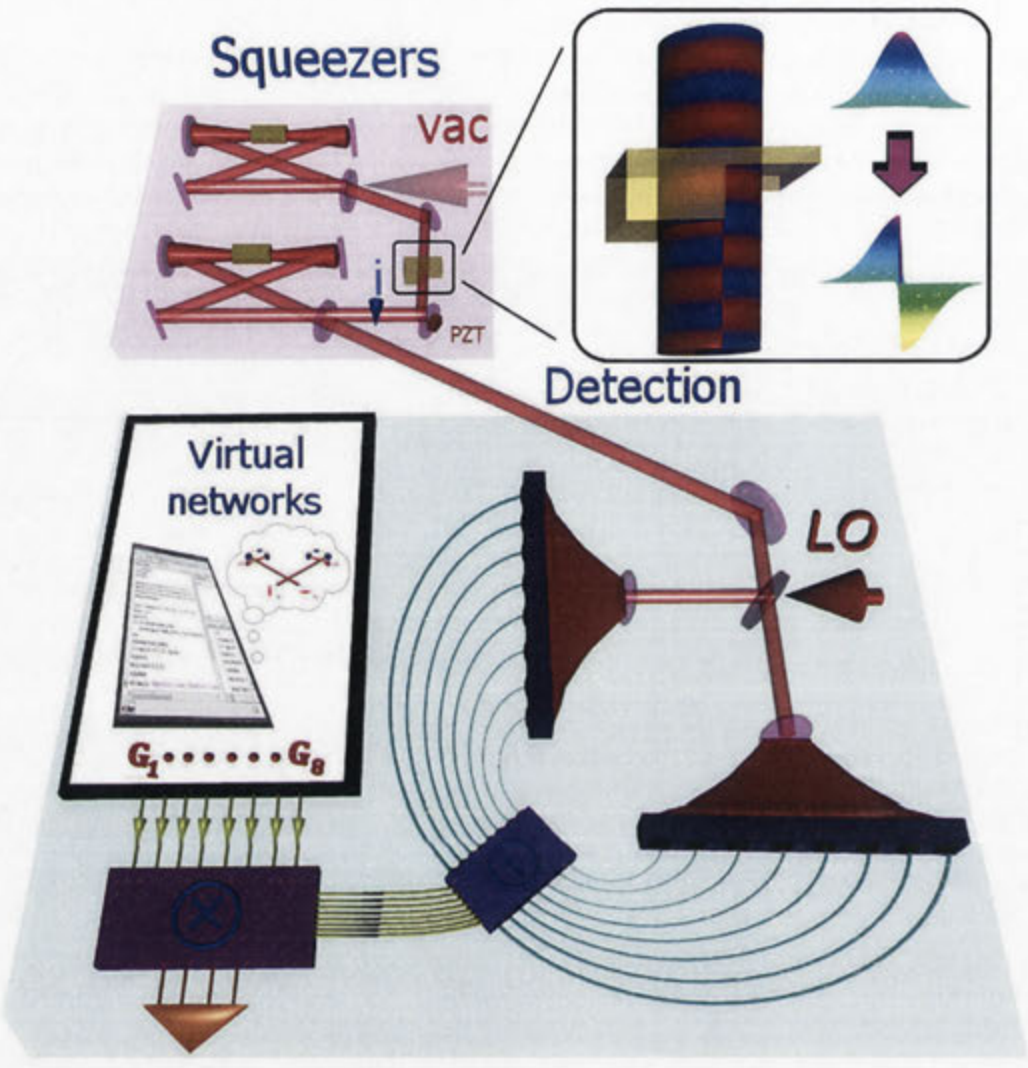

Figure 6.4: Experimental setup. Squeezed light is prepared and combined in *squeezers* with a piezo electric transducer (PZT) controlling the phase between the two squeezed modes, locked in quadrature. Vacuum modes (vac) co-propagate so that the beam exiting *squeezers* and entering *detection* contains 8 measurable spatial modes. Multi-pixel homodyne detection (MPHD) is used to measure the quadrature amplitudes of the beam in 8 different regions, in *detection*. Local oscillator (LO) gives a reference to phase quadratures. A PC is used to calculate electronic gain functions G_n via the notion of *virtual networks*. The detected beam is then projected onto a basis of measured modes (see equation 1). (**Inset**) Flip mode (FM) generation; half of the wave is phase retarded by half a wavelength, flipping the electric field amplitude.

A note on terminology

I use 'detection' when referring to the process of converting light to photo-current; shining the signal beam onto the MPHD. 'Measurement' refers to the calculated process of combining the weighted photo-currents in order to access the desired spatial mode, or the desired combination of spatial modes.

6.2.3 Measuring spatial modes

By employing custom-made MPHDs that each contain an array of 8 photodiodes (see Fig. 6.4), we detect the light in 8 spatial regions and assign individual electronic gains to each spatial region. The linear combination of the 8 gain-adjusted photocurrents constitutes the measurement of one mode. More generally, we can express the measurement process of a complete set of spatial modes in one beam by the following:

$$\hat{\mathbf{a}} = \mathbf{U}\hat{\mathbf{i}} \tag{6.1}$$

$$= \mathbf{U}_{\text{net}}\mathbf{U}_{\text{in}}^{\text{N}}\hat{\mathbf{i}}, \tag{6.2}$$

where $\hat{\mathbf{a}} = (\hat{a}_1, \cdots, \hat{a}_N)^{\text{T}}$ is the set of N measured modes projected by the $N \times 8$ unitary matrix $\mathbf{U}$ acting on the 8 homodyne-subtracted photocurrent operators $\hat{\mathbf{i}} = (\hat{i}_1, \cdots, \hat{i}_8)^{\text{T}}$.

$\mathbf{U}_{\text{in}}^{\text{N}}$ is an $N \times 8$ matrix made up of the top N rows of $\mathbf{U}_{\text{in}}$, the orthogonal 8×8 unitary matrix that recovers the important set of 8 unmixed spatial modes that span the input basis. Input modes are then mixed via $\mathbf{U}_{net}$, which emulate linear optics networks, given by the $N \times N$ matrix:

$$\mathbf{U}_{\text{net}} = \begin{pmatrix} v_1^1 & v_2^1 & \cdots & v_N^1 \\ v_1^2 & v_2^2 & \cdots & v_N^2 \\ \vdots & \vdots & \ddots & \vdots \\ v_1^N & v_2^N & \cdots & v_N^N \end{pmatrix}, \tag{6.3}$$

where $v_p^n \in \mathbb{R}$.

This allows us to uniquely define a mode $\hat{a}_n$ by the 8 real numbers in the nth row of U, which we will label as the mode's gain vector G_n, such that $\hat{a}_n = G_n\hat{\mathbf{i}}$. Therefore each spatial mode that we measure, whether belonging to the input basis or an entangled mode basis, is defined by a unique pattern within the light beam.

These spatial mode patterns, represented by Gaussian profiles modulated by respective electronic gains G_n, are shown visually in Fig. 6.5, while the detection stage of Fig. 6.4 shows how we implement this experimentally. The spatial modes are orthogonal to each other, spanning a basis so that the independent measurement of each mode is possible [70, 71].

6.2.4 Input basis

The first spatial mode in the input basis is the fundamental Gaussian mode of the Hermite-Gauss basis, the TEM_{00}. We choose not to work in the Hermite-Gauss basis, however, as this basis is not optimal for our detection scheme. As we are using a multi-photodiode detector, we choose the pixel basis for maximum efficiencies. This means that we will have sharp transitions in the amplitude profiles of our spatial modes. The phase-flipped Gaussian mode is used as the second mode in the basis. This is simply a TEM_{00} with one half of its spatial amplitude phase flipped. It is clear to see that these two modes are orthogonal, as the overlap between them is zero:

$$\int_{-\infty}^{+\infty} f_G(x) f_F(x) dx = 0. \tag{6.4}$$

As our multi-pixel detector has 8 pixels, we are concerned with discretised mode vectors that represent the modes in the pixel basis:

$$\sum_{n}^{8} f_G[n] f_F^{\text{T}}[n] = 0. \tag{6.5}$$

In order to gain some intuition regarding our spatial mode basis, we first consider an idealised basis that consists of equal intensity components. This can be considered to be the spatial profile

of the light normalised by a Gaussian profile. It follows that the first two modes in the idealised pixel basis have the following mode vectors:

$$f_G = \frac{1}{\sqrt{8}}\begin{pmatrix} 1 & 1 & 1 & 1 & 1 & 1 & 1 & 1 \end{pmatrix}, \qquad f_F = \frac{1}{\sqrt{8}}\begin{pmatrix} 1 & 1 & 1 & 1 & -1 & -1 & -1 & -1 \end{pmatrix}. \tag{6.6}$$

The remaining 6 mode vectors are calculated via the singular value decomposition of the matrix containing the Gaussian mode vector and the flip-mode vector as its rows. An orthonormal basis is found by computing the null space of this matrix. We obtain a matrix that contains all 8 mode vectors, defined to be the idealised input mode matrix.

The idealised input matrix $\mathbf{U}_{\text{ideal}}$ is defined as follows:

$$\mathbf{U}_{\text{ideal}} = \frac{1}{\sqrt{8}}\begin{pmatrix} 1 & 1 & 1 & 1 & 1 & 1 & 1 & 1 \\ 1 & 1 & 1 & 1 & -1 & -1 & -1 & -1 \\ 1 & 1 & -1 & -1 & 1 & 1 & -1 & -1 \\ -1 & 1 & 1 & -1 & 1 & -1 & -1 & 1 \\ 1 & -1 & 1 & -1 & 1 & -1 & 1 & -1 \\ -1 & 1 & 1 & -1 & -1 & 1 & 1 & -1 \\ -1 & 1 & -1 & 1 & 1 & -1 & 1 & -1 \\ -1 & -1 & 1 & 1 & 1 & 1 & -1 & -1 \end{pmatrix}, \tag{6.7}$$

with $\mathbf{U}^*_{\text{ideal}}\mathbf{U}_{\text{ideal}} = \mathbf{I}$.

Figure 6.5 displays this idealised input mode basis scaled by a Gaussian envelope.

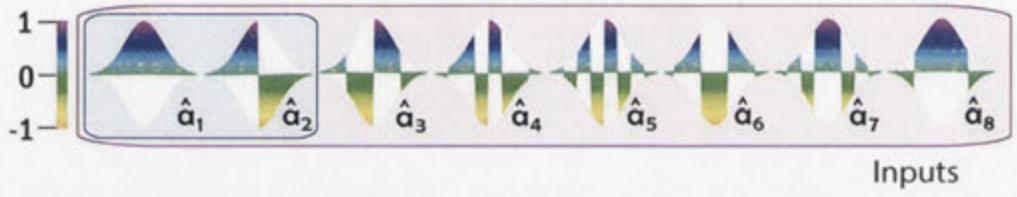

Figure 6.5: Input basis spatial mode patterns. There are 8 orthogonal spatial modes that we may input into different linear optics networks. These spatial modes are scaled by Gaussian envelopes.

The input matrix needed to extract the experimentally measured data is created in an analogous way, however we need to account for the Gaussian amplitude envelope of the light. This is taken into account when building the multipixel detector and as a result each diode has a different response that we need to account for[2]. In order to measure the fundamental mode of the input basis, the TEM_{00}, we must scale the multipixel detector by the following electronic gain vector:

$$[0.1022 \quad 0.2655 \quad 0.3966 \quad 0.5117 \quad 0.5117 \quad 0.3966 \quad 0.2655 \quad 0.1022] \tag{6.8}$$

These gain factors were found via a genetic algorithm written in MATLAB that minimised over the recovered squeezing value of the first input mode. The genetic algorithm mimics an evolutionary process and is designed to approach the global minimum of the parameter space by including environmental disturbances to kick the algorithm out of local minima. Alternatively, Jean-Francois Morizur's thesis contains a treatment on this detector including a methodology of how to extract gain factors via the transfer functions [38]. Morizur's recovered gain factors are close to those employed here. Perhaps unsurprisingly, the gain vector I use here is optimal and recovers the measured quantum state with higher levels of squeezing than those calculated by Morizur's transfer function method. In general I favour an algorithm to find the numerical optimum, due to the usual existence of experimental imperfections. Where applicable, I use the numerical solve and minimize functions from Wolfram Mathematica. It is important however, to also compute

[2]The outer photodiodes are designed to have higher amplification compared to the inner photodiodes.

analytical solutions when appropriate in order to verify the validity of the found solutions.
Experimentally, the input basis is created in the following way. First, two amplitude squeezed modes are created via optical parametric amplification (OPA). The first mode is converted to a flip mode (FM) by phase delaying half its beam by half a wavelength, π (see inset of Fig. 6.4). This is achieved by using a flip-mode generating waveplate, similar to that outlined in [69]. The FM is overlapped in quadrature with the Gaussian mode (GM) output of the second OPA upon reflection of its output coupler [72]. These two squeezed modes are the first two modes of the input basis: $\hat{a}_1$ and $\hat{a}_2$. Six co-propagating vacua modes are measured by calculating G_n vectors that are orthogonal to both $\hat{a}_1$ and $\hat{a}_2$, as in the example of idealised mode vectors.

These vacua modes (labelled $\hat{a}_3 ... \hat{a}_8$) complete the experimental input mode basis (see Fig. 6.5). Measuring these modes amounts to matching the detection basis by following equation (1) and setting $\mathbf{U}_{\text{net}} = \mathbf{I}$.

The experimental input matrix $\mathbf{U}_{\text{in}}$ is defined as follows:

$$\mathbf{U}_{\text{in}} = \begin{pmatrix} 0.1022 & 0.2655 & 0.3966 & 0.5117 & 0.5117 & 0.3966 & 0.2655 & 0.1022 \\ 0.1022 & 0.2655 & 0.3966 & 0.5117 & -0.5117 & -0.3966 & -0.2655 & -0.1022 \\ -0.3492 & -0.4439 & 0.7700 & -0.2967 & 0.0000 & 0.0000 & 0.0000 & 0.0000 \\ -0.4506 & -0.5728 & -0.2967 & 0.6172 & 0.0000 & 0.0000 & 0.0000 & 0.0000 \\ -0.5852 & 0.4181 & -0.0485 & -0.0625 & 0.4764 & -0.4058 & -0.2717 & -0.1046 \\ -0.4536 & 0.3241 & -0.0376 & -0.0485 & -0.4058 & 0.6855 & -0.2106 & -0.0811 \\ -0.3037 & 0.2170 & -0.0251 & -0.0324 & -0.2717 & -0.2106 & 0.8590 & -0.0543 \\ -0.1169 & 0.0835 & -0.0097 & -0.0125 & -0.1046 & -0.0811 & -0.0543 & 0.9791 \end{pmatrix} \tag{6.9}$$

with $\mathbf{U}_{\text{in}}^{*}\mathbf{U}_{\text{in}} = I$. Each row of $\mathbf{U}_{\text{in}}$ represents the 8 electronic gains that match the detection basis to the input modes. For example, the top row recovers the standard Gaussian TEM_{00} mode (GM), and the second row recovers the phase-flipped Gaussian mode (FM). By setting $\mathbf{U}_{\text{net}} = I$ we can label each row of $\mathbf{U}_{\text{in}}$ as G_{n}^{in}. Formally, $\mathbf{U}_{\text{in}}^{N} = (\mathbf{I}_{\text{N}}\ \mathbf{O}_{\text{N},(8-\text{N})})\mathbf{U}_{\text{in}}$, where $\mathbf{O}_{\text{N},(8-\text{N})}$ is a zero matrix of size N by $(8 - N)$.
Each spatial mode is characterised by the continuous-variable (CV) quadrature operators $\hat{x}$ and $\hat{p}$ of the electric field operator. The $\hat{x}$ and $\hat{p}$ variance measurements of the eight modes in the input basis are shown in Fig. 6.6a,b as well as table 6.1, for a parametric gain of $G = 20$.

Input	$\triangle^2\hat{p}$ **(dB)**	$\triangle^2\hat{p}$ **(r)**	$\triangle^2\hat{x}$ **(dB)**	$\triangle^2\hat{x}$ **(r)**
1	-4.37	-0.50	11.19	1.29
2	-3.72	-0.43	10.18	1.17
3	-0.09	-0.01	0.07	0.01
4	-0.04	0.00	0.09	0.01
5	-0.11	-0.01	0.21	0.02
6	-0.00	0.00	-0.07	-0.01
7	-0.05	-0.01	0.31	0.04
8	-0.05	-0.01	0.22	0.02

Table 6.1: Measured variances of input basis. All variances given in dB have uncertainties ±0.05 dB.

Here, our two squeezed modes have variances $\langle[\Delta p_1]^2\rangle = -4.37 \pm 0.05$dB and $\langle[\Delta p_2]^2\rangle = -3.72 \pm 0.05$dB below the standard quantum noise, and the variances of the vacua are verified to equal quantum noise with a small but non-zero amount of noise associated with each vacuum mode. These non-zero noise contributions arise from imperfect linear combinations of the 8 photodiodes when producing the orthogonal mode basis. Conceptually, they can be understood by appreciating that any slight misalignment in either of the two squeezed beams on the MPHD will lead to asymmetry that is amplified in the vacuum mode recovery process. Note that any diffraction from the flip-mode generating waveplate contributes to these noise values. The very low noise values indicate the precision of the imaging and mode-matching setup. A separate issue is the large

anti-squeezing values for both of the squeezed modes, a consequence of the large parametric gain necessary to increase the squeezing values in the face of a lossy MPHD.

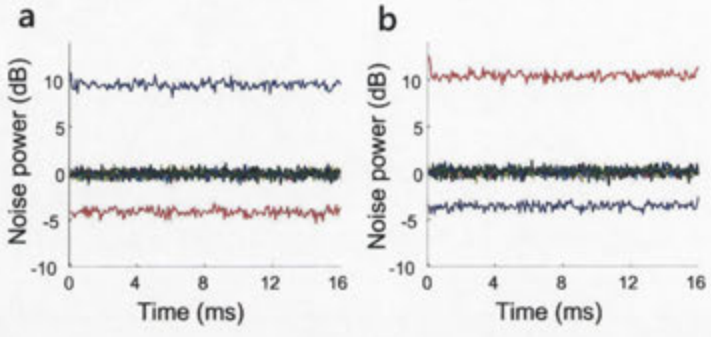

Figure 6.6: Noise variance measurements of the input spatial modes. (**a**) $\hat{x}$ quadrature measurements of the input mode basis. The squeezed $\langle[\Delta\hat{x}_1]^2\rangle$ is shown in the red and anti-squeezed $\langle[\Delta\hat{x}_2]^2\rangle$ is shown in the blue. The $\hat{x}$ quadrature variances of the 6 vacua modes are measured to equal quantum noise (0dB). (**b**) $\hat{p}$ quadrature measurements. The anti-squeezed $\langle[\Delta\hat{p}_1]^2\rangle$ is shown in the red and squeezed $\langle[\Delta\hat{p}_2]^2\rangle$ is shown in the blue. The p quadrature variances of the 6 modes are again measured to equal quantum noise, confirming they are vacua.

6.2.5 Entangled mode bases

Programming a virtual network amounts to calculating the precise expression of $\mathbf{U}_{net}$. The unitaries we have access to in programming the virtual networks are beam-splitters and π phase shifts. $\mathbf{U}_{net}$ is the concatenation of all of these unitaries that make up a linear optics network. The π phase shift is equivalent to multiplying $\hat{a}$ by -1. Note that arbitrary relative phase shifts are forbidden as each measurement naturally corresponds to detection at a fixed phase defined by a shared reference beam, the local oscillator. Optimising networks due to asymmetries in squeezing levels are important in certain situations. I provide a treatment of these situations in appendix A. Here, we characterise the entanglement present in our multi-partite quantum states by the van Loock-Furusawa criteria. Under these conditions, optimising networks by biasing the beam-splitters has a minimal effect.

The most intuitive virtual network we create is the 2-mode EPR state [6] that is treated in section 6.1. Here we engineer spatial mode patterns that have no spatial overlap; the left half of the beam is entangled with the right half (see Fig. 6.2). Note that spatial separation is not a condition for spatial orthogonality, and the 2-mode case is a unique example. The Gaussian mode and the flip mode clearly share spatial overlap, and are also clearly spatially orthogonal. Entangled modes belonging to other bases share spatial overlap but are nevertheless spatially orthogonal. In the following treatment, spatial modes measured in an entangled mode basis are given a superscript N to distinguish them from modes in the input basis; a_1^2 and a_2^2 represent the two modes spanning the $N = 2$-mode EPR basis. In general, we construct networks pertaining to N modes by concatenating $N - 1$ virtual beam-splitters with vacua on unused input ports. This is a highly efficient approach to creating multimode entanglement, as the time-consuming tasks of mode matching and alignment are replaced with the ease of programming.

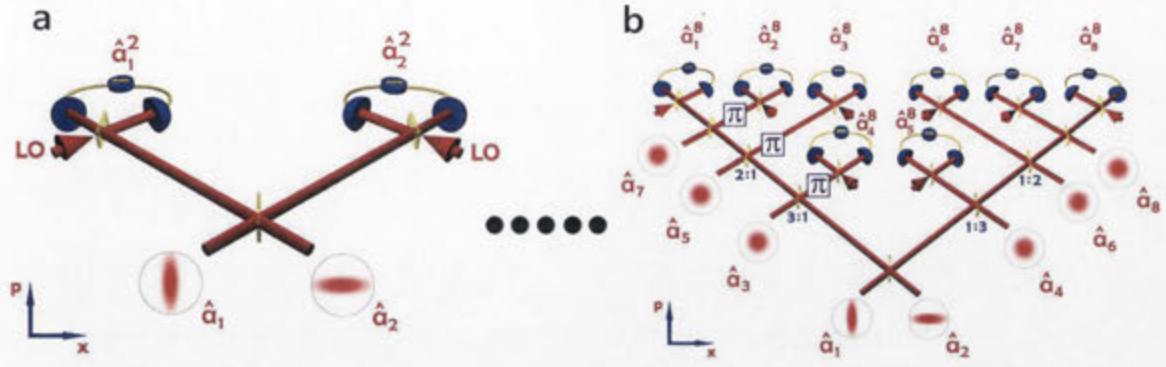

Figure 6.7: Multimode entanglement via emulated linear optics networks. Squeezed light and vacua are mixed together using unitary operations in order to produce entangled mode states. Unless otherwise stated beam-splitters are 50% reflective. Superscripts denote mode basis and subscripts denote mode number. (**a**) The emulated linear optics network used to measure 2-mode EPR entanglement ($\mathbf{U}^2_{\rm net}$). (**b**) 8-mode entanglement via a calculated concatenation of beam-splitter and π phase shift operations ($\mathbf{U}^8_{\rm net}$). The dots between **a** and **b** imply virtual networks for $N = 3...7$, not shown for brevity.

6.2.6 Network for 2-qumode state

The linear optics network for the ideal and symmetric 2-mode EPR basis is simply a balanced beam-splitter:

$$\mathbf{U}^2_{\rm net} = B(\frac{1}{\sqrt{2}}) = \begin{pmatrix} \frac{1}{\sqrt{2}} & \frac{1}{\sqrt{2}} \\ \frac{1}{\sqrt{2}} & -\frac{1}{\sqrt{2}} \end{pmatrix} \tag{6.10}$$

From equation 6.2 we get:

$$\begin{aligned} \begin{pmatrix} \hat{a}^2_1 \\ \hat{a}^2_2 \end{pmatrix} &= \frac{1}{\sqrt{8}} \mathbf{U}^2_{\rm net} \mathbf{U}^2_{\rm in} \hat{\mathbf{i}} \\ &= \frac{1}{\sqrt{8}} \begin{pmatrix} \frac{1}{\sqrt{2}} & \frac{1}{\sqrt{2}} \\ \frac{1}{\sqrt{2}} & -\frac{1}{\sqrt{2}} \end{pmatrix} \begin{pmatrix} 1 & 1 & 1 & 1 & 1 & 1 & 1 & 1 \\ 1 & 1 & 1 & 1 & -1 & -1 & -1 & -1 \end{pmatrix} \hat{\mathbf{i}} \\ &= \frac{1}{\sqrt{8}} \begin{pmatrix} \sqrt{2} & \sqrt{2} & \sqrt{2} & \sqrt{2} & 0 & 0 & 0 & 0 \\ 0 & 0 & 0 & 0 & \sqrt{2} & \sqrt{2} & \sqrt{2} & \sqrt{2} \end{pmatrix} \hat{\mathbf{i}} \\ &= \begin{pmatrix} \hat{G}^2_1 \\ \hat{G}^2_2 \end{pmatrix} \hat{\mathbf{i}}, \end{aligned}$$

from which we see that indeed $\hat{G}^2_1$ and $\hat{G}^2_2$ share no part of the detected light. We show this ideal EPR basis in Fig. 6.8 in order to emphasise the spatial separation. Note that the factor $\frac{1}{\sqrt{8}}$ has been omitted from the scale in Fig. 6.8 for clarity.

6.2.7 Networks for 2 to 8 qumode states

For even-numbered mode bases ($N = 2, 4, 6, 8$), the method for creating the virtual network is as follows. The two squeezed modes a_1 and a_2 are combined on a balanced beam-splitter. As the output of this first beam-splitter is an EPR state, we refer to this from now on as the EPR beam-splitter (EBS). The EBS outputs are symmetrically combined with $N - 2$ vacua, as in Fig. 6.7. Any beam-splitter in the remaining network is then given by $\hat{B}(cos^{-1}1/\sqrt{\frac{N}{2} - n})$, where n is the number of beam-splitters between the EBS and the beam-splitter in question. For $N = 4$ and

$N = 6$ and $N = 8$, mode output 2 is swapped with mode output N-1. For N=8, an additional swap of output modes 4 and 5 is made. For odd-numbered mode bases ($N = 3, 5, 7$), the method is the same with the following modifications. The EBS has its reflectivity changed to $r = \frac{1}{2} - \frac{1}{2N}$. (See for example references [73, 74] for more details on $N = 3$). The vacua are mixed using beamsplitters as above, with one output arm having one less vacuum input. π phase shifts are applied to all beam-splitter outputs on the left of the EBS except for the one left output exiting the last beam-splitter. Mode outputs 1 and $N - 1$ are swapped, and the network for $N = 7$ has an additional swap between output modes 3 and 4.
The homodyne gains g_i are optimised using a genetic algorithm[3], in order to maximally violate the van Loock-Furusawa inequalities. These gains g_i scale the contributions of the quadrature variances and are independent from calculations regarding $\mathbf{U}_{\text{net}}$. Here, optimal homodyne gains are calculated using two measures: minimising the mean of the $N - 1$ inequalities; and minimising the variance of the set of inequalities. A trade-off between the two measures is needed, and preference is given to minimising the mean of the inequalities.

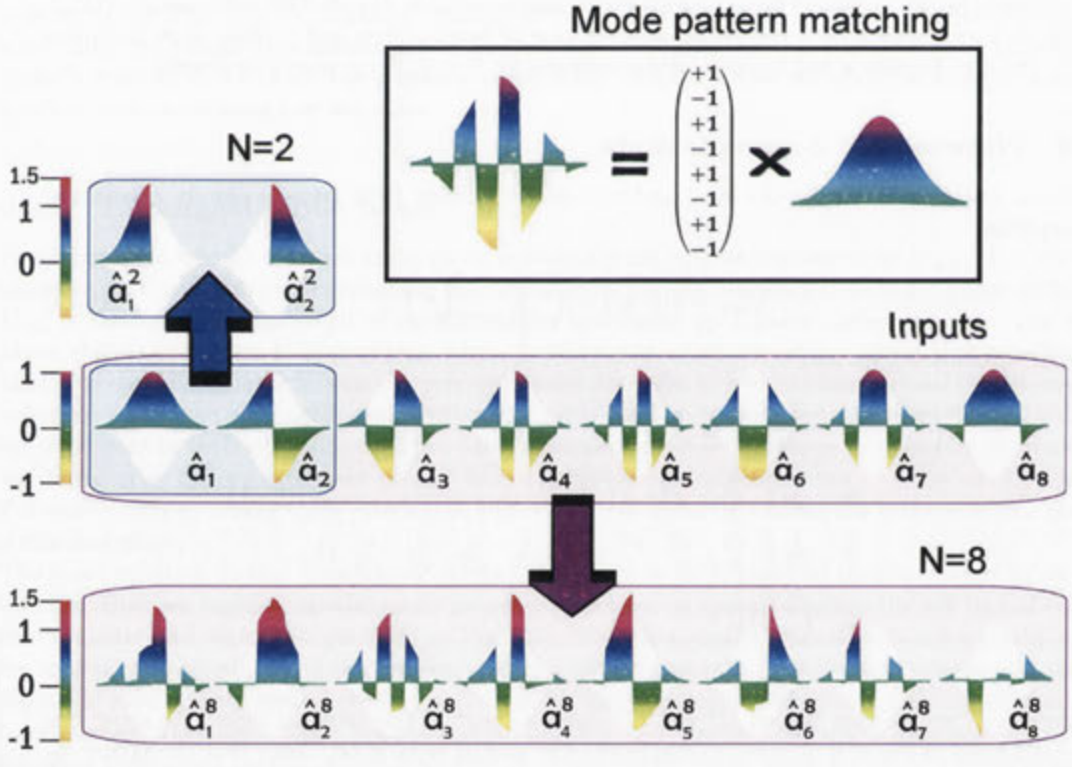

Figure 6.8: Spatial mode patterns. Measured modes are defined by spatial patterns of electric field amplitudes. Shown in the top right box is an example of how the spatial mode pattern for $\hat{a}_5$ is matched by applying 8 electronic gain values (G_5) to the detected Gaussian profile ($\hat{\mathbf{i}}$). The basis of input modes $\hat{a}_1 \ldots \hat{a}_8$ is shown in the middle row. The arrows represent a mapping via the virtual networks $\mathbf{U}^2_{\text{net}}$ (blue) and $\mathbf{U}^8_{\text{net}}$ (violet) onto the respective bases of entangled modes; the top row shows the symmetric EPR or 2-mode basis, while the bottom row shows the 8-mode basis. Superscripts denote mode basis and subscripts denote mode number. Each basis is orthogonal; the mode profiles shown here are scaled by Gaussian envelopes. The spatial mode bases for N=3 to N=7 are not shown for brevity.

[3]The algorithm is a variation of one employed and discussed in section 6.2.4

6.3 Verifying entanglement

In general we emulate a network, produce an entangled state, and then characterise it by calculating noise statistics. Different combinations of the quadrature variances will allow us to verify the existence of different levels of entanglement. In order to verify entanglement between measured modes we use the well-established van Loock-Furusawa inseparability criteria [74]. For an N-mode entangled state, it is sufficient to satisfy $N-1$ inseparability inequalities:

$$\begin{aligned}
&\textbf{(I)} \quad \langle[\Delta(\hat{x}_1 - \hat{x}_2)]^2\rangle + \langle[\Delta(\hat{p}_1 + \hat{p}_2 + g_3\hat{p}_3 + ... + g_N\hat{p}_N)]^2\rangle < 1, \\
&\cdots \\
&\cdots \\
&\textbf{(N-1)} \quad \langle[\Delta(\hat{x}_{N-1} - \hat{x}_N)]^2\rangle + \langle[\Delta(g_1\hat{p}_1 + ... + g_{N-2}\hat{p}_{N-2} + \hat{p}_{N-1} + \hat{p}_N)]^2\rangle < 1.
\end{aligned} \tag{6.11}$$

with free parameters g_i, to be optimised for maximum inseparability. We have omitted the superscript N here for clarity, as the above holds for any mode basis. The subscripts n of $\hat{x}$ and $\hat{p}$ here indicate the nth mode in the N-mode basis.

Table 6.2 summarises the measured degrees of inseparability for all $N-1$ inequalities in each experimentally generated N-mode basis, given in Roman numerals.

N	**I**	**II**	**III**	**IV**	**V**	**VI**	**VII**	**Avg.**
2	0.39							0.39
3	0.56	0.56						0.56
4	0.64	0.63	0.64					0.64
5	0.69	0.69	0.70	0.70				0.69
6	0.73	0.73	0.75	0.74	0.74			0.74
7	0.77	0.78	0.77	0.76	0.77	0.77		0.77
8	0.79	0.79	0.78	0.81	0.79	0.80	0.79	0.79

*Uncertainties are ± 0.01 in all cases.

Table 6.2: Inseparability of entangled modes based on the van Loock-Furusawa criteria. Each row shows that for a basis of N quantum modes, the $N-1$ values obtained from quadrature variances are well below 1. This verifies entanglement of the N modes.

The terms in equation (6.11) measure the degree of correlations between any two modes in a given basis. For the modes to be inseparable each of these correlation variances (correlations in the $\hat{x}$ quadrature and anti-correlations in the $\hat{p}$ quadrature[4]) must be in the quantum regime, that is below the normalised quantum noise of two units of vacua.
Figure 6.9. shows this to be the case in our experimental measurements. Although we are limited here to 8 modes due to our detection scheme, this scheme is scalable to higher numbers of mode entanglement even without increasing the number of squeezing resources, as shown in the simulation traces of Fig. 6.10. As we increase the simulated number of modes in the basis up to 30, the degree of inseparability approaches the classical bound of 1 due to the vacuum noise penalty for each additional unsqueezed mode input. Entanglement is shown to hold here however, even with current squeezing levels.

[4]These correlations are a consequence of our method of squeezed light generation. In other circumstances it would be possible to have correlations in $\hat{p}$ and anti-correlations in $\hat{x}$.

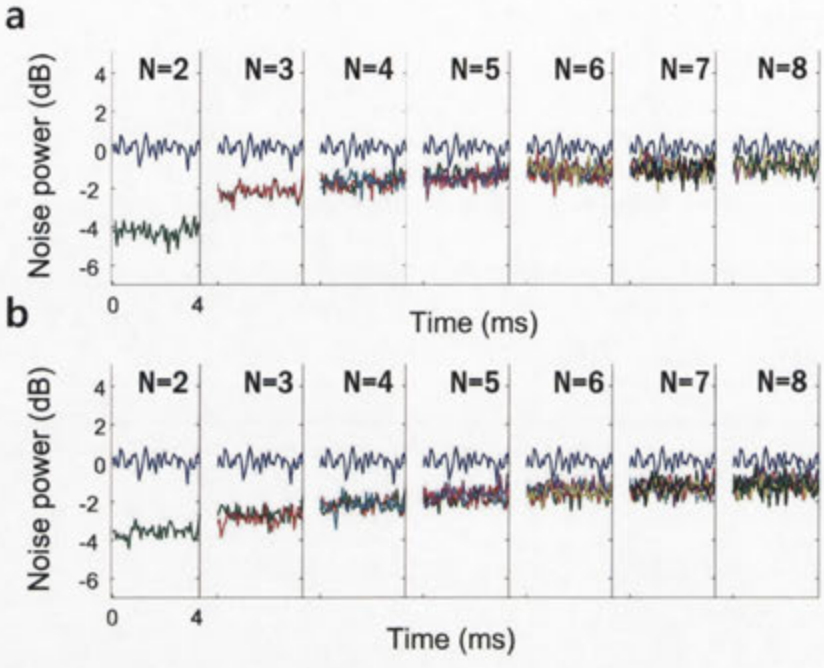

Figure 6.9: Noise variance measurements of the entangled spatial modes. (**a**) These variances show the $\hat{x}$ quadrature correlations between modes as in the first half of the L.H.S. of equation (6.11) of the text. Every column shows $N-1$ traces of $\hat{x}$ quadrature correlations below shot noise, as well as the blue shot noise trace (0 dB) normalised to two units of vacua. Each green trace shows $\langle[\Delta(\hat{x}_1^{\mathrm{N}} - \hat{x}_2^{\mathrm{N}})]^2\rangle$ for each N-mode basis. Each new colour represents the other N-1 variance correlation traces of equation 6.11. (**b**) Correlations between measured modes in $\hat{p}$ quadrature, second half of the L.H.S. of equation (6.11). Each green trace now shows $\langle[\Delta(\hat{p}_1^{\mathrm{N}} + \hat{p}_2^{\mathrm{N}} + g_3\hat{p}_3^{\mathrm{N}} + ... + g_N\hat{p}_N^{\mathrm{N}})]^2\rangle$. The traces overlapping show that each pair of modes is entangled with the same strength as any other pair of modes, a result of optimising for symmetry in the virtual networks.

Importantly, there is very little loss incurred during the transformation of the squeezed input modes into a set of entangled modes, as can be seen by the agreement of the theoretical predictions and the experimental values of Fig. 6.10. This equates to near-perfect mode matching at every virtual beam-splitter. Figure 6.10 explores how inseparability scales with different squeezing levels. Measuring a larger number of inseparable modes experimentally requires only an increase in the number of photodiodes in the MPHD, and importantly no modification of the optical setup. Note that this in general is not true for other quantum states of light such as cluster states or multi-partite states that demonstrate EPR steering. In those instances, the number of squeezed inputs must be increased accordingly.

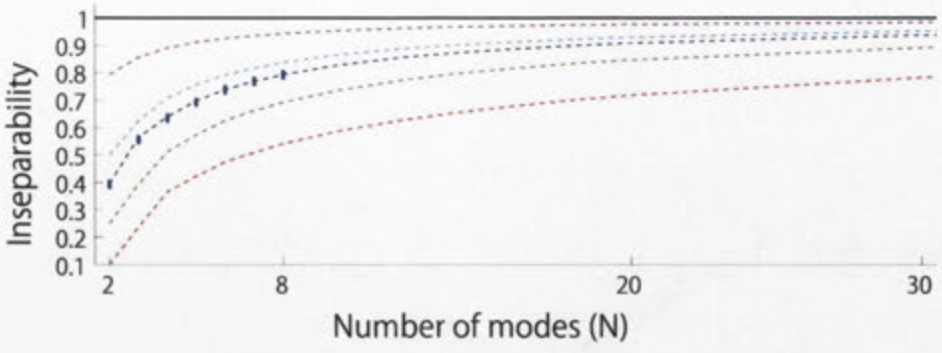

Figure 6.10: Inseparability for different entangled mode bases. The solid black line represents the bound of separability. Dashed lines represent theory. All traces have two squeezed inputs and $N-2$ vacua modes, as in the experiment. What changes is the amount of squeezing in the two squeezed inputs, assumed here to be symmetric with equal anti-squeezing. From the top we have: -1 dB (magenta); -3 dB (cyan); experimental parameters (blue); experimental values (blue markers); -6 dB (green); and -10 dB (red).

Note that the very small, but non-zero, noise contributions of our measured vacua modes do not show up as notable discrepancies with regard to the inseparability theory here. This is due to the relative insensitive nature of inseparability to anti-squeezing, and mixedness of our quantum states. When measuring a stricter form of entanglement such as EPR steering, as detailed in appendix A, these discrepancies become noticeable.

I will briefly mention here that it is an open question as to how useful a quantum state with only minimal inseparability might be. Its usefulness depends on the protocol in which the quantum state is used as a resource. See for example references [75, 76, 62] for discussions on photonic quantum technologies and quantum communication protocols.

Characterisation of emulated networks

We now present the networks for each of the $N = 2$ up to $N = 8$ mode entangled states. We also tabulate the van Loock-Furusawa variances, along with the optimisation gain values for the relevant $\hat{p}$ quadrature expressions. Uncertainties have been omitted from the tables for clarity. For each van Loock-Furusawa inequality, the uncertainty is ± 0.01.

6.3.1 2 qumodes

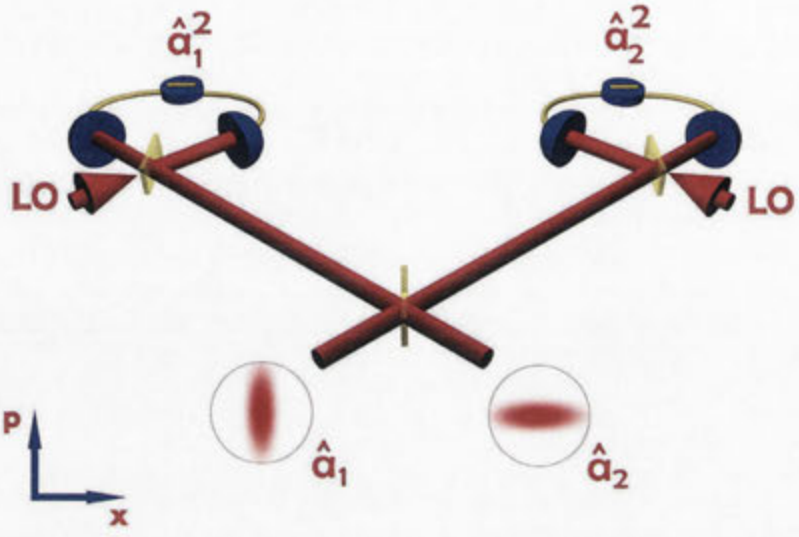

Figure 6.11: 2-qumode entangled state schematic. Two squeezed modes are combined on a balanced beam-splitter. The 2 modes are combined with a $\frac{\pi}{2}$ relative phase between them.

VLF variances	Value
$\Delta^2_{\mathrm{VLF}}(\hat{x}_1) = \Delta^2(\hat{x}_1 - \hat{x}_2)$	0.18
$\Delta^2_{\mathrm{VLF}}(\hat{p}_1) = \Delta^2(\hat{p}_1 + \hat{p}_2)$	0.21
$\{\mathrm{I}\}\ \Delta^2_{\mathrm{VLF}}(\hat{x}_1) + \Delta^2_{\mathrm{VLF}}(\hat{p}_1)$	0.39

The 2-qumode entangled state is measured as described in section 6.1. The quadrature variances described by equation 6.11 are tabulated above. The quadrature variance in the $\hat{x}$ quadrature is smaller than the quadrature variance in the $\hat{p}$ quadrature due to the asymmetric squeezing of the two input modes. The van-Loock Furusawa criterion is satisfied, as $0.39 < 1$, indicating full inseparability. Shown below is a snippet of the source code that emulates this network.

```
G=[0.1022 0.2655 0.3966 0.5117 0.5117 0.3966 0.2655 0.1022];
G=G./norm(G);                       % gain vector for mode projections
a1_pattern=[1 1 1 1 -1 -1 -1 -1]; % phase-flipped mode
a2_pattern=[1 1 1 1 1 1 1 1];       % Gaussian TEM00 mode
a1_gains=G*diag(a1_pattern,0);      % G1 for projecting to a1
a2_gains=G*diag(a2_pattern,0);      % G2 for projecting to a2
a1x=a1_gains*data_x';               % a1 input mode from detected data
a2x=a2_gains*data_x';               % a2 input mode from detected data

r=0.5;                              % beamsplitter reflectivity
t=1-r;                              % beamsplitter transmissivity
BS=[sqrt(r) sqrt(t);sqrt(t) -sqrt(r)]; % beamsplitter matrix
BSoutx = BS*[a1x; a2x];             % mixing modes a1 and a2 on BS
HD1x=BSoutx(1,:);                   % output modes at Homodyne 1 (x)
HD2x=BSoutx(2,:);                   % output modes at Homodyne 2 (x)
```

Listing 6.1: MATLAB source code for 2-qumode network.

6.3.2 3 qumodes

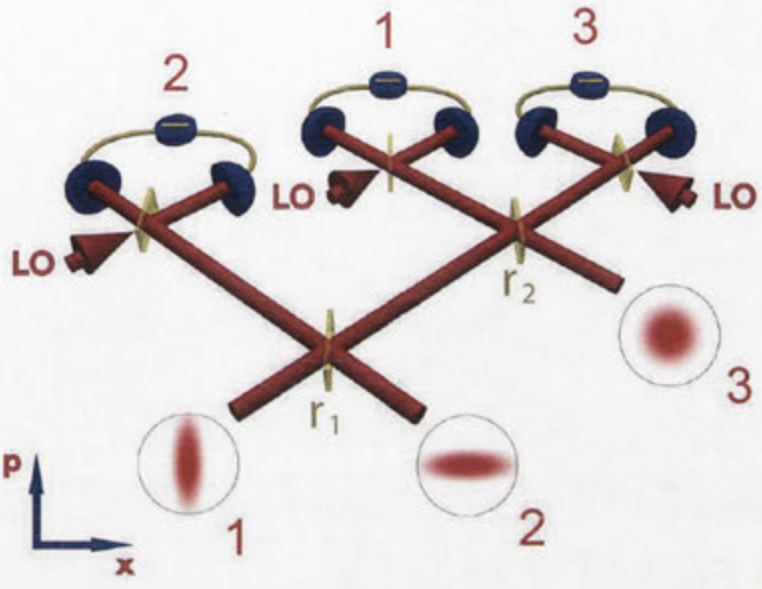

Figure 6.12: 3-qumode entangled state schematic. Two squeezed modes and a vacuum mode are combined in a tritter configuration of beam-splitters.

VLF variances	value	g_1	g_2	g_3
$\Delta^2_{\text{VLF}}(\hat{x}_1) = \Delta^2(\hat{x}_1 - \hat{x}_2)$	0.26			
$\Delta^2_{\text{VLF}}(\hat{x}_2) = \Delta^2(\hat{x}_2 - \hat{x}_3)$	0.26			
$\Delta^2_{\text{VLF}}(\hat{p}_1) = \Delta^2(\hat{p}_1 + \hat{p}_2 + g_3\hat{p}_3)$	0.30			0.82
$\Delta^2_{\text{VLF}}(\hat{p}_2) = \Delta^2(g_1\hat{p}_1 + \hat{p}_2 + \hat{p}_3)$	0.30	0.82		
{I} $\Delta^2_{\text{VLF}}(\hat{x}_1) + \Delta^2_{\text{VLF}}(\hat{p}_1)$	0.56			
{II} $\Delta^2_{\text{VLF}}(\hat{x}_2) + \Delta^2_{\text{VLF}}(\hat{p}_2)$	0.55			
$mean[\Delta^2_{\text{VLF}}(\hat{x}) + \Delta^2_{\text{VLF}}(\hat{p})]$	0.56			

The measured tripartite inseparability is summarised above. The 3-qumode state is an interesting multi-partite state to investigate because it has the unique advantage of being the smallest and simplest entangled state that is larger than the bipartite case. The first time this continuous-variable analogue of the GHZ state was demonstrated was by Aoki and the Furusawa Lab in 2003 [73]. The difference in the current demonstration is of course that our tripartite state is contained within one beam.

The first beam-splitter here has a reflectivity of $r = \frac{1}{3}$, and the second (last) beam-splitter is balanced. Note also that the output qumodes 1 and 2 have been swapped. This is semantic and the swap is performed in order to align the labels with the van Loock-Furusawa criteria.

6.3.3 4 qumodes

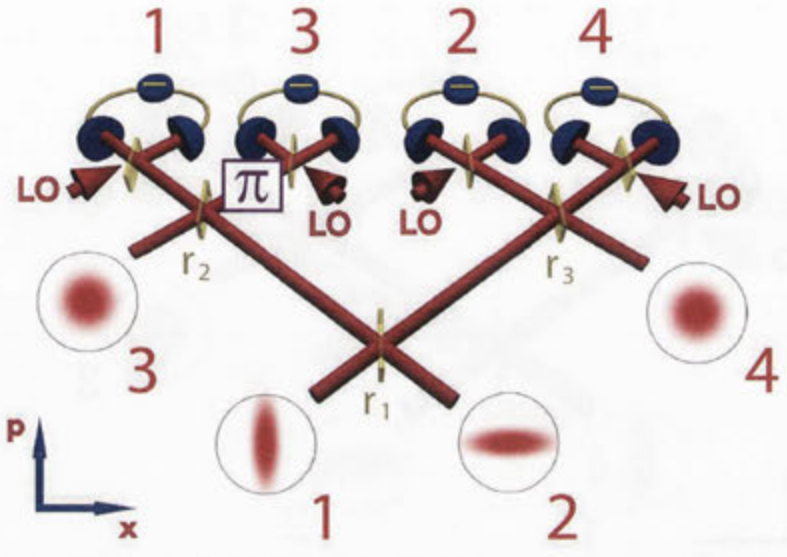

Figure 6.13: 4-mode entangled state schematic. Two squeezed modes and two vacua modes are combined on 3 balanced beam-splitters.

VLF variances	value	g_1	g_2	g_3	g_4
$\Delta^2_{\text{VLF}}(\hat{x}_1) = \Delta^2(\hat{x}_1 - \hat{x}_2)$	0.34				
$\Delta^2_{\text{VLF}}(\hat{x}_2) = \Delta^2(\hat{x}_2 - \hat{x}_3)$	0.33				
$\Delta^2_{\text{VLF}}(\hat{x}_3) = \Delta^2(\hat{x}_3 - \hat{x}_4)$	0.34				
$\Delta^2_{\text{VLF}}(\hat{p}_1) = \Delta^2(\hat{p}_1 + \hat{p}_2 + g_3\hat{p}_3 + g_4\hat{p}_4)$	0.30			0.41	0.40
$\Delta^2_{\text{VLF}}(\hat{p}_2) = \Delta^2(g_1\hat{p}_1 + \hat{p}_2 + \hat{p}_3 + g_4\hat{p}_4)$	0.30	0.44			0.40
$\Delta^2_{\text{VLF}}(\hat{p}_3) = \Delta^2(g_1\hat{p}_1 + g_2\hat{p}_2 + \hat{p}_3 + \hat{p}_4)$	0.30	0.44	0.40		
{I} $\Delta^2_{\text{VLF}}(\hat{x}_1) + \Delta^2_{\text{VLF}}(\hat{p}_1)$	0.64				
{II} $\Delta^2_{\text{VLF}}(\hat{x}_2) + \Delta^2_{\text{VLF}}(\hat{p}_2)$	0.63				
{III} $\Delta^2_{\text{VLF}}(\hat{x}_3) + \Delta^2_{\text{VLF}}(\hat{p}_3)$	0.64				
$mean[\Delta^2_{\text{VLF}}(\hat{x}) + \Delta^2_{\text{VLF}}(\hat{p})]$	0.64				

The 4-qumode state is interesting for a variety of reasons. It is the smallest multi-partite state that offers symmetry. This means that even if the input modes have asymmetric squeezing values, the first beam-splitter is still optimal when balanced. It is also the smallest state that allows for different beam-splitter networks (with appropriate phase shifts) leading to different entanglement structures. Although beyond the scope of the current chapter, we refer the reader to references [34, 59] for a treatment on how different configurations of 4-qumode networks lead to various graph state shapes; specifically a square, linear, and T-shaped cluster state.

The 3 beam-splitters in this network are all balanced. Note the phase shift on the 2nd output of the left beam-splitter, as well as the swapping of mode labels between modes 2 and 3.

6.3.4 5 qumodes

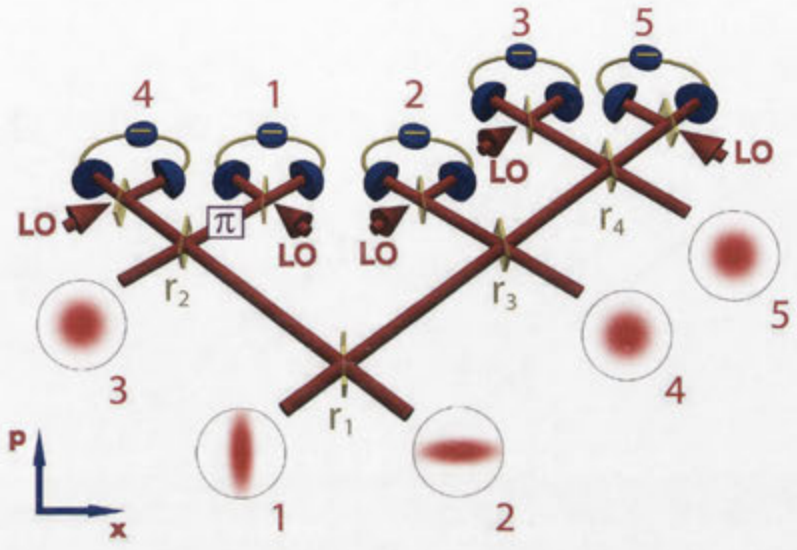

Figure 6.14: 5-mode entangled state schematic. Two squeezed modes and two vacua modes are combined on 4 beam-splitters.

VLF variances	value	g_1	g_2	g_3	g_4	g_5
$\Delta^2_{\text{VLF}}(\hat{x}_1) = \Delta^2(\hat{x}_1 - \hat{x}_2)$	0.36					
$\Delta^2_{\text{VLF}}(\hat{x}_2) = \Delta^2(\hat{x}_2 - \hat{x}_3)$	0.36					
$\Delta^2_{\text{VLF}}(\hat{x}_3) = \Delta^2(\hat{x}_3 - \hat{x}_4)$	0.37					
$\Delta^2_{\text{VLF}}(\hat{x}_4) = \Delta^2(\hat{x}_4 - \hat{x}_5)$	0.36					
$\Delta^2_{\text{VLF}}(\hat{p}_1) = \Delta^2(\hat{p}_1 + \hat{p}_2 + g_3\hat{p}_3 + g_4\hat{p}_4 + g_5\hat{p}_5)$	0.32			0.44	0.30	0.42
$\Delta^2_{\text{VLF}}(\hat{p}_2) = \Delta^2(g_1\hat{p}_1 + \hat{p}_2 + \hat{p}_3 + g_4\hat{p}_4 + g_5\hat{p}_5)$	0.32	0.42			0.30	0.42
$\Delta^2_{\text{VLF}}(\hat{p}_3) = \Delta^2(g_1\hat{p}_1 + g_2\hat{p}_2 + \hat{p}_3 + \hat{p}_4 + g_5\hat{p}_5)$	0.33	0.42	0.40			
$\Delta^2_{\text{VLF}}(\hat{p}_4) = \Delta^2(g_1\hat{p}_1 + g_2\hat{p}_2 + g_3\hat{p}_3 + \hat{p}_4 + \hat{p}_5)$	0.34	0.42	0.40	0.44		
{I} $\Delta^2_{\text{VLF}}(\hat{x}_1) + \Delta^2_{\text{VLF}}(\hat{p}_1)$	0.69					
{II} $\Delta^2_{\text{VLF}}(\hat{x}_2) + \Delta^2_{\text{VLF}}(\hat{p}_2)$	0.68					
{III} $\Delta^2_{\text{VLF}}(\hat{x}_3) + \Delta^2_{\text{VLF}}(\hat{p}_3)$	0.70					
{IV} $\Delta^2_{\text{VLF}}(\hat{x}_4) + \Delta^2_{\text{VLF}}(\hat{p}_4)$	0.70					
$mean[\Delta^2_{\text{VLF}}(\hat{x}) + \Delta^2_{\text{VLF}}(\hat{p})]$	0.69					

The 5-qumode network is an extension of the asymmetric network we observed in the tripartite case. The first beam-splitter has reflectivity $r_1 = \frac{2}{5}$. The right-hand side then can be viewed as a 3-qumode network with $r_3 = \frac{1}{3}$ and $r_4 = \frac{1}{2}$ while the left-hand side takes on a 2-qumode network with a balanced beam-splitter, $r_2 = \frac{1}{2}$.

6.3.5 6 qumodes

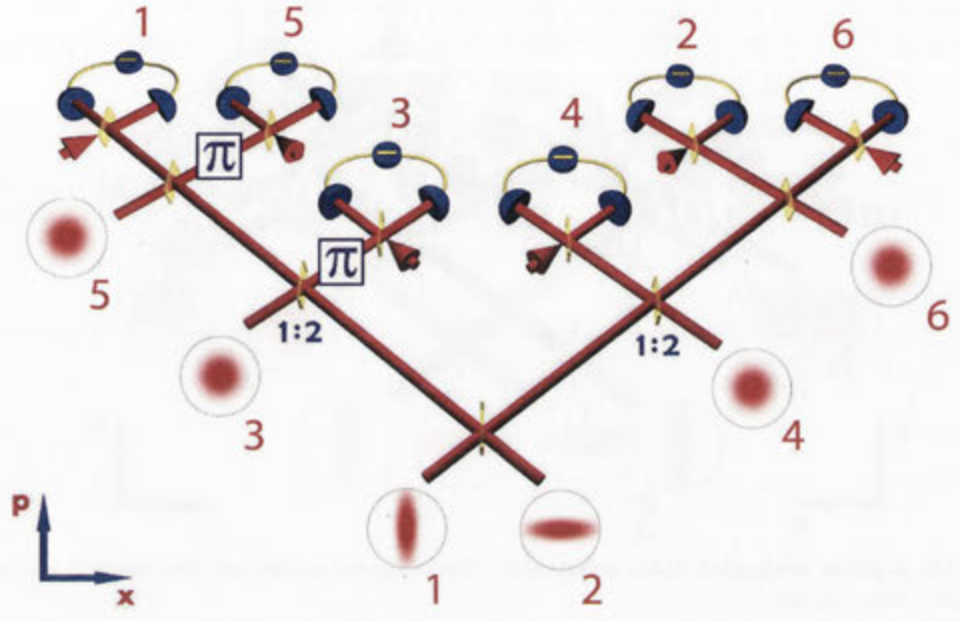

Figure 6.15: 6-mode entangled state schematic. 2 squeezed modes and 4 vacua modes are combined on 5 beam-splitters.

VLF variances	value	g_1	g_2	g_3	g_4	g_5	g_6
$\Delta^2_{\mathrm{VLF}}(\hat{x}_1) = \Delta^2(\hat{x}_1 - \hat{x}_2)$	0.38						
$\Delta^2_{\mathrm{VLF}}(\hat{x}_2) = \Delta^2(\hat{x}_2 - \hat{x}_3)$	0.38						
$\Delta^2_{\mathrm{VLF}}(\hat{x}_3) = \Delta^2(\hat{x}_3 - \hat{x}_4)$	0.38						
$\Delta^2_{\mathrm{VLF}}(\hat{x}_4) = \Delta^2(\hat{x}_4 - \hat{x}_5)$	0.39						
$\Delta^2_{\mathrm{VLF}}(\hat{x}_5) = \Delta^2(\hat{x}_5 - \hat{x}_6)$	0.40						
$\Delta^2_{\mathrm{VLF}}(\hat{p}_1) = \Delta^2(\hat{p}_1 + \hat{p}_2 + g_3\hat{p}_3 + g_4\hat{p}_4 + g_5\hat{p}_5 + g_6\hat{p}_6)$	0.35			0.33	0.32	0.31	0.31
$\Delta^2_{\mathrm{VLF}}(\hat{p}_2) = \Delta^2(g_1\hat{p}_1 + \hat{p}_2 + \hat{p}_3 + g_4\hat{p}_4 + g_5\hat{p}_5 + g_6\hat{p}_6)$	0.35	0.35			0.32	0.31	0.31
$\Delta^2_{\mathrm{VLF}}(\hat{p}_3) = \Delta^2(g_1\hat{p}_1 + g_2\hat{p}_2 + \hat{p}_3 + \hat{p}_4 + g_5\hat{p}_5 + g_6\hat{p}_6)$	0.36	0.35	0.33			0.31	0.31
$\Delta^2_{\mathrm{VLF}}(\hat{p}_4) = \Delta^2(g_1\hat{p}_1 + g_2\hat{p}_2 + g_3\hat{p}_3 + \hat{p}_4 + \hat{p}_5 + g_6\hat{p}_6)$	0.36	0.35	0.33	0.33			0.31
$\Delta^2_{\mathrm{VLF}}(\hat{p}_5) = \Delta^2(g_1\hat{p}_1 + g_2\hat{p}_2 + g_3\hat{p}_3 + g_4\hat{p}_4 + \hat{p}_5 + \hat{p}_6)$	0.35	0.35	0.33	0.33	0.32		
{I} $\Delta^2_{\mathrm{VLF}}(\hat{x}_1) + \Delta^2_{\mathrm{VLF}}(\hat{p}_1)$	0.73						
{II} $\Delta^2_{\mathrm{VLF}}(\hat{x}_2) + \Delta^2_{\mathrm{VLF}}(\hat{p}_2)$	0.73						
{III} $\Delta^2_{\mathrm{VLF}}(\hat{x}_3) + \Delta^2_{\mathrm{VLF}}(\hat{p}_3)$	0.75						
{IV} $\Delta^2_{\mathrm{VLF}}(\hat{x}_4) + \Delta^2_{\mathrm{VLF}}(\hat{p}_4)$	0.74						
{V} $\Delta^2_{\mathrm{VLF}}(\hat{x}_5) + \Delta^2_{\mathrm{VLF}}(\hat{p}_5)$	0.74						
mean$[\Delta^2_{\mathrm{VLF}}(\hat{x}) + \Delta^2_{\mathrm{VLF}}(\hat{p})]$	0.74						

The 6-qumode network can be seen as a concatenation of a 2-qumode network (balanced beam-splitter) with 3-qumode networks on each side of the outputs.

6.3.6 7 qumodes

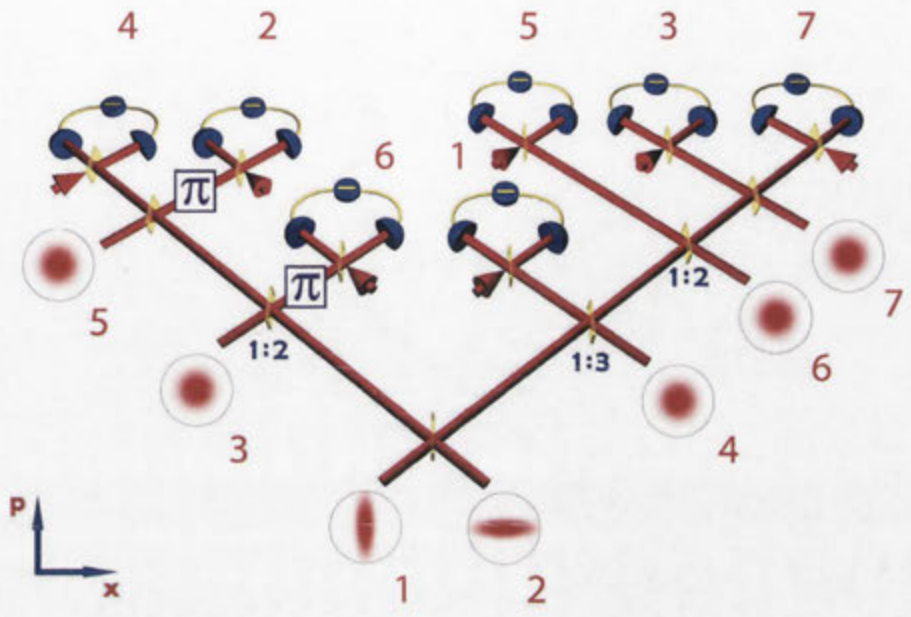

Figure 6.16: 7-mode entangled state schematic. 2 squeezed modes and 5 vacua modes are combined on 6 beam-splitters.

VLF variances	value
$\Delta^2_{\text{VLF}}(\hat{x}_1) = \Delta^2(\hat{x}_1 - \hat{x}_2)$	0.40
$\Delta^2_{\text{VLF}}(\hat{x}_2) = \Delta^2(\hat{x}_2 - \hat{x}_3)$	0.40
$\Delta^2_{\text{VLF}}(\hat{x}_3) = \Delta^2(\hat{x}_3 - \hat{x}_4)$	0.41
$\Delta^2_{\text{VLF}}(\hat{x}_4) = \Delta^2(\hat{x}_4 - \hat{x}_5)$	0.40
$\Delta^2_{\text{VLF}}(\hat{x}_5) = \Delta^2(\hat{x}_5 - \hat{x}_6)$	0.40
$\Delta^2_{\text{VLF}}(\hat{x}_6) = \Delta^2(\hat{x}_5 - \hat{x}_7)$	0.40
$\Delta^2_{\text{VLF}}(\hat{p}_1) = \Delta^2(\hat{p}_1 + \hat{p}_2 + g_3\hat{p}_3 + g_4\hat{p}_4 + g_5\hat{p}_5 + g_6\hat{p}_6 + g_7\hat{p}_7)$	0.38
$\Delta^2_{\text{VLF}}(\hat{p}_2) = \Delta^2(g_1\hat{p}_1 + \hat{p}_2 + \hat{p}_3 + g_4\hat{p}_4 + g_5\hat{p}_5 + g_6\hat{p}_6 + g_7\hat{p}_7)$	0.37
$\Delta^2_{\text{VLF}}(\hat{p}_3) = \Delta^2(g_1\hat{p}_1 + g_2\hat{p}_2 + \hat{p}_3 + \hat{p}_4 + g_5\hat{p}_5 + g_6\hat{p}_6 + g_7\hat{p}_7)$	0.36
$\Delta^2_{\text{VLF}}(\hat{p}_4) = \Delta^2(g_1\hat{p}_1 + g_2\hat{p}_2 + g_3\hat{p}_3 + \hat{p}_4 + \hat{p}_5 + g_6\hat{p}_6 + g_7\hat{p}_7)$	0.36
$\Delta^2_{\text{VLF}}(\hat{p}_5) = \Delta^2(g_1\hat{p}_1 + g_2\hat{p}_2 + g_3\hat{p}_3 + g_4\hat{p}_4 + \hat{p}_5 + \hat{p}_6 + g_7\hat{p}_7)$	0.37
$\Delta^2_{\text{VLF}}(\hat{p}_6) = \Delta^2(g_1\hat{p}_1 + g_2\hat{p}_2 + g_3\hat{p}_3 + g_4\hat{p}_4 + g_5\hat{p}_5 + \hat{p}_6 + \hat{p}_7)$	0.37
{I} $\Delta^2_{\text{VLF}}(\hat{x}_1) + \Delta^2_{\text{VLF}}(\hat{p}_1)$	0.78
{II} $\Delta^2_{\text{VLF}}(\hat{x}_2) + \Delta^2_{\text{VLF}}(\hat{p}_2)$	0.78
{III} $\Delta^2_{\text{VLF}}(\hat{x}_3) + \Delta^2_{\text{VLF}}(\hat{p}_3)$	0.77
{IV} $\Delta^2_{\text{VLF}}(\hat{x}_4) + \Delta^2_{\text{VLF}}(\hat{p}_4)$	0.76
{V} $\Delta^2_{\text{VLF}}(\hat{x}_5) + \Delta^2_{\text{VLF}}(\hat{p}_5)$	0.76
{VI} $\Delta^2_{\text{VLF}}(\hat{x}_6) + \Delta^2_{\text{VLF}}(\hat{p}_6)$	0.77
mean$[\Delta^2_{\text{VLF}}(\hat{x}) + \Delta^2_{\text{VLF}}(\hat{p})]$	0.77

There are only 2 unique gain values for the p-quadratures,

$$g_1 = g_3 = g_5 = g_7 = 0.31 \qquad \text{and} \qquad g_2 = g_4 = g_6 = 0.24. \tag{6.12}$$

6.3.7 8 qumodes

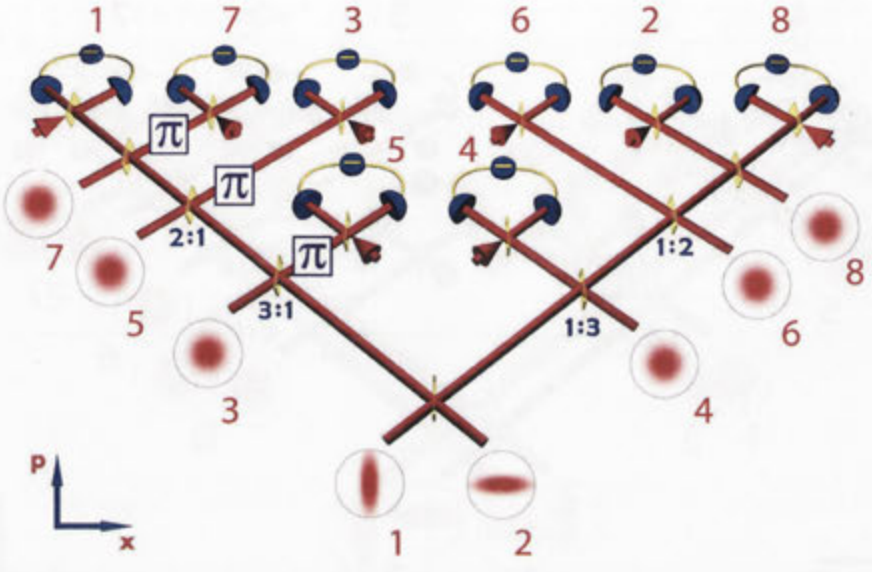

Figure 6.17: 8-mode entangled state schematic. 2 squeezed modes and 6 vacua modes are combined on 7 beam-splitters.

VLF variances	value
$\Delta^2_{\mathrm{VLF}}(\hat{x}_1) = \Delta^2(\hat{x}_1 - \hat{x}_2)$	0.42
$\Delta^2_{\mathrm{VLF}}(\hat{x}_2) = \Delta^2(\hat{x}_2 - \hat{x}_3)$	0.42
$\Delta^2_{\mathrm{VLF}}(\hat{x}_3) = \Delta^2(\hat{x}_3 - \hat{x}_4)$	0.41
$\Delta^2_{\mathrm{VLF}}(\hat{x}_4) = \Delta^2(\hat{x}_4 - \hat{x}_5)$	0.41
$\Delta^2_{\mathrm{VLF}}(\hat{x}_5) = \Delta^2(\hat{x}_5 - \hat{x}_6)$	0.41
$\Delta^2_{\mathrm{VLF}}(\hat{x}_6) = \Delta^2(\hat{x}_5 - \hat{x}_7)$	0.42
$\Delta^2_{\mathrm{VLF}}(\hat{x}_7) = \Delta^2(\hat{x}_5 - \hat{x}_8)$	0.41
$\Delta^2_{\mathrm{VLF}}(\hat{p}_1) = \Delta^2(\hat{p}_1 + \hat{p}_2 + g_3\hat{p}_3 + g_4\hat{p}_4 + g_5\hat{p}_5 + g_6\hat{p}_6 + g_7\hat{p}_7 + g_8\hat{p}_8)$	0.37
$\Delta^2_{\mathrm{VLF}}(\hat{p}_2) = \Delta^2(g_1\hat{p}_1 + \hat{p}_2 + \hat{p}_3 + g_4\hat{p}_4 + g_5\hat{p}_5 + g_6\hat{p}_6 + g_7\hat{p}_7 + g_8\hat{p}_8)$	0.37
$\Delta^2_{\mathrm{VLF}}(\hat{p}_3) = \Delta^2(g_1\hat{p}_1 + g_2\hat{p}_2 + \hat{p}_3 + \hat{p}_4 + g_5\hat{p}_5 + g_6\hat{p}_6 + g_7\hat{p}_7 + g_8\hat{p}_8)$	0.37
$\Delta^2_{\mathrm{VLF}}(\hat{p}_4) = \Delta^2(g_1\hat{p}_1 + g_2\hat{p}_2 + g_3\hat{p}_3 + \hat{p}_4 + \hat{p}_5 + g_6\hat{p}_6 + g_7\hat{p}_7 + g_8\hat{p}_8)$	0.40
$\Delta^2_{\mathrm{VLF}}(\hat{p}_5) = \Delta^2(g_1\hat{p}_1 + g_2\hat{p}_2 + g_3\hat{p}_3 + g_4\hat{p}_4 + \hat{p}_5 + \hat{p}_6 + g_7\hat{p}_7 + g_8\hat{p}_8)$	0.38
$\Delta^2_{\mathrm{VLF}}(\hat{p}_6) = \Delta^2(g_1\hat{p}_1 + g_2\hat{p}_2 + g_3\hat{p}_3 + g_4\hat{p}_4 + g_5\hat{p}_5 + \hat{p}_6 + \hat{p}_7 + g_8\hat{p}_8)$	0.38
$\Delta^2_{\mathrm{VLF}}(\hat{p}_7) = \Delta^2(g_1\hat{p}_1 + g_2\hat{p}_2 + g_3\hat{p}_3 + g_4\hat{p}_4 + g_5\hat{p}_5 + g_6\hat{p}_6 + \hat{p}_7 + \hat{p}_8)$	0.38
{I} $\Delta^2_{\mathrm{VLF}}(\hat{x}_1) + \Delta^2_{\mathrm{VLF}}(\hat{p}_1)$	0.79
{II} $\Delta^2_{\mathrm{VLF}}(\hat{x}_2) + \Delta^2_{\mathrm{VLF}}(\hat{p}_2)$	0.79
{III} $\Delta^2_{\mathrm{VLF}}(\hat{x}_3) + \Delta^2_{\mathrm{VLF}}(\hat{p}_3)$	0.78
{IV} $\Delta^2_{\mathrm{VLF}}(\hat{x}_4) + \Delta^2_{\mathrm{VLF}}(\hat{p}_4)$	0.81
{V} $\Delta^2_{\mathrm{VLF}}(\hat{x}_5) + \Delta^2_{\mathrm{VLF}}(\hat{p}_5)$	0.79
{VI} $\Delta^2_{\mathrm{VLF}}(\hat{x}_6) + \Delta^2_{\mathrm{VLF}}(\hat{p}_6)$	0.80
{VI} $\Delta^2_{\mathrm{VLF}}(\hat{x}_7) + \Delta^2_{\mathrm{VLF}}(\hat{p}_7)$	0.79
mean$[\Delta^2_{\mathrm{VLF}}(\hat{x}) + \Delta^2_{\mathrm{VLF}}(\hat{p})]$	0.79

All gains in the quadrature variances above have the same value; $g_i = 0.25$.

6.3.8 Cluster states

In order to demonstrate the versatility of our programmable networks, we also engineer entangled states with different structures. More specifically, we measure cluster states, which are detailed in sections 2.6, 9.3.1, and 10.3.1 of this thesis. Cluster states have been attracting attention in the last decade or so, for their potential in one-way quantum computing schemes [30, 77, 32]. The chapters in part III of this thesis detail an exploration of cluster states in the context of one-way quantum computing. In this section, we give a very brief summary and present results relevant to the current experiment.

Cluster states are a type of highly entangled Gaussian graph state, and they satisfy the set of nullifiers, or quadrature relations $(\hat{p}_a - \sum_{b\in N_a} \hat{x}_b) \to 0$. As infinite squeezing would require infinite energy and are thus unrealisable, we are limited to the production of approximate cluster states in the laboratory, and there have been demonstrations of 4-mode, 6-mode, and 8-mode continuous-variable spatial mode cluster states thus far [59, 78, 79, 80, 61].

In order to measure cluster states in one beam, we must be able to access the correct quadratures of each entangled mode. Here we have the freedom to create and measure linear cluster states, however measuring arbitrary cluster shapes would require modifying the optical setup, and is beyond the scope of the current demonstration. We present results for the generation of 2, 3, and 4-mode linear cluster states, which are graphically depicted in Fig. 6.18.

The difference between a two-mode cluster state and a two-mode EPR state is a Fourier transform on one mode. The Fourier transform is a rotation in phase space of $\frac{\pi}{2}$ degrees: $F = R(\pi/2) = \begin{pmatrix} cos\pi/2 & -sin\pi/2 \\ sin\pi/2 & cos\pi/2 \end{pmatrix} = \begin{pmatrix} 0 & -1 \\ 1 & 0 \end{pmatrix}$. Therefore we get $F\begin{pmatrix} \hat{x} \\ \hat{p} \end{pmatrix} = \begin{pmatrix} -\hat{p} \\ \hat{x} \end{pmatrix}$. It follows that the homodyne measurements we perform in the 2-mode cluster basis $\{p_1 - x_2, p_2 - x_1\}_{cluster}$ and the 2-mode EPR basis $\{x_1 - x_2, p_1 + p_2\}_{EPR}$ are equivalent. Therefore we may perform local Fourier transforms so long as we can match the homodyne detection basis for individual modes. It is important to note that this convenient basis change will not always be possible for different clusters. Hence we are limited here to the generation of linear cluster states, as one consequence. Note, however, that by shaping the local oscillator we may have access to arbitrary cluster states within the one beam. While out of the scope of the current experiment, the implementation is feasible with current technologies.

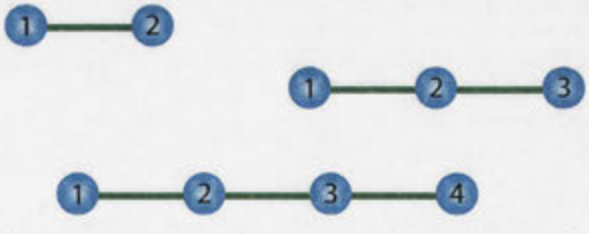

Figure 6.18: Linear cluster states. 2-mode, 3-mode, and 4-mode un-weighted linear cluster states are depicted as graphs with vertices and edges. The green links (edges) indicate entanglement of unity strength. The numbered spheres represent quantum modes of light.

The generation of a 4-mode linear cluster state by the conventional method of a physical beamsplitter network is detailed in section 9.3.1 of this thesis, and a 3-mode cluster is described in section 10.3.1.

6.3.9 Measuring 2, 3, and 4-mode cluster states

The criteria for verifying the measurements of the various cluster states are given below [34, 59]:

$$\begin{aligned} &\mathbf{N=2} \\ &\mathbf{I} \quad \langle[\Delta(\hat{p}_1 - \hat{x}_2)]^2\rangle + \langle[\Delta(\hat{p}_2 - \hat{x}_1)]^2\rangle < 1, \end{aligned} \tag{6.13}$$

$$\begin{aligned} &\mathbf{N=3} \\ &\mathbf{I} \quad \langle[\Delta(\hat{p}_1 - \hat{x}_2)]^2\rangle + \langle[\Delta(\hat{p}_2 - \hat{x}_1 - \hat{x}_3)]^2\rangle < 1, \\ &\mathbf{II} \quad \langle[\Delta(\hat{p}_2 - \hat{x}_1 - \hat{x}_3)]^2\rangle + \langle[\Delta(\hat{p}_3 - \hat{x}_2)]^2\rangle < 1, \end{aligned} \tag{6.14}$$

$$\begin{aligned} &\mathbf{N=4} \\ &\mathbf{I} \quad \langle[\Delta(\hat{p}_1 - \hat{x}_2)]^2\rangle + \langle[\Delta(\hat{p}_2 - \hat{x}_1 - \hat{x}_3)]^2\rangle < 1, \\ &\mathbf{II} \quad \langle[\Delta(\hat{p}_2 - \hat{x}_1 - \hat{x}_3)]^2\rangle + \langle[\Delta(\hat{p}_3 - \hat{x}_2 - \hat{x}_4)]^2\rangle < 1, \\ &\mathbf{III} \quad \langle[\Delta(\hat{p}_3 - \hat{x}_2 - \hat{x}_4)]^2\rangle + \langle[\Delta(\hat{p}_4 - \hat{x}_3)]^2\rangle < 1, \end{aligned} \tag{6.15}$$

$$\begin{aligned} &\mathbf{N=5} \\ &\mathbf{I} \quad \langle[\Delta(\hat{p}_1 - \hat{x}_2)]^2\rangle + \langle[\Delta(\hat{p}_2 - \hat{x}_1 - \hat{x}_3)]^2\rangle < 1, \\ &\mathbf{II} \quad \langle[\Delta(\hat{p}_2 - \hat{x}_1 - \hat{x}_3)]^2\rangle + \langle[\Delta(\hat{p}_3 - \hat{x}_2 - \hat{x}_4)]^2\rangle < 1, \\ &\mathbf{III} \quad \langle[\Delta(\hat{p}_3 - \hat{x}_2 - \hat{x}_4)]^2\rangle + \langle[\Delta(\hat{p}_4 - \hat{x}_3 - \hat{x}_5)]^2\rangle < 1, \\ &\mathbf{IV} \quad \langle[\Delta(\hat{p}_4 - \hat{x}_3 - \hat{x}_5)]^2\rangle + \langle[\Delta(\hat{p}_5 - \hat{x}_4)]^2\rangle < 1. \end{aligned} \tag{6.16}$$

Table 6.3 summarises the more stringent inseparability required for un-weighted cluster states. Weighted cluster states have non-unity strength entanglement links between modes, and conversely un-weighted cluster states have all unity strength entanglement links (all homodyne gains $\{g_i\}$ in equation (6.11) are set to 1). The relevant inseparability inequalities satisfy the cluster state quadrature relationship written in the form of equation (6.11), and are written out explicitly in equations (6.16).

N	I	II	III	IV	Avg.
2	0.39				0.39
3	0.49	0.70			0.59
4	0.79	0.67	0.84		0.76
5	0.79	0.67	1.10	1.18	0.93

*Uncertainties are ± 0.01 in all cases.

Table 6.3: Inseparability of cluster states.

Note that not all of the inequalities for $N = 5$ are below the quantum threshold normalised to 1.0. For this reason the $N = 5$-mode cluster state is not measured to be fully inseparable and therefore is not a valid quantum state with respect to this criteria. We confirm that un-weighted cluster states require higher levels of squeezing due to the more stringent conditions of inseparability than conventional entangled states such as GHZ-like states.

6.4 Experimental details

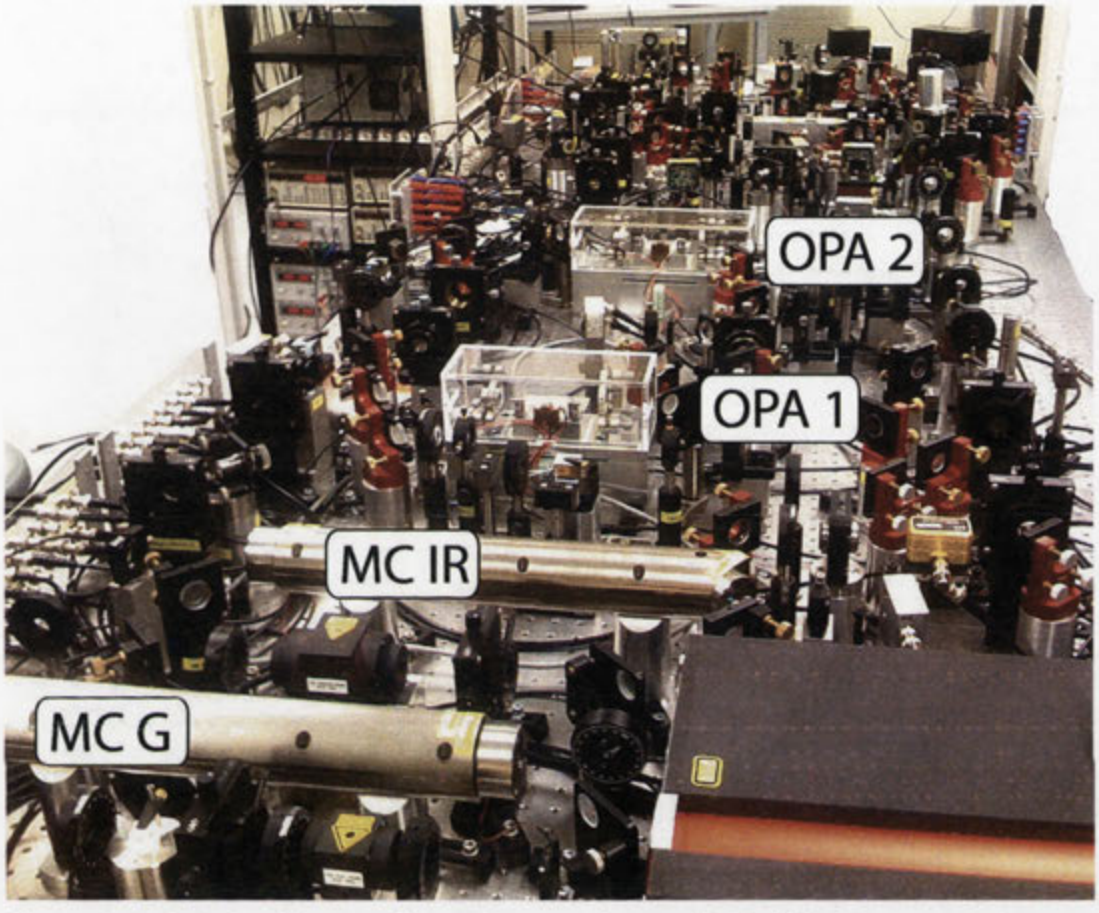

Figure 6.19: Optical table containing entire experiment. MC G: Mode-cleaning cavity for green (532 *nm*); MC IR: Mode-cleaning cavity for infra-red (1064 *nm*); OPA: Optical parametric amplifier.

Around 300 precisely positioned optical elements comprise the optical setup of this experiment. In general we use mirror mounts from Radiant Dyes, lenses from Newport, and all of the cavities are custom-made.

6.4.1 Optimised squeezers

Two squeezers were used in this experiment. Identical in design and near identical in performance, both were initially constructed by Jiri Janousek. A full treatment is offered in section 5.2.1 of this thesis. The purity and strength of the measured squeezing has been greatly improved for the current experiment. The leading contributors were an improvement in the feedback systems used for phase locking, improvements in mode matching and alignment, and the replacing of lossy optical elements and mirror mounts that had undesirable mechanical frequencies.

Cavity	OPL	T	FWHM	FSR	finesse
OPA 1	275mm	0.10	19MHz	1.1GHz	57
OPA 2	275mm	0.10	19MHz	1.1GHz	57

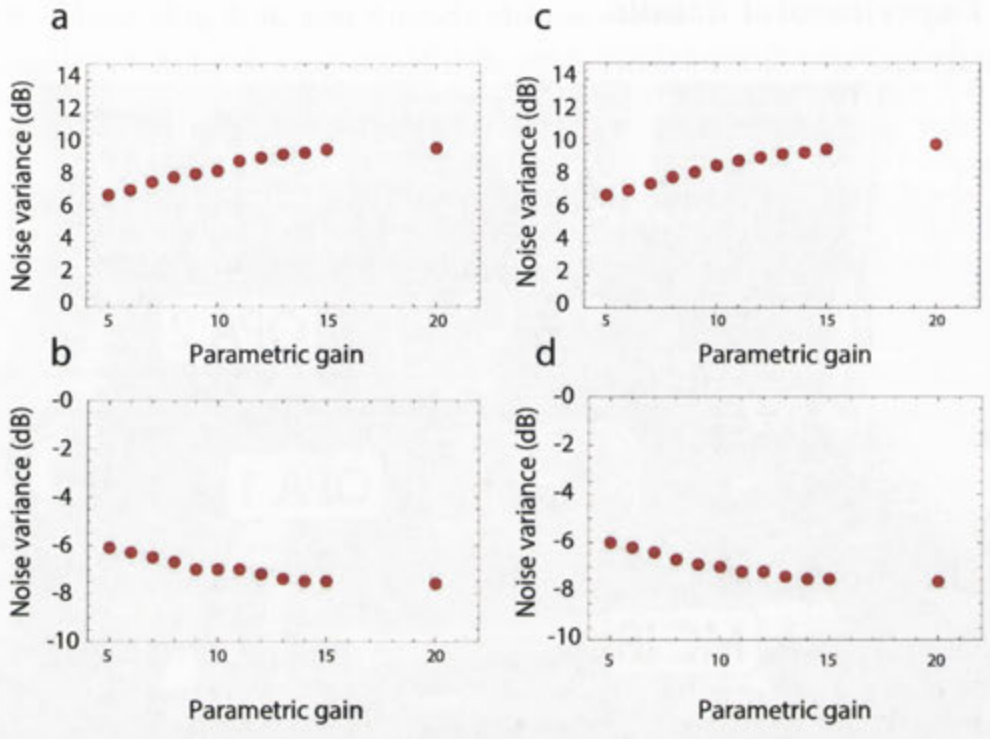

Figure 6.20: Squeezing and anti-squeezing values of 2 OPAs. Both OPAs are remarkably similar in performance. Uncertainties are ±0.2 dB.

Squeezing values for varying parametric gains are plotted above and tabulated below. The parametric gain is varied via the optical power of the pump field (range of 10 mW to 300 mW).

Gain	OPA 1 Sqz (dB)	OPA 1 A-Sqz (dB)	OPA 2 Sqz (dB)	OPA 2 A-Sqz (dB)
5	-6.1	6.9	-6	6.9
6	-6.3	7.2	-6.2	7.2
7	-6.5	7.7	-6.4	7.6
8	-6.7	8	-6.7	8
9	-7	8.2	-6.9	8.3
10	-7	8.4	-7	8.7
11	-7	9	-7.2	9
12	-7.2	9.2	-7.2	9.2
13	-7.4	9.4	-7.4	9.4
14	-7.5	9.5	-7.5	9.5
15	-7.5	9.7	-7.5	9.7
20	-7.6	9.8	-7.6	10
30	-7.8	10.6	-7.7	10.5
40	-7.9	11	-7.8	11
50	-7.9	11.2	-7.8	11.3
75	-8	11.5	-7.9	11.6
100	-8	11.8	-7.9	11.7

We find that the two squeezers offer remarkably similar performances, indicative of the reliability and repeatability of the performances of these OPAs. Uncertainties are ±0.2 dB.

These squeezing measurements were taken using high efficiency single-photodiode detectors at the same plane of detection as the multi-photodiode homodyne detectors (MPHD). Figure 6.21 shows the detection station of the optical setup. Note the cylindrical lenses placed before the MPHDs in order to make the beam highly elliptical for the linear photodiode array.

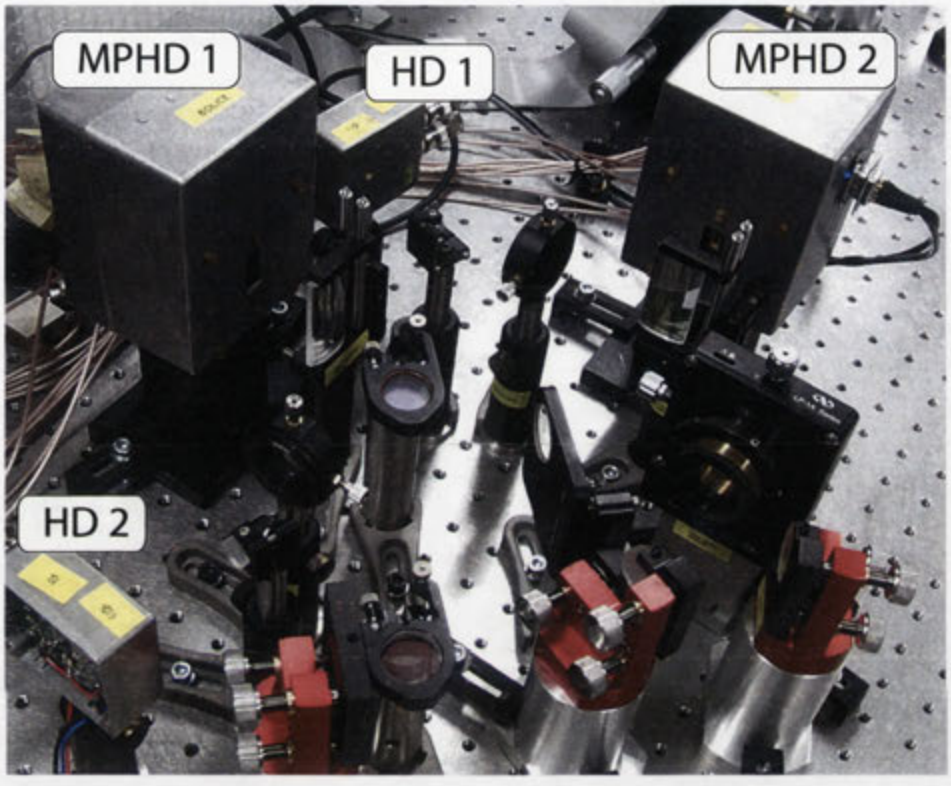

Figure 6.21: Detection station of experimental set up. MPHD: multi-pixel homodyne detector; HD: homodyne detector.

6.4.2 Feedback control of cavities and optical phases

We employed Pound-Drever-Hall (PDH) phase locking in order to apply feedback to various cavities. Error signals were created using analogue electronics (mixers from Mini-Circuits) and National Instruments LabVIEW was used to program the locking logic via software PIDs. The different frequencies of phase modulations used for PDH locking are tabulated below.

System:	Laser	OPA 1	OPA 2	Beat
Modulation:	12 MHz	7 MHz	16 MHz	4, 5 MHz

As an example, let us discuss the first optical parametric amplifier (OPA 1). The reflected field from OPA 1 is detected, and the AC signal is mixed down and filtered in order to produce an error signal. The electro-optic modulator (EOM) that the beam is passed through in order to receive the phase modulation at 7 MHz is driven by a function generator outputting a sinusoidal wave of amplitude 3.5 V peak to peak.
Locking to de-amplification (relative phase between pump and signal) is performed with the same AC signal, however the phase of the electronic local oscillator is shifted by $\frac{\pi}{2}$. This is achieved

practically, by first scanning the phase of the pump beam (via a PZT outside the cavity) and monitoring the OPA PID output and varying the electronic phase until any oscillations are flattened out. Next we monitor the de-amplification PID output and vary the phase shifter in order to maximise the error signal. Note that changing the lengths of the cables will change the electronic phase as well.

Co-propagating modes

The squeezed beam exiting the first OPA is converted into a flip-mode via propagation through a flip-plate. The flip-pate consists of two $\frac{\lambda}{2}$ wave-plates of unequal size stuck together such that one half of the beam sees 1 wave-plate and the other half sees both. This ensures that half the beam is π out of phase, and therefore orthogonal to the output of the second OPA. This technique is not perfect as the top wave-plate was not perfectly cut and we observe a 3% optical loss from scattering as well as diffraction. The scattered light is detectable, differentiating it from losses due to poor anti-reflection coatings, and exits the imaging setup as loss.
When OPA 2 is locked, by reflecting the flip-mode off the output-coupler, the flip mode will be reflected from a near perfect mirror as the flip-mode will not resonate within the cavity. Note that when OPA 2 is scanned, the flip-mode will see a 90% reflection from the output-coupler, as the mirror is $r = 0.9$.
Due to the spatial composition of the two modes, when they are propagating in phase, only one-half of the beam will be visible on a CCD camera, due to destructive interference on the other half. Balancing intensities then between the two halves ensures a phase of $\frac{\pi}{2}$ between the modes. A DC error signal is used to ensure that the intensities are balanced.

Error signals for MPHD phase locking

In order to measure the desired spatial mode at the homodyne station, we create an error signal from combinations of the detected photocurrent. The error signal is used in order to lock the reference local oscillator to the desired phase relative to the signal beam. The homodyne visibilities were 99.2% and 99.4% for OPAs 1 and 2, respectively.

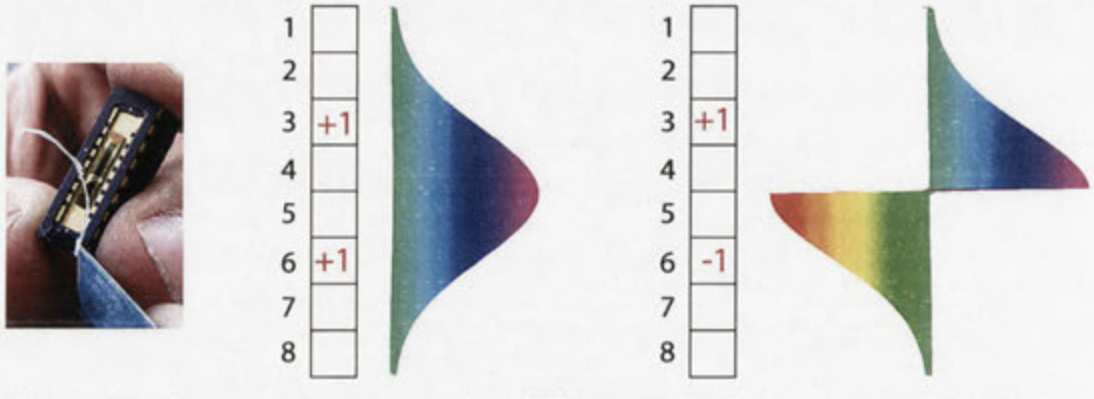

Figure 6.22: Error signal generation from MPHD signals. The linear array of photodiodes is shown on the left. A protective window is being carved off in order to increase the efficiency. Different combinations of photodiodes 3 and 6 will recover spatially orthogonal modes, leading to different error signals.

We can lock to the Gaussian mode by taking the sum of channels 3 and 6 and mixing down at 16 MHz (phase modulation of OPA 2). Conversely, we can lock the flip mode by taking the difference of channels 3 and 6 and mixing down at 7 MHz (phase modulation of OPA 1). The AC signals of the MPHD channels are used. In practise we also monitor the 4 corresponding DC signals

from the 2 MPHDs. As the two MPHDs are balanced in power, we can ensure the correct phase exists between the two orthogonal modes by matching the powers between pairs of DC signals. For example, to lock to the Gaussian mode, we would ensure that channels 3 and 6 from MPHD 1 have the same power, whereas to lock to the flip mode we would ensure that channel 3 from MPHD 1 and channel 6 from MPHD 2 had the same DC power.

6.4.3 Data analysis

Data acquisition

We use an 8-channel Digitizer from National Instruments (PXI-5105) to acquire the AC signals from the photo-detectors. This data acquisition (DAQ) card has a 60MHz bandwidth and a 12-bit vertical resolution. A custom script in National Instruments LabVIEW was written by Jean-Francois Morizur, Boris Hage, and myself that can be used to acquire the 8 signals with full control over various parameters such as acquisition rate and vertical range. As detailed in chapter 3 of this thesis, these parameters must be optimised in order to operate the acquisition process in a sensible and efficient regime.

Repeatability of experiment

The experiment was repeated many times under various conditions to ensure repeatability and statistical significance of the results. During the fine-tuning stage of the experimental setup, after the optical layout and electronic testing of the components was completed, measurements were taken daily over several weeks and were found to be consistent. The final data set comprised of 50 $\hat{x}$ quadrature measurements and 50 $\hat{p}$ quadrature measurements, where each measurement was 1,000,000 data points in length.

Data processing

Figure 6.23 shows the data at various stages of processing. Shown here is the signal beam detected in the $\hat{x}$ quadrature, and the exact same process is applied for the detection in the $\hat{p}$ quadrature. Each plot contains all 8 channels from the multi-photodiode homodyne detector. While each channel in each data set contains 10^6 points, only 5000 points are shown in the figure for clarity. Note the scale of amplitude differs dramatically for each stage of processing.
A sample of the source code required to process the data at the various stages is shown alongside the plots. The source code is written in MATLAB. Starting from the top, the raw data is read in from the photodetectors via a DAQ card. We cannot quite make out 8 channels, but we can see that there are roughly 3 amplitude levels. The magenta and cyan are out of phase, the gold and grey are in phase, and apart from the blue in the centre the other channels are hidden behind the layers. The band-pass filter is implemented in two stages, first by low-pass filtering and then by applying a high-pass filter. We see that the amplitude levels are decreased by an order of 100, and the data is clearly qualitatively different. The same process is carried out for the shot noise, which is then used to normalise the signal beam data. The parameters describing the bandpass filter is shown in the listing below the figure. Hage and Morizur helped me to design the digital filter.
The normalised data is then ready for manipulation in the programmable networks. We have arrived at the filtered and normalised 8 homodyne-subtracted photo-current operators $\hat{\mathbf{i}} = (\hat{i}_1, \cdots, \hat{i}_8)^{\mathrm{T}}$ described in equation (6.2).

Plots at different stages of data processing

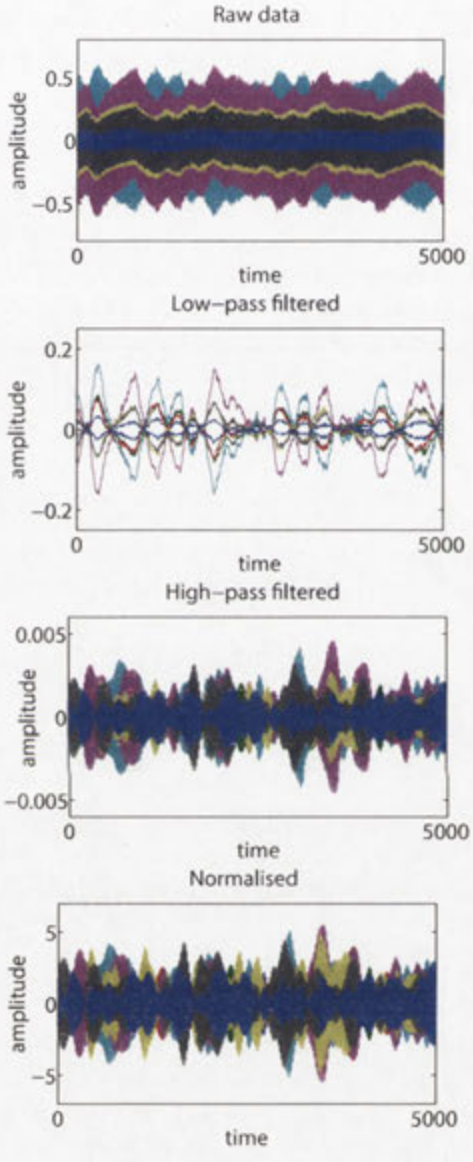


```
f=('\data\x_35.tdms');
[f_x]=convertTDMS(false,f);
Ch=[1 3 4 5 6 7 8 9];
for c=1:8
 data_x(c,:)=f_x.Data(1,Ch(c)).Data;
end
```

```
[b,a]=ellip(no,Rp,Rs,2*fu/fs);
for k=1:8
 data_x(k,:)=filter(b,a,data_x(k,:));
end
```

```
[b,a]=ellip(no,Rp,Rs,2*fl/fs,'high');
for k=1:8
 data_x(k,:)=filter(b,a,data_x(k,:));
end
```

```
cs=cov(shot_noise');
snV=diag(cs,0).^(-0.5)'
data_x=data_x'*diag(snV);
```

Figure 6.23: **Plots of data at various stages**. Source code shown on right.

```
%% global bandpass filter parameters
no=8; % order n
Rp=.1; % dB of ripple in passband
Rs=90; % stopband dB down from the peak value in passband
fs=60e6; %sampling frequency
fu=2.99e6; % resolution bandwidth
fl=2.98e6; % 10kHz RBW
```

Listing 6.2: parameters used for bandpass filter in MATLAB.

6.5 Conclusion

Emulating linear optics networks by mixing copropagating spatial modes is a highly efficient method for generating multimode entanglement. Otherwise arduous and potentially lossy tasks such as mode matching during the construction of a linear optics network are performed effortlessly and in a lossless manner via software-controlled combinations of the spatial modes. We have shown that although correlations weaken if more squeezing resources are not added, (non-cluster) entangled modes scale here as the number of orthogonal modes measurable within the beam. The maximum number of measurable modes corresponds directly to the number of photodiodes in each pair of the multi-pixel detectors. We have demonstrated this by measuring $N = 2, 3, 4, 5, 6, 7$, and 8-mode entanglement within one beam, including up to 4 mode cluster states, switching between them in real time. The ability to perform a wide range of protocols and optimise networks for asymmetry using just one optical setup offers versatility to future networks that will utilise entanglement as a resource.

6.5.1 Further possibilities

The entanglement demonstrated in the current work allows for such protocols as quantum teleportation [81, 82, 19]. To perform complex protocols such as one-way measurement based quantum computations [83], we need to increase the degrees of freedom in our detection scheme as follows. First, we need to introduce the ability to measure each mode in an arbitrary phase quadrature at the MPHD. This may be achieved by manipulating the phases between the copropagating entangled modes. By introducing a unitary mode-shaping device such as that explained in chapter 5 of this thesis, as well as references [54, 57, 38], such access to individual phases becomes possible. These papers describe a process of manipulating both the amplitudes and phases of spatial modes in a lossless fashion via an adaptive process utilizing a network of deformable mirrors and lenses. Second, in order to perform teleportation-based computations, we require the ability to feed-forward the measurement results of arbitrary cluster nodes to remaining cluster nodes. This may be realised by combining a specifically shaped displacement beam containing the necessary phase space displacements with the beam containing the co-propagating modes. By shaping the displacement beam to spatially match a specific mode to be displaced, it will interfere only with the desired mode owing to the orthogonal nature of the spatial mode basis. While these modifications are feasible with existing technologies, we conclude that this is a non-trivial technical challenge.

6.5.2 Purity or mixedness of input states

With regard to entanglement, as defined by the inseparability criteria, the most important parameter is the amount of squeezing in the optical mode. The amount of anti-squeezing present in the state has a minimal effect. However, when considering a stricter criterion such as EPR steering (a form of non-locality), anti-squeezing values will quickly degrade the quality of the quantum state. This mixedness, or asymmetry in squeezing values, can be accounted for in some conditions by creating asymmetric networks that have a bias towards different inputs. As each unique beamsplitter reflectivity in our virtual networks changes the mapping of $\mathbf{U}_{\text{net}}$, formally the beam of light in our experimental setup contains an infinite number of mode bases. The versatility of our scheme comes from being able to match the detection basis to a network that has been optimised for an arbitrary set of inputs. This is explored in appendix A.

6.5.3 The Cast

The main researchers involved in this project were myself, Jean-Francois, Jiri, and later Boris, all supervised by Hans. This project was conducted between August 2010 and April 2012, at the

Department of Quantum Science, The Australian National University.

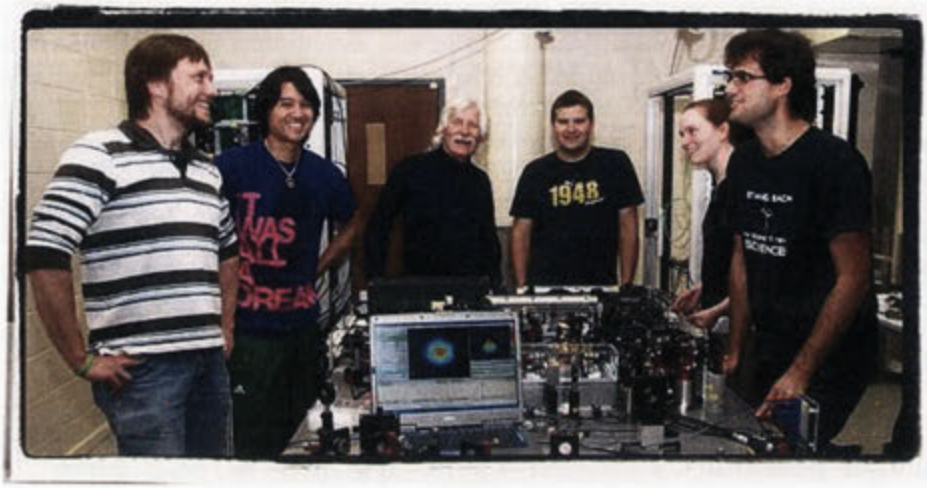

Figure 6.24: Quantum Imaging Team at the ANU Department of Quantum Science (2011). (Left to Right) Boris Hage, Seiji Armstrong, Hans Bachor, Jiri Janousek, Kate Wagner, Jean-Francois Morizur.

Chapter 7

Ultra-large temporal-mode cluster states

The idea of multiplexing spatial modes in one beam was shown to be successful, as we saw in the previous chapters. We were able to emulate various linear optics networks in order to generate and measure a variety of entangled mode bases. The experiments also exposed several limitations, however, both of a fundamental and a technical nature. We saw that increasing the number of spatial regions of light the detector had access to would increase the number of entangled modes we could measure in the one beam. However, this was shown to be true only for the particular class of inseparable states that we created, and importantly not true for cluster states. When we briefly explored the computationally useful cluster states, we found that the method was entirely not scalable, due to the more severe conditions on squeezing levels for cluster state generation. This is a fundamental limitation. Further, due to the nature of spatial multiplexing, it is difficult to spatially separate the individual quantum modes after the cluster state has been generated. While this is a technical limitation, it exposes an unnecessary level of complexity that is inherent to the spatial multiplexing scheme.
A similar, yet altogether different approach is to multiplex quantum modes of light in the time domain. As we will see in this chapter, temporally orthogonal modes are remarkably scalable. Further, they are individually accessible, allowing us to develop an efficient theory of quantum computation using the generated states.

The research explored in this chapter appears in the following journal publication:

- S. Yokoyama, R. Ukai, S. Armstrong, C. Sornphitphatphong, T. Kaji, S. Suzuki, J-I. Yoshikawa, H. Yonezawa, N. Menicucci, A. Furusawa. *Ultra-large-scale continuous-variable cluster states multiplexed in the time domain.* Nature Photonics **7**, 982-986 (2013).

7.1 Background and motivation for the experiment

The desire was to entangle together a very large number of modes. Historically, the first entanglement experiments began surfacing around the 1980s. Since then progress regarding the scaling of entangled states has been relatively slow compared with the accelerated interest in performing elegant experiments demonstrating various uses for entangled systems. An idea borrowed from the well established telecommunications industry for boosting bandwidth is to consider multiplexing the information carriers within one channel. Apart from our investigations in spatially orthogonal channels, there is also excellent research being conducted in regard to frequency-mode multiplexing. Two groups leading the charge are Olivier Pfister's group at the University of Virginia, and Nicolas Treps' group at the Laboratoire Kastler Brossel. The third natural option when considering a domain in which to multiplex quantum light is the time domain. This has the advantage of

being mathematically similar to the frequency domain (being only a Fourier transform away), and also allowing for spatially separated quantum modes of light.
Our experiment produced ultra-large cluster states that were multiplexed in the time domain, and was based on a theoretical proposal by Nicolas Menicucci from the University of Sydney. Menicucci gave a talk at the Conference on Quantum Communication, Measurement and Communication 2010 in Brisbane describing a scheme for creating large cluster states with a well-understood structure, via a conceptually simple setup. I described the scheme to the Cluster Group at the Furusawa Laboratories at the University of Tokyo the following year, and we began interpreting the theoretical proposal into a language that experimentalists could understand. A group of 6 of us built and performed the experiment in 12 months.

7.1.1 Defining the quantum mode of light

We have some freedom in defining our quantum modes of light. We can consider them for example as spatial, frequency, polarisation, or temporal modes. In most continuous-variable quantum optics experiments [84] a quantum mode is encoded within a single side-band pair at a fixed frequency away from the carrier. The positive (upper) and negative (lower) sidebands either side of the carrier frequency are typically added together and the collective pair is defined as one quantum mode. It is possible to measure each frequency sideband individually, for example by resonator detection, which has been developed by Paulo Nussenzweig's group in Sao Paolo in collaboration with Claude Fabre's group in France [85]. In the vast majority of quantum optics experiments dealing with sidebands however, homodyne detection is used, which cannot resolve the upper and lower sidebands individually.
An alternative is to consider wave-packets of light, separated by a certain time, as independent single modes of light. The separation time will be inversely proportional to the bandwidth of the cavity producing the light. This characterisation of a quantum mode as a temporal mode, not dissimilar to a pulse of light in a laser beam, has the concept of one-beam multiplexing inherently built in. Remarkably, this method of producing quantum modes allows us to re-use the optical components that comprise the linear optics network, for each temporal mode. Importantly, to scale up the number of modes produced, we need not add any more optical components. We will ultimately be limited by the amount of time we can coherently produce, control, and measure the successive wave packets within the beam.

Temporal orthogonality of sideband modes

Quantum modes that are encoded within sidebands are typically in the low MHz, with a typical bandwidth Δf in the tens of kHz. The wavepacket of the qumode then has spatial length $\frac{c}{\Delta f}$ and temporal length $\frac{1}{\Delta f}$. These lengths are independent of light power, or number of photons, and could even describe a wavepacket containing a single photon [24]. The sideband frequency f is chosen such that the squeezing is optimised, and there is no interference from modulations at other sideband frequencies used for feedback control. At the Furusawa Lab, University of Tokyo, where they employ a SolsTiS laser from M Squared, the sideband frequencies are chosen to be around $f = 1$ MHz. At the Department of Quantum Science, Australian National University, Diablo lasers from Innolight are popular, and there the sideband frequencies are chosen to be around $f = 2.8$ MHz. In general the lower the frequency the more squeezing there is, however there is usually noise at very low frequencies due to laser relaxation oscillations and other technical sources. Regardless of the sideband frequency f, the bandwidths used in both labs is $\Delta f = 30$ kHz.
A sideband qumode of bandwidth 30 kHz will then have a spatial length of $10km$ and a temporal length of 33 μs. This means that every 33 μs we will get a wavepacket that is orthogonal to the one behind and in front of it in the beam. These spatial and temporal lengths are relatively very large when considering interacting them to create an entangled state. Figure 7.1 shows a sequence

of orthogonal temporal quantum modes (qumodes) for a temporal length T.

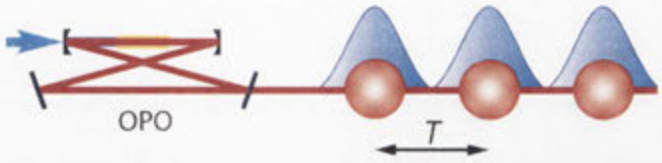

Figure 7.1: Temporal modes from OPO. Qumodes are encoded as wavepackets of light separated by a time T. The bandwidth of the cavity dictates T.

Since these temporal qumodes are independent, we must interact them with the other qumodes in order to create an entangled state. One way to do this would be to delay each qumode at some point in the circuit so that it can interact with a qumode at a neighbouring temporal position. In Fig. 7.2 we see two equivalent schemes for generating a linear cluster state. The figures are taken from a theoretical proposal by Nicolas Menicucci and Tim Ralph [52].

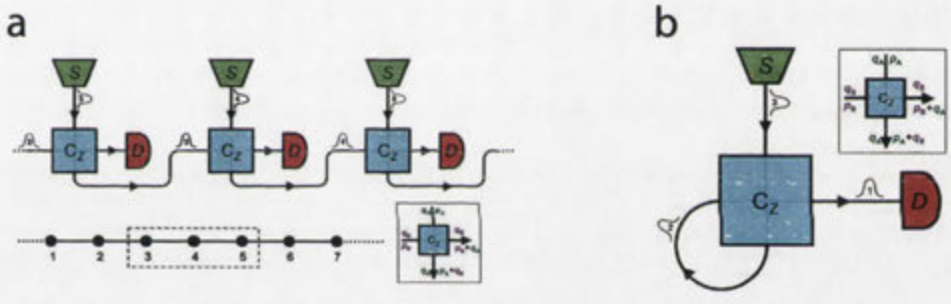

Figure 7.2: Equivalent methods for creating a large cluster state. (a) N squeezer and N C_Z gates are employed in order to create an N-qumode cluster state. (b) One squeezer and one C_Z gate are used iteratively to produce an N-qumode cluster state. Figure created by Nicolas Meniccuci, and appears in [52].

Figure 7.2 (a) shows the conventional approach of preparing N squeezers and mixing the N beams in order to create an N-qumode cluster state. Figure 7.2 (b) displays an equivalent schematic that employs multiplexing, allowing us to have only *one* squeezer, and *one* device for mixing the qumodes, in order to create an N-qumode cluster state. This is a beautiful idea that comes from a sound understanding of the flexibility we have in defining the qumodes. There are several issues with this scheme that ultimately made it not feasible, but we benefit greatly from the idea. The main drawback is that the implementation of a Controlled Z gate is experimentally difficult [33]. Returning to Fig. 7.2 briefly, we note that the physical size of the delay in (b) will be dictated precisely by the spatial length of the qumodes. The shorter the delay the better, as longer optical paths incur loss through mode mismatch and propagation losses. If we were to employ the typical sideband qumodes as detailed above, the optical delay line would need to be on the order of $10km$! This is clearly impractical, as the losses occurred from propagation losses (either in fibres or free space) would be too great. For this reason we need to consider different encodings of qumodes that will allow for much shorter time delays. As time and frequency are conjugate Fourier pairs, intuitively we might consider broadband light, or multimode light containing many frequencies, that will necessarily have narrow temporal widths.

7.1.2 Quantum modes in time and frequency domains

Quantum modes in frequency domain

In this section we formulate the precise meaning of quantum modes in both the frequency domain and the time domain. Several theses include a treatment on this formulation, and I encourage the reader to read for example references [25, 86] or if the reader is familiar with Japanese then [87, 88].
In chapter 2 we introduced the annihilation and creation operators as ladder operators of excitations of the quantum harmonic oscillator. Here, we re-formulate the operators in terms of oscillations of an electromagnetic field at frequency ω, or equivalently a plane wave of frequency ω,

$$\hat{a} \to \hat{a}(\omega) = \hat{a}_\omega, \qquad \hat{a}^\dagger \to \hat{a}^\dagger(\omega) = \hat{a}^\dagger_\omega. \tag{7.1}$$

It follows that for each frequency ω there is an associated Hamiltonian that describes the quantum mode at ω

$$\hat{H}_\omega = \omega(\hat{n}_\omega + \frac{1}{2}) = \omega(\hat{a}^\dagger_\omega \hat{a}_\omega + \frac{1}{2}). \tag{7.2}$$

These frequency modes are independent and orthogonal, meaning that there is no overlap between them. Therefore we get the following commutation relations:

$$[\hat{a}(\omega), \hat{a}^\dagger(\omega')] = \delta(\omega - \omega'), \qquad [\hat{a}(\omega), \hat{a}(\omega')] = 0. \tag{7.3}$$

Continuous light and pulsed light

A continuous-wave light beam approaching infinite duration (Fig. 7.3(a)) would represent a single frequency qumode, whereas an ultrashort pulse of light (Fig. 7.3(b)) would represent a wide spectrum of frequencies.

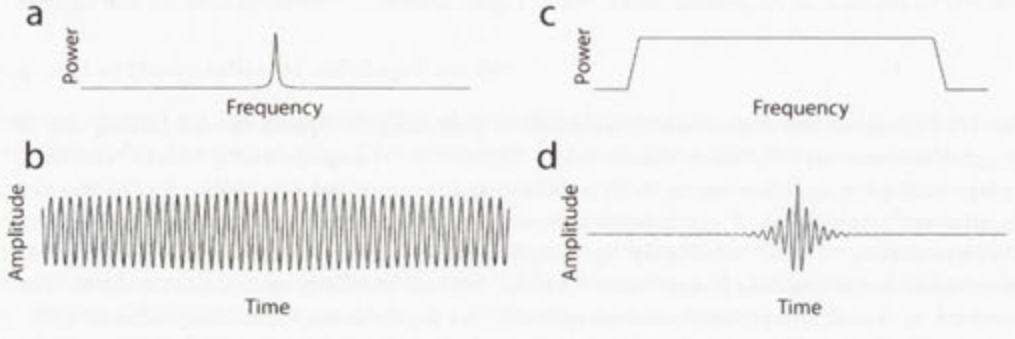

Figure 7.3: Wavepackets of light. (a) continuous-light of extremely long temporal length corresponding to a single frequency band. (b) Ultra-short pulse of light corresponding to ultra-high bandwidth in frequency space.

By considering a continuous-wave light beam to be sequential pulses of finite duration, we may define qumodes to be wave-packets with certain temporal mode functions that define their shape, and temporal width.

Formally, we define time-domain annihilation (and creation) operators by recognising that they

Figure 7.4: Pulsed light within continuous light. Pulses of light propagating within a continuous-wave beam.

are related to the frequency-domain operators via a Fourier transform

$$\hat{a}(t) = \frac{1}{\sqrt{2\pi}} \int_{-\infty}^{+\infty} \hat{a}(\omega) e^{-i\omega t} d\omega, \qquad \hat{a}^\dagger(t) = \frac{1}{\sqrt{2\pi}} \int_{-\infty}^{+\infty} \hat{a}^\dagger(\omega) e^{-i\omega t} d\omega \tag{7.4}$$

$$\hat{a}(\omega) = \frac{1}{\sqrt{2\pi}} \int_{-\infty}^{+\infty} \hat{a}(t) e^{+i\omega t} dt, \qquad \hat{a}^\dagger(\omega) = \frac{1}{\sqrt{2\pi}} \int_{-\infty}^{+\infty} \hat{a}^\dagger(t) e^{+i\omega t} dt \tag{7.5}$$

with the following commutator relations

$$[\hat{a}(t), \hat{a}^\dagger(t')] = \delta(t - t'), \qquad [\hat{a}(t), \hat{a}(t')] = 0. \tag{7.6}$$

As emphasised in ref [86] we can arrive at these different bases in time and frequency domains via different decompositions of the Maxwell equations, and we remark that a multimode treatment of light is possible without considering the quantum properties of light.

Wavepackets of light as quantum modes

We can now define a basis of wavepacket qumodes, allowing us to treat each qumode as a quantum harmonic oscillator in a basis that is indpendent of both the time and frequency domains. For every n we define a qumode $\hat{a}_n$ as

$$\hat{a}_{f_n} = \int_{-\infty}^{+\infty} \hat{a}(t) f_n(t) dt, \tag{7.7}$$

where $f_n(t)$ is referred to as the temporal mode function that defines the wavepacket qumode. We describe a set of orthonormal functions $f_n(t)$ that satisfy the commutation relation $[\hat{a}_n, \hat{a}_m^\dagger] = \delta_{mn}$, and the normalisation condition

$$\int_{-\infty}^{+\infty} f_n(t) f_m^*(t) dt = \delta_{mn}. \tag{7.8}$$

This is the basis in which the experiment is operated, allowing us to achieve relatively short spatial and temporal lengths of qumodes, on the orders of tens of metres and hundreds of nanoseconds, respectively. Re-writing in terms of the quadrature operators, and implementing time windows on the integrals we get

$$\hat{x}_{f_n} = \int_{-\frac{T}{2}}^{+\frac{T}{2}} \hat{x}(t - nT) f_n(t) dt, \tag{7.9}$$

$$\hat{p}_{f_n} = \int_{-\frac{T}{2}}^{+\frac{T}{2}} \hat{p}(t - nT) f_n(t) dt. \tag{7.10}$$

Finding the optimal temporal mode function is relatively straightforward, and we found that the shape isn't as important as the temporal duration of $f_n(t)$. Ukai provides a treatment of various temporal mode functions investigated for the experiment in [87], and an elegant approach based on the eigenfunction expansion of the autocorrelation function is suggested in [89]. I optimised the mode function using a genetic algorithm and found differences to be minimal from what is expected by employing a standard Gaussian or Lorentzian of sensible temporal width.
We employ a Gaussian temporal mode filter $f(t) \propto \mathrm{e}^{-(\Gamma t)^2}$ which is normalised as $\int_{-T/2}^{T/2} |f(t)|^2 \, \mathrm{d}t = 1$. The optimal bandwidth Γ was found to be $\Gamma = 2\pi \times 2.75$ MHz ($1/\Gamma \sim 58$ ns). T is dependent on the fiber length and is found to be 160 ns.

7.1.3 Potential implementations of time-delayed circuits

The schematic suggested by Nick Menicucci in [52] and Fig. 7.2 is difficult to implement because the C_Z gate requires online squeezing. This gate has been demonstrated by Miwa and co-researchers at the Furusawa Lab [33], but was found to be quite complex and requires high squeezing levels for even modest entanglement strengths.

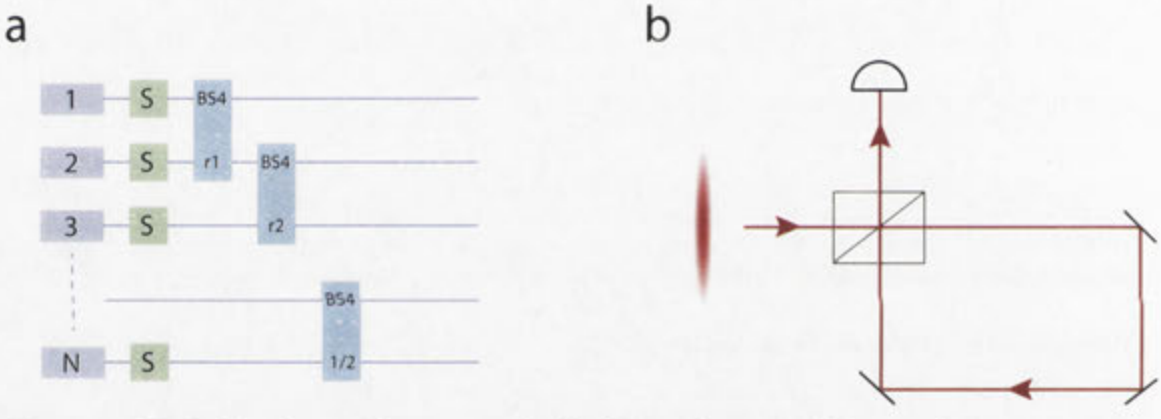

Figure 7.5: Equivalent beamsplitter networks for linear clusters. a) N squeezed resources are interferred with $N-1$ beamsplitters to create an N-mode cluster state. b) One squeezer produces orthogonal squeezed mode wave-packets that are mixed on a variable beamspltiter with time-delayed iterations of one output port. Fourier transforms omitted in both schematics for clarity.

Another option would be to replace the C_Z gate by a linear optics network so that the squeezers can be taken offline, as suggested by Peter van Loock [34]. We consider the beamsplitter networks of Fig. 7.5. The schematics are conceptually equivalent, with local Fouriers omitted for clarity. The reason why Fig. 7.5 (b) is a valid scheme is of course because we are treating the qumodes as wave-packets, or temporal modes, and the optical delay line is made longer than the temporal separation needed to ensure orthogonality.
The main drawback of the one beam-splitter network of Fig. 7.5(b) is that the beam-splitter ratio must be changed for each incoming qumode. While this can be achieved using ultra-fast electronics and polarisation optics (for example in [90]), the unavoidable impediment is that the size of the output state must be known from the beginning. As the reflectivity of the beamsplitter operating on the first qumode will be $r = \frac{N-1}{N}$, where N is the size of the output state, this means that N must be specified initially. Stated another way, the cluster cannot be made to continue indefinitely and to an arbitrary size. This has not been a problem until now, as cluster states were limited to under 10 modes [78, 59, 47, 61]. However, as we will see, we create clusters that are several orders of magnitude larger, and the ability to extend qumodes on the end of the cluster becomes important. Next, we present our scheme that overcomes all of the shortcomings discussed so far.

7.1.4 Experimental overview

Our experimental schematic is shown in Fig. 7.6. The generated dual-rail structure was first suggested by Menicucci in [22], where a detailed theoretical investigation is performed using graphical calculus [36].

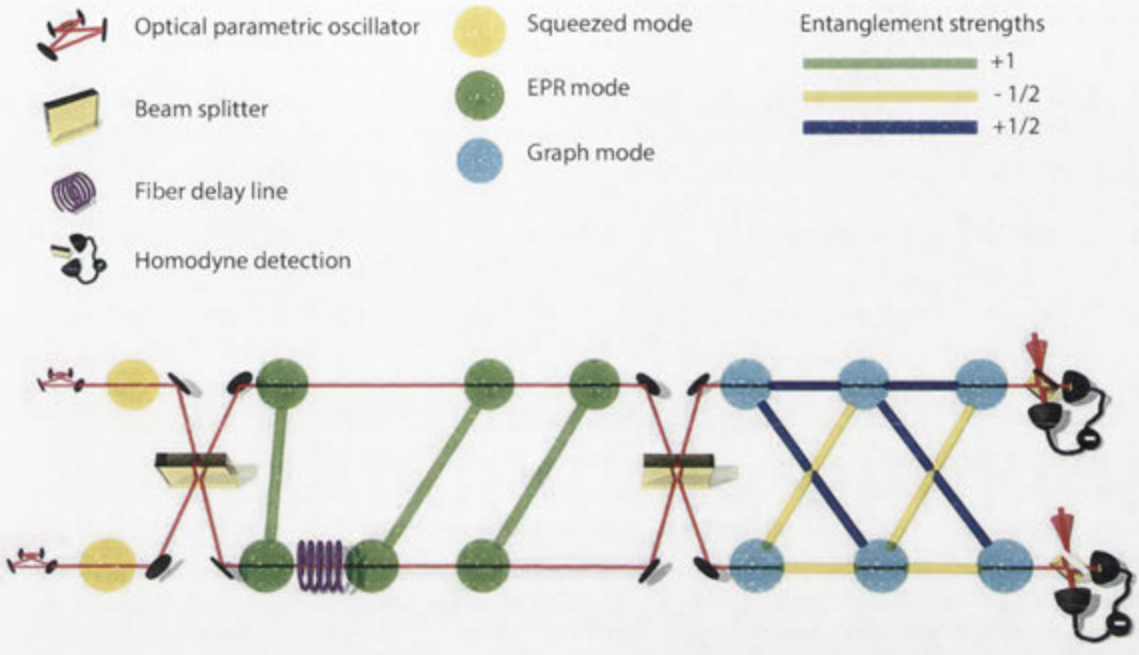

Figure 7.6: Experimental Setup. Shown as coloured spheres are depictions of the temporal modes at various stages of propagation. Squeezed modes are mixed on a beam splitter to create EPR modes. EPR modes are then mixed to create the graph modes. The coherent collection of graph modes that remain entangled below the threshold constitute the cluster state.

We create two continuous-wave squeezed beams and weave entanglement links between them in a criss-cross fashion. This is achieved by mixing the two beams on two beamsplitters with one beam undergoing a temporal delay in between the mixing. The squeezed beams are mixed first to create entangled beams, which are then mixed in a staggered fashion to create the graph state. The time delay induced by the optical delay line is precisely equal to the temporal separation between the qumodes, (here around 160 ns). This ensures that qumodes in the top rail will become entangled with the qumodes in the bottom rail that are one temporal position away, both in the future and the past.
The delay line is implemented via an optical fiber. The length of the fiber is crucial as it determines the temporal widths of the wavepacket qumodes. Fibers of several lengths were tried and tested before we chose $l = 30m$ in order to optimise the squeezing bandwidth available from our OPOs.

Animation of experimental setup

A short animation was made that shows the propagation of the qumodes at various stages of the schematic. It can be found at http://www.youtube.com/watch?v=gor29QIP9Ls

7.2 The dual-rail EPR-graph state

Here we provide a detailed treatment of the quantum state generated by our experimental schematic shown in Fig. 7.6. The treatment follows the graphical calculus presented in [36], which was briefly introduced in section 2.6.3.

Every N-mode zero-mean Gaussian pure state can be uniquely represented by an undirected, complex-weighted graph whose adjacency matrix $\mathbf{Z}$ is an $N \times N$ complex symmetric matrix with positive definite imaginary part. We therefore have $\mathbf{Z} = i\mathbf{U} + \mathbf{V}$, where $\mathbf{U} = \mathbf{U}^{\mathrm{T}}$ and $\mathbf{V} = \mathbf{V}^{\mathrm{T}}$ are real and $\mathbf{U} > 0$. In this chapter, we make no distinction between a graph and its adjacency matrix. Any Gaussian pure state $|\psi_{\mathbf{Z}}\rangle$ satisfies the following nullifier relation with respect to its graph $\mathbf{Z}$:

$$(\hat{\mathbf{p}} - \mathbf{Z}\hat{\mathbf{x}})\,|\psi_{\mathbf{Z}}\rangle = \mathbf{0}, \tag{7.11}$$

where $\hat{\mathbf{p}} = (\hat{p}_1, \ldots, \hat{p}_N)^T$ and $\hat{\mathbf{x}} = (\hat{x}_1, \ldots, \hat{x}_N)^T$.

We define the Gaussian pure state $|G_{EPR}\rangle$ that we name the dual-rail EPR-graph state[1] by its graph $\mathbf{Z}_E$,

$$(\hat{\mathbf{p}} - \mathbf{Z}_E\hat{\mathbf{x}})\,|G_{EPR}\rangle = \mathbf{0}, \tag{7.12}$$

where $\mathbf{Z}_E$ can be expressed in the following form,

$$\mathbf{Z}_E = i(\cosh 2r)\mathbf{I} - i(\sinh 2r)\mathbf{G}, \tag{7.13}$$

where r is the initial squeezing parameter of the squeezed states that are output from the OPOs, and we have introduced a CV cluster state graph $\mathbf{G}$ which represents an ideal and unphysical state, in the limit of infinite squeezing.

The full graph for $\mathbf{Z}_E$ is presented in Fig. 7.7, following the graphical calculus of [22].

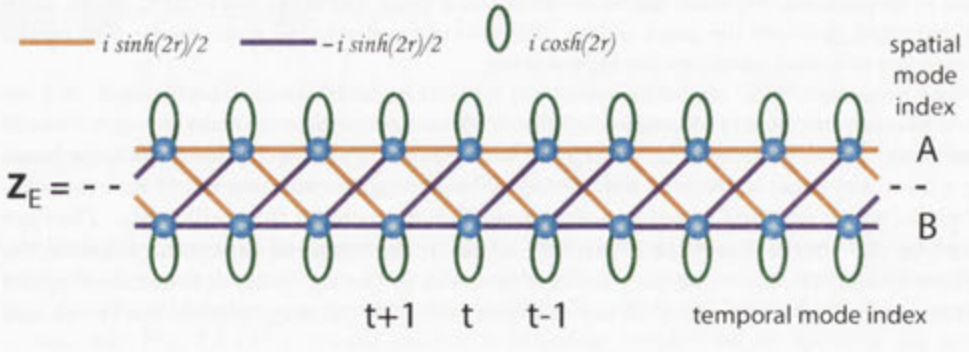

Figure 7.7: The full graph [22, 36, 37] for the dual-rail EPR-graph state. r is the initial squeezing parameter of the squeezed states emitted by the OPO. The orange (purple) edges have positive- (negative-) imaginary weight $\pm\frac{1}{2}\sinh 2r$, and the green self-loops have positive-imaginary weight $i\cosh 2r$. See ref. [22] for its derivation using a simplified graphical representation.

With respect to the graph $\mathbf{G}$, in the limit of infinite squeezing, we arrive at the following approximate nullifiers for the dual-rail EPR-graph state:

$$\begin{aligned}(\hat{\mathbf{x}} - \mathbf{G}\hat{\mathbf{x}})|G_{EPR}\rangle &\xrightarrow{r\to\infty} 0,\\ (\hat{\mathbf{p}} + \mathbf{G}\hat{\mathbf{p}})|G_{EPR}\rangle &\xrightarrow{r\to\infty} 0.\end{aligned} \tag{7.14}$$

[1] Note that in reference [37] we refer to the dual-rail EPR-graph state as the Extended EPR state.

$\mathbf{G}$ is bipartite and self-inverse ($\mathbf{G}^2 = \mathbf{I}$). Note that due to the dual-rail nature of our dual-rail EPR-graph states, $\mathbf{G}$ will be restricted to increasing by two dimensions at a time, i.e. n will always be even.

Equivalence to the cluster state

The dual-rail EPR-graph state is locally equivalent (up to $\frac{\pi}{2}$ phase shifts on half the modes) to a cluster state[2]. As such, and as explored in section 8.7, the dual-rail EPR-graph state is a universal resource for measurement-based quantum computing. In fact, due to the nature of the measurement-based operations, by implementing simple rotations to the homodyne measurements (for example $\hat{x} \to \hat{p}$ and $\hat{p} \to -\hat{x}$) the dual-rail EPR-graph state need not be converted to a cluster state at the time of state preparation in order to carry out universal quantum computations. Formally, the graph $\mathbf{Z}_C$ corresponding to the cluster state is given by the following:[3]

$$\mathbf{Z}_C = i(\operatorname{sech} 2r)\mathbf{I} + (\tanh 2r)\mathbf{G}. \tag{7.15}$$

The full graph for $\mathbf{Z}_C$ is presented below for comparison

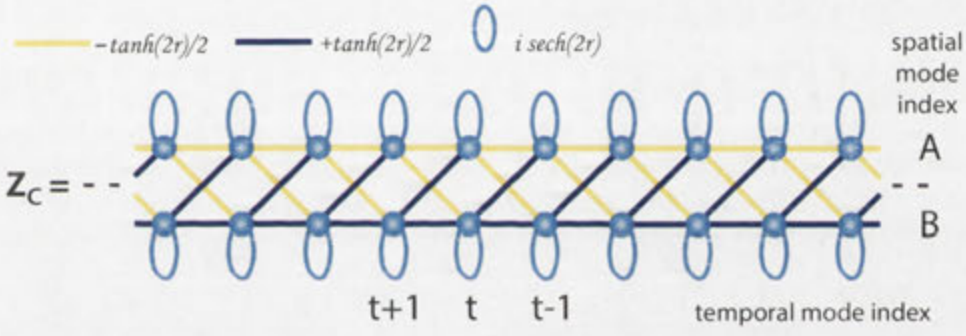

Figure 7.8: The full graph [22, 36, 37] for the CV cluster state. This graph is obtained by phase shifting both spatial modes in every other time index of the extended EPR state, where r is the initial squeezing parameter of the squeezed states emitted by the OPO. The blue (yellow) edges have positive- (negative-) real weight $\pm\frac{1}{2}\tanh 2r$, and the light blue self-loops have positive-imaginary weight $i\operatorname{sech} 2r$.

Given that the dual-rail EPR-graph state is equivalent up to phase shifts to the cluster state, one might imagine that state preparation and measurement of both states are of comparable difficulty. They are not. The dual-rail EPR-graph state is experimentally a lot simpler to generate for two reasons. First, the phase locks are not straightforward for the cluster state. This is treated in section 7.4.2. Second, and more importantly, the measurement scheme for state verification is greatly simplified for the dual-rail EPR-graph state. We can simply measure all of the qumodes in both rails in the same quadrature, so that we only need 2 measurement runs (all in $\hat{x}$, then all in $\hat{p}$) per measurement of the entire state, similar to a 2-mode EPR state. Of course, we must then repeat these 2 measurement runs thousands of times in order to gain statistics. In contrast, measuring a cluster state would require many more measurements as neighbouring modes will be in a different quadrature, and so different combinations must be measured. Further, this requires high speed (MHz∽GHz) switching of the local oscillator phase, which imposes another non-trivial technical demand to the setup.

[2]See section 8.7 for a detailed treatment on how to generate both the dual-rail EPR-graph state and a cluster state with linear optics, differing only by Fourier transforms on half of the modes.

[3]Note that explicit expressions for both $\mathbf{Z}_E$ and $\mathbf{Z}_C$ were derived by Nicolas Menicucci and appear in the supplementary material of [37].

Structure of the dual-rail EPR-Graph state

We consider the dual-rail EPR-graph state to be one possible extension of EPR states to an ultra-large basis. This follows from the nullifiers being composed of either position or momentum eigenvectors, familiar from the EPR formalism. Indeed, we see that the familiar 2-mode EPR state can be derived from this formalism. When we restrict the graph $\mathbf{G}$ to contain only 2 modes, we get

$$\mathbf{G} = \begin{pmatrix} 0 & 1 \\ 1 & 0 \end{pmatrix}. \tag{7.16}$$

We then get the following:

$$\begin{pmatrix} \hat{x}_1 \\ \hat{x}_2 \end{pmatrix} - \mathbf{G}\begin{pmatrix} \hat{x}_1 \\ \hat{x}_2 \end{pmatrix} |G_{EPR}\rangle \longmapsto \begin{pmatrix} \hat{x}_1 \\ \hat{x}_2 \end{pmatrix} - \begin{pmatrix} 0 & 1 \\ 1 & 0 \end{pmatrix}\begin{pmatrix} \hat{x}_1 \\ \hat{x}_2 \end{pmatrix} |EPR\rangle, \tag{7.17}$$

$$\begin{pmatrix} \hat{p}_1 \\ \hat{p}_2 \end{pmatrix} + \mathbf{G}\begin{pmatrix} \hat{p}_1 \\ \hat{p}_2 \end{pmatrix} |G_{EPR}\rangle \longmapsto \begin{pmatrix} \hat{p}_1 \\ \hat{p}_2 \end{pmatrix} + \begin{pmatrix} 0 & 1 \\ 1 & 0 \end{pmatrix}\begin{pmatrix} \hat{p}_1 \\ \hat{p}_2 \end{pmatrix} |EPR\rangle, \tag{7.18}$$

which gives the following nullifiers:

$$\{\hat{x}_1 - \hat{x}_2,\ \hat{p}_1 + \hat{p}_2\}, \quad \{\hat{x}_2 - \hat{x}_1,\ \hat{p}_2 + \hat{p}_1\} \tag{7.19}$$

that correspond to the familiar 2-mode EPR state. See section 2.6.3 for a treatment on nullifiers.

The graph $\mathbf{G}$ that describes the dual-rail EPR-graph state of arbitrary length can be written in matrix form explicitly as:

$$\mathbf{G} = \begin{pmatrix}
0 & g_{in} & -g_{in} & 0 & 0 & 0 & 0 & \cdots & 0 & 0 & 0 \\
g_{in} & 0 & 0 & g_c & -g_c & 0 & 0 & \cdots & 0 & 0 & 0 \\
-g_{in} & 0 & 0 & g_c & -g_c & 0 & 0 & \cdots & 0 & 0 & 0 \\
0 & g_c & g_c & 0 & 0 & g_c & -g_c & \cdots & 0 & 0 & 0 \\
0 & -g_c & -g_c & 0 & 0 & g_c & -g_c & \cdots & 0 & 0 & 0 \\
0 & 0 & 0 & g_c & g_c & 0 & 0 & \cdots & 0 & 0 & 0 \\
0 & 0 & 0 & -g_c & -g_c & 0 & 0 & \cdots & 0 & 0 & 0 \\
\vdots & \vdots & \vdots & \vdots & \vdots & \vdots & \vdots & \ddots & \vdots & \vdots & \vdots \\
\vdots & \vdots & \vdots & \vdots & \vdots & \vdots & \vdots & \ddots & \vdots & \vdots & \vdots \\
0 & 0 & 0 & 0 & 0 & 0 & 0 & \cdots & 0 & 0 & g_{out} \\
0 & 0 & 0 & 0 & 0 & 0 & 0 & \cdots & 0 & 0 & g_{out} \\
0 & 0 & 0 & 0 & 0 & 0 & 0 & \cdots & g_{out} & g_{out} & 0
\end{pmatrix} \tag{7.20}$$

where we have introduced the edge weights g_{in} and g_{out} corresponding to the end nodes of the graph for considerations of using finite-length dual-rail EPR-graph states experimentally. $g_{in} = g_{out} = \frac{1}{\sqrt{2}}$ and $g_c = \frac{1}{2}$ for an arbitrarily large state, derived by Heisenberg evolutions of the linear optics circuit describing our experimental setup, see Fig. 7.6. The matrix $\mathbf{G}$ is of dimension $n \times n$, where n is the number of modes in the graph state. The graph is given below in Fig. 7.9:

From equations 7.14 and 7.20 we arrive at the approximate nullifiers that describe the dual-rail EPR-graph state. The smallest nullifiers contain 4 modes each. We will look at a more intuitive set of nullifiers first, and see that they are comprised of the 4-mode nullifiers.
We see from the graph that any mode in the dual-rail EPR-graph state, in either rail, is connected by edges to 4 neighbouring modes. We denote the top rail with an A, and the bottom rail with a B. If we select an arbitrary mode in rail A at time t, and also an arbitrary mode in rail B at time t, we can view the section of the graph that is relevant to these modes only, by observing the two sub-graphs shown in Fig. 7.10.

From Fig. 7.10 we can obtain the relevant expressions for the nullifiers by the following method.

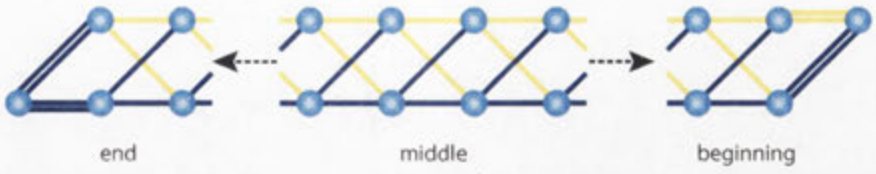

Figure 7.9: Graphical representation of entire graph state G. The graph can be separated into 3 sections. The yellow links indicate a negative weighting. The blue links indicate a positive weighting. The value of the weight depends on how many links there are with other modes. Here, a single link denotes a weighting of $\frac{1}{2}$, while a double link denotes a weighting of $\frac{1}{\sqrt{2}}$. There are no imaginary weighted self loops as this is an unphysical and ideal graph in the limit of $r \to \infty$.

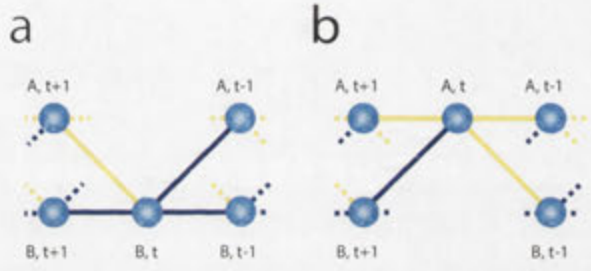

Figure 7.10: Sub-graphs for the dual-rail EPR-graph state. Each mode is graphically connected to 4 other modes in adjacent temporal locations; the pair in the future, and the pair in the past. Only the complete edges from the perspective of modes at time t are drawn. The other edges are indicated by dashed lines.

derived from equations 7.14 and 7.20. From the perspective of mode $\{A,T\}$, the links to neighbouring modes give the edge weights corresponding to the terms in the linear combinations of quadrature operators that will form the nullifier. From equation 7.14 we observe a difference between the $\hat{x}$ quadrature nullifiers and the $\hat{p}$ quadrature nullifiers is a negative sign. This leads to the following rule for determining the nullifier from a sub-graph. For the $\hat{x}$ quadrature, a yellow link indicates a positive weighting with respect to the linear combination of the two modes it connects. And for the $\hat{p}$ quadrature, a yellow link indicates a negative weighting with respect to the linear combination of the two modes it connects. Accordingly, for the $\hat{x}$ quadrature, a blue link indicates a negative weighting with respect to the linear combination of the two modes it connects, and for the $\hat{p}$ quadrature, a blue link indicates a positive weighting with respect to the linear combination of the two modes it connects. Following these rules, we arrive at the following nullifiers:

$$\{\hat{x}_t^A - \frac{1}{2}(\hat{x}_{t+1}^B - \hat{x}_{t+1}^A - \hat{x}_{t-1}^B - \hat{x}_{t-1}^A), \quad \hat{p}_t^A + \frac{1}{2}(\hat{p}_{t+1}^B - \hat{p}_{t+1}^A - \hat{p}_{t-1}^B - \hat{p}_{t-1}^A)\}, \tag{7.21}$$

$$\{\hat{x}_t^B - \frac{1}{2}(\hat{x}_{t-1}^A + \hat{x}_{t-1}^B - \hat{x}_{t+1}^A + \hat{x}_{t+1}^B), \quad \hat{p}_t^B + \frac{1}{2}(\hat{p}_{t-1}^A + \hat{p}_{t-1}^B - \hat{p}_{t+1}^A + \hat{p}_{t+1}^B)\}. \tag{7.22}$$

We can view the 5-mode sub-graphs as the combination of opposite facing 4-mode sub-graphs. Linear combinations of nullifiers are themselves nullifiers. From this we see that the links between rails A and B at the same temporal index will cancel when the opposite-facing nullifiers are combined, due to the difference in sign while having the same weight.

From Fig. 7.11 we see that there are 4 nullifiers for each quadrature that can be constructed that each contain 4 modes. If we view the 4 nullifiers as comprising a square, then each nullifier will be from the viewpoint of a different corner node in the square. When reading the nullifiers from

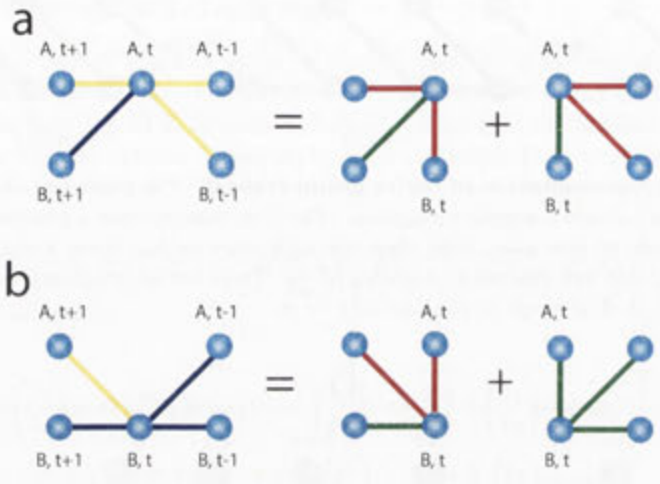

Figure 7.11: Linear combinations of sub-graphs. Each 5-mode sub-graph is a linear combination of two 4-mode sub-graphs. All edges omitted except for those connected to modes at time t. Blue (yellow) edge weights have positive- (negative-) real weights $\pm\frac{1}{2}$, while green (red) edge weights have positive- (negative-) real weights ± 1.

the 4-mode graphs, we must follow the following rules. For the $\hat{x}$ quadrature, a red link indicates a positive weighting with respect to the linear combination of the two modes it connects, and a green link indicates a negative weighting with respect to the linear combination of the two modes it connects. For the $\hat{p}$ quadrature, a red link indicates a negative weighting with respect to the linear combination of the two modes it connects in adjacent temporal positions, and a green link indicates a positive weighting with respect to the linear combination of the two modes it connects in adjacent temporal positions. For the $\hat{p}$ quadrature, when the link is between two modes in the same temporal position (between rails A and B), a red link indicates a positive weighting, and a green link indicates a negative weighting. Following these rules, we arrive at the following nullifiers:

$$\{\hat{x}_t^A + \hat{x}_t^B + \hat{x}_{t+1}^A - \hat{x}_{t+1}^B,\ \hat{p}_t^A + \hat{p}_t^B - \hat{p}_{t+1}^A + \hat{p}_{t+1}^B\}, \tag{7.23}$$

$$\{\hat{x}_t^A - \hat{x}_t^B + \hat{x}_{t-1}^A + \hat{x}_{t-1}^B,\ \hat{p}_t^A - \hat{p}_t^B - \hat{p}_{t-1}^A - \hat{p}_{t-1}^B\}, \tag{7.24}$$

$$\{\hat{x}_t^B + \hat{x}_t^A + \hat{x}_{t+1}^A - \hat{x}_{t+1}^B,\ \hat{p}_t^B + \hat{p}_t^A - \hat{p}_{t+1}^A + \hat{p}_{t+1}^B\}, \tag{7.25}$$

$$\{\hat{x}_t^B - \hat{x}_t^A - \hat{x}_{t-1}^A - \hat{x}_{t-1}^B,\ \hat{p}_t^B - \hat{p}_t^A + \hat{p}_{t-1}^A + \hat{p}_{t-1}^B\}. \tag{7.26}$$

Derivation of graph

We can build up the graph **G** from a series of 2-mode EPR pairs in order to understand the final graph structure.

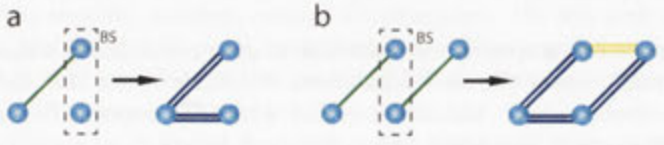

Figure 7.12: Distribution of edge weights after a beam-splitter operation. The green links denote unity strength edge weights. Upon interaction on a balanced beam-splitter (denoted by dashed box with BS label) the edges are distributed to become weights of $\pm\frac{1}{\sqrt{2}}$.

Figure 7.12(a) considers 1 EPR pair mixing on a beam-splitter with 1 qumode. We see that the edge weight is distributed between the independent qumode and the *other* mode in the EPR pair. This might seem counter-intuitive at first, as one might expect the two modes that interact on the beam-splitter to form an edge between them. A clear mind will realise however, that as one half of an EPR pair is a thermal mode, upon a beam-splitter interaction with another thermal mode no direct correlations can form between them. The re-distribution of the edge link (and corresponding weakening of the edge weighting) is the consequence of the mixing.
The 8-mode graph state, which is the smallest size of graph **G** that allows us to see each section of the graph structure properly, is arrived at by mixing together the 4-mode graphs derived in Fig. 7.12. Shown in Fig. 7.13, the edge links are again re-distributed so that the middle section of the dual-rail EPR-graph state has edge links of strength $\pm\frac{1}{2}$.

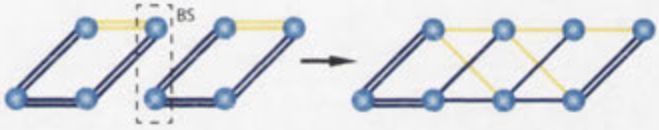

Figure 7.13: The dual-rail EPR-graph state G from sub-graphs. Upon interaction on a balanced beam-splitter (denoted by dashed box with BS label) the edge links in the sub-graphs are distributed to become weights of $\pm\frac{1}{2}$.

Heisenberg evolutions that lead to dual-rail EPR-graph

We now derive the dual-rail EPR-graph state via Heisenberg evolutions of the complex amplitudes. This will lead to expressions for the variances of these nullifiers due to finite squeezing.

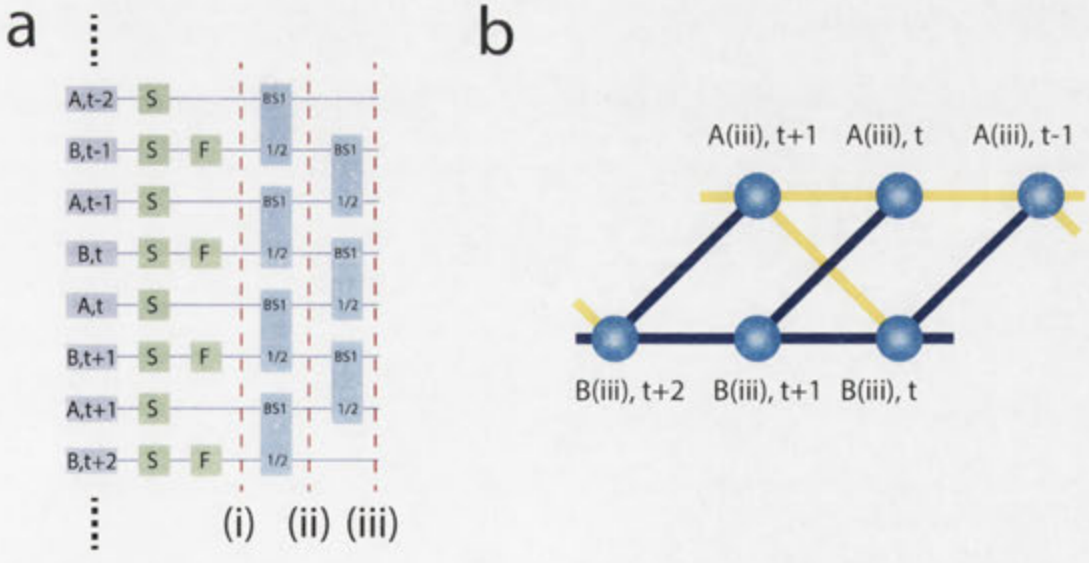

Figure 7.14: Linear optics network for the generation of dual-rail EPR-graph state. (a) Small section of the linear optics network. S: squeezing operation, F: Fourier transform, BS1: beam-splitter operation. (b) The resulting sub-graph corresponding to the dual-rail EPR-graph state.

The qumodes in step (i) of the evolution have had the squeezing operator acted on them, as can be seen in Fig. 7.14 (a). The squeezing operation is given by $S(r) = \left(\begin{smallmatrix} e^r & 0 \\ 0 & e^{-r} \end{smallmatrix}\right)$, and as all inputs

to the circuit are initially vacuua, the figure represents offline squeezing. The Fourier transform is given as $F = \left(\begin{smallmatrix} 0 & -1 \\ 1 & 0 \end{smallmatrix}\right)$. Both operations act on the column vector $\left(\begin{smallmatrix} \hat{x} \\ \hat{p} \end{smallmatrix}\right)$ containing the quadrature operators in the Heisenberg picture. Qumodes in rail B have undergone Fourier transforms so that the complex amplitudes $\hat{a}_t^{A(\mathrm{i})}$ and $\hat{a}_t^{B(\mathrm{i})}$ of the initial state in step (i) are represented as

$$\text{(i)} \qquad \hat{a}_t^{A(\mathrm{i})} = \mathrm{e}^{r_A}\hat{x}_t^{A(0)} + i\,\mathrm{e}^{-r_A}\hat{p}_t^{A(0)}, \qquad \hat{a}_t^{B(\mathrm{i})} = \mathrm{e}^{-r_B}\hat{x}_t^{B(0)} + i\,\mathrm{e}^{r_B}\hat{p}_t^{B(0)}, \tag{7.27}$$

where $\mathrm{e}^{-r_B}\hat{x}_t^{B(0)}$ and $\mathrm{e}^{-r_A}\hat{p}_t^{A(0)}$ are the squeezed quadratures of the squeezed state at temporal location t in the spatial location B and A, respectively. We have the following mean values and variances:

$$\langle \hat{x}_t^{A(0)} \rangle = \langle \hat{p}_t^{A(0)} \rangle = \langle \hat{x}_t^{B(0)} \rangle = \langle \hat{p}_t^{B(0)} \rangle = 0, \tag{7.28}$$

$$\langle (\hat{x}_t^{A(0)})^2 \rangle = \langle (\hat{p}_t^{A(0)})^2 \rangle = \langle (\hat{x}_t^{B(0)})^2 \rangle = \langle (\hat{p}_t^{B(0)})^2 \rangle = \frac{1}{4}. \tag{7.29}$$

After combining the qumodes through the action of a beam-splitter they become

$$\text{(ii)} \qquad \begin{pmatrix} \hat{a}_t^{A(\mathrm{ii})} \\ \hat{a}_{t+1}^{B(\mathrm{ii})} \end{pmatrix} = \hat{B}^{\dagger}_{A(t),B(t+1)} \begin{pmatrix} \hat{a}_t^{A(\mathrm{i})} \\ \hat{a}_{t+1}^{B(\mathrm{i})} \end{pmatrix} \hat{B}_{A(t),B(t+1)} = \frac{1}{\sqrt{2}} \begin{pmatrix} -1 & 1 \\ 1 & 1 \end{pmatrix} \begin{pmatrix} \hat{a}_t^{A(\mathrm{i})} \\ \hat{a}_{t+1}^{B(\mathrm{i})} \end{pmatrix}. \tag{7.30}$$

$$\text{(ii)} \qquad \begin{pmatrix} \hat{a}_{t-1}^{A(\mathrm{ii})} \\ \hat{a}_t^{B(\mathrm{ii})} \end{pmatrix} = \hat{B}^{\dagger}_{A(t-1),B(t)} \begin{pmatrix} \hat{a}_{t-1}^{A(\mathrm{i})} \\ \hat{a}_t^{B(\mathrm{i})} \end{pmatrix} \hat{B}_{A(t-1),B(t)} = \frac{1}{\sqrt{2}} \begin{pmatrix} -1 & 1 \\ 1 & 1 \end{pmatrix} \begin{pmatrix} \hat{a}_{(t-1)}^{A(\mathrm{i})} \\ \hat{a}_t^{B(\mathrm{i})} \end{pmatrix}. \tag{7.31}$$

At this stage in the experimental circuit there is an optical delay line on rail B, as shown in Fig. 7.6. The result is to stagger the EPR pairs as shown graphically in Fig. 7.14(b). The qumodes are unchanged, and we see that when we mix the pairs on the last beam-splitter the temporal indices are now matching. The final complex amplitudes of the output state are given as:

$$\begin{aligned} \text{(iii)} \qquad \begin{pmatrix} \hat{a}_t^{B(\mathrm{iii})} \\ \hat{a}_t^{A(\mathrm{iii})} \end{pmatrix} &= \hat{B}^{\dagger}_{B(t),A(t)} \begin{pmatrix} \hat{a}_t^{B(\mathrm{ii})} \\ \hat{a}_t^{A(\mathrm{ii})} \end{pmatrix} \hat{B}_{B(t),A(t)} = \frac{1}{\sqrt{2}} \begin{pmatrix} -1 & 1 \\ 1 & 1 \end{pmatrix} \begin{pmatrix} \hat{a}_t^{B(\mathrm{ii})} \\ \hat{a}_t^{A(\mathrm{ii})} \end{pmatrix} \\ &= \frac{1}{2} \begin{pmatrix} \hat{a}_t^{B(\mathrm{i})} - \hat{a}_t^{A(\mathrm{i})} + \hat{a}_{t+1}^{B(\mathrm{i})} - \hat{a}_{t-1}^{A(\mathrm{i})} \\ \hat{a}_t^{B(\mathrm{i})} - \hat{a}_t^{A(\mathrm{i})} + \hat{a}_{t+1}^{B(\mathrm{i})} + \hat{a}_{t-1}^{A(\mathrm{i})} \end{pmatrix}. \end{aligned} \tag{7.32}$$

Re-labelling the complex amplitudes as $\hat{a}_t^A = \hat{a}_t^{A(\mathrm{iii})}$ and $\hat{a}_t^B = \hat{a}_t^{B(\mathrm{iii})}$, this allows us to extract the following ideal nullifiers of the extended EPR state:

$$\hat{x}_t^A + \hat{x}_t^B + \hat{x}_{t+1}^A - \hat{x}_{t+1}^B = 2\,\mathrm{e}^{-r_B}\hat{x}_{t+1}^{B(0)}, \tag{7.33}$$

$$\hat{p}_t^A + \hat{p}_t^B - \hat{p}_{t+1}^A + \hat{p}_{t+1}^B = 2\,\mathrm{e}^{-r_A}\hat{p}_t^{A(0)}. \tag{7.34}$$

Therefore, we can calculate the nullifier variances which determine the theoretical bound of the inseparability criterion [74],

$$\langle (\hat{x}_t^A + \hat{x}_t^B - \hat{x}_{t+1}^B + \hat{x}_{t+1}^A)^2 \rangle = \mathrm{e}^{-2r_B} < \frac{1}{2}, \tag{7.35}$$

$$\text{and} \quad \langle (\hat{p}_t^A + \hat{p}_t^B + \hat{p}_{t+1}^B - \hat{p}_{t+1}^A)^2 \rangle = \mathrm{e}^{-2r_A} < \frac{1}{2}. \tag{7.36}$$

This shows that the sufficient condition for inseparability is satisfied when the squeezing levels of each OPO is greater than -3 dB, measured after propagation through the circuit.

Effect of beam-splitter phase on graph

As described in the section 3.2, when modelling a beam-splitter there are four possibilities of where to impart the π phase shift due to there being four ports. This results in four possibilities of linear optics networks that concatenate these beam-splitters, leading to four possibilities of edge weight polarities, as shown in Fig. 7.15.

Figure 7.15: Polarity of edge weights as function of beam-splitter phase. There are four possible configurations of the polarities of the edge weights in graph **G** depending on which port of the beam-splitter sees the π phase shift.

Networks employing $B^{(1)}$ correspond to (a), $B^{(2)}$ to (b), $B^{(3)}$ to (c), and $B^{(4)}$ to (d). The four expressions for the beam-splitter are given below as:

$$B^{(1)}(\sqrt{r}) = \begin{pmatrix} -\sqrt{r} & \sqrt{t} \\ \sqrt{r} & \sqrt{t} \end{pmatrix}, \qquad B^{(2)}(\sqrt{r}) = \begin{pmatrix} \sqrt{r} & -\sqrt{t} \\ \sqrt{r} & \sqrt{t} \end{pmatrix}, \tag{7.37}$$

$$B^{(3)}(\sqrt{r}) = \begin{pmatrix} \sqrt{r} & \sqrt{t} \\ -\sqrt{r} & \sqrt{t} \end{pmatrix}, \qquad B^{(4)}(\sqrt{r}) = \begin{pmatrix} \sqrt{r} & \sqrt{t} \\ \sqrt{r} & -\sqrt{t} \end{pmatrix}. \tag{7.38}$$

Experimentally it won't always be possible to correctly predict where the phase shift has been imparted, and the best strategy is to apply the different nullifiers to the measured data. For this reason it is extremely important to design a flexible data acquisition and measurement infrastructure.

7.3 Experimental details

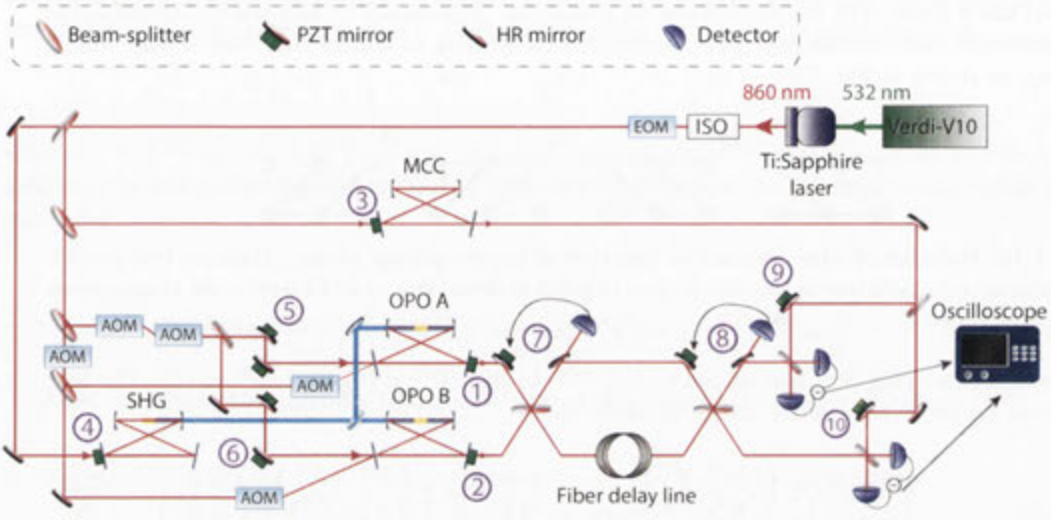

Figure 7.16: Experimental schematic for the generation of ultra-large-scale cluster states. OPO: optical parametric oscillator; EOM: electro-optic modulator; ISO: Faraday optical isolator; AOM: acousto-optic modulator; MCC: mode cleaning cavity; PZT: piezo-electric transducer; SHG: second-harmonic generation.

The light source used for this experiment is a continuous-wave Titanium:Sapphire laser (SolsTiS-SRX, from M Squared Lasers) operating at 860 nm. This laser is in turn pumped by a laser-diode-pumped and frequency doubled Nd:YVO_4 laser (Verdi V-10 from Coherent) operating at 532 nm. A 10 W beam from the pump laser results in a 1.9 W beam output from the Titanium:Sapphire laser. As can be seen in Fig. 7.16 the fundamental beam at 860 nm output from the laser is passed through an optical isolator (ISO; FI850-5SV, from Linos) and an electro-optic-modulator (EOM; PM25, from Linos) that imparts phase modulation of 16.5 MHz which will be used for locking the four cavities on resonance by employing the Pound-Drever-Hall (PDH) technique. The four cavities are as follows:

- **Second harmonic generation (SHG) cavity:** Used to generate a strong beam at the second harmonic frequency, corresponding to a wavelength of 430 nm. This will be used to pump the two optical parametric oscillators.
- **2 × Optical parametric Oscillators (OPOs):** Used to generate squeezed light.
- **Mode cleaning cavity:** Used to generate a reference beam termed the local oscillator for homodyne detection.

7.3.1 Optical parametric oscillators

Squeezed light is generated by parametric down conversion, utilising optical parametric oscillators (OPOs). The light generated is in a squeezed vacuum state, due to the omission of a seed beam, in contrast with the optical parametric amplifiers (OPAs) detailed in sections 5.2.1 and 6.4.1. The OPO and OPA are conceptually very similar devices. The OPO employed here is also type I (both photons in down-converted pair in the same polarisation) operated under threshold, and employs a quasi-phase matched periodically poled $KTiOPO_4$ (PPKTP) non-linear crystal similar to the OPAs detailed in other chapters.

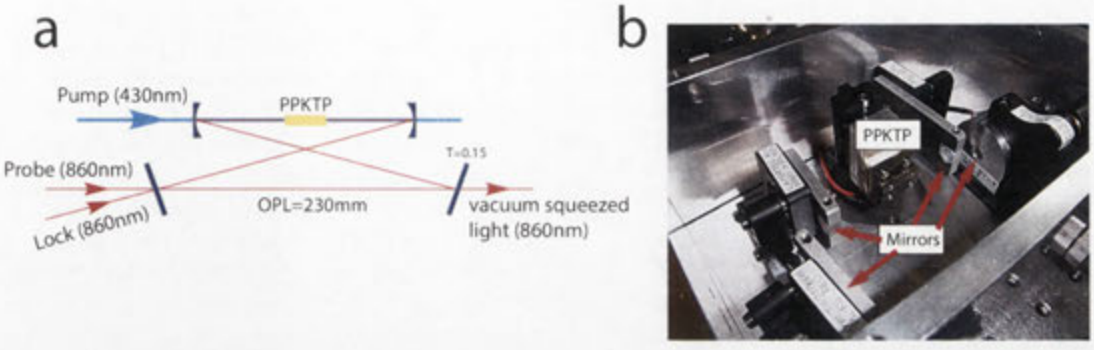

Figure 7.17: Optical parametric oscillators (OPOs) used or generating squeezed wave-packet modes. The optical beam path is relatively short (230 mm), leading to a broad linewidth ($\approx$ 33 MHz). This leads to qumode temporal lengths of 160 ns. This is the time separation needed to ensure the orthogonality of qumodes. (a) Experimental schematic of OPO. (b) Photograph of actual OPO.

Even though the qumodes here are wave-packet modes, as described in section 7.1.2, the generation of continuous-wave squeezed light follows the same physical process from the descriptions in sections 5.2.1 and 6.4.1 where the qumode is a sideband-mode. The sideband modes are still present, and could be used, but we define the qumodes to be wave-packet modes for the temporal lengths to be shorter, as described in section 7.1.2. The difference here is not in the generation of the qumodes, but rather the method of measurement and data analysis performed, as we will see.
Two OPOs were built from scratch for the present experiment. The reason we did not want to use the OPOs used in previous experimental setups in the same lab (those used in the cluster state experiments of chapters 9 and 10) is that the optical path lengths (OPLs) were not the shortest they could be, which means the squeezing bandwidths were not as large as they could be. Intuitively, a larger bandwidth equates to a larger amount of information, which also equates to larger levels of squeezing that can be recovered. Perhaps more importantly, it also translates to a smaller temporal length over which the wave-packet is defined.
Typical OPOs employed at the Furusawa laboratory have an OPL of around 500 mm. The newly designed OPOs were made to be relatively compact, with OPLs of 230 mm. With the transmission coefficient of the output couplers 0.149 and 0.154, respectively, the full width at half maximum (FWHM) values for the OPOs are 33.7 MHz and 33.8 MHz respectively.

Cavity	OPL	T	FWHM	FSR	finesse	intra-cavity loss
OPO A	230 mm	0.149	33.7 MHz	1.3 GHz	38	0.41%
OPO B	230 mm	0.154	33.8 MHz	1.3 GHz	38	0.30%

Table 7.1: Cavity parameters of optical parametric oscillators used to generate squeezed light.

The two OPOs used for the temporal-mode experiment are identical in design and manufacture. Each OPO has three inputs, as shown in Fig. 7.17. They are described below.

1) **The Pump beam** (430 nm; Blue) is used to facilitate parametric down conversion. It does this by pumping the 10mm long non-linear crystal (PPKTP) within the cavity. In a loss-less scanario, there will be one blue photon (of frequency 2ω) entering the crystal, and two infra-red photons (each of frequency ω) exiting the crystal. The optical power of this beam was around $100mW$.

2) **The Lock beam** (860 nm; Infra-red) is used in order to precisely and actively control the

optical path length of the cavity, and to hold it (lock) it on resonance. This is done by employing the phase modulation of 16.5 MHz from the EOM directly after the isolator in Fig. 7.16 and employing PDH phase locking. As we do not want the lock beam to interfere with the probe beam, the beam profile of the lock beam is modified in order to create a spatially orthogonal mode before propagating it in the reverse direction to both the pump and probe beams. A glass plate is placed in its beam path before it enters the cavity so that the mode is converted to a TEM_{01} mode. Now as the TEM_{00} and TEM_{01} modes will resonate at different frequencies, an acousto-optic modulator (AOM)[4] is used to tune the frequency of the TEM_{01} mode to match the resonance of the TEM_{00} mode in the cavity. In this way, the TEM_{01} mode propagating in the reverse direction does not interfere with the output squeezed vacuum TEM_{00} mode.

3) **The Probe beam** (860 *nm*; Infra-red) is used in order to lock the relative phase of the pump beam. It is phase modulated before entering the cavity (140 kHz for OPO A, 210 kHz for OPO B) and the sidebands are used to facilitate the locking of relative phases in other parts of the optical setup. During the measurement phase, the power is set to around $10\,\mu W$ in order to generate vacuum squeezing.

3.5) There is also an **alignment beam** that is used to align the cavity during the initial construction. It is reverse seeded, and is also used to generate blue light (430 *nm*) in a second harmonic generation configuration. This blue light will be travelling down the pump beam's optical path, but in the reverse direction, making it useful to align the optical path that couples the doubler and the OPO.

Piezo-electric transducers (PZTs) are attached to the output couplers of the OPOs in order to apply active feedback control and lock the OPOs on resonance. These are housed in custom-made housings with the mirror up tight up against a rubber O-ring in order to increase the resonance frequency of the PZT system. In this way a typical phase locking bandwidth of around 2 to 5 kHz can be increased to 30 to 40 kHz.

Parametric gain of OPO

The parametric gains of OPO A for different pump power values are tabulated in table 7.2. OPO B values are nearly identical.

Power (mW)	**25**	**50**	**75**	**100**	**125**	**150**	**175**	**200**
G_+	1.88	2.63	3.57	4.78	6.36	9.16	13.0	20.6
G_-	0.64	0.55	0.48	0.45	0.42	0.39	0.36	0.34

Table 7.2: Parametric gain of OPO A. Measurements taken by Toshiyuki Kaji.

The parametric gain region is actively controlled via the PZT on the probe beam, which controls the relative phase between the probe beam and the pump beam. This is in contrast to the OPA described in section 5.2.1 where a PZT controls the pump beam in order to lock the parametric gain.

Squeezing from the OPO

We operate both OPOs at parametric gains of 4.1, chosen after repeated runs of the experiment under different conditions. As we can see in table 7.4, a parametric gain of 4.0 is achieved at around 100 mW. This doesn't correspond to the highest level of squeezing, or even the highest purity of

[4]TEF-110-60-860, from Brimrose.

Power (mW)	25	50	75	100	125	150	175	200
Squeezing (dB)	-3.59	-4.95	-6.02	-6.20	-6.41	-7.32	-6.87	-6.29
Anti-squeezing (dB)	3.99	6.18	7.89	9.67	11.0	12.6	13.9	15.9

Table 7.3: Squeezing values of OPO A at 1 MHz sideband. Measurements taken by Toshiyuki Kaji. Uncertainties are ±0.05 dB.

the generated squeezed light. It does however correspond to the regime where the most amount of squeezing can be recovered in the measurements of the nullifiers that determine the cluster state. This is due to the trade-off between purity and highest squeezing levels, found for our case to be at parametric gains of 4.1.

Mode cleaning cavity

The mode cleaning cavity (MCC) is a bow-tie cavity, also of width an OPL of 230 mm. Unlike the OPO there is no non-linear crystal inside, and this cavity is used to spatially and spectrally filter the beam in order to create a reference beam for high efficiency mode-matching at the homodyne detectors. The input and output couplers both have transmission coefficients of 5 %, and the FWHM is 54 MHz and the finesse is 25. The interference visibilities using the local oscillator beam generated from the MCC is above 98 % for every free-space mode[5].

7.3.2 Second Harmonic Generation

A bow-tie cavity of similar design to the OPOs was constructed in order to generate a second harmonic beam, used to pump the OPOs with 430 nm light. This cavity is termed the second harmonic generation (SHG) cavity, and has an OPL of 500 mm, which is more than twice that of the OPOs. The reason for this is mechanical stability, as SHG cavities are notoriously difficult to keep on resonance when compared to regular bow-tie cavities such as mode cleaning cavities, or even OPOs. The non-linear crystal employed is a $KNbO_3$ (potassium niobate) crystal, of dimensions 10 $mm \times 3\ mm \times 3\ mm$. The input coupler has a transmission coefficient of 0.1. Almost 500 mW of pump power at 430 nm is generated. We use around 100 mW for each OPO.
There is also a reference cavity that is used in between the SHG cavity and the OPOs, in order to mode match the pump beam to the probe beam entering the OPOs.

7.3.3 Fiber delay line

To implement the temporal delay line on the bottom rail, necessary for staggering the EPR pairs so that they interact with neighbouring modes, we employ an opitcal fiber. The optical fiber employed is a polarisation maintaining SM85-PS-U40A fiber from Fujikura. To minimise the insertion loss into the fiber, we employ fiber patch cords with anti-reflection coating at 860 nm on both ends of the fiber[6]. We were able to fabricate arbitrary lengths of fiber cables by splicing the patch cords and the bare fibers together. We used single aspheric lenses with AR coatings for focusing and collimating the beam for optimal mode matching into the fiber. In order to optimise the coupling between the free space TEM_{00} mode and the LP_{01} fiber mode, we worked in collaboration with FMD Corporation to develop a fiber alignment device (FA 1000S) which is now commercially available through FMD Corporation. The average interference visibility of spatial modes before and after the delay line was 95 %. The throughput of the entire optical fiber delay line was 92 %, which is relatively very high for fiber-coupled light. As we are injecting squeezed light into the delay line it was critical that we achieved this high efficiency as any optical power loss would quickly

[5] See [91] for more details.
[6] (PMJ-3A3A-850-5/125-1-2-1-AR2, from OZ Optics)

degrade the squeezing and therefore the entanglement. The fiber was placed inside a thermally insulated box with vibration-proof padding in order to increase the stability of the phase lock, as early testing revealed that small temperature fluctuations led to devastating changes of the optical path length and therefore a very unstable phase lock. After the insulation box was installed, the performance of the phase lock improved dramatically.

7.4 Digital control of optics and electronics

A custom-made digital control suite was created for this experiment, primarily using software written using National Instruments LabVIEW as well as field-programmable-gate-arrays (FPGAs) from National Instruments. The digital control suite is treated in detail in section 4.3. Here I will focus on the performance of the control suite and the consequences for the experiment. Figure 7.18 displays a portion of the graphical user interface that was developed in order to control the various systems.

Figure 7.18: Portion of the control suite used to actively control ten optical systems.

There are ten systems that require active feed-back control:

1) **OPO A:** straightforward PDH cavity lock with DC monitor for real-time state determination.
2) **OPO B:** as above.
3) **Mode cleaning cavity:** as above.
4) **Second harmonic generation cavity:** Less straightforward cavity lock due to smaller operation window of stability. Precise determination of gain parameters is necessary.
5) **Parametric gain A:** straightforward interference lock for parametric de-amplification.
6) **Parametric gain B:** as above.
7) **EPR beam-splitter:** relative phase lock between p-squeezed and x-squeezed beams.
8) **Graph beam-splitter:** Difficult phase lock due to noisy error signal; light from the bottom rail has undergone an optical fiber delay line of 30 m leading to phase fluctuations from temperature changes.
9) **Homodyne A:** relative phase lock for local oscillator to determine measurement angle.
10) **Homodyne B:** as above.

Figure 7.16 displays the locations of each of these systems, and the piezo-electric-transducers (PZTs) that control their respective optical path lengths. Each of the ten systems will have a corresponding set of controls that will be accessible via the tab structure shown in Fig. 7.18, with the system tabs displayed on the bottom of the structure.
Each of the ten systems are controlled by nearly identical logic in the custom-made LabVIEW

modules (termed VIs). The VIs are programmed to operate in what is termed a state machine architecture. This means that there are different states that a system can be in, and ultimately which state the particular system is in will be determined by a combination of user inputs, automated logic based on real-time monitors, and the behaviour of the other systems.
Ultimately, the LabVIEW VIs will determine the precise voltage to output via high voltage amplifiers to the 10 different PZTs that precisely control the ten respective systems. In the state machine architecture of the VIs, each system can be acted on by one of 4 states:

Figure 7.19: The 4 possible states of each system. Each system exists in one of these states at any instant.

1) Safe: Output 0 voltages and falsify all booleans. Basically, do nothing.
2) Hold: Pause the output voltage and hold the system constant until further notice.
3) Scan: Apply a variable saw-tooth wave voltage in order to scan the system's optical path length.
4) Lock: Apply a PII controller on the error signal and implement a phase lock on the system.

Each system can have its state changed at a rate of up to 500 kHZ. The "Safe" state is included primarily for debugging uses. When new logic is being tested, it is very useful to have a safety option that is accessed via a kill switch in case the control system takes on any unexpected behaviours. The "Scan" and "Lock" states are used in tandem; optimal regions of the error signal are found first by scanning the relative beam path and when a user-defined threshold is passed, the system will enter the "lock" state. The "Hold" state is extremely powerful and provides a very stable constant voltage for the duration of its state. This is very difficult to achieve with analogue electronics, as capacitors will necessarily have a finite discharge time, for example. Further, in analogue electronics it is difficult to design a system that will immediately return to the previous mode of operation after a hold period, as integrator values from the PI controller will no longer be optimal.

7.4.1 Sample and hold

A keen reader may have spotted a potential impediment to the performance of our experiment from the details provided so far. We have defined our qumodes to be wave-packet modes that have a broadband profile in frequency space. And yet we are employing phase modulation for PDH locking, that will degrade the measured squeezing in the wave-packet mode due to the large phase noise. This is indeed a non-trivial problem. In order to apply some sort of feedback control, as well as being able to measure the wave-packet modes without phase modulation noise peaks, we designed a control system that has an inherent compromise. In a technique known as "sample and hold", we sample the feedback signal and apply active feedback control for a certain time, then switch off all control and hold the present value constant while measurements are taken.

There are numerous electronic devices that require being switched between two states in order to facilitate phase-modulation-free measurement. For this reason we generate four TTL signals from the same digital control suite that provides phase locking for the ten optical systems. The controls for these TTL signals can be seen on the right panel of Fig. 7.18 and the synchronised timing is displayed in Fig. 7.20. The programming logic that generates and synchronises the TTL signals can be found in the VI detailed in section 4.3.4.

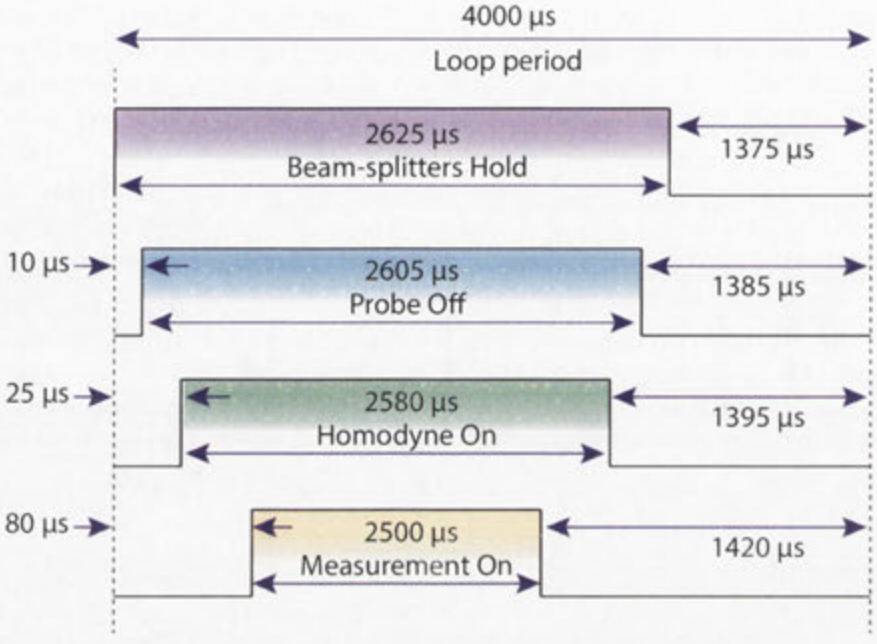

Figure 7.20: Synchronised timing of FPGA generated trigger signals. Four TTL signals are generated and exit the FPGA card in order to switch on and off various electronic systems.

We see from Fig. 7.20 that the loop period is 4000 μ seconds, with a duty cycle of 62.5% biased towards the measurement phase. The first thing to happen at the start of the cycle is that all of the ten optical systems are put on hold. This is denoted via the "Beam-splitters Hold" TTL signal, which is placed in the ON state for 2625 μ seconds. This TTL is generated on board of one of the two FPGA cards used for the ten systems, and is sent as a digital trigger through a PXI trigger line which can operate at rates of up to 40 MHz. This is an efficient method of synchronising VIs across different FPGA cards in a network, or even between different while loops in the same VI[7]. For the duration of the "Beam-splitters Hold" signal in the ON state, all of the ten systems are in the "Hold" state, with all integrator values being held constant.
After a safety buffer of 10 μ seconds, the "Probe Off" TTL signal is switched to an ON state. This TTL is sent to various analogue switches[8] that are placed in circuits that drive EOMs and AOMs. In all cases, the switches are placed before amplifiers as shown in Fig. 7.21.

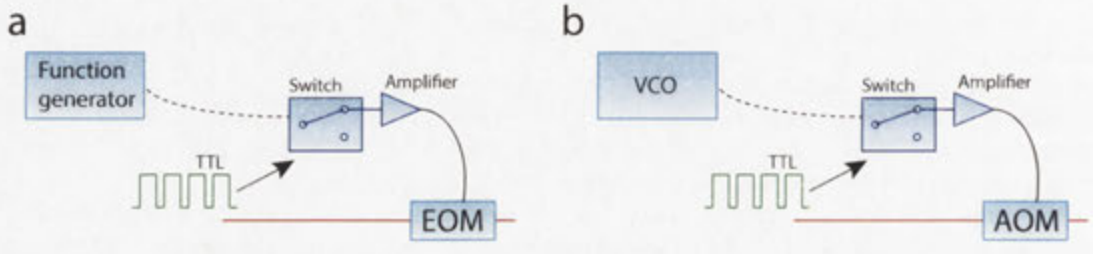

Figure 7.21: Switching signals that drive various electronics via TTL signals. (a) an electro-optic-modulator (EOM) is switched on and off. (b) an acousto-optic-modulator (AOM) is switched on and off. VCO; voltage controlled oscillator.

[7]Another option would be to employ a local or global variable, but I recommend avoiding this due to possible race conditions
[8]High Isolation Switch, ZASWA-2-50DR+, from Mini-Circuits)

We employ AOMs[9] as optical switches. As can be seen in Fig. 7.16, two AOMs are used in sequence to switch the probe beam on and off (system 5 and system 6, for OPO A and OPO B, respectively). AOMs are built around a crystal where a standing sound wave is generated with two electrodes from an oscillating electrical signal. The sound wave induces spatial modulations of the refractive index of the crystal, which in turn induces Brillouin scattering of the incoming light and interference effects occur that are similar to Bragg diffraction. Scattered photons are shifted in frequency, and this can be used to engineer fast light switches, up to tens of MHz.
As the ten optical systems remain in the "Hold" state, the lack of an error signal (in turn due to the lack of phase modulation from the probe beam) is not a problem, and the PII controller will simply pick up where it left off when the control phase is activated again. 25 μ seconds after the start of the cycle, and 15 μ seconds after the both the probe beam and the EOM have been switched off, the "Homodyne On" phase is turned to the ON state. The relevant TTL signal that is sent to the homodyne detection circuit causes a switch to be placed to the ON state when the TTL is in the ON state, and this allows the homodyne current to be sent to the data acquisition system, via the relevant electronics (a series of low pass filters and amplifiers). This is done in order to protect the circuit from unwanted phase modulation that might saturate the circuit when the feedback control is in the ON state.
After waiting a further 55 μ seconds from when the homodyne circuit has been switched on (80 μ seconds from the beginning of the cycle) the TTL that is sent to the data acquisition system is turned to the ON state, which initiates the acquisition of data. This is done via a high-speed oscilloscope with custom-written acquisition software[10]. We use a Tektronix DPO7054 digitizer operating at 200 M samples per second to record the two signals from Homodyne A and Homodyne B. The quantum efficiencies of our homodyne detectors are above 99 %, and the bandwidths are above 20 MHz. The local oscillator powers are set to 10 mW for every homodyne measurement.

7.4.2 Phase control of interferometer

The optical circuit between the outputs of the OPOs and the homodyne detection stage may be viewed as a Mach-Zehnder interferometer (MZI) with asymmetric arm lengths. The asymmetry in path lengths is intentional of course, and is due to the optical fiber delay line in the bottom rail.

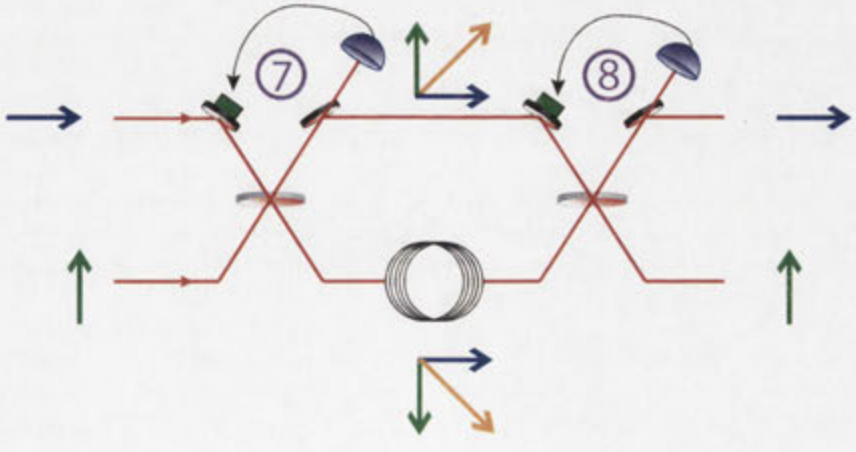

Figure 7.22: Phase modulation through a Mach-Zehnder interferometer. The blue and green arrows represent orthogonal phase modulations on carrier beams.

[9] AOM 3080-125
[10] The acquisition software was written in Visual Basic by Ryuji Ukai and appears in reference [87].

Phase modulation on respective carrier beams are represented by coloured arrows in the depiction of the MZI in Fig. 7.22. We see that in this configuration the relative phase between the respective carriers is $\frac{\pi}{2}$ at the output of the MZI, facilitating a straightforward generation of an error signal used for phase locking. Note that if one arm experienced a Fourier transform, as in the original proposal by Menicucci [36], the carriers would be in phase and it would be a non-trivial issue to engineer the correct phase lock. This technical issue was one of two impediments that led us to generate dual-rail EPR-graph states, rather than strictly phase correct cluster states.

7.5 Results

As is common procedure with these experiments, after the generation of the experimental setup, we conducted measurement runs and fine tuning of the system for roughly two months. When the experimental setup began producing reliable and repeatable results, we performed the final run of the experiment and conducted data acquisition in a controlled and unchanging setting for roughly six hours. In order to completely characterise the dual-rail EPR-graph state, we repeatedly take measurements in three regimes. First, we set both local oscillators to the $\hat{x}$ quadrature and measure all of the $\hat{x}$ nullifiers that comprise the dual-rail EPR-graph state. Second, we set both local oscillators to the $\hat{p}$ quadrature and measure all of the $\hat{p}$ nullifiers that comprise the dual-rail EPR-graph state. Third, we take shot noise measurements by blocking the signal beam in order to have a reference.

- We recorded 8400 oscilloscope frames of data for the $\hat{x}$ quadrature measurements, and 10800 frames of data for the $\hat{p}$ quadrature measurements.
- Each frame contains 500,000 data points, which was sampled at 200 MHz to measure 2500 μs worth of data, corresponding to data at 5 ns increments.
- Our temporal modes have a temporal width T of 160 ns, corresponding to 32 data points per mode.
- We have therefore measured $2500\mu s \div 160\ ns = 15625$ wave-packet modes in each of the two rails.

7.5.1 Temporal mode function

The repeated measurement runs allowed us to fine tune the temporal mode filter each time in order to produce the optimal temporal mode function for our experiment. The procedure was as follows: read in 300 frames of shot noise measurements, read in 300 frames of $\hat{x}$ measurements, apply the temporal mode filter to both data sets, normalise the $\hat{x}$ traces to shot noise, apply the relevant nullifier on each mode, and output the mean variance over the entire dual-rail EPR-graph state from the 300 frames.

This led to the optimum filter described in section 7.1.2, which has a Gaussian profile $f(t) \propto e^{-(\Gamma t)^2}$, of bandwidth $\Gamma = 2\pi \times 2.75$ MHz ($1/\Gamma \sim 58\ ns$). T is 160 ns, and due to unequal cable lengths in the homodyne to data acquisition circuits, optimal nullifier variances are found when the two channels are shifted one sample point (5 ns) with respect to each other. This is equivalent to phase shifting one mode roughly 3% with respect to the other mode (5 ns with respect to the 160 ns temporal width). Figure 7.23 shows the 32-element discretised temporal mode function integrating over homodyne photo-current.

Temporal modes exiting OPO A were measured before entering the MZI in order to characterise their squeezing levels. After applying the temporal mode function displayed in Fig. 7.23, squeezing and anti-squeezing values were measured for a varying pump power, and are tabulated in table 7.4.

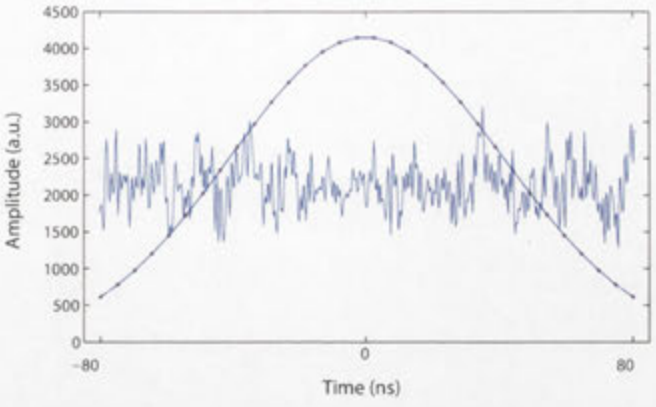

Figure 7.23: Temporal mode function. The homodyne photo-current was integrated over this mode function to produce the measurement of one temporal mode.

Power (mW)	25	50	75	100	125	150	175	200
Squeezing (dB)	-3.60	-4.67	-5.39	-6.14	-6.43	-6.53	-6.60	-6.16
Anti-squeezing (dB)	3.90	6.16	7.82	9.26	10.7	12.2	13.3	14.9

Table 7.4: Squeezing values of OPO A for wave-packet modes. Measurements taken by Toshiyuki Kaji. Uncertainties are ±0.05 dB.

As we can see from table 7.4, the recovered squeezing level is comparable to that of the 1 MHz sideband mode, as displayed in table 7.3.

7.5.2 Measuring the dual-rail EPR-graph state

As detailed in section 7.4.1, the data acquisition is triggered by the "Measurement ON" TTL pulse when it is in the ON state. Within the digital control suite there are monitors that are compared against user-defined thresholds. This logic is automated such that if any of the crucial phase locks are misbehaving or operating outside of the specified window of operation, the "Measurement ON" TTL will remain in the OFF state until everything has been resolved. Importantly, once the stability has been deemed suitable, and the "Measurement ON" TTL has been switched to the ON state, no matter how the system behaves during the measurement, the frame worth of data that is measured is deemed a faithful representation of the dual-rail EPR-graph state. This is to ensure that there is no cherry picking of the data, and no post-selection.
Expanding on this idea, it is then equivalent to perform measurements on each cycle of the "Sample and Hold" routine, and then post-process the data in order to set a similar threshold. Of course, stringent care must be taken to ensure the validity of this process. We therefore set some important rules:

1. A measurement run is deemed unsuitable and will be discarded if and only if the experimental setup was not in its usual conditions at the beginning of the measurement run.

2. If the experimental setup is in a representative state and a measurement run has begun, the frame's worth of data will be kept and included in the statistical analysis.

Ultimately, our technique was to set a relaxed threshold during measurement, and then to set a slightly more precise threshold during data analysis. Figure 7.24 displays the measurements of 100 frames worth of data, plotted in terms of the variances of each temporal mode's nullifier.

This data has been temporally filtered, normalised to shot noise, and had nullifiers applied to each temporal mode, before the variances were plotted. The horizontal axis corresponds to 2500 μ seconds of data, plotted here in terms of the temporal-mode position of each wave-packet mode in the dual-rail EPR-graph state.

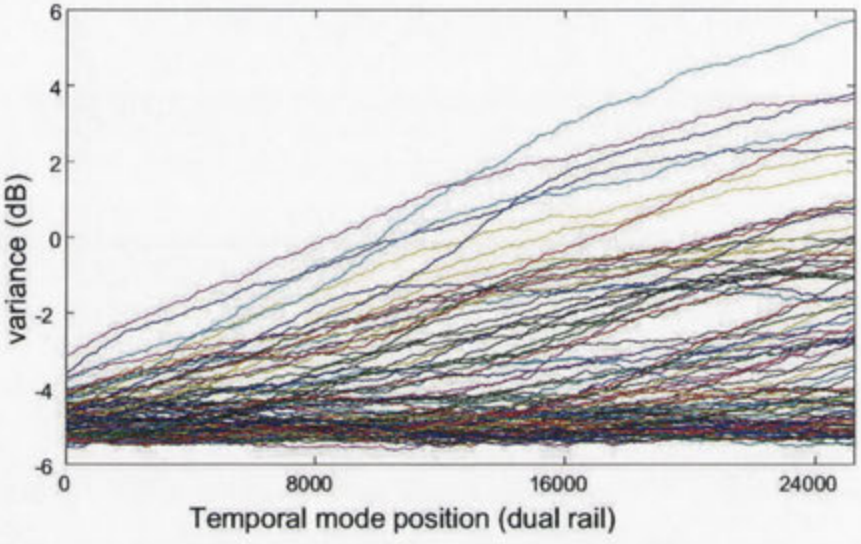

Figure 7.24: Evolutions in phase space of individual dual-rail EPR-graph states. The nullifier variances of 100 dual-rail EPR-graph states are shown to evolve based on their starting value. Each coloured trace represents the measurement of an individual dual-rail EPR-graph state.

The nullifier expression applied to each temporal mode is given as:

$$\{\hat{x}_t^B + \hat{x}_t^A + \hat{x}_{t+1}^A - \hat{x}_{t+1}^B\}, \tag{7.39}$$

see section 7.2 for the derivation of the nullifier. There is qualitatively a lot that can be learnt from the evolutions in phase space of the individual measurements of the dual-rail EPR-graph state, shown in Fig. 7.24. Note that in order to measure the variance of an individual frame, we could not average over the other frames, and so a horizontal moving window of 1200 data points was used. The underlying assumption is that during 1200 data points (6 μ seconds) the change in phase space is minimal.

We notice that no trace begins above a nullifier variance of -3dB. This is due to the relaxed thresholds imposed during the TTL logic. We also notice that this threshold is not precise enough, and is indicative of the experimental setup not being returned to its usual mode of operation. Remember that before each measurement run begins, the phase locks have been placed on hold for 2625 μ seconds (see Fig. 7.20) and have had 1375 μ seconds to return the experiment to its usual state. Every so often this process does not work, and the experiment is not returned to its usual state. This is the case when the nullifier variances of the first 100 temporal modes or so have low values, close to -3 dB. In this case, we see that indeed these traces evolve rapidly in phase space and wave-packet modes towards the end of the dual-rail EPR-graph state (around temporal mode positions of 24,000) will have nullifier variances as large as positive 3 dB.

We also see that when the dual-rail EPR-graph state begins with a very low nullifier variance, the entire state will remain at a similar level for the duration of the measurement. However, we are not allowed to select just the traces that remain in optimal states, as this would be cherry picking the data, and would not be a fair representation of the experiment that we performed. Taking into account the two conditions imposed on whether or not to discard data, we set another threshold

of -4.7 dB which was calculated to be below the mean variance of the dual-rail EPR-graph state nullifiers in their usual state of operation. While Fig. 7.24 shows only 100 traces, the calculation of this threshold was conducted by analysing 8400 traces. Our final data set comprises of 4270 frames for $\hat{x}$ quadrature measurements and 4191 frames for $\hat{p}$ quadrature measurements.

7.5.3 Correlations in quadrature measurements

We first take a qualitative look at how the nullifiers manifest as correlations between quadrature amplitudes. Shown in Fig. 7.25 are $\hat{x}$ quadrature measurements of various temporal modes. Subfigure(a) displays 30 quadrature amplitudes of the wave-packet mode $\hat{x}_t^A$ as it propagates 30 temporal positions. The quadrature amplitudes are randomly distributed around the mean, as we expect. Subfigures (b),(c),(d), and (e) display the quadrature measurements of wave-packet modes $\hat{x}_{t+1}^A$, $\hat{x}_{t-1}^A$, $\hat{x}_{t+1}^B$, and $\hat{x}_{t-1}^B$, respectively, all in red, with the measurements of $\hat{x}_t^A$ shown in blue for comparison. We see that there are no correlations between these modes individually, which reveals the entanglement structure of the dual-rail EPR-graph state. This is in fact why the entire dual-rail EPR-graph state is robust to local measurements, as is a fundamental property of cluster states[11].

The patterns in subfigures (b) and (c) of Fig. 7.25 arise because we are observing 30 successive wave-packet modes and comparing them to 30 successive wave-packet modes in adjacent temporal positions. Consequently, we arise at the red trace being time shifted in the forwards and backwards directions with respect to the blue trace, in subfigures (b) and (c), respectively. What is relevant here, and what we must compare are the quadrature measurements between two wave-packet modes at any one instant in time. Stated another way, we must compare the amplitudes of the blue and red data points at each temporal position. When this is done it is evident that there are no correlations in amplitude between any two wave-packet modes.
Figure 7.25(f) displays the linear combination of the wave-packet modes shown in subfigures (b),(c),(d),(e) in red, and we see a remarkable fit between this linear combination and the wave-packet mode $\hat{x}_t^A$. The linear combination is precisely the nullifier, shown next to subfigure (f). This shows that although each wave-packet mode is entangled to its neighbours, in order to properly make use of the correlations, the entire nullifier must be measured. This is a key feature of the dual-rail EPR-graph states, and cluster states in general. Measurements in the $\hat{p}$ quadrature reveal identical features with the appropriate nullifier.

7.5.4 Parametric plots of EPR-like correlations in nullifiers

Here, we take a qualitative look at how the correlations manifest for the nullifiers at different temporal positions. Whereas Fig. 7.25 displayed evidence of correlations within one nullifier for 30 temporal positions, in order to quantify the correlations we must fix the temporal mode position and compare the 4000 frames worth of measurement data. As a first step, we parametrically plot different linear combinations that comprise different nullifiers in order to visualise the correlations.

Figure 7.26 shows the wave-packet mode $\hat{x}_t^A$ parametrically plotted against the linear combination of $\hat{x}_{t+1}^B - \hat{x}_{t+1}^A - \hat{x}_{t-1}^B - \hat{x}_{t-1}^A$ for two different temporal positions, $t = 1$ and $t = 15600$. Perfect correlations would be represented by a straight line on the diagonal. Any broadening is a result of finite squeezing, and therefore imperfect correlations. Both temporal positions display strong correlations, and it is clear that the correlations are stronger at $t = 1$ due to the measurements being made closer to when the active feedback control of the circuit was in the ON state.

[11] Recall that the dual-rail EPR-graph state is equivalent to the cluster state up to local phase.

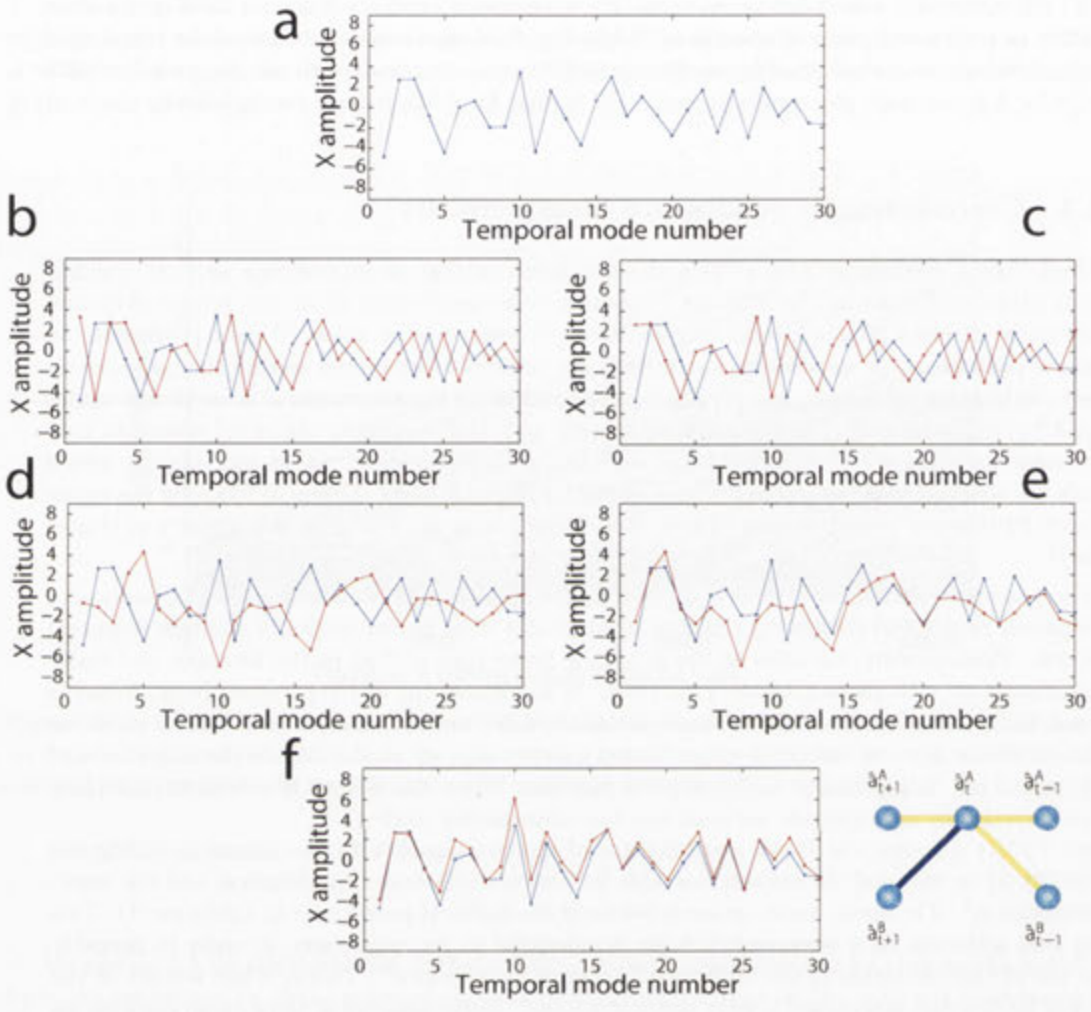

Figure 7.25: Quadrature correlations in $\hat{x}$. All figures show amplitudes of wave-packet mode $\hat{x}_t^A$ in blue. The following wave-packet modes are shown in red: (b) $\hat{x}_{t+1}^A$, (c) $\hat{x}_{t-1}^A$, (d) $\hat{x}_{t+1}^B$, (e) $\hat{x}_{t-1}^B$. (f) Nullifier expression $\hat{x}_{t-1}^A + \hat{x}_{t-1}^B - \hat{x}_{t+1}^A + \hat{x}_{t+1}^B$ shown in red.

7.5.5 Phase space evolutions of dual-rail EPR-graph states

In order to quantify the correlations, and therefore the entanglement present in the dual-rail EPR-graph state, we must measure the variances of the relevant nullifiers at each temporal mode position and compare this to the threshold presented in equations 7.35. The wave-packet modes that have nullifier variances below the quantum threshold will collectively form the dual-rail EPR-graph state. Figure 7.27 shows the complete evolution in phase space of the dual-rail EPR-graph state, as told through the nullifier variances of each wave-packet mode in the state.

During the measurement time the ten optical systems described in section 7.4 drift from their optimal settings due to the lack of active feedback control. The cavities drift slightly off resonance, and the relative phases at the beam-splitters drift from their optimal values. The net result is that the dual-rail EPR-graph state will evolve in phase space so that each successive nullifier will have a degraded variance, as is evident in Fig. 7.27. The rate at which the nullifier variances degrade is indicative of the stability of our entire setup.

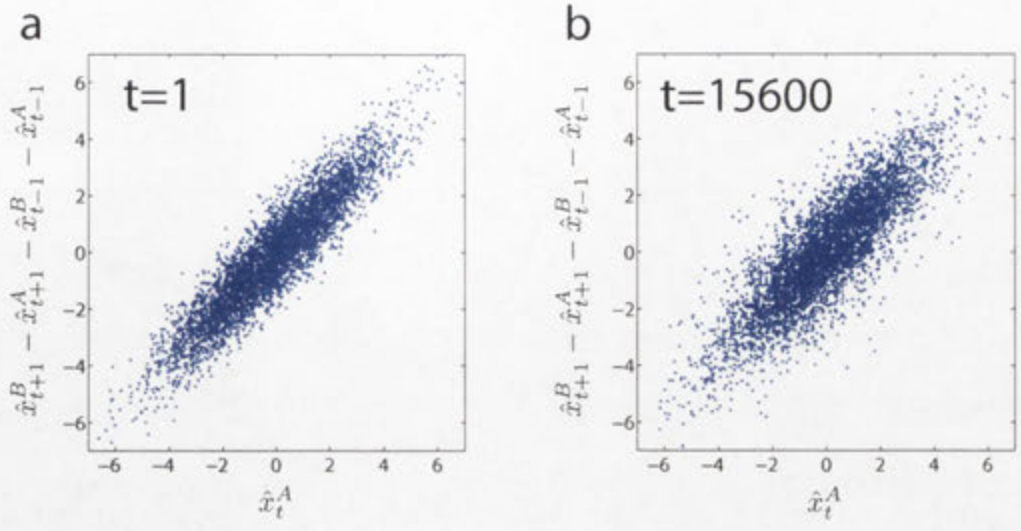

Figure 7.26: Parametric Plots of 5-mode nullifiers. (a) temporal position $t = 1$, (b) temporal position $t = 15622$.

We see that the wave-packet modes up to a temporal position of around 12,000 have associated nullifier variances below the inseparability threshold of -3 dB. As there are two modes per temporal mode position due to the dual-rail structure, this demonstrates that up to 24,000 wave-packet modes are entangled and form the dual-rail EPR-graph state[12].

7.6 Conclusions and outlook

We have presented the experimental demonstration of the largest entangled state created to date[13]. This was done by multiplexing wave-packet modes of light in the time domain, following a theoretical proposal [36].
The entangled state is so large that quantifying exactly how many modes there are is almost to miss the point. The breakthrough here is the demonstration that this technique of multiplexing in the time domain is successful, and the only reason why the entanglement degrades is a technical one, related to our control scheme.

7.6.1 The Group

The five researchers who performed this experiment are shown in the photograph of Fig. 7.28. This was taken in the lab on the day of the final measurement run on a snowy winter's day in February, 2013, at the Furusawa Laboratory at University of Tokyo.

Team members who contributed to this research project, but who are not in the photo of Fig. 7.28 are: Shigenari Suzuki, Jun-ichi Yoshikawa, Hidehiro Yonezawa, Nicolas Menicucci, and Akira Furusawa.

[12] In reference [92] we present results of "more than 10,000 entangled modes". In order to avoid confusion we presented conservative results, where the nullifier variances were averaged over a random sample of measurements, even including measurement runs that were not phase locked correctly. This was done in order to pre-emptively avoid any discussions of post-selection that might be misconstrued.

[13] As of January 2014, this was the largest entangled state by three orders of magnitude. The previous record was the 14 qubits prepared in Rainer Blatt's laboratory in Innsbruck using trapped ions [21].

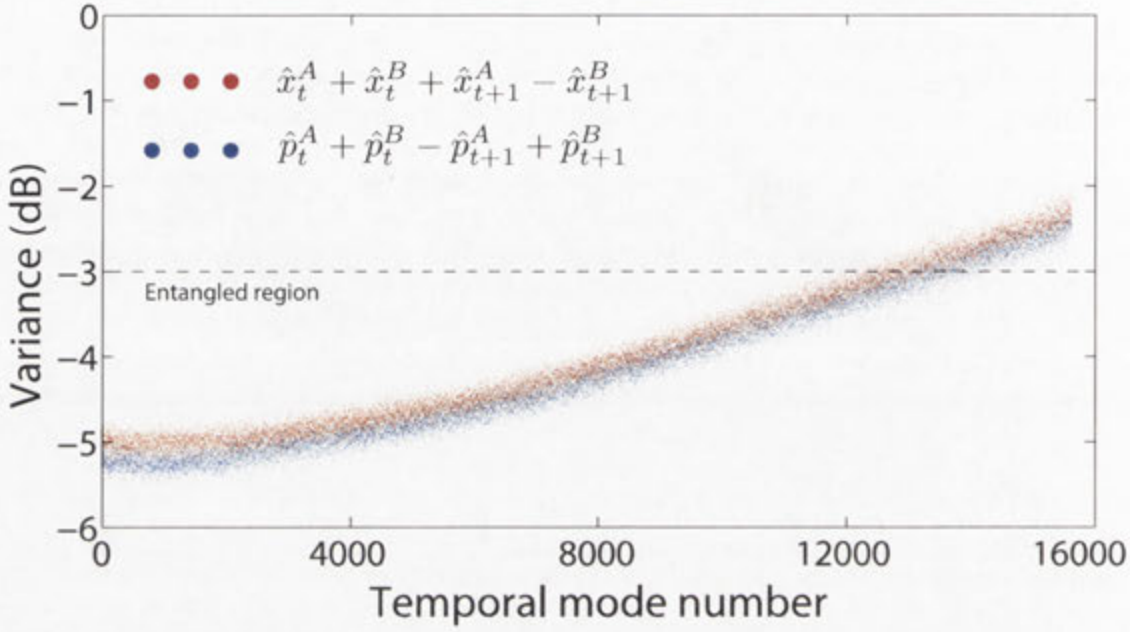

Figure 7.27: Phase evolution of entire dual-rail EPR-graph state. Shown in the red are the measured $\hat{x}$ quadrature nullifier variances, and shown in the blue are the measured $\hat{p}$ quadrature nullifier variances. The bound of separability is -3 dB denoted by the dashed line.

7.6.2 Outlook

There is a lot more than can be said about the generation of the entangled state presented in this chapter. For the sake of brevity, I list here some thoughts in the form of an outlook.

- **Rate of entanglement generation:** Entangled states created in this way will become so large that a better figure of merit than the sheer size of the entangled state would be the rate at which the entanglement can be created. Here, every 160 ns we have two more wave-packets that are entangled to the dual-rail EPR-graph state. This gives us a rate of entanglement generation of 12.5 MHz. Remarkably this is deterministic, and therefore a constant rate. This constant rate cannot be achieved by current techniques in the discrete-variables optics community, as their rate of single photon generation is probabilistic and the success rate of entanglement generation diminishes quickly as the entangled state grows larger.

- **Quantum computing with this resource state:** The dual-rail EPR-graph state is a resource for universal quantum computing. This is not a new discovery, and in fact the original proposal that this experiment is based upon [36] provides proof of this. What constitutes a small discovery is the formulation of an efficient scheme for quantum computing with the dual-rail EPR-graph state, which improves on the technique suggested in reference [36]. This is presented in section 8.7.

- **Only limited propagation through cluster currently possible:** It should be stated clearly that it is still an open problem to overcome the effects of finite squeezing introducing noise into the state during teleportations. With current technology (and present-day squeezing resources), we would only be able to use a small fraction of the 20,000 dual-rail cluster state for the use of teleportaion-based quantum computing. After only around twenty measurement and feed-forward steps the fidelity of further teleportations would not be above

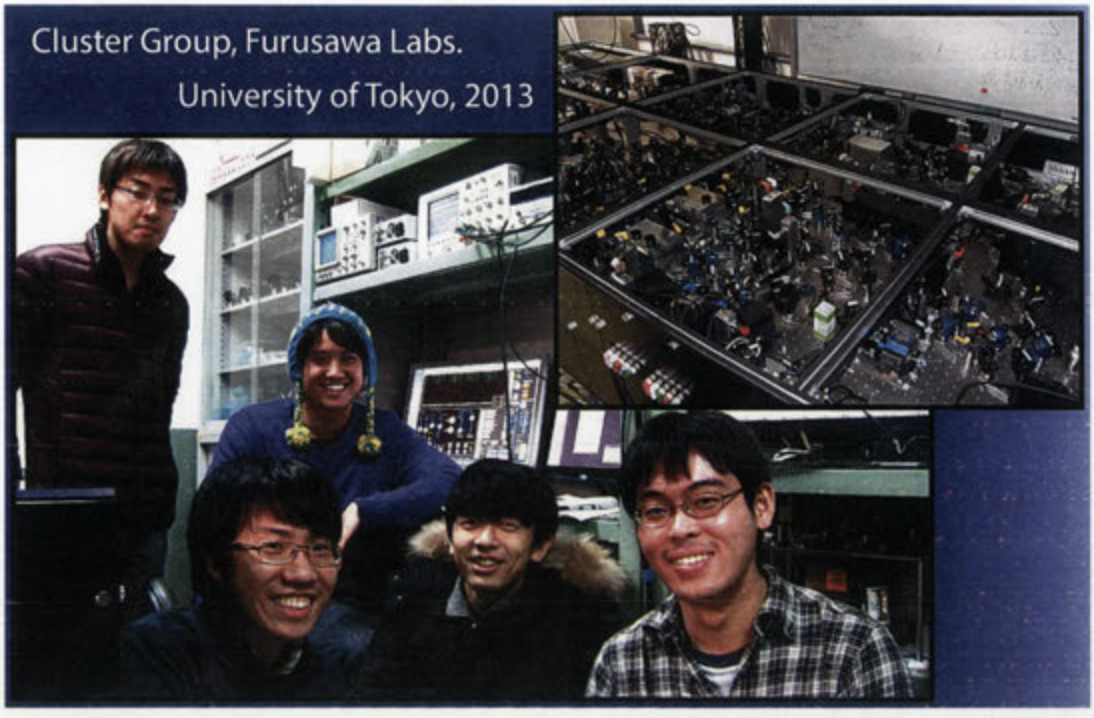

Figure 7.28: Cluster Group, University of Tokyo, February 2013. From left to right: Shota Yokoyama, Chanond Wise, Seiji Armstrong, Toshiyuki Kaji, Ryuji Ukai.

the classical limit of 0.5, and we would have lost the quantum information. This is a severe limitation of the cluster state made with present-day finite squeezing levels with no efficient error correction schemes. See for example [93] for a thorough technical treatment of the noise analysis for using the dual-rail cluster state for quantum computing.

- **Error correction:** I have said nothing about error correction, which is sorely needed for any feasible implementation of quantum computing with the dual-rail EPR-graph state as a resource. Menicucci has recently formulated a fault-tolerant scheme for quantum computing with cluster states that is not yet feasible with current technology but opens the door to improving the error threshold [94].

- **Extending to another dimension for more inputs and outputs:** In order for the dual-rail EPR-graph state to be useful for large-scale fault-tolerant quantum computing, the dimensionality must be increased. This can be done by creating a copy of the state and mixing the two together on two more beam-spltiters, as shown explicitly in [36].

Part III

Quantum computation with continuous-variable cluster states

Overview

Information is physical. In fact, information is quantum physical. The manipulation of information via the effects of quantum mechanics is the premise of quantum information science. The quantum effects that facilitate the computation are mainly entanglement, and interference.

David Deutsch offered the first formulation of quantum information in 1985 [15] when he proposed the first quantum algorithm; an algorithm that offered a modest speed-up over its classical counterpart when testing the fairness of a coin in one flip. The two prominent examples of quantum algorithms that offer substantial speed up over classical algorithms are Shor's algorithm for factoring large numbers [95] and Grover's algorithm for searching elements in a database [96]. While there have been elegant proof of principle demonstrations in various atomic, ionic, and photonic architectures, no experiment has yet outperformed their classical counterpart in terms of efficiency. The next decade will see this record broken. We are now at a stage technologically where demonstrations of quantum simulators in the next 10 years will outperform what is possible with classical computation.

Our own demonstrations of quantum information protocols are modest, and can be efficiently simulated on classical computers. They are, however, absolutely necessary within their own formulation of measurement-based quantum computing, and form the building blocks for what is to come in terms of a multimode universal quantum computer. In chapter 8 we review cluster state computation with continuous variables (CV). This differs from the original circuit-model by being a measurement based protocol. Whereas the standard model (in discrete variables) relies on sequences of quantum logic gates that process qubits, the one-way model implements computations as a sequence of measurements on an array of highly entangled qubits; the array is the so-called cluster state. A cluster state is first created as a generic resource, and the algorithms to be computed are determined by the choice and sequence of measurements, allowing us to imprint a circuit in real time as the flow of information is directed through the cluster. While chapter 8 is largely a review chapter, section 8.7 presents original research which is a modest extension of the excellent research being conducted at the Furusawa Laboratories at the University of Tokyo.

In order to simulate any desired Hamiltonian, no matter the complexity, one follows a recipe made by decomposing the Hamiltonian into a concatenation of less complex gates [97]. Importantly, in the context of CV cluster state computing, any such recipe will include no more than single-mode Gaussian gates, two-mode gates, and non-Gaussian gates. In chapter 9 we briefly describe an experiment that demonstrates universality within the one-mode Gaussian operations [98]. The resource state used was a four-mode linear cluster state, the smallest cluster that offers sufficient degrees of freedom for one-mode Gaussian universality [99]. Chapter 10 then details a tuneable entangling gate, which is a robust example of a mutlimode gate. This gate provides entanglement of tuneable strength between any two modes it acts on, in the given cluster. We demonstrate this by coupling two independent vacuum states to a three-mode cluster, and verify that after computation the output was an entangled two-mode state. The entanglement from the resource cluster, in the form of a tuneable C_z gate, is teleported onto the two input modes. The entanglement strength was entirely tuneable and can even be set to zero so that the output state is not entangled, but has no additional noise. This is important for considerations of error correction and offers control over the flow of information avoiding noisy channels in the cluster.

The toolbox we have created allows for universal multimode operations within a Gaussian setting. We are now missing just one final operation, that of a non-Gaussian nature, and we will have a universal set of gates for performing universal quantum computing. There is still much that is needed to be done before a fully fault-tolerant and large-scale quantum computer can be constructed in this regime, yet there is reason for optimism. The theoretical framework exists [32, 77, 99, 97, 94], and experimental demonstrations such as those presented in chapters 9, and 10 are paving the way for progress in this direction.

Chapter 8

Theoretical overview of quantum computing with cluster states

At the turn of the century measurement-based quantum computing was proposed. Conceptually very different from the circuit model that was originally proposed for quantum information protocols, the measurement-based approach uses as its resource a highly entangled state called a cluster state. Information and logic gates are then teleported and manipulated through the cluster, dictated by the choice of measurements.
This chapter provides a brief review of Gaussian quantum computations using cluster states in the continuous-variables (CV) regime. For a comprehensive treatment, the reader is encouraged to pursue references [75, 24, 77, 100]. Section 8.7 details original research investigated in collaboration with Ryuji Ukai at the University of Tokyo, and is a modest extension of Ukai's previous research this time applied to the context of the dual-rail EPR-graph states explored in chapter 7. We show that the dual-rail EPR-graph state is a resource for universal quantum computing, and provide an efficient scheme for one-way quantum computing with the dual-rail EPR-graph state.

The research presented in section 8.7 appears in the following journal publications:

- S. Yokoyama, R. Ukai, S. Armstrong, C. Sornphitphatphong, T. Kaji, S. Suzuki, J-I. Yoshikawa, H. Yonezawa, N. Menicucci, A. Furusawa. *Ultra-large-scale continuous-variable cluster states multiplexed in the time domain.* Nature Photonics (Supplementary Material) **7**, 982-986 (2013).

- R. N. Alexander, S. Armstrong, R. Ukai, N. C. Menicucci. *Noise analysis of single-qumode Gaussian operations using continuous-variable cluster states.* arXiv:1311.3538, (2013).

8.1 Brief introduction to quantum computing

Quantum information processing is the arbitrary manipulation of quantum states. Formulations of quantum computing began appearing in 1985 pioneered by Richard Feynman and more rigorously by David Deutsch. Deutsch's formulation seems to have been motivated by the possibility of refuting explanations of reality not consistent with the many worlds theorem. Peter Shor [95] and Lov Grover [96] introduced important quantum algorithms in the mid 1990s that would spark a worldwide interest in quantum information processing. The quantum speed-up offered by their respective algorithms are tabulated below.

	Classical	Quantum
Shor's algorithm	$e^{L^{\frac{1}{3}}}$	L^3
Grover's algorithm	$\mathcal{O}(N)$	$\mathcal{O}(N^{\frac{1}{2}})$

Table 8.1: Quantum speedup offered by two prominent algorithms. Shor's algorithm runs in polynomial time to factor a large number L, while the best known classical algorithm works in sub-exponential time [101]. Grover's algorithm takes on the order of $N^{\frac{1}{2}}$ steps to search a database of N records, compared to an order of N steps with a classical algorithm.

Since then we have seen applications in quantum key distribution (QKD) leading to commercially available technologies [102, 103], demonstrations of modest quantum simulations of physical systems [104, 105, 106], and fruitful investigations into error correction and fault-tolerance for various quantum computing architectures[1] [108].

8.2 Continuous-variable cluster state computing

Measurement-based-quantum-computation (MBQC) is one such possible way to process quantum information, attractive due its relative ease of use once a suitable resource state has been prepared. The resource is defined to be a cluster state, comprised of an array of nodes in a graph that are entangled with each other. The measurement of a node will affect the remaining nodes in the graph, which is the fundamental feature of entanglement. By selecting suitable measurement bases and providing appropriate classical corrections, it is possible to implement an arbitrary operation on the quantum state. To date, multimode Gaussian operations have been demonstrated on CV cluster states. While this is not sufficient for universal quantum computing, the theoretical framework for universality exists and this includes fault-tolerance [94], scalable optical architectures [36, 37, 68] and non-Gaussian implementations [77, 97, 75].
We begin our discussion with a treatment on the important set of Gaussian operations.

8.3 Gaussian operations

Gaussian transformations are represented by Gaussian unitary operations that act on a Gaussian state and return a Gaussian state. They are the most experimentally feasible transformations in CV quantum optics, as they can be implemented reliably and deterministically. They form a necessary but not sufficient set of gates for universal quantum computing.

8.3.1 Gaussian states

In section 2.5 we introduced Gaussian states as those having a Gaussian-shaped Wigner function. We extend the discussion here by introducing the covariance matrices of the most common Gaussian states, before exploring Gaussian transformations.
One-mode vacuum states and coherent states have the following covariance matrix:

$$\mathbf{\Gamma}_{|0\rangle,|\alpha\rangle} = \begin{pmatrix} 1 & 0 \\ 0 & 1 \end{pmatrix} = \mathbf{I}, \tag{8.1}$$

[1] Although error correction is beyond the scope of this thesis, its importance is duly noted, and as Deutsch himself remarked: "error correction is the beginning of infinity" [107]. Further, it is interesting epistemologically that Shor's algorithm was formulated before the existence of a known error correction scheme.

and in general the covariance matrix of a an N-mode coherent state is the $2N \times 2N$ identity matrix.
A one-mode squeezed state with squeezing parameter r has the following covariance matrix:

$$\mathbf{\Gamma}_{|r\to 0\rangle}(r) = \begin{pmatrix} \mathrm{e}^{-2r} & 0 \\ 0 & \mathrm{e}^{2r} \end{pmatrix}. \tag{8.2}$$

The two-mode squeezed state, which asymptotes to the ideal Einstein-Podolsky-Rosen (EPR) state in the limit of infinite squeezing is described by the following covariance matrix:

$$\mathbf{\Gamma}_{|EPR\rangle}(r) = \begin{pmatrix} \cosh(2r) & 0 & \sinh(2r) & 0 \\ 0 & \cosh(2s) & 0 & -\sinh(2r) \\ \sinh(2r) & 0 & \cosh(2r) & 0 \\ 0 & -\sinh(2r) & 0 & \cosh(2r) \end{pmatrix}. \tag{8.3}$$

In general, any bi-partite Gaussian state has the following covariance matrix:

$$\mathbf{\Gamma}_{|\psi\rangle} = \begin{pmatrix} \langle \Delta^2 \hat{x}_1 \rangle & \frac{1}{2}\langle \hat{x}_1\hat{p}_1 + \hat{p}_1\hat{x}_1 \rangle & \frac{1}{2}\langle \hat{x}_1\hat{x}_2 + \hat{x}_2\hat{x}_1 \rangle & \frac{1}{2}\langle \hat{x}_1\hat{p}_2 + \hat{p}_2\hat{x}_1 \rangle \\ \frac{1}{2}\langle \hat{p}_1\hat{x}_1 + \hat{x}_1\hat{p}_1 \rangle & \langle \Delta^2 \hat{p}_1 \rangle & \frac{1}{2}\langle \hat{p}_1\hat{x}_2 + \hat{x}_2\hat{p}_1 \rangle & \frac{1}{2}\langle \hat{p}_1\hat{p}_2 + \hat{p}_2\hat{p}_1 \rangle \\ \frac{1}{2}\langle \hat{x}_2\hat{x}_1 + \hat{x}_1\hat{x}_2 \rangle & \frac{1}{2}\langle \hat{x}_2\hat{p}_1 + \hat{p}_1\hat{x}_2 \rangle & \langle \Delta^2 \hat{x}_2 \rangle & \frac{1}{2}\langle \hat{x}_2\hat{p}_2 + \hat{p}_2\hat{x}_2 \rangle \\ \frac{1}{2}\langle \hat{p}_2\hat{x}_1 + \hat{x}_1\hat{p}_2 \rangle & \frac{1}{2}\langle \hat{p}_2\hat{p}_1 + \hat{p}_1\hat{p}_2 \rangle & \frac{1}{2}\langle \hat{p}_2\hat{x}_2 + \hat{x}_2\hat{p}_2 \rangle & \langle \Delta^2 \hat{p}_2 \rangle \end{pmatrix}. \tag{8.4}$$

8.3.2 Unitary operations

Unitary transformations are defined by unitary operators $\hat{U}$, with $\hat{U}^\dagger\hat{U} = \hat{U}\hat{U}^\dagger = I$. Unitaries are reversible, and preserve the norms and overlaps of states. By acting on vectors in a given Hilbert space, unitary operations are used to access any other vector in the same Hilbert space. These properties make unitary transformations very important for manipulating quantum information. The action of an arbitrary unitary operator $\hat{U}$ on an operator $\hat{A}$ is described in the Heisenberg picture as $\hat{A} \to \hat{U}^\dagger\hat{A}\hat{U}$.

8.3.3 Gaussian unitary operations

Gaussian unitary operations represent interaction Hamiltonians $\hat{H}$ that are at most quadratic in $\hat{x}$ and $\hat{p}$. All unitary Gaussian transformations $\hat{U}_G$ are generated via $\hat{U}_G = e^{-i\hat{H}(\hat{a},\hat{a}^\dagger)}$. Any such unitary $\hat{U}_G$ at the Hilbert space level corresponds to a symplectic transformation in phase space. This implies a linear transformation $\mathbf{S}$ which preserves the symplectic form $\mathbf{\Omega}$ such that $\mathbf{S}^T\mathbf{\Omega}\mathbf{S} = \mathbf{\Omega}$, where $\mathbf{S}$ has real entries, and $\mathbf{\Omega} = \begin{pmatrix} \mathbf{0} & \mathbf{I_n} \\ -\mathbf{I_n} & \mathbf{0} \end{pmatrix}$.

Symplectic transformations on a $2N$-dimensional phase space form a symplectic group of degree $2N$ over the field of real numbers $\mathbb{R}$, expressed as $S \in \mathrm{Sp}(2N, \mathbb{R})$.

Gaussian transformations are represented in the Heisenberg picture by the following[2]:

$$\begin{pmatrix} \hat{\mathbf{x}}' \\ \hat{\mathbf{p}}' \end{pmatrix} = \hat{U}_G^\dagger \begin{pmatrix} \hat{\mathbf{x}}_{\mathrm{in}} \\ \hat{\mathbf{p}}_{\mathrm{in}} \end{pmatrix} \hat{U}_G = \begin{pmatrix} \mathbf{A} & \mathbf{B} \\ \mathbf{C} & \mathbf{D} \end{pmatrix} \begin{pmatrix} \hat{\mathbf{x}}_{\mathrm{in}} \\ \hat{\mathbf{p}}_{\mathrm{in}} \end{pmatrix} + \begin{pmatrix} e \\ f \end{pmatrix}, \tag{8.5}$$

with the symplectic $2N \times 2N$ matrix $\mathbf{M}_{G(N)} = \left(\begin{smallmatrix} \mathbf{A} & \mathbf{B} \\ \mathbf{C} & \mathbf{D} \end{smallmatrix}\right)$ defining the N mode Gaussian transformation. $\mathbf{A}, \mathbf{B}, \mathbf{C}$, and $\mathbf{D}$ are themselves $N \times N$ matrices with $\mathbf{A}\mathbf{D}^T - \mathbf{B}\mathbf{C}^T = \mathbf{I}$, and the quadrature operators are collected in the operator-valued vectors as in the following, $\hat{\mathbf{x}} = (\hat{x}_1, \ldots, \hat{x}_N)^T$ and $\hat{\mathbf{p}} = (\hat{p}_1, \ldots, \hat{p}_N)^T$.

[2] A reminder that in this thesis we set $\hbar = \frac{1}{2}$. Some research groups choose to set $\hbar = 2$ so that the variance of a vacuum is unity.

8.4 One-mode Gaussian operations

The resulting operators after a one-mode Gaussian transformation are always linear combinations of the input operators. We introduce again the Weyl-Heisenberg (WH) operators $\hat{X}(s) = \mathrm{e}^{-2is\hat{p}}$ and $\hat{Z}(s) = \mathrm{e}^{2is\hat{x}}$ (section 2.6.2), and note that one-mode Gaussian unitary operations transform WH operators into products of WH operators, which are therefore linear combinations of the group generators. Stabiliser states (section 2.6.2) are transformed via Gaussian operations so that a state $|S\rangle$ is mapped onto $|S'\rangle$, and the stabilisers $g(s)$ and $g'(s)$ are products of the WH operators. Then the inverse Heisenberg evolution of the qumode stabiliser completely determines the resulting state as $g(s) \to g'(s) = \hat{U}g(s)\hat{U}^\dagger$.

8.4.1 Displacement

The displacement operators are the WH operators as discussed in section 2.6.2. The action of $\hat{Z}(s) = \mathrm{e}^{2is\hat{x}}$ is to impart a phase space displacement in momentum by s:

$$\begin{pmatrix} \hat{x} \\ \hat{p} \end{pmatrix} \to \begin{pmatrix} \hat{x} \\ \hat{p} \end{pmatrix} + \begin{pmatrix} 0 \\ s \end{pmatrix}, \tag{8.6}$$

and $\hat{X}(s) = \mathrm{e}^{-2is\hat{p}}$ imparts a phase space displacement in position by s:

$$\begin{pmatrix} \hat{x} \\ \hat{p} \end{pmatrix} \to \begin{pmatrix} \hat{x} \\ \hat{p} \end{pmatrix} + \begin{pmatrix} s \\ 0 \end{pmatrix}, \tag{8.7}$$

where in an experimental implementation s could for example be given by the measurement results of homodyne detection as $s^\theta = \hat{x}\cos\theta + \hat{p}\sin\theta$.
The Heisenberg evolutions of $\hat{Z}$ and $\hat{X}$ are given as:

$$\hat{Z}^\dagger(s)\hat{x}\hat{Z}(s) = \hat{x}, \quad \text{and} \quad \hat{Z}^\dagger(s)\hat{p}\hat{Z}(s) = \hat{p} + s, \tag{8.8}$$

$$\hat{X}^\dagger(s)\hat{x}\hat{X}(s) = \hat{x} + s, \quad \text{and} \quad \hat{X}^\dagger(s)\hat{p}\hat{X}(s) = \hat{p}, \tag{8.9}$$

respectively. The inverse Heisenberg evolutions of $\hat{Z}$ and $\hat{X}$ are given as:

$$\hat{Z}(s)\hat{x}\hat{Z}^\dagger(s) = \hat{x}, \quad \text{and} \quad \hat{Z}(s)\hat{p}\hat{Z}^\dagger(s) = \hat{p} - s, \tag{8.10}$$

$$\hat{X}(s)\hat{x}\hat{X}^\dagger(s) = \hat{x} - s, \quad \text{and} \quad \hat{X}(s)\hat{p}\hat{X}^\dagger(s) = \hat{p}, \tag{8.11}$$

respectively.

8.4.2 Rotation

A phase rotation of a single qumode $\hat{a}$ is governed by the rotation operator $\hat{R}(\theta) = \mathrm{e}^{i\theta\hat{a}^\dagger\hat{a}}$ as:

$$\hat{a} \to \hat{R}^\dagger(\theta)\hat{a}\hat{R}(\theta) = \hat{a}\mathrm{e}^{i\theta}. \tag{8.12}$$

Acting on the quadrature operators the rotation operator $\hat{R}$ is defined as:

$$\hat{R}(\theta) = \mathrm{e}^{i\theta\left(\hat{x}^2+\hat{p}^2\right)}, \tag{8.13}$$

so that we obtain:

$$\hat{R}^\dagger(\theta)\hat{x}\hat{R}(\theta) = \hat{x}\cos(\theta) - \hat{p}\sin(\theta), \quad \text{and} \quad \hat{R}^\dagger(\theta)\hat{p}\hat{R}(\theta) = \hat{x}\sin(\theta) + \hat{p}\cos(\theta). \tag{8.14}$$

The inverse Heisenberg evolution is given as:

$$\hat{R}(\theta)\hat{x}\hat{R}^\dagger(\theta) = \hat{x}\cos(\theta) + \hat{p}\sin(\theta), \quad \text{and} \quad \hat{R}(\theta)\hat{p}\hat{R}^\dagger(\theta) = -\hat{x}\sin(\theta) + \hat{p}\cos(\theta), \tag{8.15}$$

and its action can be seen by the rotation matrix $R(\theta)$, which is to perform a counter-clockwise rotation in phase space by the angle θ:

$$\begin{pmatrix}\hat{x}\\ \hat{p}\end{pmatrix} \to \begin{pmatrix}\cos(\theta) & -\sin(\theta)\\ \sin(\theta) & \cos(\theta)\end{pmatrix}\begin{pmatrix}\hat{x}\\ \hat{p}\end{pmatrix} = R(\theta)\begin{pmatrix}\hat{x}\\ \hat{p}\end{pmatrix}. \tag{8.16}$$

Note that $\hat{R}(\theta_1)\hat{R}(\theta_2) = \hat{R}(\theta_1 + \theta_2)$.

8.4.3 Fourier

The Fourier transform is an important instance of the rotation operator, defined as $\hat{F} = \hat{R}(\frac{\pi}{2}) = \mathrm{e}^{\imath\frac{\pi}{2}\hat{a}^\dagger\hat{a}}$. Acting on the quadrature operators, we have:

$$\hat{F} = \mathrm{e}^{\imath\frac{\pi}{2}(\hat{x}^2+\hat{p}^2)}, \quad \text{so that} \quad \hat{F}^\dagger\hat{x}\hat{F} = -\hat{p} \quad \text{and} \quad \hat{F}^\dagger\hat{p}\hat{F} = \hat{x}. \tag{8.17}$$

The Fourier transform matrix F performs the following transformation

$$\begin{pmatrix}\hat{x}\\ \hat{p}\end{pmatrix} \to \begin{pmatrix}0 & -1\\ 1 & 0\end{pmatrix}\begin{pmatrix}\hat{x}\\ \hat{p}\end{pmatrix} = F\begin{pmatrix}\hat{x}\\ \hat{p}\end{pmatrix}, \tag{8.18}$$

and the inverse Heisenberg evolutions of the Fourier transformation is given as:

$$\hat{F}\hat{x}\hat{F}^\dagger = \hat{p}, \quad \text{and} \quad \hat{F}\hat{p}\hat{F}^\dagger = -\hat{x}. \tag{8.19}$$

The Fourier transform operator $\hat{F}$ acting on the quadrature eigenstates will transform the basis as:

$$\hat{F}|x = a\rangle = |p = a\rangle, \quad \text{and} \quad \hat{F}|p = b\rangle = -|x = b\rangle, \tag{8.20}$$

and the inverse Fourier transform operator $\hat{F}^\dagger$ acts as:

$$\hat{F}^\dagger|x = a\rangle = -|p = a\rangle, \quad \text{and} \quad \hat{F}^\dagger|p = b\rangle = |x = b\rangle. \tag{8.21}$$

8.4.4 Squeezing

The squeezing operation $\hat{S} = \mathrm{e}^{ir(\hat{x}\hat{p}+\hat{p}\hat{x})}$ is given by:

$$\begin{pmatrix}\hat{x}\\ \hat{p}\end{pmatrix} \to \begin{pmatrix}\mathrm{e}^{-r} & 0\\ 0 & \mathrm{e}^{r}\end{pmatrix}\begin{pmatrix}\hat{x}\\ \hat{p}\end{pmatrix} = S\begin{pmatrix}\hat{x}\\ \hat{p}\end{pmatrix}, \tag{8.22}$$

and the squeezing operator acting on the quadrature operators gives

$$\hat{S}^\dagger(r)\hat{x}\hat{S}(r) = e^{-r}\hat{x}, \quad \text{and} \quad \hat{S}^\dagger(r)\hat{p}\hat{S}(r) = e^{+r}\hat{p}. \tag{8.23}$$

8.4.5 Quadratic phase gate

The quadratic phase gate $\hat{D}_2(g)$, sometimes referred to as the shearing gate [77], can be seen as a combination of the rotation and squeeze operators, and is given by:

$$\hat{D}_2(g) = \mathrm{e}^{ig\hat{x}^2}. \tag{8.24}$$

Its action can be described by the quadratic phase matrix as:

$$\begin{pmatrix} \hat{x} \\ \hat{p} \end{pmatrix} \to \begin{pmatrix} 1 & 0 \\ g & 1 \end{pmatrix} \begin{pmatrix} \hat{x} \\ \hat{p} \end{pmatrix} = D_2(g) \begin{pmatrix} \hat{x} \\ \hat{p} \end{pmatrix}, \tag{8.25}$$

leading to the following linear Heisenberg evolutions:

$$\hat{x} \to \hat{D}_2^\dagger(g)\hat{x}\hat{D}(g) = \hat{x}, \quad \text{and} \quad \hat{p} \to \hat{D}_2^\dagger(g)\hat{p}\hat{D}(g) = \hat{p} + g\hat{x}. \tag{8.26}$$

8.5 Controlled phase gate

The controlled phase gate C_Z is an important multimode Gaussian gate, given by:

$$\hat{C}_Z = \mathrm{e}^{2i\hat{x}_1\hat{x}_2}. \tag{8.27}$$

The C_Z gate is the CV analogue of the discrete variable CPHASE gate, in the sense that it is the gate used to create cluster states by entangling the 2 qumodes that it acts on. It is a CV quantum nondemolition (QND) interaction. Its action is described by the input-output relation:

$$\begin{pmatrix} \hat{x}_1' \\ \hat{p}_1' \\ \hat{x}_2' \\ \hat{p}_2' \end{pmatrix} = \begin{pmatrix} 1 & 0 & 0 & 0 \\ 0 & 1 & 1 & 0 \\ 0 & 0 & 1 & 0 \\ 1 & 0 & 0 & 1 \end{pmatrix} \begin{pmatrix} \hat{x}_1 \\ \hat{p}_1 \\ \hat{x}_2 \\ \hat{p}_2 \end{pmatrix}. \tag{8.28}$$

The Cz gate does nothing to the $\hat{x}$ quadrature operators, and transforms the $\hat{p}$ quadrature operators,

$$\hat{x}_1 \to \hat{x}_1, \qquad \hat{x}_2 \to \hat{x}_2, \tag{8.29}$$

$$\hat{p}_1 \to \hat{p}_1 + \hat{x}_2, \qquad \hat{p}_2 \to \hat{p}_2 + \hat{x}_1. \tag{8.30}$$

8.5.1 Universality

Decomposing a general Hamiltonian $\hat{H}(\hat{a}, \hat{a}^\dagger)$ with mode operators of arbitrary polynomial order into a set of elementary evolutions is a difficult task. Universality is defined here to be the construction of a universal set of gates that simulate Hamiltonians of arbitrary order with a finite set of gates. Such a set of gates [24, 97] for asymptotic simulations of arbitrary multimode Hamiltonians is given by:

$$\{F, Z(s), D_2(g), D_3(g), C_Z\}, \tag{8.31}$$

where we have included the cubic phase gate $\hat{D}_3(g) = \mathrm{e}^{ig\hat{x}^3}$ belonging to the family of k-th order phase gates $\hat{D}_k(g) = \mathrm{e}^{ig\hat{x}^k}$.

8.6 Gaussian operations on a linear cluster

At the heart of one-way quantum computing lies quantum teleportation [17, 18, 19], and we now discuss this elementary quantum information protocol within the framework of Gaussian unitaries developed in the previous sections. This section largely follows the research presented in references [32, 31, 77, 99].

8.6.1 Elementary teleportation circuit

The elementary quantum circuit for one-mode cluster computation [32] is shown in figure 8.1.

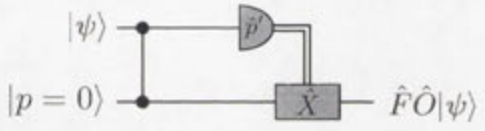

Figure 8.1: Elementary gate teleportation. The input state $|\psi\rangle$ is coupled to a momentum eigenstate with zero eigenvalue $|p=0\rangle$ via a C_Z gate (section 8.5) denoted by the vertical line. $\hat{p}'$ is the measurement, and $\hat{X}$ is the position displacement operator (equation (8.7)).

An input state $|\psi\rangle$ and a momentum squeezed vacuum state are coupled via the controlled phase gate C_Z, presented in section 8.5. The measurement denoted by $\hat{p}'$ is performed on the top rail in the measurement basis $\{\hat{O}^\dagger|p\rangle\}$ so that the measured variable is $\hat{p}' = \hat{O}^\dagger\hat{p}\hat{O}$, where $\hat{O}$ is a function of $\hat{x}$ and independent of $\hat{p}$; $\hat{O} = \mathrm{e}^{\mathrm{i}f(x)}$ [99]. After the feed-forward of the measurement, implemented by the WH position displacement operator $\hat{X}$ (equation (8.7)), the output state is $|\psi\rangle' = \hat{F}\hat{O}|\psi\rangle$.
The elementary gate for one-mode Gaussian transformations in cluster computation is the quadratic phase gate $D_2(g)$ introduced in section 8.4.5. Therefore the one-mode elementary teleportation gate $M(g) = FD_2(g)$ is defined by the following transformation:

$$M(g) = FD_2(g) = \begin{pmatrix} -g & -1 \\ 1 & 0 \end{pmatrix} \tag{8.32}$$

where g is accessible by homodyne detection and is given by $g = \tan(\theta)$.
This elementary circuit can be considered as a "half teleportation". Arbitrary one-mode transformations are then performed by concatenating sufficiently many elementary half teleportation steps. It is shown explicitly in reference [99] that a minimum of four elementary half teleportations are required to perform universal one-mode Gaussian transformations.

8.6.2 Quantum teleportation matrix

The well-known CV quantum teleportation [17, 18, 19] circuit is presented in figure 8.2.

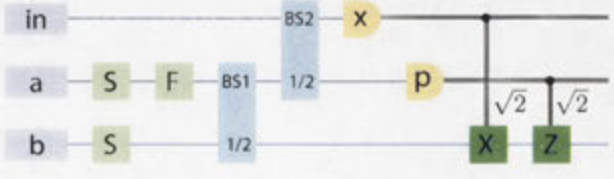

Figure 8.2: Teleportation through an EPR state with Bell measurements. All inputs are vacua. S: squeezing, F: Fourier, $BS1$,$BS2$: beam-splitter with reflectivity $\frac{1}{2}$. See section 3.2 for beam-splitter matrices.

An EPR state is created by first mixing two squeezed modes in quadrature (relative phase of $\frac{\pi}{2}$) on a balanced beam-splitter. An input state is then coupled via a balanced beam-splitter and a Bell measurement (two homodyne measurements; one in $\hat{x}$, one in $\hat{p}$) is performed and the measurement results are used to displace the output beam in each quadrature in phase space. The output state is equal to the input state. Here, the resource is the EPR state, and the input is teleported through the resource state unchanged.
If we modify the resource state to create instead a 2-mode cluster state, and perform homodyne measurements at arbitrary phase angles θ_1 and θ_2 instead of a Bell measurement, we arrive at the teleportation-based cluster computation circuit figure 8.3.

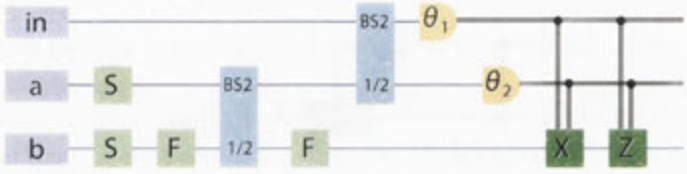

Figure 8.3: Teleportation-based computation through a cluster state with arbitrary homodyne measurements. All inputs are vacua. S: squeezing, F: Fourier, $BS2$: beam-splitter with reflectivity $\frac{1}{2}$.

The teleportation-based operation is described by the following unitary transformation,

$$\begin{pmatrix} \hat{x}_{\text{out}} \\ \hat{p}_{\text{out}} \end{pmatrix} = M_{tel}(\theta_+, \theta_-) \begin{pmatrix} \hat{x}_{\text{in}} \\ \hat{p}_{\text{in}} \end{pmatrix} \tag{8.33}$$

where $\theta_\pm = \theta_1 \pm \theta_2$, and θ_1 and θ_2 represent the two homodyne quadrature angles we measure in the circuit. The teleportation matrix M_{tel} is given in the cluster state basis as:

$$M_{tel}^{(C)}(\theta_+, \theta_-) \equiv \begin{pmatrix} \frac{\cos(\theta_-)+\cos(\theta_+)}{\sin(\theta_-)} & \frac{\sin(\theta_+)}{\sin(\theta_-)} \\ \frac{-\sin(\theta_+)}{\sin(\theta_-)} & \frac{\cos(\theta_-)-\cos(\theta_+)}{\sin(\theta_-)} \end{pmatrix} = \begin{pmatrix} a^{(C)} & b^{(C)} \\ c^{(C)} & d^{(C)} \end{pmatrix}. \tag{8.34}$$

M_{tel} is a Gaussian operation satisfying $ad - bc = 1$, as in equation (8.5). We will return to the cluster state basis after defining the teleportation matrix in another basis, relevant to the dual-rail EPR-graph state created and detailed in chapter 7.

8.7 Cluster computation on the dual-rail EPR-graph state

The dual-rail EPR-graph state, fully detailed in section 7.2, is a universal resource for MBQC. This has been shown in reference [36], along with a proposal for one possible way to implement universal MBQC. Recall that the dual-rail EPR-graph state, and its cousin the dual-rail cluster state both have a dual-rail graph. The proposal was to measure all of the nodes in the top rail in the x quadrature, essentially performing cluster state shaping [109], in order to use the structure as a CV quantum wire, that is, a linear cluster state. This is wasteful of half of the modes in the cluster, and was suggested only to prove that one possible implementation of universal MBQC existed for the state. Here, we detail how to perform a more efficient set of measurements, based on the idea of sequential teleportation.

8.7.1 Teleportation-based computation in the EPR basis

First, we define the teleportation matrix for the EPR basis. The circuit is shown in figure 8.4.

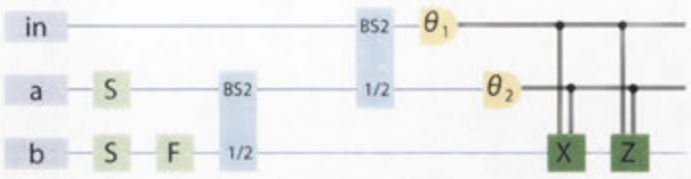

Figure 8.4: Teleportation-based computation through an EPR state with arbitrary homodyne measurements. All inputs are vacua. S: squeezing, F: Fourier, $BS2$: beam-splitter with reflectivity $\frac{1}{2}$.

We notice that the only difference from the cluster state basis is one Fourier transform after the first beam-splitter.
The teleportation matrix in the EPR basis, M_{tel}^{E}, is given by:

$$M_{tel}^{(E)}(\theta_+,\theta_-) \equiv \begin{pmatrix} \frac{-\sin(\theta_+)}{\sin(\theta_-)} & \frac{\cos(\theta_-)-\cos(\theta_+)}{\sin(\theta_-)} \\ \frac{-\cos(\theta_-)-\cos(\theta_+)}{\sin(\theta_-)} & \frac{-\sin(\theta_+)}{\sin(\theta_-)} \end{pmatrix} = \begin{pmatrix} a^{(E)} & b^{(E)} \\ c^{(E)} & d^{(E)} \end{pmatrix}, \tag{8.35}$$

where again, $ad - bc = 1$ and this represents a Gaussian operation.
We note that $M_{tel}^{(C)}(\theta_+,\theta_-) = FM_{tel}^{(E)}(\theta_+,\theta_-)$.

Familiar operations from teleportation matrices

Here we look at different forms of M_{tel} in both bases for different measurement angles in order to gain some intuition. Note that this is similar to the derivation in reference [99], yet the derivation here differs due to the different linear optics network used to define M_{tel}.
In the EPR basis when we perform a Bell measurement ($\theta_0 = 0$, $\theta_1 = \frac{\pi}{2}$) the result is a standard teleportation; the output is equal to the input, and the identity operation has been performed. In the Cluster state basis a Bell measurement will output a Fourier transformed version of the input state. Performing a Bell measurement with respect to the (θ_+,θ_-) basis, such that $\theta_+ = 0, \theta_- = \frac{\pi}{2}$, achieved for example with $\theta_0 = -\frac{\pi}{4}, \theta_1 = \frac{\pi}{4}$ performs the identity operation.
In a similar fashion to [99] we impose the condition $\sin(\theta_-) > 0$ in order to keep the elements of $M_{tel}(\theta_+,\theta_-)$ from going to infinity. We outline specific cases in order to gain intuition regarding the teleportation matrices.

$$M_{tel}^{(C)}(0,\theta_-) = \begin{pmatrix} \frac{1+\cos(\theta_-)}{\sin(\theta_-)} & 0 \\ 0 & \frac{1-\cos(\theta_-)}{\sin(\theta_-)} \end{pmatrix} = \begin{pmatrix} \frac{1}{\tan(\frac{1}{2}\theta_-)} & 0 \\ 0 & \tan(\frac{1}{2}\theta_-) \end{pmatrix} \tag{8.36}$$

from which we can define $r = \ln\tan(\frac{1}{2}\theta_-)$ in order to show that this is a squeezing operation,

$$M_{tel}^{(C)}(0,\theta_-) = \begin{pmatrix} \mathrm{e}^{-r} & 0 \\ 0 & \mathrm{e}^{r} \end{pmatrix} = S(r). \tag{8.37}$$

Accordingly,

$$M_{tel}^{(E)}(0,\theta_-) = F^\dagger M_{tel}^{(C)}(0,\theta_-) = F^\dagger S(r) \tag{8.38}$$

Consider $\theta_- = \frac{\pi}{2}$,

$$M_{tel}^{(C)}(\theta_+,\frac{\pi}{2}) = \begin{pmatrix} \cos(\theta_+) & \sin(\theta_+) \\ -\sin(\theta_+) & \cos(\theta_+) \end{pmatrix} = R(-\theta_+) \tag{8.39}$$

with once again

$$M_{tel}^{(E)}(\theta_+, \frac{\pi}{2}) = F^\dagger M_{tel}^{(C)}(\theta_+, \frac{\pi}{2}) \tag{8.40}$$

A single teleportation in the cluster state basis can therefore be represented as

$$M_{tel}^{(C)}(\theta_+, \theta_-) = M_{tel}^{(C)}(\frac{\theta_+}{2}, \frac{\pi}{2}) M_{tel}^{(C)}(0, \theta_-) M_{tel}^{(C)}(\frac{\theta_+}{2}, \frac{\pi}{2}) \tag{8.41}$$

$$= R(-\frac{\theta_+}{2}) S(r) R(-\frac{\theta_+}{2}) \tag{8.42}$$

It was shown in reference [99] that the teleportation matrix in the cluster state basis M_{tel}^{C} followed by two elementary half teleportation gates $M(g_1)$ and $M(g_2)$ is sufficient to demonstrate an arbitrary one-mode Gaussian operation.
In the next section we show that two sequential teleportations in the EPR basis is also sufficient for an arbitrary one-mode Gaussian operation. This is perhaps unsurprising, as the two bases differ only by a Fourier transform. What is nice about this result however, is that it allows us to formulate a method of MBQC on the dual-rail EPR-graph state as a sequence of teleportations, leading to an efficient method of universal MBQC.

8.7.2 Universal one-mode Gaussian operations with teleportation

It was shown in reference [110] that an arbitrary matrix in $\mathrm{Sp}(2, \mathbb{R})$ can be decomposed into a rotation, followed by a squeezing operation, followed by a rotation.
We now show that two sequential teleportations [111], in both the cluster basis and the EPR basis, are sufficient to implement an arbitrary one-mode Gaussian, following the aforementioned decomposition. We begin with a treatment in the cluster state basis, as this is the standard resource for cluster state computation.

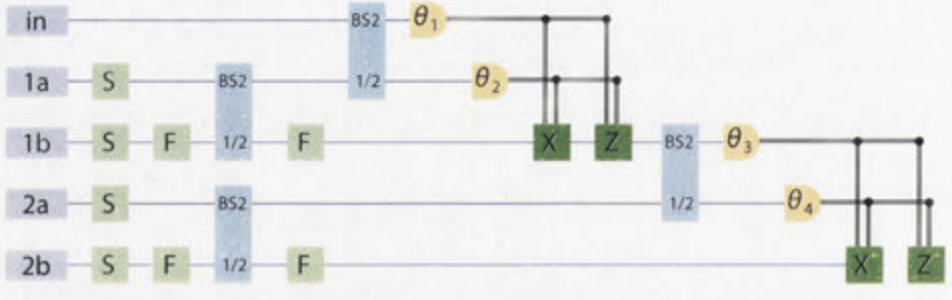

Figure 8.5: Two sequential teleportations in the cluster state basis. All inputs are vacua. S: squeezing, F: Fourier, $BS2$: beam-splitter with reflectivity $\frac{1}{2}$.

In the two-sequential teleportation circuit in the cluster state basis of figure 8.5 we have access to four homodyne measurement angles and label them as θ_1, θ_2, θ_3, and θ_4. We then define $\theta_{1\pm} = \theta_1 \pm \theta_2$ and $\theta_{2\pm} = \theta_3 \pm \theta_4$.
Now let the one-mode Gaussian transformation that is achieved through the two-sequential teleportation circuit be defined by the matrix $M_{2tel}^{C}(\theta_{1+}, \theta_{1-}, \theta_{2+}, \theta_{2-}) = M_{tel}^{C}(\theta_{2+}, \theta_{2-}) M_{tel}^{C}(\theta_{1+}, \theta_{1-})$. From equation (8.42) we have:

$$M_{tel}^{C}(\theta_{2+}, \theta_{2-}) M_{tel}^{C}(\theta_{1+}, \theta_{1-}) = R(-\frac{\theta_{2+}}{2}) S(r(\theta_{2-})) R(-\frac{\theta_{2+}}{2}) R(-\frac{\theta_{1+}}{2}) S(r(\theta_{1-})) R(-\frac{\theta_{1+}}{2}) \tag{8.43}$$

We know from [110, 99] that if we can decompose the operation into the sequence of rotation, squeeze, rotation, as in $M_{2tel}^{C} = R_{\phi 1} S_\xi R_{\phi 2}$, with the freedom to set each operation independently from the others, then this is sufficient proof that we have enough degrees of freedom to perform

arbitrary one-mode Gaussian transformations.
We therefore choose $\theta_{2-} = \frac{\pi}{2}$ such that we can set $S(r(\theta_{2-}))$ equal to the Identity, in order to obtain the correct sequence of operations.
Specifically, end up with $M^{C}_{2tel}(\theta_{1+}, \theta_{1-}, \theta_{2+}, \theta_{2-}) = R(-\theta_{2+} - \frac{\theta_{1+}}{2})S(r(\theta_{1-}))R(-\frac{\theta_{1+}}{2})$. We can see that these three terms can be arbitrarily set by θ_{2+}, θ_{1-}, and θ_{1+}, respectively. Remember θ_{2-} is chosen such that $S(r(\theta_{2-}))$ is equal to the Identity.

EPR basis

As the EPR basis is related by a Fourier transform, we can write M^{E}_{tel} as

$$M^{(E)}_{tel}(\theta_+, \theta_-) = F\, M^{(C)}_{tel}(\frac{\theta_+}{2}, \frac{\pi}{2}) M^{(C)}_{tel}(0, \theta_-) M^{(C)}_{tel}(\frac{\theta_+}{2}, \frac{\pi}{2}) \tag{8.44}$$

$$= R(\frac{\pi}{2})R(-\frac{\theta_+}{2})S(r)R(-\frac{\theta_+}{2}) \tag{8.45}$$

$$= R(\frac{\pi}{2} - \frac{\theta_+}{2})S(r)R(-\frac{\theta_+}{2}), \tag{8.46}$$

and we will obtain for the four measurement angles corresponding to the EPR basis,

$$M^{E}_{2tel}(\theta_{1+}, \theta_{1-}, \theta_{2+}, \theta_{2-}) = M^{E}_{tel}(\theta_{2+}, \theta_{2-}) M^{C}_{tel}(\theta_{1+}, \theta_{1-})$$

the following expression for the sequential teleportation in the EPR basis:

$$M^{E}_{tel}(\theta_{2+}, \theta_{2-}) M^{E}_{tel}(\theta_{1+}, \theta_{1-}) = R(\frac{\pi - \theta_{2+}}{2})S(r(\theta_{2-}))R(-\frac{\theta_{2+}}{2})R(\frac{\pi - \theta_{1+}}{2})S(r(\theta_{1-}))R(-\frac{\theta_{1+}}{2}),$$

which can be similarly set to $M^{E}_{2tel}(\theta_{1+}, \theta_{1-}, \theta_{2+}, \theta_{2-}) = R(\pi - \theta_{2+} - \frac{\theta_{1+}}{2})S(r(\theta_{1-}))R(-\frac{\theta_{1+}}{2})$, by setting $S(r(\theta_{2-}))$ is equal to the Identity by our choice of θ_{2-}.
We have therefore shown that two successive applications of the teleportation matrix M^{E}_{tel} for the EPR basis is sufficient to perform arbitrary one-mode Gaussian operations. It follows that the rich theory of multimode gates and non-Gaussian elements [32, 77, 75] available for the cluster state is also applicable to the dual-rail EPR-graph state.

Gaussian parallelism

Due to the parallelism of Gaussian unitaries, the two circuits shown in figure 8.6(a) and (b) are equivalent. That is, instead of performing sequential teleportations we may achieve the equivalent operations by first creating the entire state, and then performing the homodyne measurements and feed-forward at the end.

I have re-labelled the modes to the circuit to be easily compared with the Heisenberg evolutions discussed in section 7.2. Figure 8.6(c) shows the graph of the generated dual-rail EPR-graph state. The dashed line represents a beam-splitter coupling of the input to the dual-rail EPR-graph state. See section 7.2 for details on the dual-rail EPR-graph state.

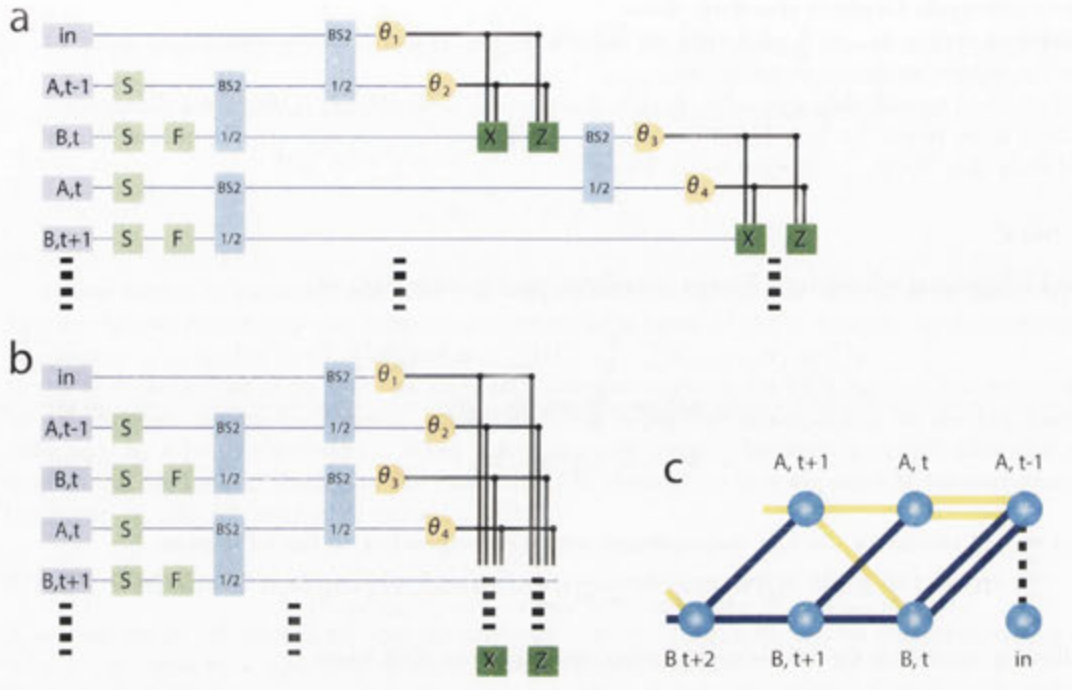

Figure 8.6: Gaussian parallelism of operators. The two circuits (a) and (b) perform equivalent operations. (c) Graph of the generated dual-rail EPR-graph state (see section 7.2).

8.8 Summary and conclusion

In this chapter we have briefly reviewed cluster state computing in the continuous-variables regime. The treatment here focused on Gaussian operations, which perform transformations on Gaussian states and leave the state as a Gaussian. We then spent some time detailing quantum teleportation, and then framed teleportation-based operations in the context of the Gaussian operations developed earlier in the chapter. The dual-rail EPR-graph state, which was experimentally generated [37], and detailed in chapter 7, was shown to fit nicely within the context of the teleportation-based Gaussian quantum computations. In the next two chapters we will look at experiments that perform some of the operations that we introduced in this chapter. Specifically, in chapter 9 the experimental demonstration of arbitrary one-mode Gaussian operations are presented. Finally, in chapter 10 we detail the experimental demonstration of a multimode gate.

Chapter 9

One-way Gaussian operations for cluster computation

The one-way quantum computer is a universal quantum computer. This means that when a large-scale and fault-tolerant one-way quantum computer is eventually built, it will have the ability to describe an arbitrary multimode Hamiltonian evolution. In order to progress towards this ultimate goal, we can demonstrate a set of operations that comprise a subset of this universal quantum computer. This is possible by recognising that there is a set of universal unitary transformations such that concatenations of the elements in the set will allow you to simulate any operator on a certain Hilbert space [97]. In this chapter we describe an experimental demonstration of a necessary, yet not sufficient set of transformations for universality. These are the one-mode Gaussian transformations [99].

The research presented in this chapter appears in the following journal publication[1]:

- R. Ukai, N. Iwata, Y. Shimokawa, S. Armstrong, A. Politi, J-I. Yoshikawa, P. van Loock, A. Furusawa. *Demonstration of Unconditional One-Way Quantum Computations for Continuous Variables.* Physical Review Letters **106**, 240504 (2011).

9.1 The resource: linear 4-mode cluster state

The resource state used for this computation is a 4-mode linear cluster state. This cluster state can be viewed as a blank quantum circuit board, and is shown graphically in Fig. 9.1. The homodyne measurement angles at which each node of the cluster is measured, along with the feed-forward gains to the final output mode will determine the quantum operation that is performed.

Figure 9.1: Four-mode linear cluster state. Resource state for demonstrations of one-way quantum computing; can be viewed as a blank quantum circuit board. Each numbered circle denotes a quantised optical mode (qumode), and the green links between them have edge weights of unity, as defined in the graphical calculus of reference [22], and treated in section 7.2.

The 4-mode linear cluster is the smallest cluster state that can be prepared that offers enough degrees of freedom to implement an arbitrary one-mode Gaussian transformation, as was shown in reference [99]. These Gaussian transformations correspond to arbitrary Hamiltonians that are

[1]Statement of contribution: I was not involved in the experimental demonstration of the squeezing operation, which was an extension of the Fourier transform experiment, performed on the same optical setup with minor modifications.

quadratic in $\hat{x}$ and $\hat{p}$. The experimental apparatus that forms the optics network used to generate the resource state was constructed prior to this experiment and was reported in [59].

9.2 Linear unitary Bogoliubov transformations

The quantum teleportation of an arbitrary quantum state corresponds to the identity operation. When the state is manipulated during the teleportation such that the output is not same as the input, a one-way quantum computation has been performed. When the input and output states are both Gaussian states, the transformation performed was a Gaussian operation. These Gaussian operations are referred sometimes referred to as linear unitary Bogoliubov (LUBO) transformations [34, 99]. We will use the terms Gaussian and LUBO interchangeably when discussing transformation.

For a single optical mode, in order to demonstrate an arbitrary LUBO operation, we must demonstrate the ability to perform arbitrary displacements, rotations, and squeezing operations in phase space [98].

9.2.1 Fourier transformation

The Fourier transformation $\hat{F} = \hat{R}(\frac{\pi}{2})$ performs a 90° rotation in phase space. Figure 9.2 shows an abstract illustration of our experimental implementation of the Fourier transformation.

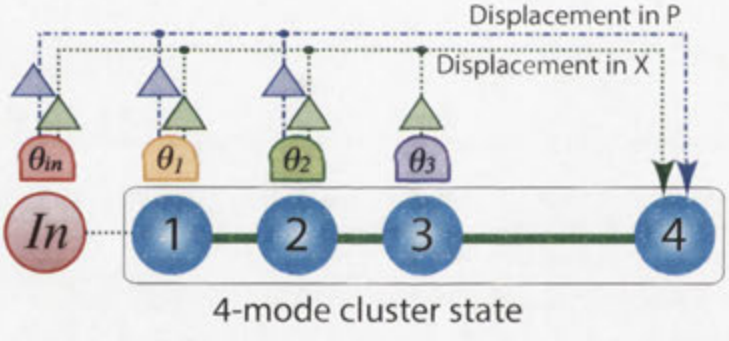

Figure 9.2: Abstract illustration of arbitrary one-mode transformations. (a) An input is teleported and manipulated through a 4-mode linear cluster. The cluster state acts as a blank quantum circuit board. The four measurement angles determine the circuit that is printed onto the state and read out via the output. This is a modified version of the figure which appears in [98], originally created by Ukai.

An arbitrary input state is coupled to the blank quantum circuit board, which is here a 4-mode linear cluster state. In the experiment we use both a coherent state and a vacuum state as inputs. The measurements required to achieve these operations are efficient homodyne detections with quadrature angles θ_i, which are easily controllable by adjusting the local oscillator phases in the homodyne detectors.

The total procedure then consists of the teleportation-based [17, 112, 19] coupling $\hat{M}_{tel}(\theta_{in}, \theta_1)$, followed by two elementary, measurement-based, one-mode operations $\hat{M}(\theta_i)$ [34, 33, 77]:

$$|\psi_{out}\rangle = \hat{M}(\theta_3)\hat{M}(\theta_2)\hat{M}_{tel}(\theta_{in}, \theta_1)|\psi_{in}\rangle. \tag{9.1}$$

The generalised teleportation operator $\hat{M}_{tel}$ was introduced in section 8.6.2 and $\hat{M}(\theta_i)$ is related to the elementary half teleportation gate $\hat{M}(g)$ of equation (8.32) by $g = \tan(\theta)$. The teleportation-based coupling operation can be decomposed as a rotation in phase space, squeezing, and another rotation in phase space: $\hat{M}_{tel}(\theta_{in},\theta_1) = \hat{R}(-\theta_+/2)\hat{S}(r)\hat{R}(-\theta_+/2)$ with $r = \log\tan(\theta_-/2)$ and

$\theta_{\pm} = \theta_{in} \pm \theta_1$.
The one-mode operations are also decomposed into the rotation, squeezing, rotation operators, given by: $\hat{M}(\theta_i) = \hat{R}(\phi_i)\hat{S}(r_i)\hat{R}(\phi_i)$ with $r_i = \log \frac{\sqrt{k_i^2+4}+k_i}{2}, \phi_i = \frac{\pi}{2} - \tan^{-1}\frac{\sqrt{k_i^2+4}-k_i}{2}$, and $k_i = 1/\tan\theta_i$.

Now as the Fourier transformation performs the following:

$$\begin{pmatrix} \hat{x}_{out} \\ \hat{p}_{out} \end{pmatrix} = \begin{pmatrix} 0 & -1 \\ 1 & 0 \end{pmatrix} \begin{pmatrix} \hat{x}_{in} \\ \hat{p}_{in} \end{pmatrix}, \tag{9.2}$$

the following equation must be satisfied in order to compute the necessary homodyne angles:

$$M(\theta_3)M(\theta_2)M_{tel}(\theta_{in},\theta_1) = \begin{pmatrix} 0 & -1 \\ 1 & 0 \end{pmatrix}. \tag{9.3}$$

The Fourier transformation is implemented by choosing the homodyne measurement quadrature angles $(\theta_{in},\theta_1,\theta_2,\theta_3)$ as $(90°, 0°, 90°, 90°)$, see [98] for details.

The effect of each measurement on the cluster can be seen in Fig. 9.3.

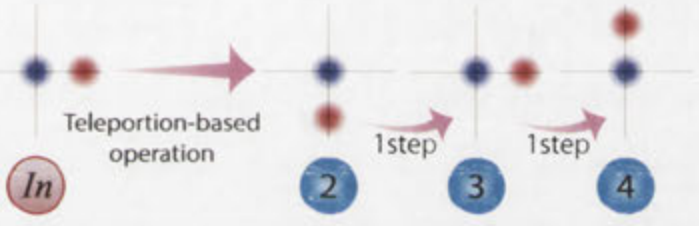

Figure 9.3: Fourier transformation through the four-mode cluster. The effect of each measurement can be seen in phase space. This is a modified version of the figure which appears in [98], originally created by Ukai.

9.2.2 Squeezing

The squeezing operation was implemented by the same method[2], following the teleportation-based measurement and feed-forward scheme of Fig. 9.2. The squeezing transformation performs the following:

$$\begin{pmatrix} \hat{x}_{out} \\ \hat{p}_{out} \end{pmatrix} = \begin{pmatrix} 10^{-\frac{d}{20}} & 0 \\ 0 & 10^{\frac{d}{20}} \end{pmatrix} \begin{pmatrix} \hat{x}_{in} \\ \hat{p}_{in} \end{pmatrix}, \tag{9.4}$$

where d is the squeezing parameter given in units of (dB) familiar to the experimentalist, related to the squeezing parameter r by the relation $10^{\frac{d}{10}} = e^{2r}$. The input states are transformed through each teleportation step as can be visualised in phase space in Fig. 9.4.

The homodyne measurement angles $(\theta_{in},\theta_1,\theta_2,\theta_3)$ needed to perform 3, 6, and 10 dB x-squeezing operations are given by the following:

[2] Although performed using the same equipment, I was not present during the testing phase and did not participate in the experiment.

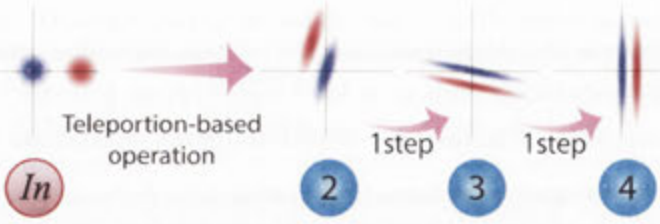

Figure 9.4: Squeezing transformation through the 4-mode cluster. The effect of each measurement can be seen in phase space. This is a modified version of the figure which appears in [98], originally created by Ukai.

$$\begin{aligned} &(-42.5°, 62.4°, 63.5°, 76.0°), \\ &(-41.4°, 72.2°, 41.9°, 74.4°), \\ \text{and } &(-47.7°, 79.2°, 25.9°, 78.4°). \end{aligned} \tag{9.5}$$

9.3 Experimental details

The experimental schematic is shown in Fig. 9.5. Each measurement depicted by an angle is a homodyne measurement. The scaled measurements are then fed-forward to 2 electro-optic-modulators in order to perform 2 displacements in phase space. The reflectivities of each beam-splitter are shown on the schematic below each beam-splitter.

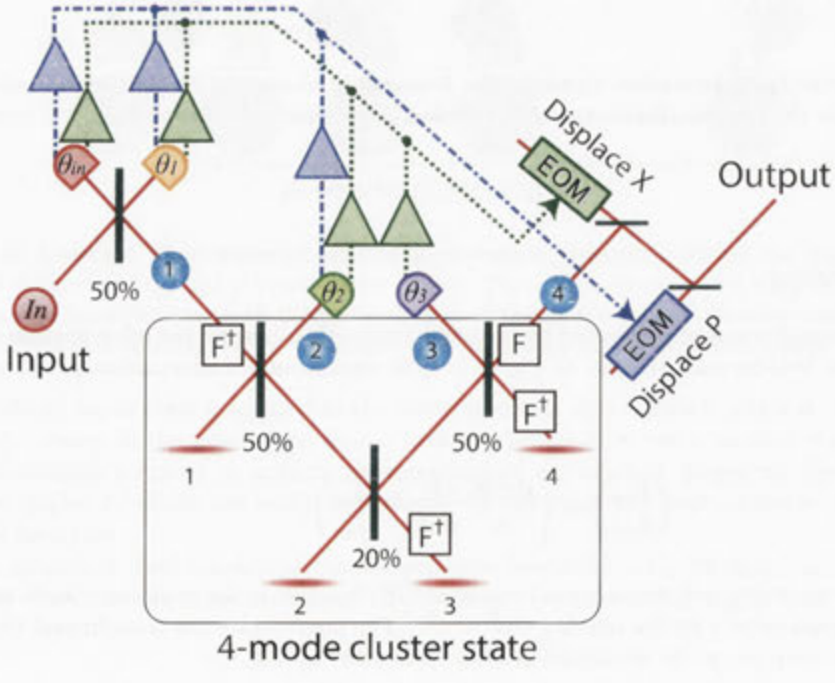

Figure 9.5: Experimental setup of arbitrary one-mode transformations. We use a 4-mode linear cluster state as a resource and teleport an input state through. Beam-splitter reflectivities given as percentages. F denotes a local Fourier transform (equation (8.25)), and $F^\dagger$ denotes an inverse Fourier. This is a modified version of the figure which appears in [98], originally created by Ukai.

For this experiment our light source is a continuous wave titanium sapphire laser producing light at the fundamental wavelength of 860 nm and an optical power of about 1.7 W. We define our quantum modes in this experiment to be frequency sideband modes at 1 MHz, with a linewidth (resolution bandwidth) of 30 kHz. The measured phase interference visibilities were between 95.5% and 98.5% for the entire optical setup.

9.3.1 Generation of the resource state

The four-mode linear cluster state is generated by mixing squeezed light on a beam-splitter network. More specifically 4 vacuum squeezed outputs were mixed on 3 beam-splitters with the necessary passive phase rotations between the 4 beams. The schematic for the generation of the resource state is shown in Fig. 9.6.

Figure 9.6: Schematic for the generation of the 4-mode linear cluster state. Four squeezed beams are combined on three beam-splitters with various phase shifts in order to generate a linear 4-mode cluster state.

The unitary describing this network is given as:

$$U = F_4 F_2^\dagger B_{34}^{(4)}\left(\frac{1}{\sqrt{2}}\right) B_{12}^{(3)}\left(\frac{1}{\sqrt{2}}\right) B_{23}^{(3)}\left(\frac{2}{\sqrt{5}}\right) F_3^\dagger F_4^\dagger S_1(s_1) S_2(s_2) S_3(s_3) S_4(s_4). \tag{9.6}$$

We choose to omit the squeezing operators from hereon in to ensure the network only comprises beam-splitter operations and relative phase shifts. This is experimentally more appropriate as our squeezed light is generated offline. The unitary matrix describing the network that transforms 4 independent p-squeezed modes into the linear 4-mode cluster state is then given as:

$$U = \begin{pmatrix} \frac{1}{\sqrt{2}} & \frac{1}{\sqrt{10}} & -\frac{2}{\sqrt{10}}i & 0 \\ \frac{1}{\sqrt{2}}i & -\frac{1}{\sqrt{10}}i & -\frac{2}{\sqrt{10}} & 0 \\ 0 & -\frac{2}{\sqrt{10}} & -\frac{1}{\sqrt{10}}i & -\frac{1}{\sqrt{2}}i \\ 0 & -\frac{2}{\sqrt{10}}i & -\frac{1}{\sqrt{10}} & -\frac{1}{\sqrt{2}}, \end{pmatrix} \tag{9.7}$$

which lead to the following Heisenberg evolutions of the qumodes:

$$\begin{pmatrix} \hat{x}_1^{(\text{cluster})} + i p_1^{(\text{cluster})} \\ \hat{x}_2^{(\text{cluster})} + i p_2^{(\text{cluster})} \\ \hat{x}_3^{(\text{cluster})} + i p_3^{(\text{cluster})} \\ \hat{x}_4^{(\text{cluster})} + i p_4^{(\text{cluster})} \end{pmatrix} = U \begin{pmatrix} \hat{x}_1 + i p_1 \\ \hat{x}_2 + i p_2 \\ \hat{x}_3 + i p_3 \\ \hat{x}_4 + i p_4 \end{pmatrix}, \tag{9.8}$$

$$= \begin{pmatrix} \frac{1}{\sqrt{2}}e^{s_1}\hat{x}_1^{(0)} + \frac{1}{\sqrt{10}}e^{s_2}\hat{x}_2^{(0)} + \frac{2}{\sqrt{10}}e^{-s_3}\hat{p}_3^{(0)} \\ -\frac{1}{\sqrt{2}}e^{-s_1}\hat{p}_1^{(0)} + \frac{1}{\sqrt{10}}e^{-s_2}\hat{p}_2^{(0)} - \frac{2}{\sqrt{10}}e^{s_3}\hat{x}_3^{(0)} \\ -\frac{2}{\sqrt{10}}e^{s_2}\hat{x}_2^{(0)} + \frac{1}{\sqrt{10}}e^{-s_3}\hat{p}_3^{(0)} + \frac{1}{\sqrt{2}}e^{-s_4}\hat{p}_4^{(0)} \\ \frac{2}{\sqrt{10}}e^{-s_2}\hat{p}_2^{(0)} + \frac{1}{\sqrt{10}}e^{s_3}\hat{x}_3^{(0)} - \frac{1}{\sqrt{2}}e^{s_4}\hat{x}_4^{(0)} \end{pmatrix} + i \begin{pmatrix} \frac{1}{\sqrt{2}}e^{-s_1}\hat{p}_1^{(0)} + \frac{1}{\sqrt{10}}e^{-s_2}\hat{p}_2^{(0)} - \frac{2}{\sqrt{10}}e^{s_3}\hat{x}_3^{(0)} \\ \frac{1}{\sqrt{2}}e^{s_1}\hat{x}_1^{(0)} - \frac{1}{\sqrt{10}}e^{s_2}\hat{x}_2^{(0)} \frac{2}{\sqrt{10}}e^{-s_3}\hat{p}_3^{(0)} \\ -\frac{2}{\sqrt{10}}e^{-s_2}\hat{p}_2^{(0)} - \frac{1}{\sqrt{10}}e^{s_3}\hat{x}_3^{(0)} - \frac{1}{\sqrt{2}}e^{s_4}\hat{x}_4^{(0)} \\ -\frac{2}{\sqrt{10}}e^{s_2}\hat{x}_2^{(0)} + \frac{1}{\sqrt{10}}e^{-s_3}\hat{p}_3^{(0)} - \frac{1}{\sqrt{2}}e^{-s_4}\hat{p}_4^{(0)} \end{pmatrix}. \tag{9.9}$$

We can therefore calculate the precise expressions for the nullifiers, which are given as:

$$\hat{p}_1 - \hat{x}_2 = \sqrt{2}e^{-s_1}\hat{p}_1^{(0)}, \tag{9.10}$$

$$\hat{p}_2 - \hat{x}_1 - \hat{x}_3 = -\frac{5}{\sqrt{10}}e^{-s_3}\hat{p}_3^{(0)} - \frac{1}{\sqrt{2}}e^{-s_4}\hat{p}_4^{(0)}, \tag{9.11}$$

$$\hat{p}_3 - \hat{x}_2 - \hat{x}_4 = \frac{1}{\sqrt{2}}e^{-s_1}\hat{p}_1^{(0)} - \frac{5}{\sqrt{10}}e^{-s_2}\hat{p}_2^{(0)}, \tag{9.12}$$

$$\hat{p}_1 - \hat{x}_2 = -\sqrt{2}e^{-s_4}\hat{p}_4^{(0)}, \tag{9.13}$$

consistent with the formalism detailed in section 2.6 as all of these four nullifiers will tend to 0 as the squeezing parameters s_1, s_2, s_3, s_4 approach infinity. As infinite squeezing is unphysical, we are left with finite noise of the magnitude precisely quantified by these nullifier expressions.

9.3.2 Optical parametric oscillators

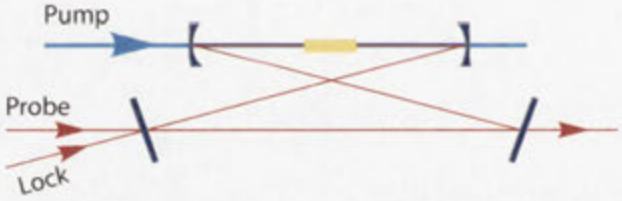

Figure 9.7: Optical parametric oscillators used in cluster state experiments. A non-linear crystal (PPKTP) is placed inside a bow-tie cavity in order to enhance the type I non-linear interaction, and produce squeezed light. The sideband at 1MHz is used to measure and observe squeezing.

The squeezed vacuum states were generated using four identical sub-threshold optical parametric oscillators (OPO) each employing a 10 *mm* long periodically poled $KTiOPO_4$ crystal. Each OPO is a bow-tie cavity with optical path lengths of 500 *mm*. A second harmonic generation (SHG) cavity is employed in order to pump each OPO with the second harmonic of the fundamental beam, at 430 *nm*. The SHG cavity has the same dimensions as each of the OPOs, but we use a $KNbO_3$ crystal instead of PPKTP for the stronger non-linearity. The OPOs used for the generation of the 4-mode cluster state have three inputs:

1) **The Pump beam** (430 *nm*; Blue) is used to facilitate parametric down conversion. It does this by pumping the non-linear crystal within the cavity. In a loss-less scanario, there will be one blue photon entering the crystal, and two infra-red photons exiting the crystal. In this setup, the power of this beam was around 100 mW.

2) **The Lock beam** (860 *nm*; Infra-red) is used in order to control the optical path length of the cavity, and to lock it on resonance. As we don't want the lock beam to interfere with the probe beam, the beam profile is modified in order to create a spatially orthogonal mode. A glass

plate is placed in the beam path such that the mode is converted to a TEM_{01} mode. Now as the TEM_{00} and TEM_{01} modes will resonate at different frequencies, an AOM is used to tune the frequency of the TEM_{01} mode to match the resonance of the TEM_{00} mode in the cavity. In this way, the TEM_{01} mode propagating in the reverse direction doesn't interfere with the output squeezed vacuum TEM_{00} mode.

3) **The Probe beam** (860 nm; Infra-red) is used in order to lock the relative phase of the pump beam. It is modulated before entering the cavity (hundreds of kHz) and the sidebands are used to facilitate the locking of relative phases in other parts of the optical setup. During the measurement phase, the power is set to around 10 μW in order to generate vacuum squeezing.

3.5) There is also an **alignment beam** that is used to align the cavity during the initial construction. It is reverse seeded, and is also used to generate blue light (430 nm) in a second harmonic generation configuration. This blue light will be travelling down the pump beam's optical path, but in the reverse direction, making it useful to align the optical path that couples the doubler and the OPO.

The optical path lengths and output coupler transmission coefficients are summarised in table 9.1.

Cavity	**OPL**	T
OPO Cluster 1	500mm	0.120
OPO Cluster 2	500mm	0.123
OPO Cluster 3	500mm	0.146
OPO Cluster 4	500mm	0.122

Table 9.1: Cavity parameters for four OPOs.

On average, for each cavity the full-width at half-maximum (FWHM) was 17.4 MHz, the free-spectral range (FSR) was 650 MHz, and the finesse was 38.

9.3.3 Verification of the cluster state

In order to verify that the generated quantum state is a 4-mode linear cluster state, each individual entanglement link between the cluster nodes must be measured and the variance of the relevant nullifier must be below a quantum threshold of inseparability. The nullifiers and their measured variances of the cluster state are tabulated below. Each nullifier can be seen as measuring the correlations of neighbouring modes, from the point of view of each of the cluster modes. This is shown graphically in the table for each nullifier.

The entire state is therefore shown to be fully inseparable, as the measured values are below the threshold of 1 [74].

9.3.4 Phase locks

The relative phases between the optical beams depicted in Fig. 9.5 are actively controlled via feedback electronics. Where applicable the Pound-Drever-Hall (PDH) technique is employed [46]. This is the only experiment presented in this thesis where digital control of the phase locks was not employed. All of the feedback electronics used was analogue. Custom-made servo amplifiers and demodulation circuits were designed and created by Ukai and Yukawa [98].

Nullifier variance	Experimental measurement
$\langle\Delta(\hat{p}_1 - \hat{x}_2)^2\rangle$	$0.29 \pm 0.01 (-5.4 \pm 0.2dB)$
$\langle\Delta(\hat{p}_2 - \hat{x}_1 - \hat{x}_3)^2\rangle$	$0.26 \pm 0.01 (-5.8 \pm 0.2dB)$
$\langle\Delta(\hat{p}_3 - \hat{x}_2 - \hat{x}_4)^2\rangle$	$0.30 \pm 0.01 (-5.3 \pm 0.2dB)$
$\langle\Delta(\hat{p}_4 - \hat{x}_3)^2\rangle$	$0.27 \pm 0.01 (-5.8 \pm 0.2dB)$

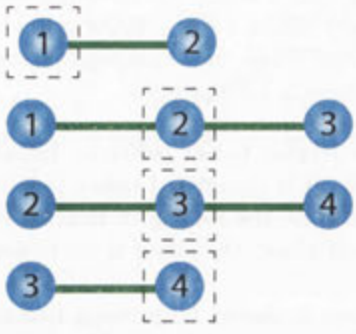

Table 9.2: Measured variances of 4-mode cluster state nullifiers.

The frequencies at which the beams are modulated in order to generate error signals are tabulated below:

System	Type of control	Modulation frequency
Cluster state generation		
OPO 1 parametric gain	AC lock	210 kHz
OPO 2 parametric gain	AC lock	140 kHz
OPO 3 parametric gain	AC lock	98 kHz
OPO 4 parametric gain	AC lock	98 kHz
Beam-splitter ($B^3_{23}(20\%)$	DC lock	
Beam-splitter ($B^3_{12}(50\%)$	AC lock	140 kHz
Beam-splitter ($B^4_{34}(50\%)$	AC lock	210 kHz

Table 9.3: Modulation frequencies of cluster state generation phase locks

9.3.5 Feed-forward of measurements

The electrical circuit required to implement the feed-forward of measurements consists of amplifiers, step attenuators, and filters. The complete circuit is shown in Fig. 9.8.

As we can see the 4th mode of the cluster state is displaced both in x and p in order to complete the teleportation-based measurement results necessary to implement the Fourier transformation. A phase space displacement is optically implemented by interfering a bright displacement beam on a $r = 99.5\%$ beam-splitter with the signal beam. Most of the signal is reflected, and a small but sufficient contribution of the displacement beam is transmitted and the effect is to perform the required phase space displacement on the signal beam. The precise displacement is specified by the gain-adjusted measurement results sent to the electro-optic modulators (EOM) that the displacement beam is propagated through.

In a regular teleportation circuit the measurement results from one homodyne detection will be fed-forward to one EOM. Here, as there are 4 optical modes in the circuit board (the cluster state) we must take combinations of each measurement result. Solving the Heisenberg evolutions for the linear optics network shown in Fig. 9.5 produces the following:

$$\begin{pmatrix} \hat{x}_{out} \\ \hat{p}_{out} \end{pmatrix} = \begin{pmatrix} 0 & 1 \\ -1 & 0 \end{pmatrix} \begin{pmatrix} \hat{x}_{in} \\ \hat{p}_{in} \end{pmatrix} + \begin{pmatrix} -\sqrt{2}t_1 + t_3 \\ \sqrt{2}t_i n t_2 \end{pmatrix}, \tag{9.14}$$

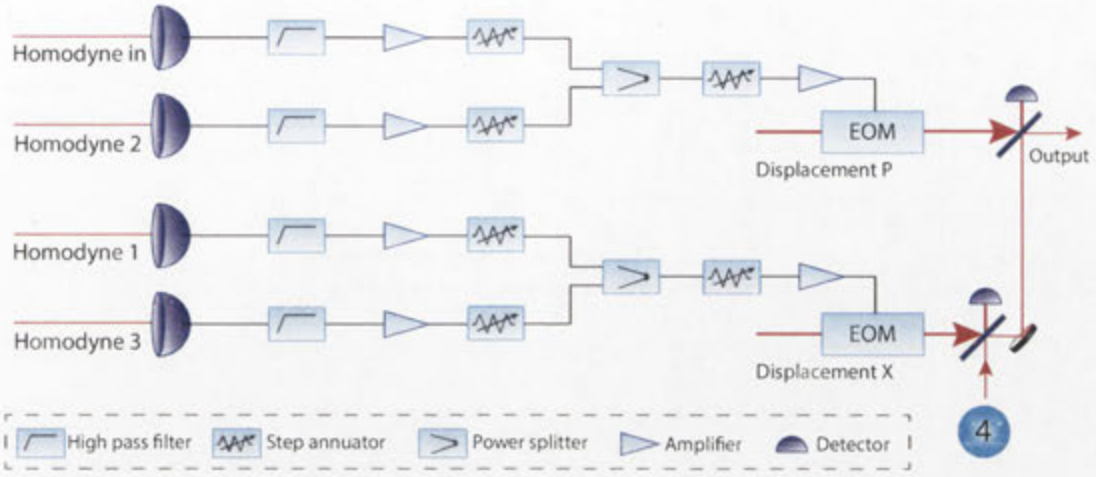

Figure 9.8: Classical channel for Fourier Transformation. Measurement results are combined and fed-forward to electro-optic-modulators (EOM) for phase space displacements.

where we have omitted the extra noise from finite squeezing here for brevity. Therefore the precise expressions to feed-forward are given by:

$$-\begin{pmatrix} -\sqrt{2}t_1 + t_3 \\ \sqrt{2}t_i n t_2 \end{pmatrix}. \tag{9.15}$$

This tells us that the scaled results of homodyne detections 1 and 3 are to displace mode 4 in the x quadrature, and the scaled results of homodyne detections in and 2 are to displace mode 4 in the p quadrature, which we see corresponds to the feed-forward circuit shown in Fig. 9.8. Details of the phase locks are tabulated below.

System	Type of control	Modulation frequency
Cluster computation		
Input mode homodyne measurement	AC lock	140 kHz x, 210 kHz p
mode 1 homodyne measurement	AC lock	140 kHz x, 210 kHz p
mode 2 homodyne measurement	AC lock	210 kHz p, 140 kHz x
mode 3 homodyne measurement	AC lock	140 kHz x, 210 kHz p
mode 4 homodyne measurement	AC lock	210 kHz p, 140 kHz x
Feed-forward output in x	AC lock	140 kHz
Feed-forward output in p	AC lock	210 kHz

Table 9.4: Modulation frequencies of cluster computation phase locks.

9.4 Results

The measurement results for the inputs and outputs of the Fourier transformation are shown in Fig. 9.9. The coherent state input has amplitude 17.7 ± 0.2dB, and the measurement is shown by trace (ii) in Fig. 9.9(A) where the local oscillator is scanned in phase to show both x and p quadratures.

The measurements of the output state after the Fourier transformation is shown in Fig. 9.9(B).

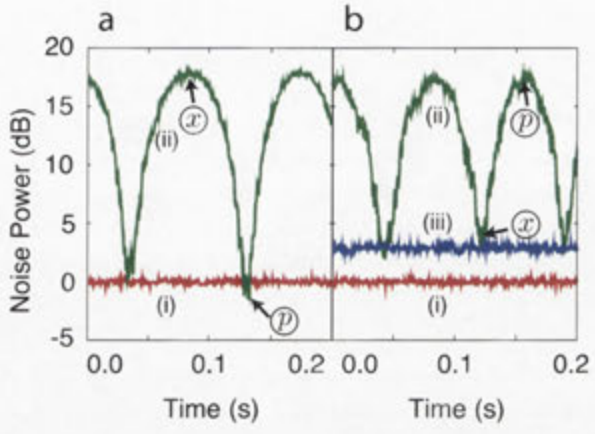

Figure 9.9: Measurements of the Fourier transformation operation. (a) Measurement results of the input state. The shot noise (reference) is shown by trace (i), and the signal is shown in trace (ii) where the local oscillator phase has been scanned in order to show both quadratures. (b) Measurement results of the output state. Trace (i) is again the shot noise, and trace (ii) is the phase-scanned output state. Trace (iii) shows the measurement results of the x quadrature with a vacuum input. Figure created by Ukai, and appears in [98].

The measurements were conducted via a spectrum analyser at measurement frequency 1 MHz with resolution bandwidth 30 kHz and video bandwidth 300 Hz. The peak level of trace (ii) in Fig. 9.9(B) is 17.5±0.2 dB higher than the shot noise level (SNL) of trace (i), which is the same amplitude as the input within errors. The peak amplitude of the input is measured in the x quadrature, while the peak amplitude of the output is obtained by measuring in the p quadrature, corresponding to a 90° rotation in phase space. These measurement results confirm that the Fourier transformation is applied to the input coherent state.
We also use a vacuum state as an input. This provides a way to quantify the quality of the Fourier transformation operation by calculating the fidelity, defined as $F = \langle \Psi_{ideal} | \hat{\rho}_{out} | \Psi_{ideal} \rangle$.
For our experimental setup, the fidelity as given above is:

$$F = \frac{2}{\sqrt{(1 + 4\Delta^2 \hat{x}_{out})(1 + 4\Delta^2 \hat{p}_{out})}}, \tag{9.16}$$

where $\Delta^2 \hat{x}_{out}$ and $\Delta^2 \hat{p}_{out}$ are the variances of the position and momentum operators of the output state, respectively [113]. We measure $\Delta^2 \hat{x}_{out} = 2.9 \pm 0.2$ dB (Fig. 9.9B(iii)), and $\Delta^2 \hat{p}_{out} = 2.8 \pm 0.2$ dB (not shown) above the SNL with our vacuum input state, which corresponds to a fidelity of F=0.68 ± 0.02. This is in good agreement with the theoretical result of $F = 0.71$, calculated by assuming an average squeezing level of −5.5dB (see section 9.3.1). Note that with infinite squeezing (although unphysical) the variances tend to zero, the blue trace of Fig. 9.9B(iii)) will equal the shot noise of trace (i) and the fidelity would equal unity.

9.5 Conclusion and outlook

The important set of universal one-mode LUBO transformations has been demonstrated in this chapter, in an optical setting by using a four-mode cluster state as a resource. We have shown the successful implementation of the Fourier transformation. The squeezing operation was performed by the same experimental setup simply with different homodyne measurement angles. The details were not presented here for the squeezing operation, as I was not involved in that stage of the experiment. They are detailed in the resulting publication of this research project [98].

In the next chapter we detail a multimode gate that allows for the coupling of an arbitrary number of inputs to a cluster state, and the ability to tune the entanglement strength between output modes. Combined with the results presented in the current chapter these operations form the set of universal multimode one-way quantum computations in a Gaussian setting.

Chapter 10

Tuneable entanglement for multimode cluster computation

Quantum networks, used for communication and computation, are formed by entangling the quantum nodes that comprise the network. Any large-scale quantum network will require the tuneability of entanglement between the quantum nodes in the network. A prominent example is the quantum internet, as envisioned by Kimble [114], which requires as much.
In the context of measurement-based quantum computation this can be achieved during the propagation of information through a cluster state, by tuning measurement bases and subsequent corrections. In this chapter we present a tuneable entangling gate, T_Z, which allows for an arbitrary number of unentangled inputs to become entangled, with precise control over the entanglement strength[1]. This control leads to teleporting entanglement onto arbitrary nodes with strengths previously unachievable. This gate is an example of a multimode gate that forms the set of universal mutlimode Gaussian operations when concatenated with the one-mode transformations presented in the previous chapter.

The research in this chapter has yet to appear in a journal publication. Detailed treatments appear in two thesis chapters at the Furusawa laboratory[2] [87, 92].

10.1 Motivation

To date there have been several impressive demonstrations of manipulating single mode inputs through cluster states, in both a deterministic setting as we saw in the previous chapter, and in reference [98], and in a post-selected regime [115]. The higher fidelities achievable in the post-selected setting come at the expense of deterministic control.
The inherent strength of measurement-based quantum computing (MBQC) lies in its ability to efficiently propagate information through a cluster state with a weighted graph [22]; a graph which has edge weights not equal to one. However, the current optical toolbox contains only fixed-strength gates, unable to make sufficient use of the underlying power in the cluster states. For example a fixed-strength multimode gate was demonstrated in [116] that utilised a four-mode cluster in order to entangle 2 input modes with a fixed, untuneable strength. The gate that was teleported onto the inputs in that demonstration was a controlled-phase gate, C_Z, detailed in section 8.5, which always produces the same amount of entanglement between nodes, and cannot be turned off. This is rather inflexible and inefficient. For efficient computation it is necessary to have full

[1] Here, we define "entanglement strength" as the amount by which the symplectic eigenvalue of the partially transposed covariance matrix of the bipartite state is below the separable threshold. See section 10.6 for details.

[2] Statement of contribution: The theory presented in this chapter was derived solely by Shota Yokoyama and Ryuji Ukai, without my contribution. The experiment was performed by Yokoyama, Ukai, and myself.

tuneability of the entanglement strength, due to the consideration of unwanted noise and errors that are inevitably propagated along with the information during computations. While tuneable entanglement has been reported between an ion and the polarization state of a single photon [117], there has not yet been a suitable way to implement this coherent control in a MBQC setting.
After introducing the T_Z gate and providing a theoretical treatment, we present a full implementation of our tuneable entanglement gate within the context of optical measurement-based quantum computation, consistent with the previous chapters in this partition of the thesis. We demonstrate a full implementation of T_Z by propagating two arbitrary, independent inputs through an optical cluster state comprised of three quantum nodes in a linear configuration. The entanglement strength is fully characterised at the output and full tuneability is verified. Full tuneability here is shown to be from zero to maximally entangled. In all instances of low entanglement strength the information of the state is preserved, an important distinction from the trivial case of destroying correlations by adding unwanted noise. Our gate is deterministic and does not rely on post-selection. Further, we show that our gate can be retrofitted to a cluster state of arbitrary size, thus paving the way for efficient and precise control of information propagation through cluster states.

10.2 The tuneable entanglement Gate

We define the *Tuneable Entanglement Gate* (T_Z) as the unitary operator

$$\hat{T}_{\mathrm{Z}}(g) = \mathrm{e}^{ig(\sum_j \hat{x}_j)^2} \tag{10.1}$$

with tuneable gain $g = \tan(\theta)$ and acting on j modes.

Our quantum states are again defined to be quadrature operators $(\hat{x}, \hat{p})$ of the electric field operator, as introduced in section 2.4.2.
$\hat{T}_{\mathrm{Z}}$ is derived from a concatenation of quadratic phase gates $\hat{D}_2(g) = \mathrm{e}^{ig\hat{x}_j^2}$, and non-unity gain controlled phase gates $(\hat{C}_{\mathrm{Z}_{j,k}} = \mathrm{e}^{2ig\hat{x}_j\hat{x}_k})$[32, 24].
The evolution of the T_Z gate acting on an optical mode $\hat{a}_j = \hat{x}_j + i\hat{p}_j$ is represented as

$$\hat{T}_{\mathrm{Z}}^{\dagger}(\hat{x}_j + i\hat{p}_j)\hat{T}_{\mathrm{Z}} = \hat{x}_j + i\left(\hat{p}_j + g\sum_k \hat{x}_k\right). \tag{10.2}$$

The real component is not affected, while the imaginary component is given additional weighted x-quadrature terms.
In order to apply the tuneable entangling gate to a cluster state that has already been created, we define the squeezed T_Z gate, which is straightforwardly defined as a concatenation of N squeezing operators and one T_Z gate:

$$\hat{S}_1 \ldots \hat{S}_{\mathrm{N}}\hat{T}_{\mathrm{Z}}(g) = \hat{S}_1 \ldots \hat{S}_{\mathrm{N}} e^{\frac{1}{\mathrm{N}}g(\hat{\mathrm{x}}_1 + \ldots + \hat{\mathrm{x}}_{\mathrm{N}})^2}. \tag{10.3}$$

We may swap the order of the squeezing operators and $\hat{T}_{\mathrm{Z}}$ if we scale the gain by half:

$$\hat{T}_{\mathrm{Z}}(\tfrac{g}{2})\hat{S}_1 \ldots \hat{S}_{\mathrm{N}} = e^{\frac{1}{\mathrm{N}}g(\hat{\mathrm{x}}_1 + \ldots + \hat{\mathrm{x}}_{\mathrm{N}})^2}\hat{S}_1 \ldots \hat{S}_{\mathrm{N}}. \tag{10.4}$$

Equations 10.3 and 10.4 are equivalent; they both describe the squeezing $\hat{T}_{\mathrm{Z}}$ operator.
The squeezed T_Z gate describes the experimentally more realistic approach, where arbitrary inputs are coupled to the cluster via beam-splitters. This of course is teleportation-based coupling; half teleportations are performed rather than a Bell measurement because only half of the beamsplitter output is measured. This squeezes the input states [118], and hence the decomposition of the

squeezed T_Z gate includes the squeezing operators.

10.2.1 Demonstration on 3-mode cluster

Our proof of principle experimental implementation of the squeezed T_Z gate considers the exemplary case of 2 arbitrary inputs that are propagated through a quantum resource with a tuneable strength of entanglement teleported onto them. The quantum resource used here is a 3-mode continuous-variable cluster state.

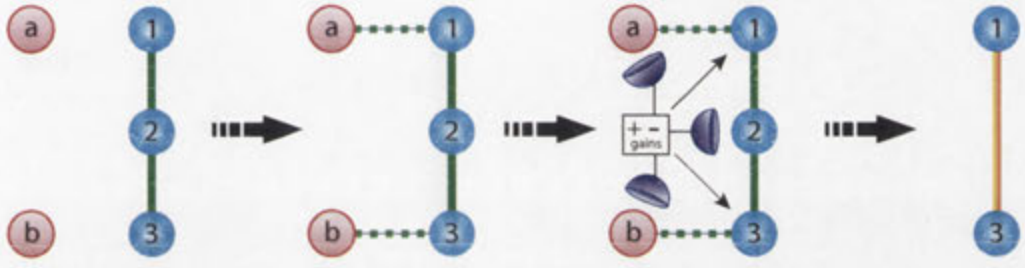

Figure 10.1: Tuneable entanglement gate on a 3-mode cluster. Two arbitrary and independent inputs a and b are teleported through the cluster and have the option of being entangled or not. The dashed green lines indicate beam-splitter coupling. The solid green lines indicate unity-gain edge weights leading to un-weighted nullifiers (see sections 2.6 and 7.2), and the multicoloured line indicates a variable-gain edge weight, leading to variable-strength entanglement.

Figure 10.1 illustrates the progression of the squeezed T_Z gate in our experimental demonstration. A 3-mode linear cluster state is prepared, and two arbitrary inputs a and b are coupled via beam-splitter interactions. The beam-splitters are balanced, and facilitate teleportation-based coupling into the cluster. Homodyne measurements in x are then performed on modes a and b, and a homodyne measurement in θ is performed on mode 2 of the cluster. The measurement results are then used to perform feed-forward corrections to modes 1 and 3, which have become output modes of the cluster state resource. The homodyne measurement angle θ on mode 2 will determine the strength of the entanglement between modes 1 and 3, which are the teleported modes a and b, respectively. See Fig. 10.3 for the full optical schematic, and Fig. 10.4 for the full electronic schematic detailing the feed-forwards.
The squeezed T_Z gate for a two-mode input is given as follows:

$$\hat{S}_1\hat{S}_2\hat{T}_{Z,2}(g) = \hat{S}_1\hat{S}_2 e^{\frac{1}{\sqrt{2}}g(\hat{x}_1+\hat{x}_2)^2} = \hat{T}_{Z,2}(\frac{g}{2})\hat{S}_1\hat{S}_2 = e^{\frac{1}{\sqrt{2}}g(\hat{x}_1+\hat{x}_2)^2}\hat{S}_1\hat{S}_2, \tag{10.5}$$

where the subscript 2 denotes that the squeezed T_Z gate is operating on 2 modes. For the rest of this chapter we will deal with the experimental demonstration and so we will omit the subscript. The squeezed T_Z gate can be decomposed into three operators:

$$\hat{T}_Z(\frac{g}{2})\hat{S}_1\hat{S}_2 = e^{i\frac{g}{2}\hat{x}_1^2}e^{i\frac{g}{2}\hat{x}_2^2}e^{2i\frac{g}{2}\hat{x}_1\hat{x}_2}\hat{S}_1\hat{S}_2, \tag{10.6}$$

comprising of two single-mode squeezing operations, two single-mode quadratic phase gates, and a two-mode controlled phase gate.
This operator describes the process of two arbitrary inputs that are coupled to a 3-mode linear cluster state and propagated through the cluster with a tuneable entangling gate being teleported onto them at the output. The gain of the graphical edge weight between the output modes is dictated by the homodyne detection angle of the central mode (mode 2) in the 3-mode linear

cluster. The input output relations are represented as

$$\begin{pmatrix} \hat{x}'_a \\ \hat{p}'_a \\ \hat{x}'_b \\ \hat{p}'_b \end{pmatrix} \rightarrow \begin{pmatrix} \hat{x}'_1 \\ \hat{p}'_1 \\ \hat{x}'_3 \\ \hat{p}'_3 \end{pmatrix} = \begin{pmatrix} \sqrt{2} & 0 & 0 & 0 \\ \frac{g}{\sqrt{2}} & \frac{1}{\sqrt{2}} & \frac{g}{\sqrt{2}} & 0 \\ 0 & 0 & \sqrt{2} & 0 \\ \frac{g}{\sqrt{2}} & 0 & \frac{g}{\sqrt{2}} & \frac{1}{\sqrt{2}} \end{pmatrix} \begin{pmatrix} \hat{x}_a \\ \hat{p}_a \\ \hat{x}_b \\ \hat{p}_b \end{pmatrix} + \hat{\boldsymbol{\delta}}, \tag{10.7}$$

where $\hat{\boldsymbol{\delta}} = (0, \hat{\delta}_1 + g\hat{\delta}_2, 0, \delta_3 + g\hat{\delta}_2)^T$ are the excess noise terms arising from finite squeezing. See equation 10.14 for expressions of these noise terms. Equation 10.7 can be decomposed into three matrices as in equation 10.6 to give:

$$\begin{pmatrix} \hat{x}'_a \\ \hat{p}'_a \\ \hat{x}'_b \\ \hat{p}'_b \end{pmatrix} \rightarrow \begin{pmatrix} \hat{x}'_1 \\ \hat{p}'_1 \\ \hat{x}'_3 \\ \hat{p}'_3 \end{pmatrix} = T_{\mathrm{Z}}(\frac{g}{2}) S_1 S_2 \begin{pmatrix} \hat{x}_a \\ \hat{p}_a \\ \hat{x}_b \\ \hat{p}_b \end{pmatrix}, \tag{10.8}$$

where we have the following matrices:

$$T_{\mathrm{Z}}(g) = \begin{pmatrix} 1 & 0 & 0 & 0 \\ g & 1 & g & 0 \\ 0 & 0 & 1 & 0 \\ g & 0 & g & 1 \end{pmatrix}, \qquad S_1 = \begin{pmatrix} \sqrt{2} & 0 & 0 & 0 \\ 0 & \frac{1}{\sqrt{2}} & 0 & 0 \\ 0 & 0 & 1 & 0 \\ 0 & 0 & 0 & 1 \end{pmatrix}, \qquad S_2 = \begin{pmatrix} 1 & 0 & 0 & 0 \\ 0 & 1 & 0 & 0 \\ 0 & 0 & \sqrt{2} & 0 \\ 0 & 0 & 0 & \frac{1}{\sqrt{2}} \end{pmatrix}. \tag{10.9}$$

We see that the single mode squeezers perform fixed-strength squeezing at 3 dB, as a result of the half-teleportation beam-splitter coupling [118].

10.3 Experimental demonstration

The same continuous-wave Ti:sapphire laser detailed in the previous chapter for the one-mode Gaussian transformation experiment is employed here. In fact, the bulk of the optics and electronic equipment used in this experiment was the same equipment used in the experiment detailed in the previous chapter. Modifications to the optical layout were designed and carried out largely by Ryuji Ukai and Shota Yokoyama. A major overhaul of the control system was requried for this experiment that would facilitate the active control and automated phase locking required to perform the measurement-based quantum computation. An extensive digital control suite was designed and implemented solely by myself. The experiment was performed by the three of us.

10.3.1 Generation of the resource state

The 3-mode linear cluster state was used in this demonstration as a blank quantum circuit board.

Figure 10.2: Generation of the 3-mode cluster state resource. Three squeezed modes are combined on two beam-splitters in order to generate a 3-mode linear cluster state. S: Squeezing operation, F: Fourier transform, $BS1$: beam-splitter with reflectivity given by ratio indicated.

The unitary describing this network is given as:

$$U = F_1 B_{12}^{(1)} \left(\frac{1}{\sqrt{2}}\right) F_1 F_2 B_{23}^{(1)} \left(\sqrt{\frac{2}{3}}\right) S_1(s_1) S_2(s_2) S_3(s_3). \tag{10.10}$$

As was the case in the generation of the 4-mode cluster state, we omit the squeezing operators from hereon in to ensure the network only comprises beam-splitter operations and relative phase shifts. The unitary matrix describing the network that transforms 3 independent p-squeezed modes into the linear 3-mode cluster state is then given as:

$$U = \begin{pmatrix} \frac{1}{\sqrt{2}} & \frac{1}{\sqrt{3}} i & -\frac{1}{\sqrt{6}} \\ \frac{1}{\sqrt{2}} i & \frac{1}{\sqrt{3}} & \frac{1}{\sqrt{6}} i \\ 0 & \frac{1}{\sqrt{3}} i & \frac{2}{\sqrt{6}}, \end{pmatrix} \tag{10.11}$$

which lead to the following Heisenberg evolutions of the qumodes:

$$\begin{pmatrix} \hat{x}_1^{(\text{cluster})} + i\hat{p}_1^{(\text{cluster})} \\ \hat{x}_2^{(\text{cluster})} + i\hat{p}_2^{(\text{cluster})} \\ \hat{x}_3^{(\text{cluster})} + i\hat{p}_3^{(\text{cluster})} \end{pmatrix} = U \begin{pmatrix} \hat{x}_1 + i\hat{p}_1 \\ \hat{x}_2 + i\hat{p}_2 \\ \hat{x}_3 + i\hat{p}_3 \end{pmatrix} \tag{10.12}$$

$$= \begin{pmatrix} \frac{1}{\sqrt{2}} e^{s_1} \hat{x}_1^{(0)} - \frac{1}{\sqrt{3}} e^{-s_2} \hat{p}_2^{(0)} - \frac{1}{\sqrt{6}} e^{s_3} \hat{x}_3^{(0)} \\ -\frac{1}{\sqrt{2}} e^{-s_1} \hat{p}_1^{(0)} + \frac{1}{\sqrt{3}} e^{s_2} \hat{x}_2^{(0)} - \frac{1}{\sqrt{6}} e^{-s_3} \hat{p}_3^{(0)} \\ -\frac{1}{\sqrt{3}} e^{-s_2} \hat{p}_2^{(0)} + \frac{2}{\sqrt{6}} e^{s_3} \hat{x}_3^{(0)} \end{pmatrix} + i \begin{pmatrix} \frac{1}{\sqrt{2}} e^{-s_1} \hat{p}_1^{(0)} + \frac{1}{\sqrt{3}} e^{s_2} \hat{x}_2^{(0)} - \frac{1}{\sqrt{6}} e^{-s_3} \hat{p}_3^{(0)} \\ \frac{1}{\sqrt{2}} e^{s_1} \hat{x}_1^{(0)} + \frac{1}{\sqrt{3}} e^{-s_2} \hat{p}_2^{(0)} \frac{1}{\sqrt{6}} e^{s_3} \hat{x}_3^{(0)} \\ \frac{1}{\sqrt{3}} e^{s_2} \hat{x}_2^{(0)} + \frac{2}{\sqrt{6}} e^{-s_3} \hat{p}_3^{(0)} \end{pmatrix}. \tag{10.13}$$

We can therefore calculate the precise expressions for the nullifiers, which are given as:

$$\hat{\delta}_1 \equiv \hat{p}_1 - \hat{x}_2 = \sqrt{2} e^{-s_1} \hat{p}_1^{(0)}, \tag{10.14a}$$

$$\hat{\delta}_2 \equiv \hat{p}_2 - \hat{x}_1 - \hat{x}_3 = \sqrt{3} e^{-s_2} \hat{p}_2^{(0)}, \tag{10.14b}$$

$$\hat{\delta}_3 \equiv \hat{p}_3 - \hat{x}_2 = \frac{1}{\sqrt{2}} e^{-s_1} \hat{p}_1^{(0)} - \frac{3}{\sqrt{6}} e^{-s_3} \hat{p}_3^{(0)}. \tag{10.14c}$$

As was the case for the 4-mode linear cluster state described in section 9.3.1, all of these three nullifiers will tend to 0 as the squeezing parameters s_1, s_2, s_3, approach infinity. The finite noise generated from imperfect squeezing resources will be teleported through the cluster, and the magnitude of the noise is quantified by these nullifier expressions.

Verification of entanglement in 3-mode cluster state

In order to verify that the generated quantum state is a 3-mode linear cluster state, each individual entanglement link between the cluster nodes must be measured and the variance of the relevant nullifier must be below a quantum threshold of inseparability. The nullifiers and their measured variances of the cluster state are tabulated below. Each nullifier can be seen as measuring the correlations of neighbouring modes, from the point of view of each of the cluster modes. This is shown graphically in table 10.1 for each nullifier.

The entire state is therefore shown to be fully inseparable, as the measured values are below the threshold of 1 [74]. Note that these measurements are taken before the coupling of the input modes, and subsequent optical network. The measured squeezing levels of the 3 squeezed vacuum states after the entire optical network has been implemented is calculated to be approximately 4.5 dB each (see section 10.4). As mentioned previously the bulk of the optics in the current experiment was

Nullifier variance	Experimental measurement
$\langle\Delta(\hat{p}_1 - \hat{x}_2)^2\rangle$	$0.29 \pm 0.01 (-5.3 \pm 0.2dB)$
$\langle\Delta(\hat{p}_2 - \hat{x}_1 - \hat{x}_3)^2\rangle$	$0.30 \pm 0.01 (-5.2 \pm 0.2dB)$
$\langle\Delta(\hat{p}_3 - \hat{x}_2)^2\rangle$	$0.28 \pm 0.01 (-5.6 \pm 0.2dB)$

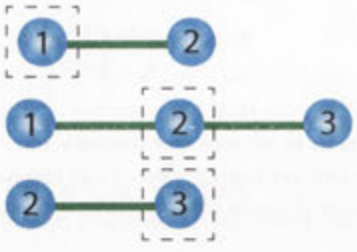

Table 10.1: Measured variances of 3-mode cluster state nullifiers.

also used in the experiment described in the previous chapter of this thesis. Specifically, the three OPOs used in this experiment are the same OPOs described in section 9.3.2. The transmissivities of the output couplers are 12.3 %, 11.8 %, and 12.1 %, respectively. The pump powers used were $62mW$, $72mW$, and $73mW$, corresponding to parametric gains for the three OPOs of 4.9, 5.2, and 5.5, respectively. These regimes were found to be optimal for the current experiment considering a trade-off between high levels of squeezing and the purity of the squeezed light.
The interference visibilities of the modes mixing at the two beam-splitters used for the generation of the cluster state resource are given in the table below.

Optical beam 1	Optical beam 2	Beam-splitter	Visibility
Sqz. 3	Sqz. 2	$B_{23}^{(1)}\left(\sqrt{\frac{2}{3}}\right)$, entangling modes 2 and 3	98.1 %
Sqz. 2	Sqz. 1	$B_{12}^{(1)}\left(\frac{1}{\sqrt{2}}\right)$, entangling modes 1 and 2	97.9 %

Table 10.2: Interference visibilities of cluster state generation. Uncertainties are ±0.1%.

"Sqz. 1"(2,3) is short for squeezed mode 1(2,3), exiting OPO 1(2,3).

10.3.2 Implementing the measurement-based quantum computation

The entire optical circuit is depicted in Fig. 10.3. Input modes are either vacuum states or coherent states, defined to be encoded within the 1 MHz sideband of the optical carrier. Two Coherent states are generated by modulating two independent optical beams with piezo-electric transducers (PZTs) at 1 MHz. These are indicated by the two blue spheres in Fig. 10.3 marked as modes a and b.

The *Cluster preparation* area of Fig. 10.3 is equivalent to the circuit diagram of the beam-splitter network shown in Fig. 10.2. The two input modes a and b are then mixed on balanced beam-splitters with the outer modes of the linear cluster, as can be seen in the *Tuneable Z Gate* area of the same figure. Once the input modes a and b have been coupled into the cluster, they are referred to as cluster modes a and b. Three homodyne detections are performed on cluster modes a, 2, and b. The two measurement angles of cluster modes a and b are fixed as x-quadrature measurements. The homodyne measurement angle of mode 2 is tuned between 0^o and 63.4^o, corresponding to different operations. For the rest of the chapter, we will assume that whenever a homodyne measurement angle θ is mentioned, we will be referring to the measurement of cluster mode 2. The seven different measurement angles used, and the corresponding $g = \tan(\theta)$ values are shown in table 10.3.

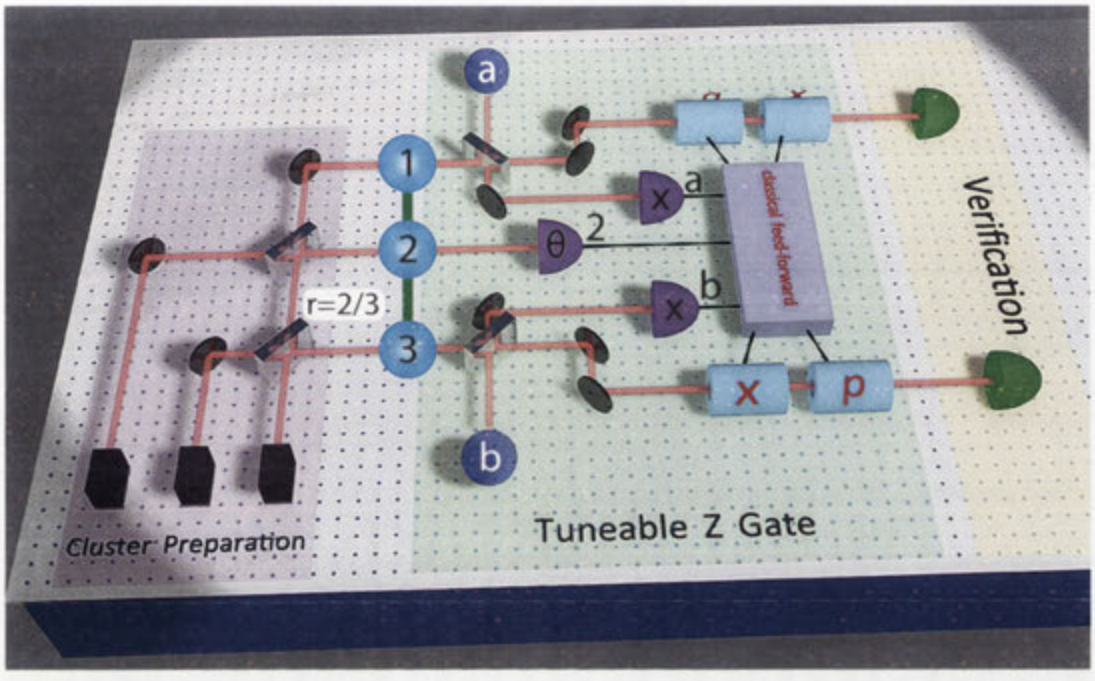

Figure 10.3: Experimental schematic of tuneable entanglement gate on a 3-mode cluster. All beam-splitters are balanced ($r = \frac{1}{2}$) with the exception of the first beam-splitter in *Cluster Preparation*, which is marked to have reflectivity $r = \frac{2}{3}$. The resource 3-mode linear cluster state is first prepared in *Cluster Praparation*. The tuneable entangling gate T_Z is implemented in *Tuneable Z Gate*, and the entanglement in the teleported output state is verified in *Verification*.

θ	0.0^o	11.3^o	26.6^o	35.3^o	45.0^o	54.7^o	63.4^o
$g = \tan(\theta)$	0	$\frac{1}{5}$	$\frac{1}{2}$	$\frac{1}{\sqrt{2}}$	1	$\sqrt{2}$	2

Table 10.3: Measurement angles of homodyne 2.

Finally, the output modes of the measurement-based quantum computation are measured in the *Verification* area of the schematic, where the level of entanglement between the output modes is quantified (see section 10.6). We now calculate the precise expressions of the feed-forward process. After the beam-splitter interactions of input modes a and b with cluster modes 1 and 3 respectively, we have the following expressions for all of the modes in the Heisenberg picture:

$$\begin{aligned}
\hat{x}_1^{(out)} + i\hat{p}_1^{(out)} &= \frac{1}{2}\hat{x}_1 - \frac{1}{\sqrt{6}}\hat{p}_2 - \frac{1}{\sqrt{12}}\hat{x}_3 + \frac{1}{\sqrt{2}}\hat{x}_a + i\left(\frac{1}{2}\hat{p}_1 + \frac{1}{\sqrt{6}}\hat{x}_2 - \frac{1}{\sqrt{12}}\hat{p}_3 + \frac{1}{\sqrt{2}}\hat{p}_a\right) \\
\hat{x}_2^{(out)} + i\hat{p}_2^{(out)} &= -\frac{1}{2}\hat{p}_1 + \frac{1}{\sqrt{3}}\hat{x}_2 - \frac{1}{\sqrt{6}}\hat{p}_3 + i\left(\frac{1}{\sqrt{2}}\hat{x}_1 + \frac{1}{\sqrt{3}}\hat{p}_2 + \frac{1}{\sqrt{6}}\hat{x}_3\right) \\
\hat{x}_3^{(out)} + i\hat{p}_3^{(out)} &= \frac{1}{2}\hat{x}_b - \frac{1}{\sqrt{6}}\hat{p}_2 + \frac{1}{\sqrt{3}}\hat{x}_3 + i\left(\frac{1}{\sqrt{2}}\hat{p}_b + \frac{1}{\sqrt{6}}\hat{x}_2 + \frac{1}{\sqrt{3}}\hat{p}_3\right) \\
\hat{x}_a^{(out)} + i\hat{p}_a^{(out)} &= -\frac{1}{2}\hat{x}_1 + \frac{1}{\sqrt{6}}\hat{p}_2 + \frac{1}{\sqrt{12}}\hat{x}_3 + \frac{1}{\sqrt{2}}\hat{x}_a + i\left(-\frac{1}{2}\hat{p}_1 - \frac{1}{\sqrt{6}}\hat{x}_2 + \frac{1}{\sqrt{12}}\hat{p}_3 + \frac{1}{\sqrt{2}}\hat{p}_a\right) \\
\hat{x}_b^{(out)} + i\hat{p}_b^{(out)} &= -\frac{1}{2}\hat{x}_b + \frac{1}{\sqrt{6}}\hat{p}_2 - \frac{1}{\sqrt{3}}\hat{x}_3 + i\left(\frac{1}{\sqrt{2}}\hat{p}_b - \frac{1}{\sqrt{6}}\hat{x}_2 - \frac{1}{\sqrt{3}}\hat{p}_3\right)
\end{aligned} \tag{10.15}$$

The 3-mode cluster state can be viewed as a blank circuit board before the homodyne measurements and subsequent feed-forward operations, with the measurement angle θ the tuneable parameter that will determine the logic circuit that is imprinted onto the cluster. The measurement results of the three homodyne detections are given as:

$$\hat{s}_a = \hat{x}_a^{(out)}, \qquad \hat{s}_2 = \hat{x}_2^{(out)} \cos(\theta) + \hat{p}_2 \sin(\theta), \qquad \hat{s}_b = \hat{x}_b^{(out)}. \tag{10.16}$$

After the homodyne detections on cluster modes a, 2, and b have been performed, but before the cluster modes 1 and 3 have been displaced in phase space by the scaled measurement results, modes 1 and 3 have the following expressions:

$$\begin{aligned}
\begin{pmatrix} \hat{x}_1^{(proj)} \\ \hat{p}_1^{(proj)} \\ \hat{x}_3^{(proj)} \\ \hat{p}_3^{(proj)} \end{pmatrix} &= \begin{pmatrix} \sqrt{2} & 0 & 0 & 0 \\ -\frac{\tan(\theta)}{\sqrt{2}} & \frac{1}{\sqrt{2}} & -\frac{\tan(\theta)}{\sqrt{2}} & 0 \\ 0 & 0 & \sqrt{2} & 0 \\ -\frac{\tan(\theta)}{\sqrt{2}} & 0 & -\frac{\tan(\theta)}{\sqrt{2}} & \frac{1}{\sqrt{2}} \end{pmatrix} \begin{pmatrix} \hat{x}_a \\ \hat{p}_a \\ \hat{x}_b \\ \hat{p}_b \end{pmatrix} + \\
&+ \begin{pmatrix} -1 & 0 & 0 \\ \tan(\theta) & \tan(\theta) & \frac{1}{\sqrt{2}\cos(\theta)} \\ 0 & -1 & 0 \\ \tan(\theta) & \tan(\theta) & \frac{1}{\sqrt{2}\cos(\theta)} \end{pmatrix} \begin{pmatrix} \hat{s}_a \\ \hat{s}_b \\ \hat{s}_2 \end{pmatrix} + \begin{pmatrix} 0 \\ \frac{1}{\sqrt{2}}\hat{\delta}_1 - \frac{1}{\sqrt{2}}\tan(\theta)\hat{\delta}_2 \\ 0 \\ \frac{1}{\sqrt{2}}\hat{\delta}_3 - \frac{1}{\sqrt{2}}\tan(\theta)\hat{\delta}_2 \end{pmatrix},
\end{aligned} \tag{10.17}$$

where the superscripts "proj" indicate that the modes have been projected into their current state by the measurements of the other cluster modes. The column vector containing the scaled nullifiers is due to finite squeezing. In the limit of infinite squeezing this nullifier column vector tends to zero. We have therefore calculated the precise phase space displacements required in order to perform our desired quantum computation. After we implement the following feed-forward:

$$\begin{aligned}
&\hat{X}_1(s_a)\,\hat{Z}_1\left(-\tan(\theta)s_a - \tan(\theta)s_b - \frac{1}{\sqrt{2}\cos(\theta)}s_2\right) \times \\
&\times \hat{X}_3(s_b)\,\hat{Z}_3\left(-\tan(\theta)s_a - \tan(\theta)s_b - \frac{1}{\sqrt{2}\cos(\theta)}s_2\right),
\end{aligned} \tag{10.18}$$

the output modes are given by:

$$\begin{pmatrix} \hat{x}_1^{(tele)} \\ \hat{p}_1^{(tele)} \\ \hat{x}_3^{(tele)} \\ \hat{p}_3^{(tele)} \end{pmatrix} = \begin{pmatrix} \sqrt{2} & 0 & 0 & 0 \\ -\frac{\tan(\theta)}{\sqrt{2}} & \frac{1}{\sqrt{2}} & -\frac{\tan(\theta)}{\sqrt{2}} & 0 \\ 0 & 0 & \sqrt{2} & 0 \\ -\frac{\tan(\theta)}{\sqrt{2}} & 0 & -\frac{\tan(\theta)}{\sqrt{2}} & \frac{1}{\sqrt{2}} \end{pmatrix} \begin{pmatrix} \hat{x}_a \\ \hat{p}_a \\ \hat{x}_b \\ \hat{p}_b \end{pmatrix} + \begin{pmatrix} 0 \\ \frac{1}{\sqrt{2}}\hat{\delta}_1 - \frac{1}{\sqrt{2}}\tan(\theta)\hat{\delta}_2 \\ 0 \\ \frac{1}{\sqrt{2}}\hat{\delta}_3 - \frac{1}{\sqrt{2}}\tan(\theta)\hat{\delta}_2 \end{pmatrix}, \tag{10.19}$$

where the superscripts "tele" indicate that the teleportation process has been performed.

10.3.3 Feed-forward of measurement results

In order to implement the classical corrections necessary to complete the measurement-based quantum computations, we employ displacement beams that interfere with cluster modes 1 and 3 imparting desired phase space displacements. The complete circuit is displayed in Fig. 10.4.

The gains are calculated and implemented in the following way. First we apply phase modulation at 1 MHz to the probe beam of OPO 3, so that it appears on $\hat{x}_3$. Then while measuring x at homodyne a, we feed-forward the result scaled by $gain_{a\to 1x}$ to cluster mode 1 via EOM $1x$.

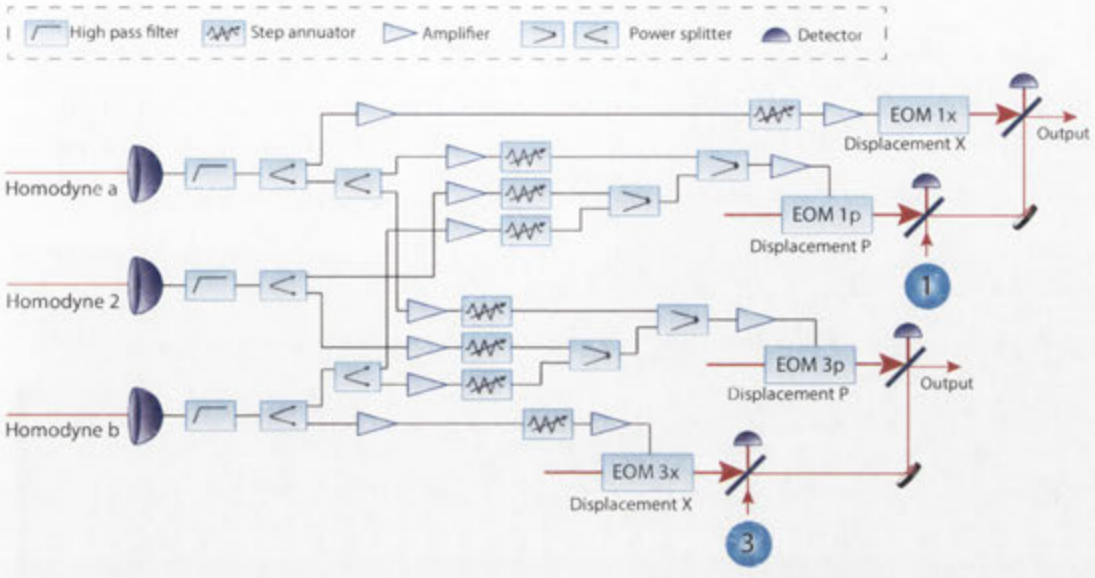

Figure 10.4: Classical channel for implementing squeezed T_Z gate. All amplifiers before step attenuators have phase shifters included in their circuit. EOM: electro-optic modulator.

While viewing the modulation peak on a spectrum analyser we adjust the gain until the peak disappears, indicative of a precise gain value. We can calculate the precise value that the gain $gain_{a\to 1x}$ has been set to by referring to the Heisenberg evolutions expressed in equations (10.15). The coefficients of $\hat{x}_3$ are $\frac{1}{\sqrt{12}}$ for cluster mode a, and $-\frac{1}{\sqrt{12}}$ for cluster mode 1. Therefore by solving the following expression,

$$gain_{a\to 1x}\left(\frac{1}{\sqrt{12}}\hat{x}_3\right) - \frac{1}{\sqrt{12}}\hat{x}_3 = 0, \tag{10.20}$$

we arrive at $gain_{a\to 1x} = 1$.

- We repeat this procedure with the same modulation on $\hat{x}_3$ but this time feed-forward the homodyne measurement of cluster mode b in x to EOM $3x$ and set the gain to $gain_{b\to 3x} = 1$.
- We then apply phase modulation to OPO 2, so that it appears on $\hat{x}_2$ and feed-forward the x measurement of homodyne 2 to EOM $1p$ and set the gain to $gain_{2\to 1p} = -\frac{1}{\sqrt{2}}$.
- With the same phase modulation on $\hat{x}_3$ and the same homodyne measurement result, we feed-forward to EOM $3p$ and set the gain to $gain_{2\to 3p} = -\frac{1}{\sqrt{2}}$.

Next we apply phase modulation on $\hat{x}_3$ and feed-forward the measurement results of two homodyne detections to EOM $1p$ in order to set the correct gain.

- The two homodyne measurements are x at homodyne a and p at homodyne 2. This allows us to set the gain to $gain_{a\to 1p} = -\sqrt{2}gain_{2\to 1p}$. As we set the gain to $gain_{2\to 1p} = -\frac{1}{\sqrt{2}}$ previously, we are left with $gain_{a\to 1p} = 1$.
- We repeat the above procedure with the same modulation on $\hat{x}_3$ and the same homodyne measurements x at homodyne a, and p at homodyne 2, and feed-forward to EOM $3p$. We arrive at $gain_{a\to 3p} = 1$.
- Again with the same modulation on $\hat{x}_3$ we now feed-forward the homodyne measurements of x at homodyne b, and p at homodyne 2 to EOM $1p$ in order to set $gain_{b\to 1p} = -\frac{1}{2}$.

- Finally with the same modulation and homodyne measurements we feed-forward to EOM $3p$ and set the gain to $gain_{b\to 3p} = -\frac{1}{2}$.

We have therefore set the gains of each of the 8 electronic signals that are fed to the 4 EOMs, depicted in Fig. 10.4. While the precise values of these gains are now known due to the procedure specified above, they are not precisely equal to the desired gains required to implement the feed-forward operation derived in equation 10.18. Finally, we make the following adjustments:

- Scale $gain_{a\to 1p}$ and $gain_{a\to 3p}$ by $-\tan(\theta)$, by adjusting the relevant step annuators in Fig. 10.4 by $-20\log_{10}(\tan(\theta))\,dB$,
- Scale $gain_{b\to 1p}$ and $gain_{b\to 3p}$ by $2\tan(\theta)$, by adjusting the relevant step annuators in Fig. 10.4 by $-20\log_{10}(2\tan(\theta))\,dB$,
- Scale $gain_{2\to 1p}$ and $gain_{2\to 3p}$ by $\frac{1}{\cos(\theta)}$, by adjusting the relevant step annuators in Fig. 10.4 by $-20\log_{10}\left(\frac{1}{\cos(\theta)}\right)dB$.

Mode overlaps by visibility

The interference visibilities of the various modes being mixed at beam-splitters quantify the mode overlaps, and affect the efficiency of the cluster computation. In order to measure the visibilities at the beam-splitters in the *Tuneable Z Gate* area of the optical network, some of the OPO outputs need to be blocked to ensure that the beams we are interfering only have one mode each. For example, cluster mode 1 is a mixture of the three squeezed modes generated by the three OPOs. When we are measuring the visibility between the input mode a and cluster mode 1, we need to block two of the squeezed outputs in the *Cluster Preparation* area so that we can measure the precise mode overlap of the two beams. The visibilities of every pair of beams mixed in during the *Tuneable Z Gate* phase of the schematic are given in the table 10.4.

Mode; beam 1	Beam 2	Beam-splitter	Visibility
Sqz. 2; Cluster 1	Input a	Teleportation-based coupling of input mode a	97.4 %
Sqz. 2; Cluster 3	Input b	Teleportation-based coupling of input mode b	96.9 %
Sqz. 2; Cluster a	Local oscillator 1	Homodyne measurement of cluster mode a	96.1 %
Sqz. 2; Cluster 2	Local oscillator 2	Homodyne measurement of cluster mode 2	98.1 %
Sqz. 3; Cluster b	Local oscillator 3	Homodyne measurement of cluster mode b	97.7 %
Sqz. 2; Cluster 1	Displacement $1x$	Feed-forward to cluster mode 1 output in x	97.2 %
Sqz. 2; Cluster 1	Displacement $1p$	Feed-forward to cluster mode 1 output in p	98.0 %
Sqz. 3; Cluster 3	Displacement $3x$	Feed-forward to cluster mode 3 output in x	97.9 %
Sqz. 3; Cluster 3	Displacement $3p$	Feed-forward to cluster mode 3 output in p	98.1 %

Table 10.4: Interference visibilities for the *Tuneable Z Gate*. Uncertainties are ±0.1%.

For the beams containing multiple modes, the mode being interfered is indicated in the first column of the table by the specification of which mode in which beam is propagating. "Sqz. 2" is short for squeezed mode 2, exiting OPO 2. The assumption is that the other modes have been blocked at the output of their respective OPOs.

10.3.4 Digital control of the experiment

Previous experiments performed on the same optical bench [98, 116] were pushing the limits in terms of complexity, and ultimately stability. Keeping all of the phase locks in the desired regimes while performing sufficient measurements to gather statistics about the output states was becoming

increasingly infeasible. For this reason we completely re-designed the control system for the current experiment. Whereas previous experiments had relied solely on analogue electronics, the new control system was built around field-programmable gate arrays (FPGAs), leading to fully digital control of all of the phase locks. The control system is briefly outlined in section 4.2. The entire system can be viewed as an extension of a system developed by Ben Sparkes, described in reference [49].

Hardware and software

A total of 5 FPGA cards are used, each from National Instruments (NI). We use 4 × NI PXI-7853R cards and 1 × NI PXI-7854R card, housed in a 5-slot PXI chassis (NI PXI-1033).

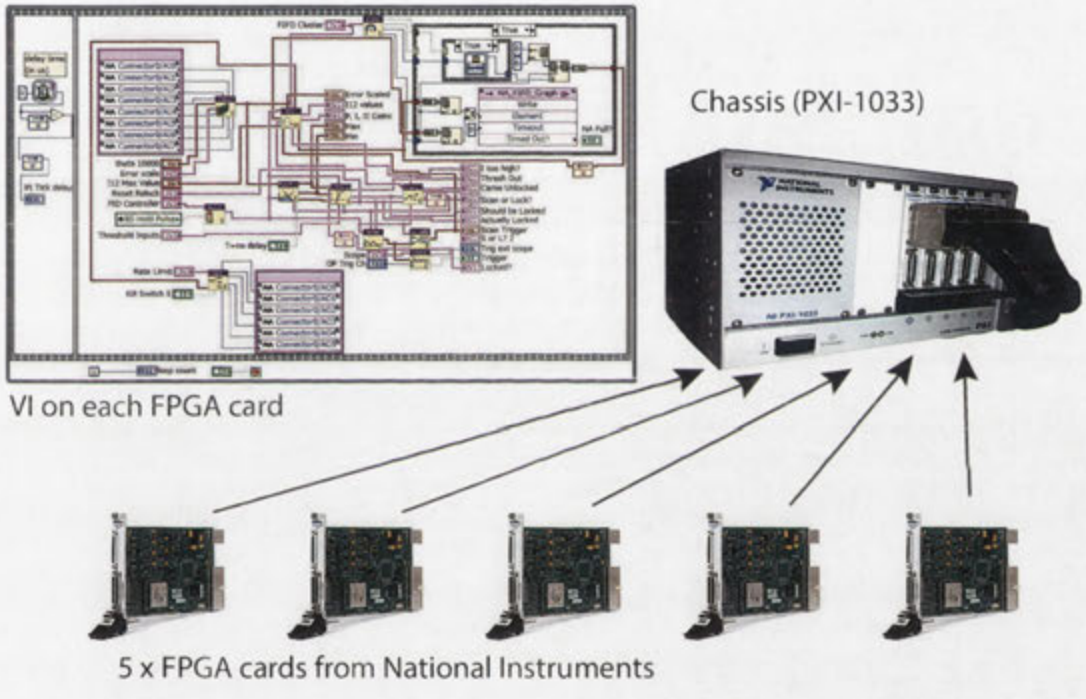

Figure 10.5: Overview of digital control suite. Digital logic that implements the control of various phase locks is compiled on field-programmable gate array cards that are housed in a PXI chassis external to the PC. Each of the 5 FPGA cards has a similar version of the control software that has been compiled independently. All control is then performed via a graphical user interface running on the PC.

A modest quantum optics experiment in a typical lab might employ one or two FPGA cards. The complexity of the current experiment is captured well by the fact that we must employ 5 cards, as shown in Fig. 10.5. Each of the FPGA cards has 8 analogue inputs with analogue to digital converters (ADCs) capable of up to 750 kHz sampling, at a resolution of 16 bits. There are 8 corresponding outputs of the same resolution, with digital to analogue converters (DACs) running at up to 1 MHz. The suite is limited by the loop speed of the software (termed the VI) running on the FPGA which was clocked to be typically between 400 and 550 kHz for our implementation. Breakout boxes for BNC inputs and outputs were custom made based on the SCB-68A input/output boxes from NI. The software used to program the digital control suite was National Instruments LabVIEW 2010, operating on Windows 7, 64-bit, on a desktop PC. The entire suite contains more than 300 individual subVIs that are accessed and controlled by one top level VI that is running on the PC.

Phase locks

There are 33 phase locks across the 5 FPGA cards. Each of the FPGAs runs a compiled variation of the VI outlined in Fig. 10.5. Each phase lock is controlled via a PII controller (proportional gain, integrator gain, and integrator^2 gain) that is a modified version of a custom-made controller designed by Sparkes [49], and can be seen in Fig. 10.6.

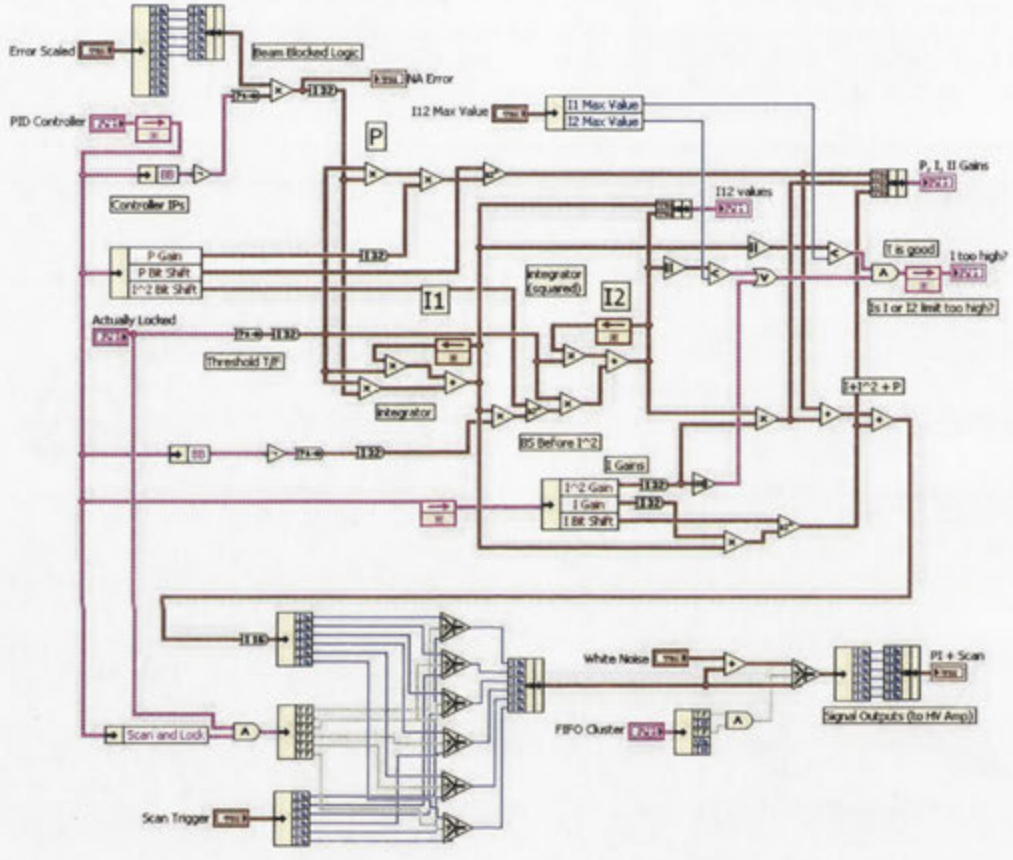

Figure 10.6: PII controller used for phase locks. Each of the 33 phase locks are controlled via this PII controller. The logic shown was written in National Instruments LAbVIEW 2010. The controller is a modified version of the PII controller designed by Ben Sparkes [49].

There are broadly three types of systems that require active control in this experiment. First, there are 4 cavities that need to be held on resonance. These are the 3 OPOs and a mode cleaning cavity employed to provide a reference local oscillator beam for the homodyne detections. These phase locks have error signals generated from mixed down AC signals from detectors in a Pound-Drever-Hall (PDH) configuration. DC signals from the same detectors serve as monitors for automated locking and re-locking control based on threshold logic. If the scanned cavity is above or below a certain user-specified threshold value, boolean logic is employed to determine whether or not the cavity is on resonance, and appropriate action will be taken. Second, we have the parametric gains of the OPOs, with error signals again generated externally before being fed into the control suite via the ADCs on the FPGA cards. A monitor is also used here, generated on-board by taking the square of the error signal, ensuring that the monitor is always a positive value.

Finally, we have the phase locks of two beams mixing on beam-splitters. Apart from the unique $r = \frac{1}{3}$ beam-splitter used to generate the first entanglement link in the 3-mode cluster state, which is a DC lock, the remaining phase locks all employ PDH configurations, with two error signals per beam-splitter. The two error signals are from sideband modes that are $\frac{\pi}{2}$ out of phase in quadrature, and can be used to lock the relative phase at 0^o, or at 90^o, or at any angle in between. For the arbitrary angle phase lock, employed for homodyne measurements, the two orthogonal error signals are added together so that the measured quadrature is given by $\hat{x}\cos(\theta) + \hat{p}\sin(\theta)$. Details of the phase locks are tabulated in table 10.5.

System	Input 1	Modulation	Input 2	Modulation
Cavities:				
OPO 1	error signal	11.2 MHz	Monitor	DC
OPO 2	error signal	11.2 MHz	Monitor	DC
OPO 3	error signal	11.2 MHz	Monitor	DC
Mode cleaner	error signal	11.2 MHz	Monitor	DC
Parametric gain:				
OPO 1	error signal	233 kHz		
OPO 2	error signal	138 kHz		
OPO 3	error signal	98 kHz		
Beam-splitters:				
Cluster 33 %	error signal	DC		
Cluster 33 % offset		Logic		
Cluster 50 %	error signal x	233kHz	error signal p	138kHz
Input a coupling	error signal x	233kHz	error signal p	138kHz
Input b coupling	error signal x	233kHz	error signal p	138kHz
Homodyne a	error signal x	138kHz	error signal p	233kHz
Homodyne b	error signal x	138kHz	error signal p	233kHz
Homodyne 1	error signal x	138kHz	error signal p	233kHz
Homodyne 2	error signal x	233kHz	error signal p	138kHz
Homodyne 3	error signal x	138kHz	error signal p	233kHz
Displacement 1 x	error signal x	233kHz	error signal p	138kHz
Displacement 1 p	error signal x	233kHz	error signal p	138kHz
Displacement 3 x	error signal x	233kHz	error signal p	138kHz
Displacement 3 p	error signal x	233kHz	error signal p	138kHz

Table 10.5: Phase locks synchronised in digital control suite.

Automated Locking and dependencies

Apart from the obvious advantage of ease of reconfigurability offered by digital electronics when compared to analogue electronics, there is another huge selling point, without which the control and measurement processes of this current experiment might simply have been infeasible. This is the automation aspect afforded by digital electronics. An elaborate automation scheme was designed, based on logic created by Sparkes [49], to synchronise the 33 phase locks across the 5 FPGA cards. Each phase lock was aware of its place in a network of dependencies, so that if a phase lock failed anywhere in the system, the phase locks that are dependent on this phase lock would be put on hold until the failure was resolved by the automated re-locking logic. This automated re-locking logic would prove to be vital in such a complex network of phase locks, and led to efficient control and measurement of the experimental setup.

The control suite used 36 analogue inputs of the total 40 available across the 5 FPGA cards. On average, over 90 % of the total resources on each FPGA card was used by the VIs. The PXI-7853R cards host a Virtex-5 LX85 system, while the PXI-7854R cards host a Virtex-5 LX110, which at present boasts the largest number of resources (including logic gates and memory) in this product family.

10.4 Results

In order to characterise the performance of our experimental squeezed T_Z gate, we carry out two verification schemes.

- First, we input **coherent states** and measure the amplitudes of the phase quadratures of the output modes. From this we can determine whether or not the input-output relationship (the coefficients of a linear transformation) has been faithfully re-created.
- Second, we input **vacuum states** and fully characterise the output state by measuring the covariance matrix. We do this for seven different regimes of T_Z, illustrating the tuneability of entanglement inherent to the T_Z gate.

Purities of electro-optic modulators

It is important to make sure that the EOMs are only applying modulations in the desired quadrature, as any modulation in the unwanted quadrature will manifest as phase noise that degrades the squeezing. To ensure this we first lock the displacement beams together with the signal beam (to be displaced in phase space), and then send a 1 MHz sine wave to the EOM, and measure this sideband on a spectrum analyser in both x and p. We see from Figs 10.7 and 10.8 that there is roughly 30 dB of difference in noise power at the 1 MHz sideband between the two signals in all four cases, indicating excellent purity for each EOM.

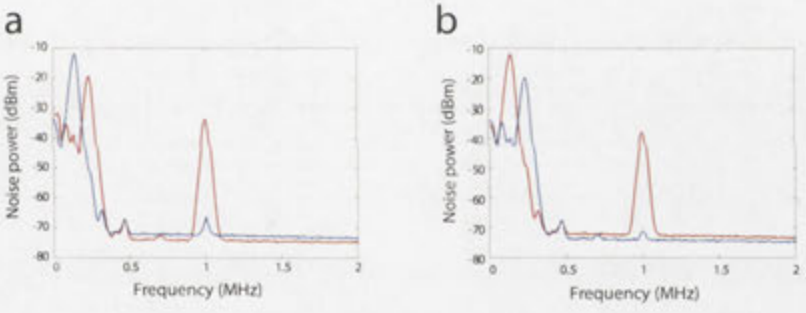

Figure 10.7: Purities of the two electro-optic modulators (EOM) for mode 1. (a) Phase modulation in x. Red trace is x quadrature, blue trace is p quadrature. (b) Phase modulation in p. Red trace is p quadrature, blue trace is x quadrature.

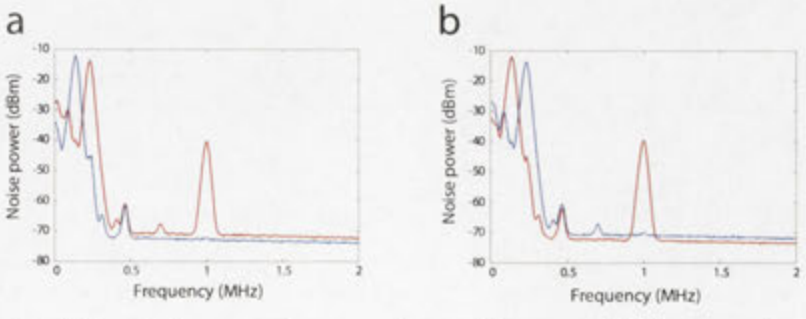

Figure 10.8: Purities of the two electro-optic modulators (EOM) for mode 3. (a) Phase modulation in x. Red trace is x quadrature, blue trace is p quadrature. (b) Phase modulation in p. Red trace is p quadrature, blue trace is x quadrature.

10.5 Characterising the input-output relations

The interference visibilities of the *Verification* stage of the experiment (see Fig. 10.3) are given in the table 10.6.

Mode; beam 1	Beam 2	Beam-splitter	Visibility
Sqz. 2; Cluster a	Local oscillator a	Homodyne measurement of cluster mode a	98.1 %
Sqz. 3; Cluster b	Local oscillator b	Homodyne measurement of cluster mode b	97.7 %

Table 10.6: Interference visibilities of the *Verification* stage. Uncertainties are ±0.1%.

The total propagation losses of the optical beams from the various OPOs to the homodyne detectors are up to 9 %, and the quantum efficiencies of the detectors are greater than 99 %.

10.5.1 Vacuum state inputs

The first characterisation of the experimental squeezed T_Z gate was performed using vacuum state inputs as modes a and b.

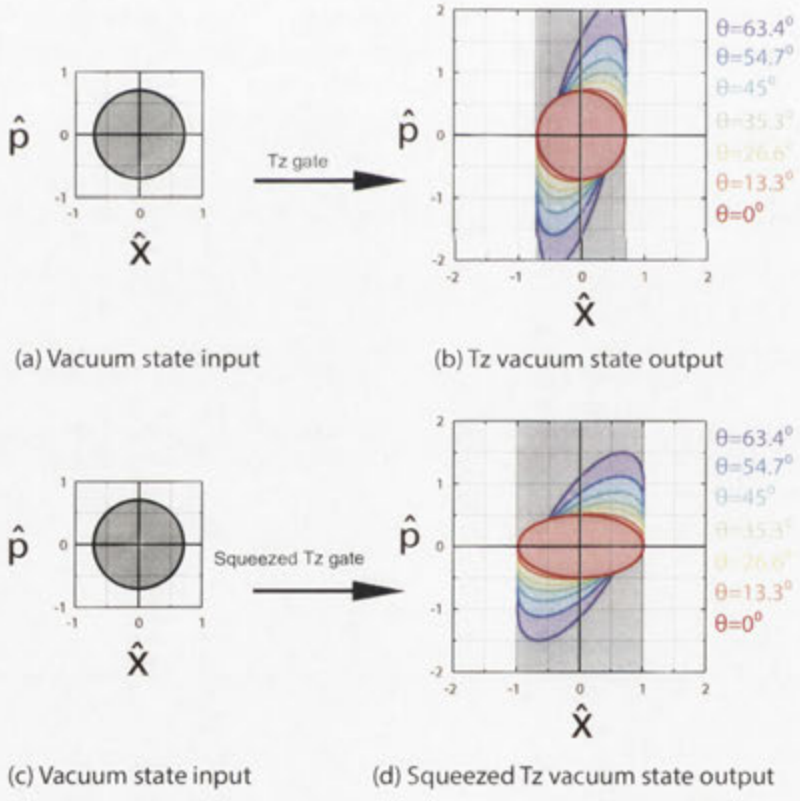

Figure 10.9: Phase space representations of theoretical T_Z and squeezed T_Z gates acting on vacuum inputs. (a) and (c) The input state is a quantum noise limited vacuum state, with equal quadrature amplitudes. (b) The theoretical output state of the T_Z gate with a vacuum input, for various measurement angles θ. (d) The theoretical output state of the squeezed T_Z gate for various θ. This figure is a modified version of a figure originally created by Yokoyama.

In order to understand the phase space distribution of the squeezed T_Z gate, we first look at

the phase space distribution of the T_Z gate, shown for theoretical values in Fig. 10.9. For all of phase-space plots, we assume a Gaussian distribution and a zero-mean value, consistent with vacuum states.

For a measurement angle of $\theta = 0°$, the corresponding gains in the T_Z off-diagonals are $g = \tan(0) = 0$ and so the T_Z simply performs an identity operation (see equation (10.9)). This is shown in Fig. 10.9(b) by the vacuum state output for $\theta = 0°$. For increasing values of θ, we see that the x quadrature is unchanged, and the p quadrature amplitude is increased. This is consistent with the evolution described in equation 10.2.

The phase space distributions for the squeezed T_Z gate are shown in Fig. 10.9(d), again for vacuum state inputs. We see a constant broadening in x, as one expects from the 3 dB anti-squeezing in x inherent in the squeezed T_Z gate. We also see that the rate of broadening in p is slower than for the T_Z gate, due to the scaling of the T_Z matrix with squeezing ($\frac{1}{\sqrt{2}}$) and anti-squeezing ($\sqrt{2}$) values.

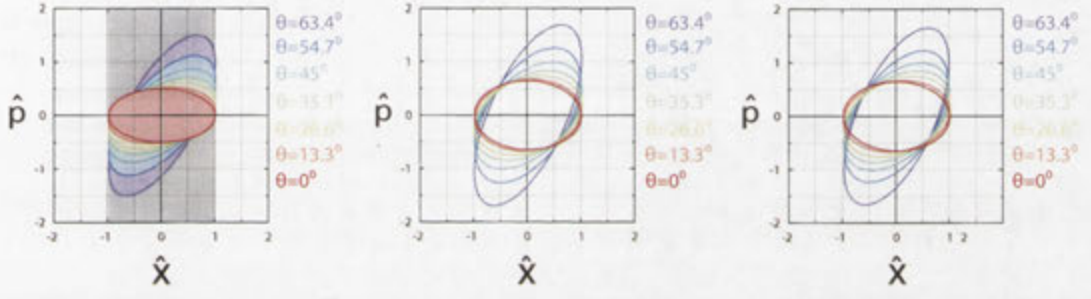

(a) Theory: Squeezed Tz output (b) HD 1: Squeezed Tz output (c) HD 3: Squeezed Tz output

Figure 10.10: Phase space representations of squeezed T_Z gates acting on vacuum inputs. (a) The theoretical output state of the squeezed T_Z gate with a vacuum input. (b) The experimentally measured output at homodyne detector (HD) 1. (c) The experimentally measured output at HD 3. This figure is a modified version of a figure originally created by Yokoyama.

Figure 10.10 displays the phase space distribution plotted for experimentally measured values, both at homodyne detector 1 and homodyne detector 3. The theoretical phase space distribution is plotted alongside for comparison. We see an excellent qualitative agreement, with a noticeable broadening in the p quadrature, due to finite squeezing in the resource cluster. We also see a near perfect match between the two experimentally measured phase space distributions at the two different homodyne measurement stations. This symmetry is indicative of well-aligned optics and well-calibrated electronics.

10.5.2 Coherent state inputs

Next, we use coherent states as inputs and perform the squeezed T_Z gate for various angles θ. We apply phase modulation to input mode a at 1 MHz so that it is a coherent state with power $\langle \hat{x}_a^2 \rangle$ =13.8 dB above the shot noise level (SNL). Note that we have $\langle \hat{p}_a^2 \rangle = \langle \hat{x}_b^2 \rangle = \langle \hat{p}_b^2 \rangle = 0$ dB. The measurement results are shown in Fig. 10.11. The power measurements in Fig. 10.11(b) and (c) are taken on a spectrum analyser at a frequency of 1 MHz with a resolution bandwidth of 30 kHz and a video bandwidth of 300 Hz.

We see that the powers in both $\hat{x}_1$ and $\hat{x}_3$ remain constant for all seven measurement angles as shown in Fig. 10.11(a). In stark contrast, the coherent amplitudes of both $\hat{p}_1$ and $\hat{p}_3$ increase with θ. The solid blue lines represent the theoretical values for a squeezing level of 4.5 dB, and we see a fairly good fit between the experimentally measured values. If we compare the two cases of $\theta = 0°$ and $\theta = 45°$, as in Fig. 10.11 (b) and (c), respectively, we see that the only change is the increases in the p quadrature, as expected. This is due to the non-zero gains in the squeezed T_Z gate inducing

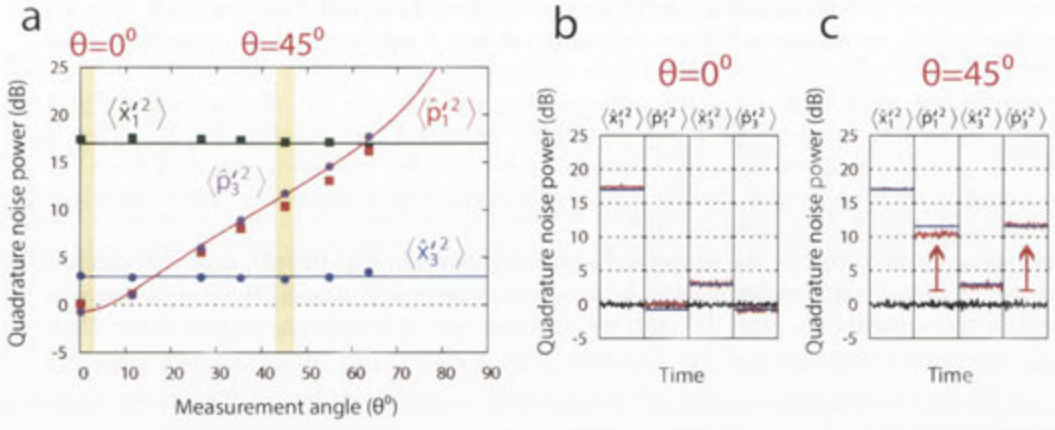

Figure 10.11: Transfer of quadrature powers after squeezed T_Z gate. Coherent amplitude has been imparted onto input mode a so that $\langle \hat{x}_a^2 \rangle = 13.8$ dB above shot noise. (a) The quadrature noise powers for the four quadratures $\hat{x}_1$, $\hat{p}_1$, $\hat{x}_3$, and $\hat{p}_3$ as a result of the squeezed T_Z gate in seven different regimes. Solid coloured lines indicate theory for 4.5 dB squeezing in resource cluster. Coloured squares and circles are experimental data points. (b) and (c) Blue lines are theoretical values for resource squeezing of 4.5 dB. Black trace represents measurements of shot noise. Red traces are experimental measurements at various quadratures. (b) Quadrature noise powers at $\theta = 0°$. (c) Quadrature noise powers at $\theta = 45°$. This figure is a modified version of a figure originally created by Yokoyama.

correlations between each mode, leading to the crosstalk of the input coherent amplitude. We repeat the same procedure for the other quadratures and observe the same qualitative agreement (not shown for brevity).
This qualitative agreement confirms the input-output relations derived in equation 10.7, and we verify that the squeezed T_Z performs as the theory predicts.

10.6 Characterising entanglement from the covariance matrix

In order to characterise the entanglement present in the bipartite output state of our squeezed T_Z gate, we employ vacuum state inputs for modes a and b and perform extensive homodyne measurements that allow us to recreate the covariance matrix of the state. This is done for seven different measurement angles at homodyne 2, each of which imprints a different quantum circuit onto the cluster state, corresponding to different measurement-based quantum computations.
The covariance matrix for a general bipartite Gaussian state is described in section 8.3.1 and given explicitly in equation 8.4. First we describe how we experimentally measure some of the less straightforward elements of the covariance matrix.

Measurements of non-commuting operators

In order to measure $\frac{1}{2}\langle \hat{x}_1\hat{p}_1 + \hat{p}_1\hat{x}_1 \rangle$ we can combine two measurements at angles that do not correspond to either $\hat{x}$ or $\hat{p}$ alone. First we set the homodyne measurement angle to $\theta = 45°$ and measure $\langle \left(\frac{1}{\sqrt{2}} (\hat{x}_1 + \hat{p}_1) \right)^2 \rangle$. Then we set the homodyne measurement angle to $\theta = -45°$ and measure $\langle \left(\frac{1}{\sqrt{2}} (\hat{x}_1 - \hat{p}_1) \right)^2 \rangle$. Then we use the fact that these two expressions can be decomposed into:

$$\langle\left(\frac{1}{\sqrt{2}}\left(\hat{x}_1+\hat{p}_1\right)\right)^2\rangle=\frac{1}{2}\left(\langle\hat{x}_1^2\rangle+\langle\hat{x}_1\hat{p}_1+\hat{p}_1\hat{x}_1\rangle+\langle\hat{p}_1^2\rangle\right), \tag{10.21}$$

$$\langle\left(\frac{1}{\sqrt{2}}\left(\hat{x}_1-\hat{p}_1\right)\right)^2\rangle=\frac{1}{2}\left(\langle\hat{x}_1^2\rangle-\langle\hat{x}_1\hat{p}_1+\hat{p}_1\hat{x}_1\rangle+\langle\hat{p}_1^2\rangle\right), \tag{10.22}$$

and by combining the measurement results in the following way, we arrive at the desired measurement:

$$\frac{1}{2}\left(\langle\left(\frac{1}{\sqrt{2}}\left(\hat{x}_1+\hat{p}_1\right)\right)^2\rangle-\langle\left(\frac{1}{\sqrt{2}}\left(\hat{x}_1-\hat{p}_1\right)\right)^2\rangle\right)=\frac{1}{2}\langle\hat{x}_1\hat{p}_1+\hat{p}_1\hat{x}_1\rangle. \tag{10.23}$$

Measurements of the other off-diagonal terms

If we set both of our homodyne measurement angles to 0^o, and employ an adder, we will perform the following measurement:

$$\langle\left(\hat{x}_1+\hat{x}_2\right)^2\rangle=\langle\hat{x}_1^2\rangle+2\langle\hat{x}_1\hat{x}_2\rangle+\langle\hat{x}_2^2\rangle. \tag{10.24}$$

Additionally, if set one homodyne measurement angle to 0^o and one to 180^o, we will perform the following:

$$\langle\left(\hat{x}_1-\hat{x}_2\right)^2\rangle=\langle\hat{x}_1^2\rangle-2\langle\hat{x}_1\hat{x}_2\rangle+\langle\hat{x}_2^2\rangle. \tag{10.25}$$

Therefore, if we combine the measurements in the following way, the outcome will be given as:

$$\frac{1}{4}\left(\langle\left(\hat{x}_1+\hat{x}_2\right)^2\rangle-\langle\left(\hat{x}_1-\hat{x}_2\right)^2\rangle\right)=\langle\hat{x}_1\hat{x}_2\rangle. \tag{10.26}$$

By employing a similar approach, with measurement angles of $\{(0,90),(0,-90)\}$ we can measure for example $\langle\hat{x}_1\hat{p}_2\rangle$. The other cross-correlation terms follow a similar decomposition.

Covariance matrices of squeezed T_Z gate output states

The first cluster state computation we perform with vacuum state inputs is the squeezed T_Z gate in the homodyne 2 measurement angle $\theta = 0^o$ regime. The three covariance matrices (CMs) corresponding to this regime are given as:

$$0^o:\begin{pmatrix}0.50&0.00&0.00&0.00\\0.00&0.13&0.00&0.00\\0.00&0.00&0.50&0.00\\0.00&0.00&0.00&0.13\end{pmatrix};\begin{pmatrix}0.49&0.00&0.00&0.00\\0.00&0.21&0.00&0.04\\0.00&0.00&0.50&0.00\\0.00&0.04&0.00&0.21\end{pmatrix};\begin{pmatrix}0.50&0.00&0.00&0.00\\0.00&0.21&0.00&0.04\\0.00&0.00&0.50&0.00\\0.00&0.04&0.00&0.21\end{pmatrix} \tag{10.27}$$

where the three CMs are arranged in the following way:
(Measurement angle: Ideal CM; Experimentally measured CM; theoretical CM for -4.5 dB cluster).

The ideal CM, assuming infinite squeezing, is shown in the left column of equation 10.27, and the theoretical CM assuming a cluster state resource with squeezing level -4.5 dB is shown in the right column. The theoretical CMs are readily calculated from equation 10.19 and are given as:

$$\Gamma=\frac{\hbar}{2}\begin{pmatrix}2&0&0&-g\\-g&\frac{1}{2}+g^2&-g&g^2\\0&-g&2&-g\\-g&g^2&-g&\frac{1}{2}+g^2\end{pmatrix}+\frac{\hbar}{2}e^{-2s}\begin{pmatrix}0&0&0&0\\0&1+\frac{3}{2}g^2&0&\frac{1}{2}+\frac{3}{2}g^2\\0&0&0&0\\0&\frac{1}{2}+\frac{3}{2}g^2&0&1+\frac{3}{2}g^2\end{pmatrix}, \tag{10.28}$$

where the second matrix is due to contributions from finite squeezing.

For the 0^o measurement angle, we have $g = \tan(\theta) = 0$ and therefore the input-output relations dictated by equation 10.7 specifies actions on the diagonal elements only. Recall that the diagonal elements of a covariance matrix represent the variances of the quadrature operators. From equation 10.27 we have 3 dB squeezing in p and 3 dB anti-squeezing in x. Since the variance of a vacuum state is $\langle \Delta^2 \hat{x}^{(0)} \rangle = \frac{\hbar}{2}$, we will have diagonal elements of $2 \times \frac{\hbar}{2} = \frac{1}{2}$ for the x quadrature terms, and $\frac{1}{2} \times \frac{\hbar}{2} = \frac{1}{8}$ for the p quadrature terms. The off-diagonal elements are all zero, indicating no cross correlations between the quadratures.
The CM constructed from experimental measurements is shown in the middle column of equation 10.27. This is to be compared to the theoretical CM assuming a cluster state resource with squeezing level -4.5 dB, shown in the right column. We see that there is a remarkable fit between the experimentally measured CM and the theory.
We repeat this cluster state computation process for six more regimes, with an increasing homodyne 2 measurement angle θ each time. These are given below in full, in the same arrangement as above.

$$11.3^o : \begin{pmatrix} 0.50 & -0.05 & 0.00 & -0.05 \\ -0.05 & 0.14 & -0.05 & 0.01 \\ 0.00 & -0.05 & 0.50 & -0.05 \\ -0.05 & 0.01 & -0.05 & 0.14 \end{pmatrix} ; \begin{pmatrix} 0.49 & -0.03 & 0.00 & -0.05 \\ -0.03 & 0.22 & -0.04 & 0.05 \\ 0.00 & -0.04 & 0.50 & -0.05 \\ -0.05 & 0.05 & -0.05 & 0.22 \end{pmatrix} ; \begin{pmatrix} 0.50 & -0.05 & 0.00 & -0.05 \\ -0.05 & 0.23 & -0.05 & 0.06 \\ 0.00 & -0.05 & 0.50 & -0.05 \\ -0.05 & 0.06 & -0.05 & 0.23 \end{pmatrix} \tag{10.29}$$

$$26.6^o : \begin{pmatrix} 0.50 & -0.13 & 0.00 & -0.13 \\ -0.13 & 0.19 & -0.13 & 0.06 \\ 0.00 & -0.13 & 0.50 & -0.13 \\ -0.13 & 0.06 & -0.13 & 0.19 \end{pmatrix} ; \begin{pmatrix} 0.50 & -0.10 & 0.01 & -0.12 \\ -0.10 & 0.27 & -0.11 & 0.11 \\ 0.01 & -0.11 & 0.50 & -0.12 \\ -0.12 & 0.11 & -0.12 & 0.28 \end{pmatrix} ; \begin{pmatrix} 0.50 & -0.13 & 0.00 & -0.13 \\ -0.13 & 0.31 & -0.13 & 0.14 \\ 0.01 & -0.13 & 0.50 & -0.13 \\ -0.13 & 0.14 & -0.13 & 0.31 \end{pmatrix} \tag{10.30}$$

$$35.3^o : \begin{pmatrix} 0.50 & -0.18 & 0.00 & -0.18 \\ -0.18 & 0.25 & -0.18 & 0.13 \\ 0.00 & -0.18 & 0.50 & -0.18 \\ -0.18 & 0.13 & -0.18 & 0.25 \end{pmatrix} ; \begin{pmatrix} 0.50 & -0.16 & 0.00 & -0.17 \\ -0.16 & 0.35 & -0.15 & 0.17 \\ 0.00 & -0.15 & 0.49 & -0.17 \\ -0.17 & 0.17 & -0.17 & 0.37 \end{pmatrix} ; \begin{pmatrix} 0.50 & -0.18 & 0.00 & -0.18 \\ -0.18 & 0.41 & -0.18 & 0.24 \\ 0.00 & -0.18 & 0.50 & -0.18 \\ -0.18 & 0.24 & -0.18 & 0.41 \end{pmatrix} \tag{10.31}$$

$$45^o : \begin{pmatrix} 0.50 & -0.25 & 0.00 & -0.25 \\ -0.25 & 0.38 & -0.25 & 0.25 \\ 0.00 & -0.25 & 0.50 & -0.25 \\ -0.25 & 0.25 & -0.25 & 0.38 \end{pmatrix} ; \begin{pmatrix} 0.50 & -0.24 & -0.01 & -0.23 \\ -0.24 & 0.50 & -0.21 & 0.32 \\ 0.01 & -0.21 & 0.49 & -0.23 \\ -0.23 & 0.32 & -0.23 & 0.50 \end{pmatrix} ; \begin{pmatrix} 0.50 & -0.25 & 0.00 & -0.25 \\ -0.25 & 0.60 & -0.25 & 0.43 \\ 0.00 & -0.25 & 0.50 & -0.25 \\ -0.25 & 0.43 & -0.25 & 0.60 \end{pmatrix} \tag{10.32}$$

$$54.7^o : \begin{pmatrix} 0.50 & -0.35 & 0.00 & -0.35 \\ -0.35 & 0.62 & -0.35 & 0.50 \\ 0.00 & -0.35 & 0.50 & -0.35 \\ -0.35 & 0.50 & -0.35 & 0.62 \end{pmatrix} ; \begin{pmatrix} 0.48 & -0.32 & -0.01 & -0.29 \\ -0.32 & 0.80 & -0.30 & 0.58 \\ -0.01 & -0.30 & 0.47 & -0.31 \\ -0.29 & 0.58 & -0.31 & 0.75 \end{pmatrix} ; \begin{pmatrix} 0.50 & -0.35 & 0.00 & -0.35 \\ -0.35 & 0.98 & -0.35 & 0.81 \\ 0.00 & -0.35 & 0.50 & -0.35 \\ -0.35 & 0.81 & -0.35 & 0.98 \end{pmatrix} \tag{10.33}$$

$$63.4^{o}: \begin{pmatrix} 0.50 & -0.50 & 0.00 & -0.50 \\ -0.50 & 1.13 & -0.50 & 1.50 \\ 0.00 & -0.50 & 0.50 & -0.50 \\ -0.50 & 1.00 & -0.50 & 1.13 \end{pmatrix}; \begin{pmatrix} 0.50 & -0.53 & 0.01 & -0.48 \\ -0.53 & 1.43 & -0.44 & 1.18 \\ 0.01 & -0.44 & 0.49 & -0.49 \\ -0.48 & 1.18 & -0.49 & 1.37 \end{pmatrix}; \begin{pmatrix} 0.50 & -0.50 & 0.00 & -0.50 \\ -0.50 & 1.75 & -0.50 & 1.58 \\ 0.00 & -0.50 & 0.50 & -0.50 \\ -0.50 & 1.58 & -0.50 & 1.75 \end{pmatrix} \tag{10.34}$$

PT-symplectic eigenvalue

In order to quantify the entanglement between the output modes in the bi-partite states produced in the seven different regimes, we compute the corresponding partial-transpose-symplectic eigenvalues from each covariance matrix. This is based on the positivity under partial transposition (PTT) criteria developed by Peres and Horodecki [119, 120, 121]. We employ this entanglement measure here since it is both necessary and sufficient for bipartite Gaussian states.

Each covariance matrix presented for the various bipartite Gaussian states have the form:

$$\Gamma = \begin{pmatrix} \mathbf{A} & \mathbf{C} \\ \mathbf{C}^{T} & \mathbf{B} \end{pmatrix}, \tag{10.35}$$

where $\mathbf{A}$, $\mathbf{B}$, and $\mathbf{C}$ are 2×2 matrices. The symplectic eigenvalues of an arbitrary two-mode Gaussian state are denoted ν_{-} and ν_{+}, defined as:

$$2\nu_{\pm}^{2} = \Delta(\Gamma) \pm \sqrt{\Delta^{2}(\Gamma) - 4\mathrm{Det}\,\Gamma}, \tag{10.36}$$

where Δ represents here the seralian, given by:

$$\Delta = \mathrm{Det}\,A + \mathrm{Det}\,B + 2\mathrm{Det}\,C. \tag{10.37}$$

Now under partial transposition, we arrive at:

$$\Gamma = \begin{pmatrix} \mathbf{A} & \mathbf{C} \\ \mathbf{C}^{T} & \mathbf{B} \end{pmatrix} \xrightarrow{\rho \to \rho^{T}} \tilde{\Gamma} = \begin{pmatrix} \mathbf{A} & \tilde{\mathbf{C}} \\ \tilde{\mathbf{C}}^{\mathbf{T}} & \mathbf{B} \end{pmatrix}, \tag{10.38}$$

where $\mathrm{Det}\,\tilde{\mathbf{C}} = -\mathrm{Det}\,\mathbf{C}$. The seralian Δ is mapped under the partial transposition to:

$$\tilde{\Delta} = \mathrm{Det}\,\mathbf{A} + \mathrm{Det}\,\mathbf{B} - 2\mathrm{Det}\,\mathbf{C}. \tag{10.39}$$

Therefore the symplectic eigenvalues under partial transposition are given as:

$$2\tilde{\nu}^{2}_{\pm} = \tilde{\Delta}\left(\tilde{\Gamma}\right) \pm \sqrt{\tilde{\Delta}^{2}\left(\tilde{\Gamma}\right) - 4\mathrm{Det}\,\tilde{\Gamma}}. \tag{10.40}$$

The PPT criterion then states that a state described by Γ is separable if and only if the smallest symplectic eigenvalue ν_{-} is $\geq \frac{\hbar}{2} = \frac{1}{4}$.

The symplectic eigenvalues of the experimentally measured covariance matrices are tabulated in table 10.7, and plotted alongside theoretical curves in Fig. 10.12.

	$\theta = 0°$	$\theta = 11.3°$	$\theta = 26.6°$	$\theta = 35.3°$	$\theta = 45°$	$\theta = 54.7°$	$\theta = 63.4°$
$\tilde{\nu}_-$	0.288	0.270	0.234	0.217	0.199	0.186	0.169
Error margin	±0.002	±0.003	±0.003	±0.003	±0.004	±0.005	±0.007

Table 10.7: Symplectic eigenvalues of seven measured covariance matrices.

Figure 10.12 displays the experimentally measured $\tilde{\nu}_-$ for the seven different measurement angles of homodyne 2.

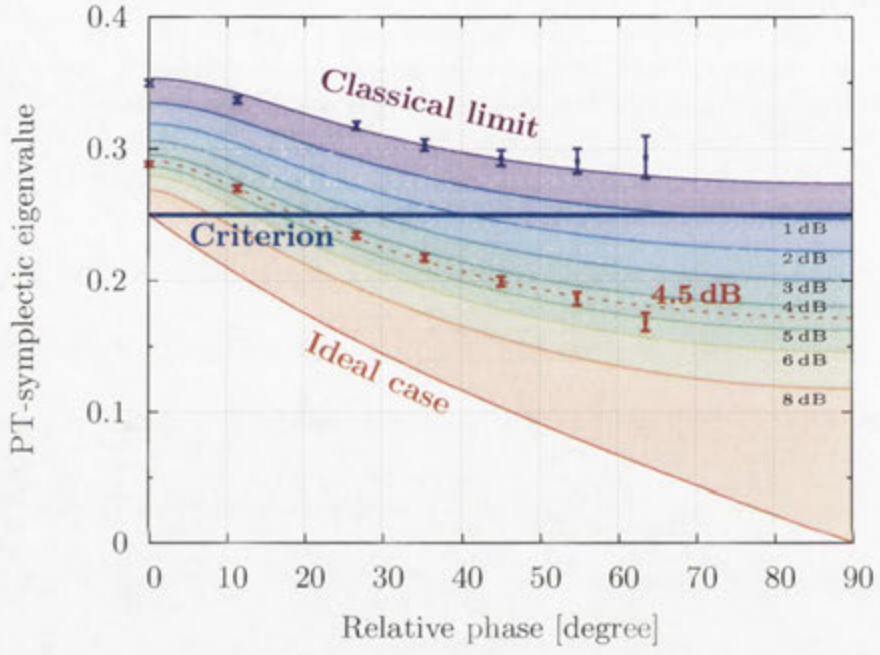

Figure 10.12: Quantifying entanglement strength for different regimes of the squeezed T_Z operations. The horizontal axis shows the tuneable parameter in the experiment, which is the homodyne measurement angle of cluster mode 2. This determines the gain $g = \tan(\theta)$ of the T_Z operation, see equation 10.19, which in turn determines the strength of entanglement quantified by the PT-symplectic eigenvalues of the covariance matrix, the vertical axis. The various coloured regions correspond to theoretical calculations based on equations 10.28 and 10.40, for different squeezing levels of the resource cluster state, which is the the blank quantum circuit board facilitating the measurement-based quantum computations. The red data points are experimentally measured $\tilde{\nu}_-$ with the resource cluster, with respective error bars. The blue data points are experimentally measured $\tilde{\nu}_-$ when the resource is simply a classical mixture of vacuum modes, with respective error bars. The quantum regime, indicated by the threshold of the entanglement measure, is below the blue line at 0.25. Figure created by Yokoyama (measurements taken by Yokoyama, Ukai, and myself).

We see that for a measurement angle of $\theta = 0°$, there exists no entanglement, as $\tilde{\nu}_-$ is above 0.25, the criteria for entanglement under the PPT criterion. As the measurement angle θ and therefore the gain $g = \tan(\theta)$ is increased, so too is the entanglement strength. The dashed red line in Fig. 10.12 corresponds to the theoretical curve assuming squeezing levels of 4.5 dB in the resource cluster state, which is shown to fit remarkably with the experimental data.
Shown by the blue data points are the results of the same experiment described, however without the resource cluster state. For this demonstration, we blocked the pump beams of the OPOs, so that there was no squeezing and the resource was effectively a classical mixture of vacuum modes.

We see that predictably there is no entanglement present at the output of the T_Z operation when the resource is not a quantum circuit board, but rather a classical circuit board that does not facilitate quantum computations.
Note that if our resource state was an infinitely squeezed cluster state, then as $\theta \to \frac{\pi}{2}$, $\tilde{\nu}_- \to 0$, which is defined to be maximum entanglement by this criteria. This is shown by the orange line labelled "Ideal case". We see that there is only zero entanglement (indicating a separable state) for $g = \tan(\theta) = 0$, and any non-zero θ will result in entanglement being teleported to the output.

10.7 Summary

We have introduced a new quantum gate, the T_Z gate, to the toolbox of continuous-variables cluster state quantum computing. A rigorous theoretical treatment of T_Z was provided, displaying its actions as a multimode gate that can be retro-fitted onto arbitrary cluster states. An efficient proof-of-principle experimental demonstration was then detailed, on a three-mode cluster state resource. Remarkably, two independent and uncorrelated input modes are teleported into the cluster, and are output with entanglement between them. Further, by operating the T_Z gate in seven different regimes, we have shown the precise and deterministic tuneability of the entanglement, even being able to turn it off. The two-mode output states were fully characterised by their covariance matrices, and the entanglement strength quantified by the symplectic eigenvalues of the partially transposed covariance matrices.
In conjunction with the one-mode Gaussian operations demonstrated in the previous chapter, we have now implemented all of the multimode Gaussian gates required to form a unviersal set of multimode Gaussian operations. We now have a two clear goals ahead of us before we can achieve universal quantum computation. These are error correction (finding a feasible fault-tolerant scheme for continuous-variable cluster state computation), and the efficient implementation of a gate that is cubic in its Hamiltonian (a non-Gaussian gate). While both of these research areas are beyond the scope of this thesis, it should be noted that there is already promising research being conducted in both areas. Specifically, Menicucci has recently provided a formulation of fault-tolerant one-way quantum computations using continuous-variable cluster states [94], and there exist at least preliminary investigations into non-Gaussian gates [122].

Chapter 11

Conclusions

11.1 Summary

This thesis has documented the main results of four and a half years of experimental and theoretical research on quantum optics and in particular large-scale entanglement and quantum teleportation as a means of facilitating quantum computation.

Large-scale entanglement

First we investigated methods of increasing the size of entangled states. Just a decade ago entangled states were still limited in size to two or three quantum entities. Prior to our demonstrations the largest entangled state in any research field comprised fourteen quantum entities (qubits encoded in trapped ions [21]). Inspired by well-established techniques and concepts from the telecommunications industry, we investigated multiplexing quantum light in order to increase the number of quantum entities that comprise an entangled state. The spatial multiplexing experiment of chapter 6, inspired by the investigations of spatial mode conversions detailed in chapter 5, led to a programmable network capable of producing entangled states containing up to eight quantum entities. While the size of the entangled state was equal to the state of the art in optical demonstrations, the real novelty of the experiment was to introduce the idea of emulating linear optics networks instead of physically building them as in the conventional manner. The next investigation into multiplexing was conducted in the time domain. This proved to be extremely successful, as we could treat the continuous-wave output of our optical parametric oscillators as a continuous sequence of well defined and orthogonal wave-packet modes, separated by as short a time as 160 ns. Each wave-packet of light is a quantised optical mode (qumode) and is individually accessible. By creating two continuous optical beams containing these sequentially propagating wave-packet modes and mixing them together by two beam-splitter interactions we generated the largest entangled state created to date by three orders of magnitude. We entangled together more than 20,000 independent qumodes. We have named the ultra-large entangled state generated in chapter 7 the dual-rail EPR-graph state, as our theoretical investigations led us to conclude that it is one possible extension of the EPR state to an ultra-large basis.

Quantum computing with cluster states

The dual-rail EPR-graph state is equivalent (up to local phase shifts) to a cluster state, and we show in chapter 8 that it may theoretically be used as a resource for universal measurement-based quantum computing. Two experimental demonstrations were then detailed in part III, each one exploring the teleportation-based Gaussian computations that the cluster states allow for. We explored how to implement arbitrary one-mode Gaussian transformations with a four-mode cluster state acting as a blank quantum circuit board. An input mode was coupled into the cluster and precisely calculated homodyne measurements on the cluster allowed for the logic of a Fourier

transform operation to be imprinted onto the cluster. This was done with a fidelity of 0.68, which importantly is above the no-cloning limit. By simply changing the measurement basis, a different set of logic gates are imprinted onto the cluster, and a different operation is performed on the input state as it is teleported through. The final demonstration was an implementation of a tuneable entanglement gate, which we introduce as a robust multimode gate that offers the full tuneability of entanglement between the modes that it acts on. After a rigorous theoretical treatment of the gate, we presented a proof-of-principle experiment. In the experimental demonstration, two independent inputs are coupled into a three-mode linear cluster state and proceed to have entanglement teleported onto them through the measurement-based cluster computation. By performing the tuneable entanglement gate in seven different regimes we verified the full tuneability of entanglement by complete measurements of each output state's covariance matrix. Symplectic eigenvalues were calculated from each partially transposed covariance matrix, and a discussion of the scope of this gate was presented. For example, the gate can be retrofitted onto pre-existing clusters of arbitrary size and shape. With this gate we have introduced tuneability to the toolbox of measurement-based quantum computation.

11.2 Outlook

Towards universal quantum information processing and quantum technologies

While the dual-rail EPR-graph state that we have generated is ultra-large, consisting of more than 20,000 individually accessible qumodes, with present-day schemes we will only be able to use about 20 of these qumodes in an actual implementation of measurement-based quantum computing. This is because the finite squeezing of the qumodes couple in noise in every step of computation, and without error correction the quantum information will be lost after only tens of computation steps. Further, the demonstrations of quantum computing detailed in this thesis are modest. They are Gaussian operations, which represent Hamiltonians that are at most quadratic in the quantum mode's position and momentum variables. As such, the class of cluster state computations demonstrated in part III can be efficiently simulated on classical computers. However, universal multimode Gaussian operations are necessary in the set of continuous-variable (CV) universal quantum gates, and will form the backbone of more sophisticated and complex implementations. The theoretical framework for a universal set of gates, including decompositions of arbitrary Hamiltonians into a finite set of gates, already exists [97, 77, 24]. Demonstrations are surfacing that are bringing us within reach of non-Gaussian gates, such as the cubic phase gate [122]. Recently, progress towards a feasible fault tolerant scheme for continuous-variable cluster state computing has also been demonstrated [94]. The tuneable entanglement gate will likely play a part in facilitating implementations of fault tolerance. While the noise introduced from finite squeezing is still a serious technical problem, it is not a fundamental issue. It is entirely likely that a universal quantum computing scheme that emerges will be a hybridised architecture, between continuous-variable systems and discrete-variable systems. The latter offers higher fidelity operations than the former, at the expense of deterministic success. One example of this type of hybridisation is the recent deterministic teleportation of a photonic qubit [44]. While beyond the scope of this thesis, the reader is encouraged to read references [76, 75, 62] for discussions on the main challenges in dealing with hybridised optical architectures, and the potential they offer. There is sufficient progress in these and other research directions that leads us to conclude that universal quantum computing in an optical platform is entirely feasible.

Appendix A

Optimising Asymmetric Networks for Multipartite EPR Steering

The programmable networks developed in chapter 6 offer us a powerful and relatively simple method for exploring various optics networks that would otherwise require much time and patience. In this appendix chapter we explore a range of beam-splitter networks, finding particular situations where it is beneficial to introduce asymmetric networks. Biasing beam-splitters towards certain outputs can help to minimise the damage done by an asymmetric input basis. As every experiment has at least some asymmetry due to realistic conditions in the lab, it is useful to provide a detailed treatment here.

Alternatively, this chapter can be viewed as a treatment on the paradoxical EPR steering. While there is a rich collection of both theoretical investigations and experimental demonstrations for EPR steering between two quantum systems, situations involving more than two quantum systems were not yet well understood. The experiments and theory detailing multipartite EPR steering in this chapter were investigated in collaboration with Margaret Reid of Swinburne University, and Qiongyi He, of Peking University.

A.1 Introduction

Schrödinger introduced the term "steering" [123] to describe the nonlocality apparent in the EPR paradox, and pointed out that these states necessarily involve entanglement. Howard Wiseman and co-workers [124, 125] have formalized the meaning of steering in terms of violations of local hidden state models, and revealed that the EPR paradox is a realization of quantum steering. In simple terms, quantum steering dictates that measurements made by one observer at a location A can apparently "steer" the state of another observer, at location B. The EPR steering type of nonlocality requires the entanglement of the systems, but is not implied by it.

The observation of genuine multipartite EPR steering has not been possible until recently as the framework necessary to understand the concept has not been available. A recent theoretical analysis has developed this framework [126].

To investigate tripartite EPR steering, three observers (Alice, Bob and Charlie) make measurements on each of three distinct systems. Following the general approach introduced by Svetlichny [127], no assumptions are made about the nature of Bob's and Charlie's systems or measurements. The systems may be entangled and there can be "spooky action-at-a-distance" between them. Alice's measurements on the other hand are the canonical observables $\hat{x}$ and $\hat{p}$ of a quantum system, and as such are constrained by the Heisenberg uncertainty relation, which we write as $\Delta\hat{x}\Delta\hat{p} \geq 1$. Bob and Charlie make measurements, and can collaborate, to give an optimized prediction for the outcome of Alice's $\hat{x}$ (or $\hat{p}$) measurement. If the product of the uncertainties in their inferences for $\hat{x}$ and $\hat{p}$ appears to defy the uncertainty relation, then we have realized an EPR steering paradox

[12, 124]. In that case, it is as though Alice's $\hat{x}$ and $\hat{p}$ values were predetermined to an accuracy that contradicts quantum mechanics [6], or else that there is an actual steering of Alice's system by Bob and Charlie's actions [123]. We symbolize this directional entanglement by the notation $BC \rightarrow A$.

We can extend to N observers, and for a given correlated state, become specific about the observables that are to be measured by the "steering" parties e.g. Bob and Charlie. In our experiment, these will be an optimized linear combination of the quadratures x_k and p_k of an optical mode k. Thus, any $N-$party state demonstrates N-partite EPR steering of the j site by the remaining set of sites $\{k\}$ if the following criterion is satisfied

$$S_{j|\{k\}} \equiv \Delta_{\text{inf}}(\hat{x}_j)\Delta_{\text{inf}}(\hat{p}_j) < 1 \tag{A.1}$$

The inference variances are given by

$$\Delta^2_{\text{inf}}(\hat{x}_j) = \Delta^2(\hat{x}_j + \sum_{k \neq j} g_{k,x} x_k) \tag{A.2}$$

$$\Delta^2_{\text{inf}}(\hat{p}_j) = \Delta^2(\hat{p}_j + \sum_{k \neq j} g_{k,p} p_k) \tag{A.3}$$

where the real numbers $g_{x,k}$ and $g_{p,k}$ are optimization parameters used to minimize the inference variances. As the calibration of the quantum noise only matters for the first site j, the measurements at the "steering" sites denoted by k are written as classical numbers, without the operator "hats".

The steering detected by equation (A.1) is "genuinely N-partite" if it cannot be explained as arising from any steering limited to $N-1$ or fewer parties. In the tripartite case, let A, B, C be the sites of Alice, Bob and Charlie. Following ref. [126], all strictly two-party steering is negated, if we can demonstrate each of

$$S_{A|\{BC\}} < 1, S_{B|\{AC\}} < 1, S_{C|\{AB\}} < 1 \tag{A.4}$$

which implies steering across all bipartitions: $BC \rightarrow A$, $AC \rightarrow B$ and $AB \rightarrow C$. This negation is sufficient to rule out any fixed two-party steering, as one would expect for pure states where only one of the bipartitions would be possible. It thus demonstrates the full inseparability, not only of the quantum density matrix, but of any three-party hidden state model that could be used to describe the system [124].

The negation does not however rule out that the steering has been created by mixing states with two-party steering across different bipartitions. To claim genuine tripartite steering, we need to eliminate this possibility. This can be done if for a single j,

$$\Delta^2_{\text{inf}}(\hat{x}_j) + \Delta^2_{\text{inf}}(\hat{p}_j) < 1 \tag{A.5}$$

where $g_{k,x} = -\frac{1}{\sqrt{2}}$ and $g_{k,p} = \frac{1}{\sqrt{2}}$ $(k \neq j)$, or, alternatively, if $S_{A|\{BC\}} + S_{B|\{AC\}} + S_{C|\{AB\}} < 1$. To demonstrate genuine N-partite steering, more inequalities are necessary.

A.1.1 Experimental overview

We employ the programmable linear optics circuit detailed in chapter 6 in order to create various multi-partite quantum states from different networks. Independent quantum modes are shaped in order to be multiplexed on the same beam. By programmatically changing the measurement basis, the scheme allows us to emulate linear optics networks in real time. Varying the contributions of different qumodes in each state is equivalent to varying the reflectivities of the different beam-

splitters in the networks. The 7 different networks that we create for this demonstration can be visualised in the programmable circuit of Figure A.1. We input 2 quadrature-squeezed modes and 6 quantum-noise limited vacuum modes into the linear optics circuit, and we have the freedom to programmatically vary each beam-splitter's reflectivity. We simply set a beam-splitter reflectivity to $r = 100\%$ and turn it into a perfect mirror when we choose not to mix a particular input mode into the state. For example, for the familiar bipartite EPR state, we set the first beam-splitter reflectivity to $r = 50\%$ and set all other beam-splitters to mirrors. The measurement returns a bipartie EPR state, and 6 unmixed vacuum modes which are discarded. In general our linear optics networks have 7 beam-splitters. In order to create an N-qumode state we set $N - 1$ of these to function as beam-splitters and the remaining $8 - N$ to function as mirrors.

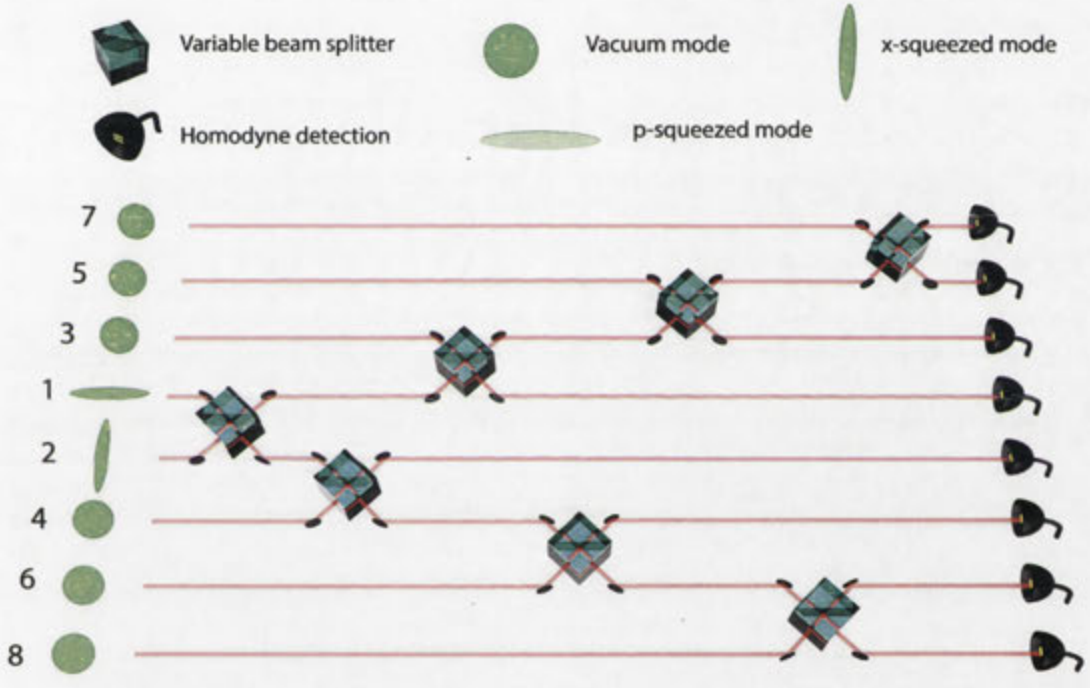

Figure A.1: Programmable Linear Optics Circuit for demonstrating steering.

Homodyne detection is employed to measure the inferred variances of each quantum mode in the state. Each mode is characterised by the conjugate quadrature operators $\hat{x}$ and $\hat{p}$ of the quantum harmonic oscillator mode of the light field. Optimal circuits are created that take into account asymmetries in squeezing values of the input modes.

In all of our networks, when the two squeezed modes are pure states and equal in squeezing magnitude, the optimal beam-splitter reflectivity of the first beam-splitter is always $r = 50\%$. This is unsurprising for the states containing an even number of qumodes. For the odd numbered states it is less intuitive, as one might expect that an unbalanced beam-splitter will favour the unbalanced network. However, this asymmetry can be balanced by the quadrature amplitude optimisation gains, owing to the larger parameter space available in optimising the inferred variances by weighting the qumodes via the gains. For two mixed states that are unequal in squeezing values, the optimal beam-splitter ratio for even numbered states is still $r = 50\%$. Although counter-intuitive, the symmetry condition makes sense considering we are characterising genuine EPR steering here, and therefore must consider all possible directions. Our symmetry breaks down for mixed-state inputs when we consider odd-numbered states. In this situation we benefit from

biasing the beam-splitters.

The most optimal networks we can create are found to have the following beam-splitter reflectivities (table A.1)

N	BS1	BS2	BS3	BS4	BS5	BS6	BS7
2	50	100	100	100	100	100	100
3	51.1	50	100	100	100	100	100
4	50	50	50	100	100	100	100
5	50.8	33.3	50	50	100	100	100
6	50	33.3	33.3	50	50	100	100
7	50.6	25	33.3	33.3	50	50	100
8	50	25	25	33.3	33.3	50	50

Table A.1: Beam-splittter reflectivities for optics networks.

Interestingly, it is only necessary to optimise the first beam-splitter in odd numbered states. We see that the reflectivities are 51.1%, 50.8%, and 50.6% for the 3−qumode, 5−qumode, and 7−qumode states, respectively.

A.1.2 Input mode basis

We operated the optical parametric amplifiers (OPAs) at parametric gain values of $G = 10$. The $\hat{x}$ and $\hat{p}$ variance measurements of the eight modes in the input basis are shown in table x, for a parametric gain of $G = 10$. The sideband frequency is $2.98kHz$ with a resolution bandwidth of $10kHz$.

Input	$\triangle^2\hat{p}$ (dB)	$\triangle^2\hat{x}$ (dB)
1	-3.64	8.89
2	-4.14	9.49
3	-0.04	-0.02
4	0.09	0.14
5	0.03	0.13
6	0.02	0.04
7	-0.03	0.24
8	-0.06	0.20

Note that the variances of the vacuum modes are not strictly equal to 0dB, as mentioned in the previous chapter. There is some technical noise that we have picked up in the process of extracting them from the measurements. Each mode vector is normalised and orthogonal to each other mode vector to very high precision, this is not the source of the discrepancies. Interestingly, I found that changing the orthonormal basis returns slightly different variance measurements for the vacuum modes. This suggests an asymmetry in the detected light.

While we did not provide a careful treatment in chapter 6, we investigate this noise here for the following reason. We see the effects of this noise more prominently in the steering experiments as opposed to the entanglement experiments. This is because the inferred variance measurements required for EPR steering contain a larger dependence on the anti-squeezing noise and asymmetric loss compared to the inseparability measurements.

Slight asymmetry in input mode basis

There is a slight asymmetry in the measurements of the two squeezed modes with respect to the 8 photodiodes used in the MPHD. This wasn't apparent in the chapter 6, largely because

the measured entanglement was quantified as inseparability, which is much less sensitive to anti-squeezing and asymmetry in general. We can exploit the asymmetric nature of EPR steering to observe this slight asymmetry. Figure A.2 shows two traces of the same data set, with slightly different theory traces. One has an offset in beam-splitter reflectivity.

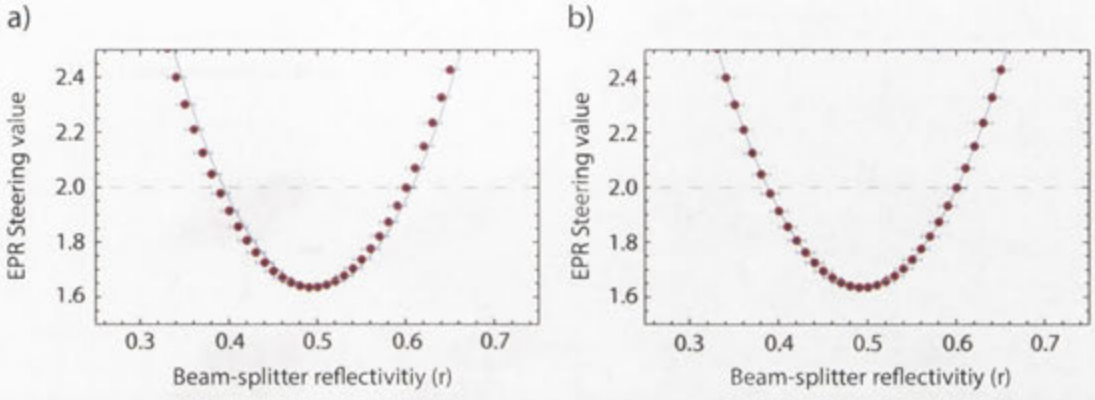

Figure A.2: Misalignment indicated by data analysis. Adjusting for a constant offset in beam-splitter reflectivity returns a perfect match between theory and experiment.

We see in (a) that there is a slight offset between theory and experiment. The theory trace here is produced by simulating exactly the same linear optics network, with the only information available about the input modes being their variances in both quadratures. The theory curve in Fig. A.2(b) is created as before but this time with a r=0.005 offset in the beam-splitter reflectivity. This suggests that we have a slight misalignment of the signal beam on the MPHD, and more specifically, photodiodes 1 to 4 detect slightly more or less light than photodiodes 5 to 8. One important assumption made in recovering the input mode basis is that the two halves were equal. In my genetic algorithm that recovers the 2 squeezed modes I imposed a condition that fixes pairs of photodiodes, so that we have the following:

$$[g1 \quad g2 \quad g3 \quad g4 \quad g4 \quad g3 \quad g2 \quad g1] \tag{A.6}$$

We therefore appreciate the slight error in measurement and include this in our error bars.

Investigations of bipartite steering were also performed. Interestingly, only losses or asymmetries introduced after the mixing beam-splitter influence any discrepancy between the two inferred variances $\Delta^2_{A|B}$ and $\Delta^2_{B|A}$. Any losses or asymmetries in squeezing before the beam-splitter is averaged out after mixing and the steering from A to B will equal the steering from B to A.

Networks for unbiased experimental conditions

When no bias is introduced regarding squeezing levels between the different input modes, the reflectivity for the first beam-splitter in the network is found by following an intuitive method. We see how many modes there will be in the reflected half of the network as a ratio of the total number of modes in the state. For an even-numbered state this will be $r = 50\%$ of course. For an odd-numbered state, it will be $\frac{N-1}{2N}$. Consider for example a 7-qumode state. There will be 3 modes in the reflected half of the network, and 4 modes in the transmitted half. Therefore the beam-splitter reflectivity will be $\frac{3}{7}$. In creating networks we consider each state that is produced by the programmable networks and compare the odd-numbered states against the networks that we would use if we had N pure and equal states. We see that the larger the state gets, the less effect the biasing of the first beam-splitter has. This is simply because the asymmetry diminishes

as the state gets larger,

$$\lim_{N\to\infty} \frac{N-1}{2N} = \frac{1}{2}. \tag{A.7}$$

A.2 Summary of results

The EPR correlations in each state can be visualised by parametrically plotting components of the inferred variance terms. This is shown in Fig. A.3.

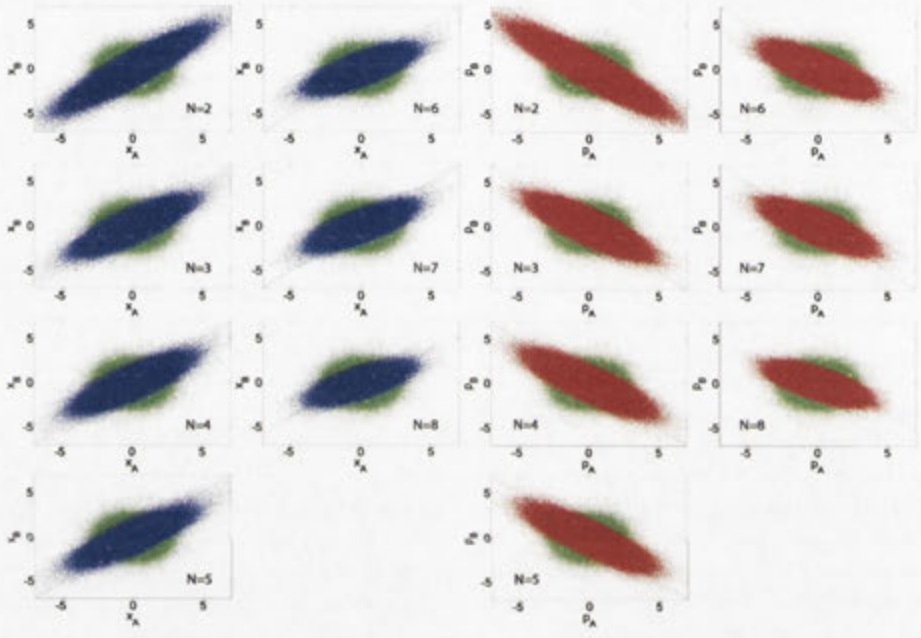

Figure A.3: Parametric plots for visualising correlations.

In all plots of Fig. A.3, the x axis is the $\hat{x}(\hat{p})$ quadrature amplitude of the first qumode in the state, and the y axis is the linear combination of the $\hat{x}(\hat{p})$ quadrature amplitudes of the remaining $N-1$ qumodes in the N-mode state. Perfect correlations would correspond to a semi-major axis of infinite length, strictly on the diagonal. This would require infinite energy and is unphysical; the eccentricities of the ellipses are indicative of finite squeezing. We see that the higher the number of qumodes in the state, the weaker the correlations become. This is evident in the slight rotation off the strictly diagonal axis in both quadratures, as well as the diminishing eccentricity of the correlation ellipses. This is due to additional vacuum contributions in our circuit as we go to higher mode numbers.

Figure A.4 quantifies the correlations in terms of the product $S^2_{j|k}$ of the inferred variances in both quadratures, termed the EPR number. For each N-mode state, there are N EPR numbers that can be tested, in order to confirm the multipartite EPR steering of each mode. Each EPR number represents the steering from one partition of the state to the other, or the direction of steering within the state.

We see that the condition $S^2_{j|k} < 1$ of equation (A.1) for the EPR steering of mode j is satisfied in each case.

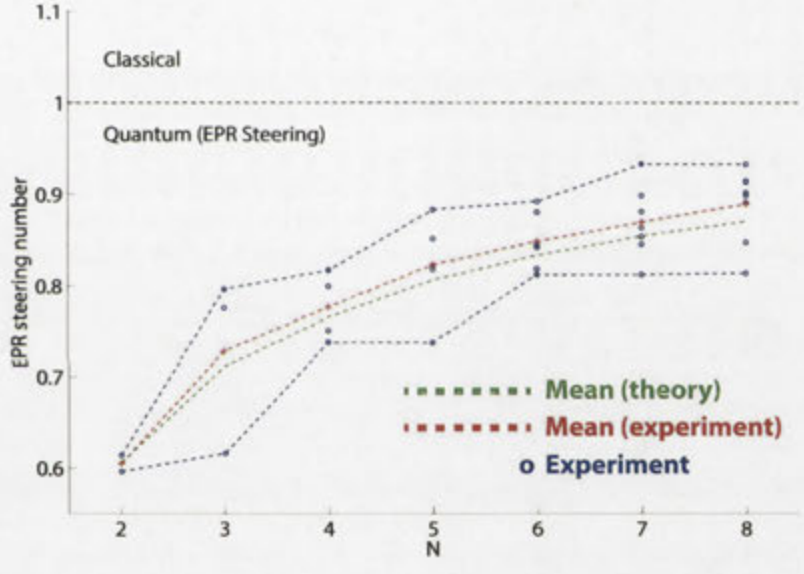

Figure A.4: Multipartite EPR steering values for the N-partite entangled states. The blue circles give for each N-partite state the N experimental values for the EPR steering number $S^2_{j|k}$, where we consider the steering of the jth mode ($j = 1,..., N$) by the remaining group k.

Bibliography

[1] R. Hanbury Brown and R. Q. Twiss, "Correlation between photons in two coherent beams of light," *Nature* **177**, 27 (1956).

[2] R. J. Glauber, *Quantum theory of optical coherence* (Wiley-VCH, Weinheim, 2007).

[3] T. H. Maiman, "Stimulated optical radiation in ruby," *Nature* **187**, 493 (1960).

[4] R. E. Slusher, L. W. Hollberg, B. Yurke, J. C. Mertz, and J. F. Valley, "Observation of squeezed states generated by four-wave mixing in an optical cavity," *Physical Review Letters* **55** (1985).

[5] L.-A. Wu, H. J. Kimble, J. L. Hall, and H. Wu, "Generation of squeezed states by parametric down conversion," *Physical Review Letters* **57**, 2520 (1986).

[6] A. Einstein, B. Podolsky, and P. Rosen, "Can quantum-mechanical description of physical reality be considered complete?," *Physical Review* **47**, 777 (1935).

[7] J. S. Bell, "On the Einstein Podolsky Rosen paradox," *Physics* **1**, 195 (1964).

[8] M. J. Matison, J. J. Murray, and M. S. Rabin, "Experimental test of local hidden-variable theories," *Physical Review D* **28**, 938 (1972).

[9] A. Aspect, P. Grangier, and G. Roger, "Experimental tests of realistic local theories via Bell's theorem," *Physical Review Letters* **47** (1981).

[10] A. Aspect, J. Dalibard, and G. Roger, "Experimental test of Bell's inequalities using time-varying analyzers," *Physical Review Letters* **49**, 1804 (1982).

[11] A. Aspect, P. Grangier, and G. Roger, "Experimental realization of Einstein-Podolsky-Rosen-Bohm gedankenexperiment: a new violation of Bell's ineqaulities," *Physical Review Letters* **49**, 91 (1982).

[12] M. D. Reid and P. D. Drummond, "Correlations of phase in nondegenerate parametric oscillation," *Physical Review Letters* **60**, 2731 (1988).

[13] Z. Y. Ou, S. F. Pereira, H. J. Kimble, and K. C. Peng, "Realization of the Einstein-Podolsky-Rosen paradox for continuous-variables," *Physical Review Letters* **68**, 3663 (1992).

[14] C. E. Shannon, "A mathematical theory of communication," *The Bell System Technical Journal* **27** (1948).

[15] D. Deutsch, "Quantum theory, the Church-Turing principle and the universal quantum computer," *Proceedings of the Royal Society A: Mathematical, Physical and Engineering Sciences* **400**, 97 (1985).

[16] R. Raussendorf and H. J. Briegel, "A one-way quantum computer," *Physical Review Letters* **86**, 5188 (2001).

[17] L. Vaidman, "Teleportation of quantum states," *Physical Review A* **49** (1994).

[18] S. L. Braunstein, "Teleportation of continuous quantum variables," *Physical Review Letters* **80**, 869 (1998).

[19] A. Furusawa, J. L. Sø rensen, S. L. Braunstein, and C. A. Fuchs, "Unconditional quantum teleportation," *Science* **282**, 706 (1998).

[20] M. A. Nielsen and I. L. Chuang, *Quantum computation and quantum information* (Cambridge University Press, 2000).

[21] T. Monz, P. Schindler, J. T. Barreiro, M. Chwalla, D. Nigg, W. a. Coish, M. Harlander, W. Hänsel, M. Hennrich, and R. Blatt, "14-qubit entanglement: creation and coherence," *Physical Review Letters* **106**, 130506 (2011).

[22] N. C. Menicucci, "Temporal-mode continuous-variable cluster states using linear optics," *Physical Review A* **83**, 062314 (2011).

[23] U. Leonhardt, *Essential Quantum Optics* (Cambridge University Press, 2010).

[24] A. Furusawa and P. van Loock, *Quantum Teleportation and Entanglement* (WILEY-VCH, 2011).

[25] W. P. Bowen, *Experiments towards a Quantum Information Network with Squeezed Light and Entanglement*, Phd thesis, The Australian National University 2003.

[26] W. Heisenberg, "U ber den anschaulichen inhalt der quantentheoretischen kinematik und mechanik," *Zeitschrift fur Physick* **43** (1927).

[27] R. J. Glauber, "Coherent and incoherent states of the radiation field," *Physical Review* **131**, 2766 (1963).

[28] E. Wigner, "On the quantum correction for thermodynamic equilibirum," *Physical Review* **40**, 749 (1932).

[29] G. Adesso, *Entanglement of Gaussian states*, Phd thesis, Universita delgi studi di Salerno 2006.

[30] M. A. Nielsen, "Cluster-state quantum computation," *Reports on Mathematical Physics* **57**, 147 (2006).

[31] J. Zhang and S. L. Braunstein, "Continuous-variable Gaussian analog of cluster states," *Physical Review A* **73**, 032318 (2006).

[32] N. Menicucci, P. van Loock, M. Gu, C. Weedbrook, T. Ralph, and M. Nielsen, "Universal quantum computation with continuous-variable cluster states," *Physical Review Letters* **97**, 110501 (2006).

[33] Y. Miwa, J.-I. Yoshikawa, P. van Loock, and A. Furusawa, "Demonstration of a universal one-way quantum quadratic phase gate," *Physical Review A* **80**, 050303 (2009).

[34] P. van Loock, C. Weedbrook, and M. Gu, "Building Gaussian cluster states by linear optics," *Physical Review A* **76**, 032321 (2007).

[35] M. Gu, *Quantum complexity, emergence and computation by measurement*, Phd thesis, The University of Queensland 2008.

[36] N. C. Menicucci, S. T. Flammia, and P. van Loock, "Graphical calculus for Gaussian pure states," *Physical Review A* **83**, 042335 (2011).

[37] S. Yokoyama, R. Ukai, S. C. Armstrong, C. Sornphiphatphong, T. Kaji, S. Suzuki, J.-I. Yoshikawa, H. Yonezawa, N. C. Menicucci, and A. Furusawa, "Ultra-large-scale continuous-variable cluster states multiplexed in the time domain," *Nature Photonics* **7**, 3 (2013).

[38] J.-F. Morizur, *Quantum protocols with transverse spatial modes*, Phd thesis, The Australian National University and The Universite Pierre et Marie Curie 2011.

[39] R. Ukai, *The generation of four-mode continuous-variable cluster states*, Honours thesis, University of Tokyo 2008.

[40] B. C. Buchler, *Electro-optic Control of Quantum Measurements*, Phd thesis, Australian National University 2001.

[41] M. S. Stefszky, *Generation and detection of low-frequency squeezing for gravitational-wave detection*, Phd thesis, Australian National University 2012.

[42] A. Yariv, *Quantum electronics*, 3rd ed. (John Wiley and Sons., Singapore, 1989).

[43] N. Lee, H. Benichi, Y. Takeno, S. Takeda, J. Webb, E. Huntington, and A. Furusawa, "Teleportation of nonclassical wave packets of light.," *Science (New York, N.Y.)* **332**, 330 (2011).

[44] S. Takeda, T. Mizuta, M. Fuwa, P. van Loock, and A. Furusawa, "Deterministic quantum teleportation of photonic quantum bits by a hybrid technique.," *Nature* **500**, 315 (2013).

[45] D. A. Shaddock, *Advanced Interferometry for Gravitational Wave Detection*, PhD thesis The Australian National University 2000.

[46] E. D. Black, "An introduction to PoundDreverHall laser frequency stabilization," *American Journal of Physics* **69**, 79 (2001).

[47] S. Armstrong, J.-F. Morizur, J. Janousek, B. Hage, N. Treps, P. K. Lam, and H.-A. Bachor, "Programmable multimode quantum networks," *Nature communications* **3** (2012).

[48] P. A. Blume, *The LabVIEW style book*, Fourth ed. (Prentice Hall, Indiana, 2010).

[49] B. M. Sparkes, H. M. Chrzanowski, D. P. Parrain, B. C. Buchler, P. K. Lam, and T. Symul, "A scalable, self-analyzing digital locking system for use on quantum optics experiments.," *The Review of scientific instruments* **82**, 075113 (2011).

[50] R. P. Feynman, "Simulating physics with computers," *International Journal of Theoretical Physics* **21**, 467 (1982).

[51] N. Menicucci, S. Flammia, and O. Pfister, "One-way quantum computing in the optical frequency comb," *Physical Review Letters* **101**, 130501 (2008).

[52] N. C. Menicucci, X. Ma, and T. C. Ralph, "Arbitrarily large continuous-variable cluster states from a single quantum nondemolition gate," *Physical Review Letters* **104** (2010).

[53] S. L. Borevich, Z. I., Krupetskii, "Subgroups of the unitary group that contain the group of diagonal matrices," *J. Math. Sci.* **17**, 1951 (1981).

[54] J.-F. Morizur, L. Nicholls, P. Jian, S. Armstrong, N. Treps, B. Hage, M. Hsu, W. Bowen, J. Janousek, and H.-A. Bachor, "Programmable unitary spatial mode manipulation.," *Journal of the Optical Society of America. A, Optics, image science, and vision* **27**, 2524 (2010).

[55] Http://www.thorlabs.com, "Thorlabs, Inc.," 2014.

[56] J. Janousek, *Investigation of non-classical light and its application in ultrasensitive measurements*, Phd thesis, Technical university of Denmark 2007.

[57] J.-F. Morizur, S. Armstrong, N. Treps, J. Janousek, and H.-A. Bachor, "Spatial reshaping of a squeezed state of light," *The European Physical Journal D* **61**, 237 (2011).

[58] S. Armstrong, "Single-photon metrology," *Nature Photonics* **6**, 636 (2012).

[59] M. Yukawa, R. Ukai, P. van Loock, and A. Furusawa, "Experimental generation of four-mode continuous-variable cluster states," *Physical Review A* **78**, 012301 (2008).

[60] C.-Y. Lu, X.-Q. Zhou, O. Gühne, W.-B. Gao, J. Zhang, Z.-S. Yuan, A. Goebel, T. Yang, and J.-W. Pan, "Experimental entanglement of six photons in graph states," *Nature Physics* **3**, 91 (2007).

[61] X. Su, Y. Zhao, S. Hao, C. Xie, and K. Peng, "Experimental preparation of eight-partite cluster state for photonic qumodes," *Optics letters* **37** (2012).

[62] J. L. O'Brien, A. Furusawa, and J. Vučković, "Photonic quantum technologies," *Nature Photonics* **3**, 687 (2009).

[63] H. W. Li, J. Wabnig, D. Bitauld, P. Shadbolt, a. Politi, a. Laing, J. L. O'Brien, and a. O. Niskanen, "Calibration and high fidelity measurement of a quantum photonic chip," *New Journal of Physics* **15**, 063017 (2013).

[64] J. Janousek, K. Wagner, J.-F. Morizur, N. Treps, P. K. Lam, C. C. Harb, and H.-A. Bachor, "Optical entanglement of co-propagating modes," *Nature Photonics* **3**, 399 (2009).

[65] M. Lassen, G. Leuchs, and U. Andersen, "Continuous variable entanglement and squeezing of orbital angular momentum states," *Physical Review Letters* **102**, 163602 (2009).

[66] M. Pysher, *No Title*, Phd thesis, University of Virginia 2011.

[67] M. Chen, N. C. Menicucci, and O. Pfister, "Experimental realization of multipartite entanglement of 60 modes of the quantum optical frequency comb," *arXiv preprint* (2013) arXiv:1311.2957v2.

[68] J. Roslund, R. Medeiros de Araujo, S. Jiang, C. Fabre, and N. Treps, "Wavelength-multiplexed quantum networks with ultrafast frequency combs," *arXiv* (2013) arXiv:1307.1216v1.

[69] V. Delaubert, D. a. Shaddock, P. K. Lam, B. C. Buchler, H.-A. Bachor, and D. E. McClelland, "Generation of a phase-flipped Gaussian mode for optical measurements," *Journal of Optics A* **4**, 393 (2002).

[70] M. Beck, "Quantum state tomography with array detectors.," *Physical Review Letters* **84**, 5748 (2000).

[71] M. Beck, C. Dorrer, and I. Walmsley, "Joint quantum measurement using unbalanced array detection," *Physical Review Letters* **87**, 253601 (2001).

[72] V. Delaubert, *Quantum imaging with a small number of transverse modes*, Phd thesis, The Australian National University and The Universite Pierre et Marie Curie 2007.

[73] T. Aoki, N. Takei, H. Yonezawa, K. Wakui, T. Hiraoka, and A. Furusawa, "Experimental creation of a fully inseparable tripartite continuous-variable state," *Physical Review Letters* **91**, 080404 (2003).

[74] P. van Loock and A. Furusawa, "Detecting genuine multipartite continuous-variable entanglement," *Physical Review A* **67**, 052315 (2003).

[75] C. Weedbrook, S. Pirandola, R. Garcia-Patron, N. J. Cerf, T. C. Ralph, J. H. Shapiro, and S. Lloyd, "Gaussian quantum information," *Reviews of Modern Physics* **84**, 621 (2011) 1110.3234.

[76] P. van Loock, "Optical hybrid approaches to quantum information," *Laser & Photonics Reviews* **5**, 167 (2011).

[77] M. Gu, C. Weedbrook, N. Menicucci, T. Ralph, and P. van Loock, "Quantum computing with continuous-variable clusters," *Physical Review A* **79**, 062318 (2009).

[78] X. Su, A. Tan, X. Jia, J. Zhang, C. Xie, and K. Peng, "Experimental preparation of quadripartite cluster and Greenberger-Horne-Zeilinger entangled states for continuous variables," *Physical Review Letters* **98**, 070502 (2007).

[79] X. Su, S. Hao, X. Deng, L. Ma, M. Wang, X. Jia, C. Xie, and K. Peng, "Gate sequence for continuous variable one-way quantum computation.," *Nature communications* **4**, 2828 (2013).

[80] M. Pysher, Y. Miwa, R. Shahrokhshahi, R. Bloomer, and O. Pfister, "Parallel generation of quadripartite cluster entanglement in the optical frequency comb," *Physical Review Letters* **107**, 030505 (2011).

[81] van Loock P and S. Braunstein, "Multipartite entanglement for continuous variables: A quantum teleportation network," *Physical Review Letters* **84**, 3482 (2000).

[82] C. H. Bennett, G. Brassard, C. Crepeau, R. Jozsa, A. Peres, and W. K. Wootters, "Teleporting an unknown quantum state via dual classical and Einstein-Podolsky-Rosen channels.," *Physical Review Letters* **70** (1993).

[83] R. Raussendorf, D. Browne, and H. Briegel, "Measurement-based quantum computation on cluster states," *Physical Review A* **68**, 022312 (2003).

[84] H.-A. Bachor and T. C. Ralph, *A Guide to Experiments in Quantum Optics* (WILEY-VCH, 2004).

[85] F. A. S. Barbosa, A. S. Coelho, K. N. Cassemiro, P. Nussenzweig, C. Fabre, M. Martinelli, and A. S. Villar, "Beyond spectral homodyne detection: complete quantum measurement of spectral modes of light," *arXiv* (2013) arXiv:1308.5650v1.

[86] H. Benichi, *Research on non-classical states experimental quantum teleportation: conditional operations, theoretical mode and tomography algorithms*, Phd thesis, The University of Tokyo 2012.

[87] R. Ukai, *Research on spatial and temporal multimode quantum information processing*, Phd thesis, The University of Tokyo 2013.

[88] Y. Miwa, *Research on the superposition of odd photon number states and the squeezing of quadrature amplitudes*, Phd thesis, The University of Tokyo 2012.

[89] O. Morin, C. Fabre, and J. Laurat, "Experimentally accessing the optimal temporal mode of traveling quantum light states," *Physical Review Letters* **111**, 213602 (2013).

[90] V. Jacques, E. Wu, F. Grosshans, F. Treussart, P. Grangier, A. Aspect, and J.-F. Roch, "Experimental realization of Wheeler's delayed-choice gedanken experiment.," *Science* **315**, 966 (2007).

[91] T. Kaji, *Research on large-scale quantum entangled state preparation*, Honours thesis, The University of Tokyo 2013.

[92] S. Yokoyama, *Research on 2-mode Gaussian operations using continuous-variable cluster states*, Masters thesis, The University of Tokyo 2012.

[93] R. N. Alexander, S. C. Armstrong, R. Ukai, and N. C. Menicucci, "Noise analysis of single-qumode Gaussian operations using continuous-variable cluster states," *arXiv preprint* , 1 (2013) arXiv:1311.3538v1.

[94] N. C. Menicucci, "Fault-tolerant measurement-based quantum computing with continuous-variable cluster states," *Physical Review Letters* **112**, 120504 (2014).

[95] P. W. Shor, "Algorithms for quantum computation : discrete logarithms and factoring," *35th Annual Symposium on the Foundations of Computer Science, 1994 Proceedings* , 124 (1994).

[96] L. K. Grover, "A fast quantum mechanical algorithm for database search," *STOC '96 Proceedings of the twenty-eighth annual ACM symposium on Theory of computing* , 212 (1996).

[97] S. Sefi and P. van Loock, "How to decompose arbitrary Continuous-Variable Quantum Operations," *Physical Review Letters* **107**, 170501 (2011).

[98] R. Ukai, N. Iwata, Y. Shimokawa, S. C. Armstrong, A. Politi, J.-I. Yoshikawa, P. van Loock, and A. Furusawa, "Demonstration of unconditional one-way quantum computations for continuous variables," *Physical Review Letters* **106**, 240504 (2011).

[99] R. Ukai, J.-I. Yoshikawa, N. Iwata, P. van Loock, and A. Furusawa, "Universal linear Bogoliubov transformations through one-way quantum computation," *Physical Review A* **81**, 032315 (2010).

[100] S. L. Braunstein and P. V. Loock, "Quantum information with continuous variables," *Reviews of Modern Physics* **77**, 513 (2005).

[101] A. K. Lenstra, H. W. Lenstra, M. S. Manasse, and J. M. Pollard, "The number field sieve," *STOC '90 Proceedings of the twenty-second annual ACM symposium on Theory of computing* , 564 (1990).

[102] Http://www.quintessencelabs.com, "QuintessenceLabs,".

[103] Http://www.idquantique.com, "id Quantique,".

[104] I. Bloch, J. Dalibard, and S. Nascimbène, "Quantum simulations with ultracold quantum gases," *Nature Physics* **8**, 267 (2012).

[105] B. P. Lanyon, C. Hempel, D. Nigg, M. Müller, R. Gerritsma, F. Zähringer, P. Schindler, J. T. Barreiro, M. Rambach, G. Kirchmair, M. Hennrich, P. Zoller, R. Blatt, and C. F. Roos, "Universal digital quantum simulation with trapped ions.," *Science* **334**, 57 (2011).

[106] R. Blatt and C. F. Roos, "Quantum simulations with trapped ions," *Nature Physics* **8**, 277 (2012).

[107] D. Deutsch, *The beginning of infinity: explanations that transform the world*, 1 ed. (Allen Lane, 2011).

[108] S. J. Devitt, W. J. Munro, and K. Nemoto, "Quantum error correction for beginners.," *Reports on progress in physics. Physical Society* **76**, 076001 (2013).

[109] Y. Miwa, R. Ukai, J.-I. Yoshikawa, R. Filip, P. van Loock, and A. Furusawa, "Demonstration of cluster-state shaping and quantum erasure for continuous variables," *Physical Review A* **82**, 032305 (2010).

[110] S. Braunstein, "Squeezing as an irreducible resource," *Physical Review A* **71**, 055801 (2005).

[111] H. Yonezawa, A. Furusawa, and P. van Loock, "Sequential quantum teleportation of optical coherent states," *Physical Review A* **76**, 032305 (2007).

[112] S. L. Braunstein, "Quantum error correction for communication with linear optics," *Nature* **394**, 47 (1998).

[113] S. L. Braunstein, C. a. Fuchs, H. J. Kimble, and P. van Loock, "Quantum versus classical domains for teleportation with continuous variables," *Physical Review A* **64**, 022321 (2001).

[114] H. J. Kimble, "The quantum internet.," *Nature* **453**, 1023 (2008).

[115] P. Walther, K. J. Resch, T. Rudolph, E. Schenck, H. Weinfurter, V. Vedral, M. Aspelmeyer, and a. Zeilinger, "Experimental one-way quantum computing.," *Nature* **434**, 169 (2005).

[116] R. Ukai, S. Yokoyama, J.-I. Yoshikawa, P. van Loock, and A. Furusawa, "Demonstration of a controlled-phase gate for continuous-variable one-way quantum computation," *Physical Review Letters* **107**, 250501 (2011).

[117] A. Stute, B. Casabone, P. Schindler, T. Monz, P. O. Schmidt, B. Brandstätter, T. E. Northup, and R. Blatt, "Tunable ion-photon entanglement in an optical cavity.," *Nature* **485**, 482 (2012).

[118] J.-I. Yoshikawa, T. Hayashi, T. Akiyama, N. Takei, A. Huck, U. Andersen, and A. Furusawa, "Demonstration of deterministic and high fidelity squeezing of quantum information," *Physical Review A* **76**, 060301 (2007).

[119] M. Horodecki, P. Horodecki, and R. Horodecki, "Separability of mixed states: necessary and sufficient conditions," *Physical Letters A* **223**, 1 (1996).

[120] A. Peres, "Separability criterion for density matrices," *Physical Review Letters* **77**, 1413 (1996).

[121] R. Simon, "Peres-horodecki separability criterion for continuous variable systems," *Physical Review Letters* **84**, 2726 (2000).

[122] M. Yukawa, K. Miyata, H. Yonezawa, P. Marek, R. Filip, and A. Furusawa, "Emulating quantum cubic nonlinearity," *Physical Review A* **88**, 053816 (2013).

[123] E. Schroedinger, "Steering," *Naturwissenschaften* **23**, 807 (1935).

[124] H. M. Wiseman, S. J. Jones, and a. C. Doherty, "Steering, entanglement, nonlocality, and the Einstein-Podolsky-Rosen paradox," *Physical Review Letters* **98**, 140402 (2007).

[125] E. Cavalcanti, S. Jones, H. Wiseman, and M. Reid, "Experimental criteria for steering and the Einstein-Podolsky-Rosen paradox," *Physical Review A* **80**, 032112 (2009).

[126] Q. Y. He and M. D. Reid, "Genuine multipartite Einstein-Podolsky-Rosen steering," *arXiv preprint* (2012) arXiv:1212.2270v1.

[127] G. Svetlichny, "Distinguishing three-body from two-body nonseparability by a Bell-type inequality," *Physical Review D* **35**, 3066 (1987).